Towards improved laboratory X-ray tomography imaging : optimization of acquisition parameters and use of photon-counting detectors

Habib Murtaza

THÈSE

Pour obtenir le grade de

DOCTEUR DE L'UNIVERSITE GRENOBLE ALPES

Spécialité : **2MGE : Matériaux, Mécanique, Génie civil, Electrochimie**

Arrêté ministériel :25 Mai 2016

Présentée par

Habib MURTAZA

Thèse dirigée par **Sabine ROLLAND DU ROSCOAT**, Maître de conférence, Université Grenoble Alpes, et
codirigée par **Luc SALVO**, Professor, Grenoble INP**,** et **Pierre LHUISSIER**, Chargé de Recherche, Grenoble INP

préparée au sein du **Laboratoire Soils, Solides, Structures et Risques** et **Laboratoire Science et Ingénierie des Matériaux et Procédés**
dans **l'École Doctorale I-MEP2 – Ingénierie – Matériaux, Mécanique, Environnement, Energétique, Procédés, Production**

Towards improved laboratory X-ray tomography imaging: optimization of acquisition parameters and use of photon-counting detectors

Thèse soutenue publiquement le **« 30 Mars 2022 »**,
devant le jury composé de :

Monsieur DANIEL BELLET
Professeur, Grenoble INP, Président
Monsieur ERIC MAIRE
Directeur de Recherche, CNRS, Rapporteur
Monsieur DOMINIQUE BERNARD
Directeur de Recherche, ICMCB CNRS, Rapporteur
Monsieur PIERRE DUMONT
Professeur, INSA Lyon, Examinateur
Madame SABINE ROLLAND DU ROSCOAT
Maître de Conférence, Université Grenoble Alpes, 3SR, Directeur de thèse
Monsieur PIERRE LHUISSIER
Chargé de Recherche, CNRS, Grenoble INP, SIMAP, Co-directrice de thèse
Monsieur LUC SALVO
Professeur, Grenoble INP, SIMAP, Co-directrice de thèse
Madame BARBARA FAYARD
Présidente Novitom, Grenoble, Invitée

Acknowledgments

This thesis is the outcome of a remarkable three-year period that I spent in Laboratory 3SR and Laboratory SIMAP in Grenoble, France. Many people had a (direct and indirect) influence on the final outcome during this time, for which I am grateful.

First and foremost, I'm extremely grateful to my supervisors, Mrs. Sabine Rolland du Roscoat, Mr. Pierre Lhuissier and Mr. Luc Salvo. Thank you for introducing me to the amazing X-ray CT imaging world. Thank you for your guidance, patience, constructive feedback and enthusiasm throughout this entire time. Without your input and persistent encouragement, this thesis would not have been possible.

Next, I would like to convey my heartfelt gratitude to all the jury members for facilitating an enjoyable and productive discussion on the day of the defense. I am especially grateful to thank the two reviewers of the manuscript, Mr. Eric Maire and Mr. Dominique Bernard, for their constructive feedback and detailed report, which was extremely valuable for further improvement. It is my pleasure to thank Mr. Daniel Bellet for accepting to be the president of the jury and to Mr. Pierre Dumont for accepting to be the thesis examiner. I'm grateful to Mrs. Barbara Fayard for accepting to be a Jury member as well. I feel lucky to have such a competent, well-known jury member; you all are a dream team.

I am thankful to the University Grenoble Alpes (UGA) IDEX-IRS for providing financial support for my thesis project. I am also thankful to Remi Granger for the amazing collaboration that we did for approximately two years while working on Photon-Counting Detectors.

I want to thank my friends and colleagues both in Laboratory 3SR and Laboratory SIMAP for their amazing support and the wonderful time we spent together over the last three years. Last but not least, I owe my deepest gratitude to my parents and siblings for their belief in me. And for being with me through thick and thin, encouraging me and keeping me sane. It would have been impossible without him.

Thank you all for making this happen!

Abstract

This study deals with developments to increase the possibilities offered by laboratory X-ray computed tomography (CT) in material science by focusing on contrast enhancement and on time resolution aspects. First, the feasibility of using a new generation photon-counting detector (PCD) in lab-CT was evaluated. The characterization of the standard imaging performances and the spectral capabilities of four PCDs were carried out and compared to a standard flat-panel detector. The potential of PCD towards spectral and single-shot K-edge imaging was investigated. Second, a model-based optimization strategy is developed to define the suitable CT scanning parameters for dynamic in situ acquisitions with an image quality allowing qualitative or quantitative analysis. The model is based on three modules: modelling noise in the feature of interest, X-ray absorption simulation tool, and the screening algorithm that outputs the different possible scanning configurations associated with the probability of detection of the interested feature size for each configuration. A real-time in-situ test with the sub-minute temporal resolution was performed with the experimentally optimized CT setup. The experimental configuration is confronted with the proposed optimization model configurations, which were found to be in-line with the chosen setup. The application corresponds to the real-time monitoring of microstructural evolution of 3D printed cellulose parts during air-drying phenomena with qualitative and quantitative analysis. It illustrates the quantitative characterization capabilities of lab-CT for high-speed in-situ imaging.

Keywords: X-ray tomography, In-situ tomography, Time-resolved imaging, Photon-counting detector, Parameter optimization, Image analysis

Resumé

Cette étude a l'objectif de développer les possibilités offertes par la tomographie à rayons X de laboratoire utilisée en science des matériaux en se concentrant sur l'amélioration du contraste et sur l'aspect de la résolution temporelle. Tout d'abord, la faisabilité de l'utilisation d'un détecteur de comptage de photons (PCD) de nouvelle génération en laboratoire CT a été évaluée. La caractérisation des performances d'imagerie standard et des capacités spectrales de quatre PCD a été réalisée et comparée à un détecteur à écran plat standard. Le potentiel de la PCD vers l'imagerie spectrale et mono-coup K-edge a été étudié. Deuxièmement, une stratégie d'optimisation basée sur un modèle est développée. Elle vise à sélectionner les paramètres de scanner appropriés pour des acquisitions dynamiques in-situ avec une qualité d'image permettant une analyse qualitative ou quantitative. Le modèle est basé sur trois modules : la modélisation du bruit dans la caractéristique d'intérêt, l'outil de simulation d'absorption des rayons X et l'algorithme de dépistage qui produit les différentes configurations de balayage possibles associées à la probabilité de détection de la taille de la caractéristique intéressée pour chaque configuration. Un test in-situ en temps réel avec une résolution temporelle inférieure à la minute a été réalisé avec la configuration CT expérimentalement optimisée comme aspect d'application de la thèse. La configuration expérimentale est confrontée aux configurations de modèle d'optimisation proposées, qui se sont révélées conformes à la configuration choisie. L'application correspond au suivi en temps réel de l'évolution microstructurale des pièces en cellulose imprimées en 3D lors des phénomènes de séchage à l'air avec analyse qualitative et quantitative. Elle illustre les capacités de caractérisation quantitative du lab-CT pour l'imagerie in-situ à grande vitesse.

Mots-Clés: Tomographie à rayons X, Tomographie in-situ, Imagerie temporellement résolue, Détecteur compteur de photons, Optimisation des paramètres, Analyse d'image

Contents

List of Figures

List of Tables

0.1 General introduction

The mechanical and physical properties of heterogeneous or structured media such as geomaterials, fiber-reinforced polymer composites, biological fabrics, or metals are strongly dependent on their microstructure: the volume fractions of the phases constituting the materials, the connectivity between the phases as well as the connectivity between the different objects (precipitates, pores, intermetallics) constituting the phases, their shape and their crystallographic orientations (in the case of crystalline materials).

The quantification of these microstructural parameters at the micro or nano-metric scale is a necessary step to a better understanding and to enrich the modelling of the behaviour of these materials. Such an understanding can also be used for materials optimization.

X-ray micro-computed tomography (CT) is an innovative technique that allows to obtain a non-destructive 3D mapping of the internal structure of the materials. It has allowed such quantification possible [Salvo et al., 2003, Maire and Withers, 2014], and has revolutionized both the experimental and numerical research in material science. X-ray CT technique can also be applied to follow the structural changes in materials during mechanical or thermal treatment in real-time and under real conditions by adding specialized experimental devices to the tomography setup, such as mechanical devices or furnaces. Such acquisitions are referred to as in-situ acquisitions or time-resolved CT or 4D imaging.

The obtained 3D datasets at different timescales of in-situ acquisitions, called 4D datasets, can be quantified for microstructure evolution [Salvo et al., 2010, Buffiere et al., 2010, Withers et al., 2021]. The quality of the microstructural analysis that can be performed depends entirely on the contrast and quality of the images obtained from X-ray CT.

Different sources can be used to perform the X-ray CT: (i) lab-based X-ray tubes that produce a divergent and polychromatic X-ray beam and offer a limited X-ray flux, (ii) synchrotron radiations that produce a coherent X-ray beam with a very high flux (at least 1000 times larger than the lab X-ray tubes).

Different modes to perform tomography are currently available with synchrotron sources such as absorption tomography, holotomography, phase-contrast tomography, diffraction contrast tomography, and spectral tomography. Laboratory tomographs, which are easier to access, appeared in early 2000, do not offer all the imaging potential of synchrotron radiation in a systemic and simple way and often remain limited to imaging in absorption mode despite some advances in phase imaging and diffraction contrast imaging [King et al., 2013, Labriet et al., 2019, Maire and Withers, 2014].

This thesis only deals with absorption tomography, so other modes are not discussed. Absorption tomography provides a 3D mapping of the sample density and relies on the fact that the intensity of the incident beam decreases exponentially with increasing propagating distance in the matter. The decrease is directly related to the linear attenuation coefficient of the material, which is further related to the density and the atomic number of the material. The larger the difference in the attenuation coefficient of materials, the more contrasted will be the image suitable for quantification.

Synchrotron absorption CT is currently used to obtain the internal structure of a

sample at a resolution of 1 µm with an acquisition time of the order of a minute or even in seconds. Developments have been made to obtain 3D data sets at nano-metric pixel sizes in a few seconds [Maire and Withers, 2014, Villanova et al., 2017]. These very short acquisition times are made possible thanks to a very high X-ray photon flux and to very sensitive and high frame-rate detectors. Moreover, due to the pink X-ray beam, very high quality and contrasted images are obtained, which can be subjected to quantitative analysis.

In laboratory tomographs, the spatial resolution is generally in the order of a few microns. Although the spatial resolution aspect has been partially solved (some laboratory tomographs allow sub-micron resolutions), the temporal resolution aspect and the discrimination power between two close chemical constituents still remain an issue to a wider range of applications with laboratory CT.

Laboratory CT is limited in comparison to the synchrotron CT on the following two major points:

- ✧ Acquisition times are significantly longer (in the order of an hour): this is due to the low power of the X-ray beam and is associated with the efficiency of the detectors (Flat-panel, CCD, or CMOS type equipped with scintillators). Due to this, high-speed in-situ acquisitions remain limited.
  Figure 1 shows the achieved pixel size against scan time for in-situ CT experiments from the literature (between 1995 and 2020) using synchrotron (red shades) and laboratory (green shades) CT. Figure 1 reveals that most of the high spatial resolution and fast scans have been performed using synchrotron CT illustrating the limitation of laboratory CT.

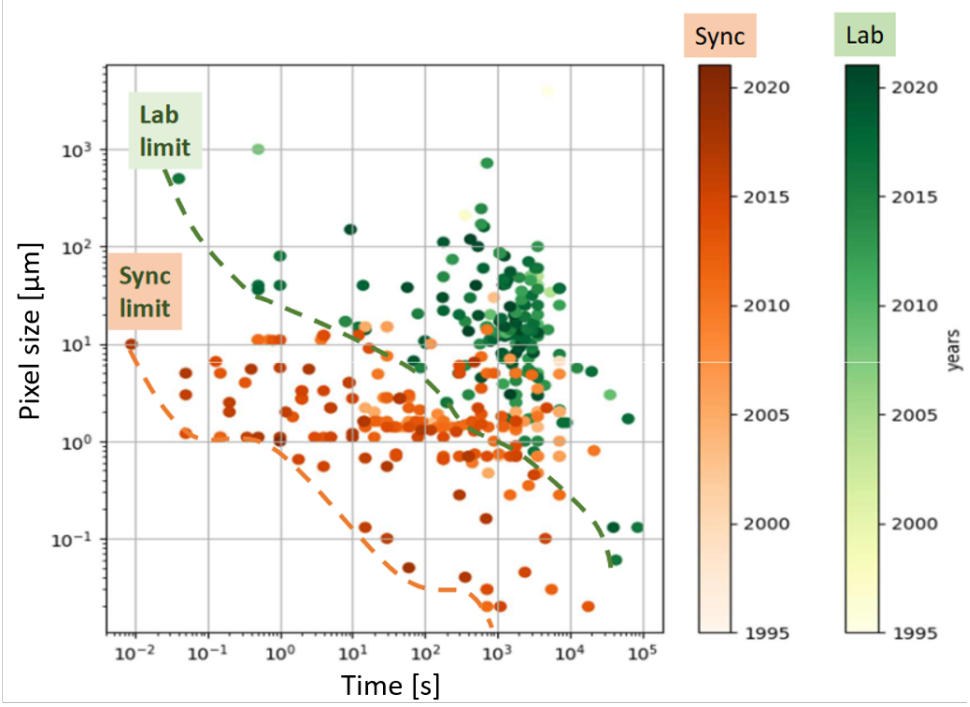

Figure 1: State of the art of in situ X-ray tomography: pixel size versus scan time illustrating the state of the art for in situ X-ray synchrotron and laboratory computed tomography. [Villanova et al., 2017, Zwanenburg et al., 2021]

✧ The image quality and the contrast obtained on the images that allow the microstructural characterization is low for materials, especially with low X-ray absorption coefficients such as biological tissues or polymers, because of the polychromaticity of the lab X-ray source beam.

The obtained image quality of a CT scan also depends on the selected acquisition parameters. These acquisition parameters are user-defined and include X-ray source, geometry, and detector parameters settings. The selection of different parameters for a CT scan will result in a difference in image quality. The influence of the acquisition parameters on the image quality was reported by a number of studies [Carmignato, 2012, Gómez and Smith, 2020, Plessis et al., 2018]; however, no accepted global optimization protocols exist for the suitable selection of acquisition parameters for a CT scan. The optimum selection of these parameters becomes even more important when high-speed scans are required during the imaging of the dynamic process because, in such cases, the image quality is further reduced due to the motion blurring.

Due to the limitation of lab-based hardware, traditionally faster in-situ acquisitions were largely performed at a synchrotron. However, limited access to synchrotrons restricts the number of experiments that can be performed; therefore, the developments in laboratory-scale tomographs have increased drastically over the last few years since they're easily accessible, small-scale, and inexpensive facilities compared to synchrotrons. This increased interest in lab-CT can also be observed in the number of publications involving faster scanning applications in the last ten years, as shown in Figure 2 [Zwanenburg et al., 2021].

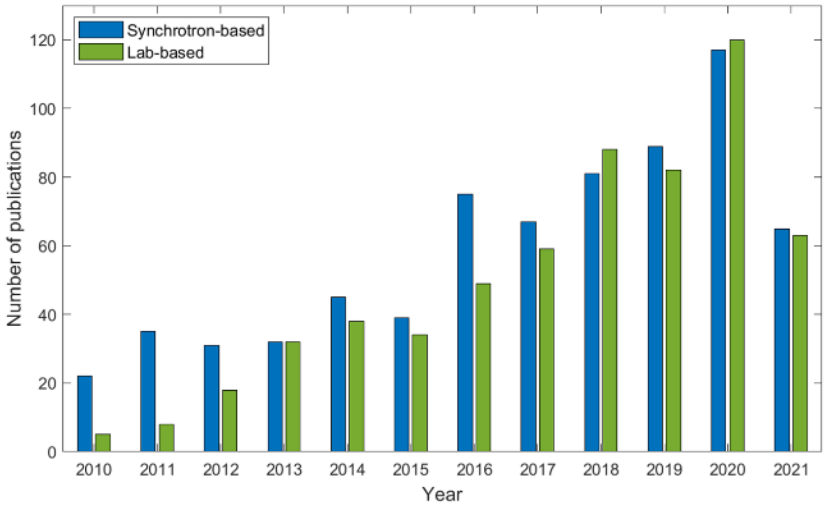

Figure 2: Publications on high-speed and in-situ scanning for synchrotron and lab-based CT over the last years. [Zwanenburg et al., 2021]

It is now possible to achieve scan acquisition time the order of a few minutes in lab-based facilities dependent on the sample, resolution, FOV, and the objective of analysis. However, faster acquisition in sub-minute timescale is still desired. Few examples can be found in the literature, with the reported scan time under sub-minute, but these scans were mainly qualitatively analyzed due to the limited image quality [Bultreys et al., 2016, Dewanckele et al., 2020]. Therefore, there is a need to improve lab-based in-situ X-ray imaging techniques so that high-speed CT capturing the dynamic material response with optimum image quality can be made and can be further subjected to quantitative analysis.

This doctoral thesis aims to improve the imaging capabilities of laboratory tomographs for contrast-enhanced imaging and for fast in-situ acquisitions with quantifiable image quality. The methodological aim of this PhD work is to develop original tools in order to improve the aforementioned capabilities of laboratory tomographs. Two possibilities were studied to achieve this objective.

- ✧ Investigating the recent possibilities offered by energy-thresholding photon-counting detectors (PCDs) for laboratory X-ray imaging, particularly in terms of contrast improvement. For this purpose, a PCD was subjected to quantitative characterization, and its potential advantages and possible drawbacks were investigated using a polychromatic laboratory X-ray source.
- ✧ Developing a global model-based optimization strategy that would guide the users through the optimization of laboratory X-ray CT acquisition parameters to perform relevant in-situ tests. An optimization model was developed for this purpose to determine the optimal CT scan setting for given sample specifications in accordance with the level of analysis to be performed on the reconstructed 3D image.

Based on the developed methodologies, real-time fast in-situ acquisitions were performed as application aspects of the thesis. An application detailed in this thesis corresponds to:

- ✧ Real-time monitoring of microstructural evolution of 3D printed parts made up of cellulose during the air-drying phenomena with fast laboratory X-ray microtomography.
  The optimization of the acquisition parameters was done in order to capture and quantify the microstructural evolution and kinetic measurements during the drying phenomena. The presented study indicates the quantitative characterization capability of laboratory tomographs for high-speed imaging.

0.2 Structure of the thesis

Following the objectives of the PhD work, this thesis is organized as follows:

✪ **Chapter 1: Literature review**

Chapter 1 presents a state of the art in terms of laboratory computed tomography. It starts with the general principle of the X-ray CT technique and the use of X-ray CT as a characterization tool in material science. The different types of analysis performed on the images are categorized into three proposed levels. An overview of classical image quality indexes to estimate the quality of a scan and the influence of the CT acquisition parameters on the image quality is presented. After, the detail about the CT acquisition parameters and their importance and effect on the image quality are introduced. The chapter then focuses on the time-resolved CT, different types and constraints to perform in-situ acquisitions, and the overview of the fast imaging in lab-CT is illustrated. Lastly, the synthesis of the literature review and the objectives of the doctoral thesis are presented.

Part I: Methodological aspects

✪ **Chapter 2: Characterization of direct photon-counting detectors and preliminary results from lab X-ray imaging**

This chapter focuses on the characterization of the imaging performance of the energy discriminating photon-counting detectors using a polychromatic X-ray laboratory source. The chapter initially introduces the photon-counting detectors, their principle advantages, and known drawbacks. Then, characteristics of four different photon-counting detectors were compared, and a suitable detector was subjected to quantitative characterization. The static and time-dependent defects of the detector were studied, and the imaging performance of the detector was compared with the standard energy-integration detector. The spectral K-edge radiographic imaging was explored as well, and the potential of such detectors for lab-based contrasted-enhanced CT imaging is discussed.

✪ **Chapter 3: Towards optimization of the acquisition parameters**

This chapter details the attempt towards the optimization of the CT acquisition parameters. The global workflow of the optimization model is illustrated, and the different modules of the optimization tool: the noise model, the X-ray absorption contrast simulation tool, the screening algorithm, and the cost function are explained with examples. Further, the efficiency of the model is demonstrated with the help of a user-defined case study. The chapter also discusses the improvement that can be implemented for a better performance of the optimization model.

Part II: Application aspects

✪ **Chapter 4: 3D real-time monitoring of air-drying of 3D printed part made up of cellulose by fast laboratory X-ray microtomography**

This chapter demonstrates the fast in-situ application performed with the laboratory CT setup. The application corresponds to monitoring the air-drying mechanism of the 3D printed cellulose cube. First, an experimental screening to optimize the CT acquisition setup to perform the high-speed in-situ test is detailed and they were confronted with the model predicted configurations. Then the detail about the 3D printed cellulose sample, the data processing and analysis techniques for qualitative, microstructural quantification, and kinetic analysis are described. The corresponding results at inter-filament and intra-filament scales are presented, explaining the air-drying mechanics of the cellulose 3D printed sample.

✪ **Chapter 6: Concluding remarks and perspectives**

This chapter summarizes the work described in the manuscript and highlights the key contributions of this work. In addition, perspectives for future works and improvements are also detailed.

A brief introduction of the 2nd in-situ application that was studied during the thesis is presented here. The application corresponds to the continuous in-situ 4D solidification of an aluminium silicon copper Al-Si-Cu alloy by fast laboratory X-ray microtomography. The experimental setup and some qualitative and quantitative characterization results are briefly presented along with the challenges faced particularly due to the limited scan resolution. Lastly, the potential of using the characterized photon-counting detector to improve the experimental setup is presented as well.

0.3 Graphical outline

1. **Literature review**

- X-ray computed tomography
- 3D image analysis and image quality
- Lab CT acquisition parameters
- In-situ acquisitions
- High-speed in-situ imaging

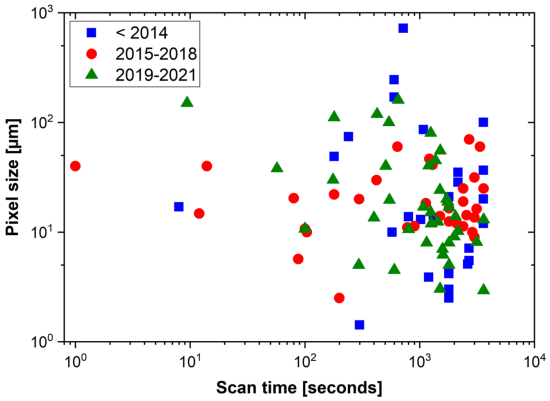

Pixel size versus scan time for the laboratory in-situ X-ray CT.

2. **Characterization of direct photon-counting detectors and preliminary results from lab X-ray imaging**

- Photon-counting detectors (PCDs)
- Characteristics of the four PCDs
- Characterization procedures
- Characterization results & comparison with flat-panel

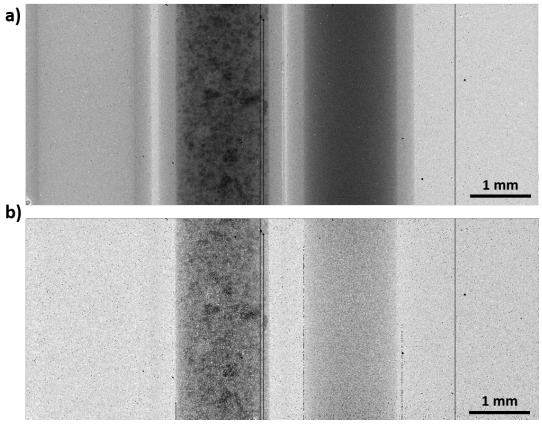

(a) Standard flat-field corrected radiograph of the (I-$BaSO_4$-H_2O) phantom recorded with energy of photons in-between 5 to 50 keV keV using Pixirad-2/Pixie-III detector. (b) KES flat-field corrected radiograph of the (I-$BaSO_4$-H_2O) phantom recorded with using energy of photons in-between 28 to 38 keV using Pixirad-2/Pixie-III detector.

3. **Towards optimization of the acquisition parameters**

- Optimization model for lab-CT
- Modelling noise in feature of interest
- X-ray absorption spectrum simulation
- Screening algorithm
- Cost function

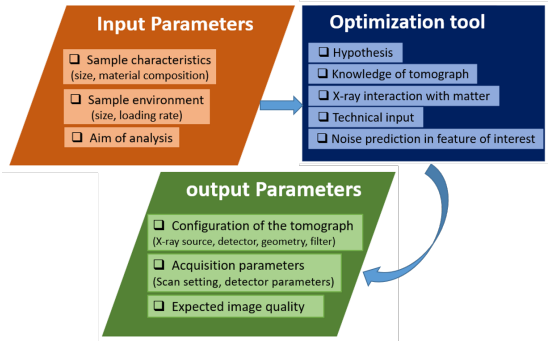

Overview of the optimization model.

4. **3D real-time monitoring of air drying of 3D printed part made up of cellulose by fast laboratory X-ray microtomography**

- Experimental screened configurations
- Optimization model configurations
- Fast lab-based in-situ acquisition
- Qualitative analysis
- Microstructural quantification
- Kinematics analysis (DVC)

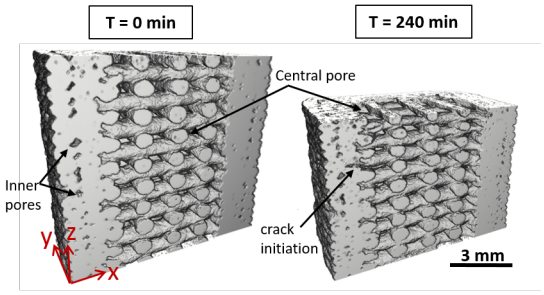

3D rendered cross-sectional view of reconstructed X-ray tomographic scans at different drying time of a 3D printed cellulose cube.

Chapter 1

Literature review

Contents

1.1 Introduction

The microstructure of the materials primarily determines their physical and mechanical properties. Therefore, quantifying the inner structure and morphological characteristics of materials is of prime importance in material science and engineering. Three-dimensional (3D) imaging of the materials can help in understanding and quantifying the microstructural properties of materials.

X-ray computed tomography (CT) is a 3D imaging technique which provides the 3D representation of the internal structure of the material that is opaque to visible light. In X-ray CT, a sample is irradiated with X-rays to create two-dimensional (2D) radiographs, and mathematical algorithms are then used to create the virtual 3D cross-sectional representation of the scanned sample highlighting its internal and external features. The 3D analysis can then be performed on the 3D reconstructed images.

Initiated in medical science with the invention of the first medical CT scanner by Hounsfield [Hounsfield, 1973], Figure 1.1, it was widely accepted in material science as a non-invasive and non-destructive technique (NDT) as the scanned sample remains undamaged and can be scanned multiple times. Technological developments and the evolution of X-ray CT over the last few decades is presented in Figure 1.1, including the invention of the first micro-computed tomograph (µ-CT) by Jim Elliott in the early 1980s [Elliott and Dover, 1982], the introduction of a practical cone-beam algorithm for direct reconstruction of two-dimensional (2D) projections [Feldkamp et al., 1984a], first results of tomographic scans with a laboratory-CT by Weitkamp et al. [Weitkamp et al., 2005] and Pfeiffer et al. [Pfeiffer et al., 2007]. Micro-CT extends the resolution of CT into the micron-scale by using X-ray sources with finer focuses, object stages with higher precision and detectors with smaller pixels. With the advancements in hardware technologies, nano-meter resolution has been achieved and scans performed with such resolution are referred to as nano-CT [Withers, 2007].

Over the last decade, X-ray CT is being used increasingly to follow the microstructural evolution of materials under controlled environmental conditions (load, temperature and corrosive environment) through the collection of multiple 3D scans to create 4D dataset (3D plus time) imaging [Salvo et al., 2003, Maire and Withers, 2014]. Such acquisitions are referred to as time-resolved or in-situ acquisitions. The invention of CMOS camera in 2010 made the fast in-situ acquisitions possible and the sub-second temporal resolution was reported [Salvo et al., 2012a]. Later, these fast in-situ scans at nano scale resolution were performed as well [Villanova et al., 2017]. Recently novel setups that further decrease the temporal resolution to 0.05 seconds and even 0.001 seconds were reported [Maire et al., 2016, Garcia-Moreno et al., 2021]; these are currently the fastest scans performed to date. All of these experiments were performed using synchrotron CT.
Synchrotrons are expensive facilities and limited access to them restrict the number of experiments that can be performed. Due to this, over last few years, developments and researches on the potential of lab-CT have increased drastically [McDonald et al., 2015, Bultreys et al., 2016].

The aim of this chapter is to introduce to the readers the basic scientific concepts used in this thesis. The chapter begins with describing the general working principle of X-ray CT and the X-ray attenuation laws that describes the phenomena, Section 1.2. Then importance

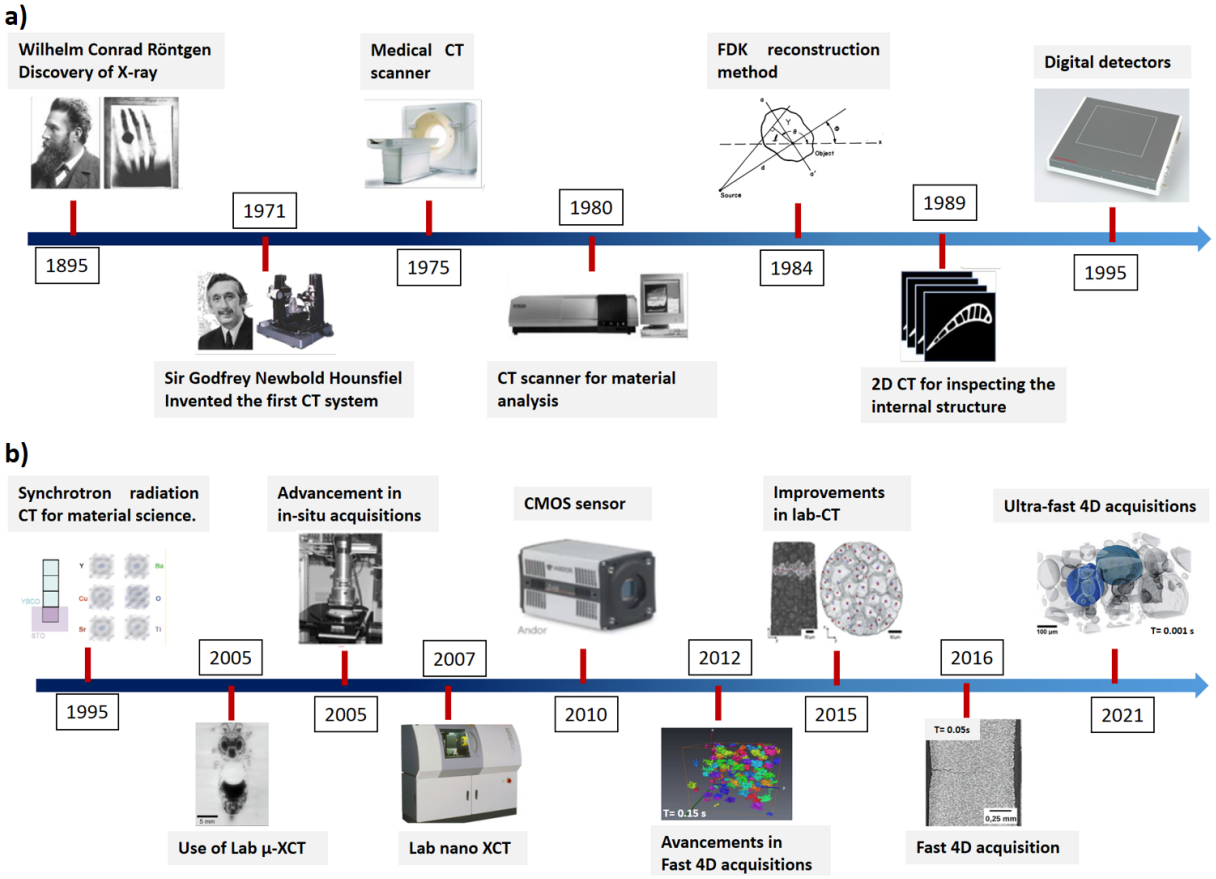

Figure 1.1: Technological developments and evolution of X-ray computed tomography over the last century.

of X-ray computed tomography as a characterization tool in material science is highlighted in Section 1.3. The different types of analysis performed on the 3D datasets are categorised into three proposed levels. Later the importance of image quality in CT is discussed in Section 1.4, including the various artifacts in X-ray CT and classical indexes that are used to estimate the image quality. The various acquisition parameters of CT and their effects on the image quality are discussed in detail in Section 1.5. Lastly, the chapter focuses on the lab-based in-situ acquisitions and highlights the various types and constraints during the in-situ acquisitions, Section 1.6, and an overview of the fast scans performed, Section 1.7, in lab-CT. Synthesis of the literature review and the objectives of the PhD thesis is presented in Section 1.8 and Section 1.9, respectively.

1.2 Principle

The lab X-ray tomography apparatus basically consists of three elements: the X-ray tube, the rotating stage and the imaging detector.

The specimen is placed on the rotation stage between the X-ray tube and the detector. The X-ray tube generates the beam of photons that interacts with the rotating specimen and after penetration, the intensity is recorded by the imaging detector creating the 2D radiographs. These radiographs are recorded at different angles throughout the 360° rotation and the reconstruction algorithms are then used to reconstruct the 3D cross-sectional image of the scanned sample. Figure 1.2 illustrates the general principle of the X-ray computed tomography.

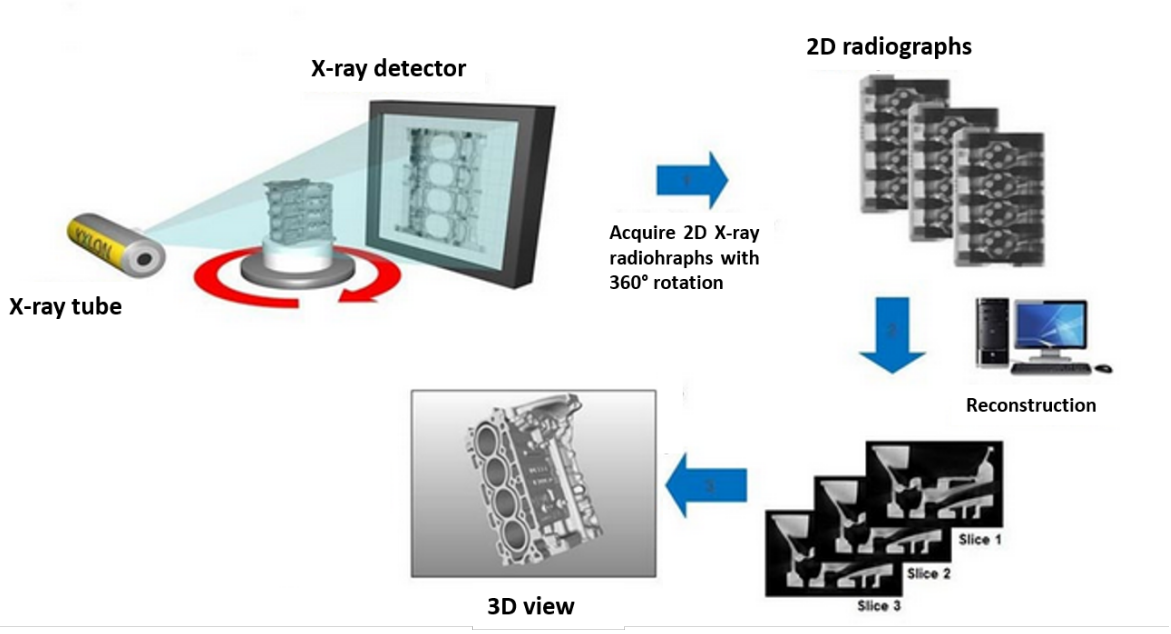

Figure 1.2: General principle of the X-ray computed tomography.

1.2.1 Laboratory and synchrotron sources

X-ray CT scan can be performed using either lab or synchrotron sources. Lab-based CT sources provide cone beam shape geometry and are polychromatic, whereas synchrotrons provide parallel beam shape geometry and can be monochromatized. Using these sources, different modes of tomography can be performed such as absorption contrast CT, phase-contrast CT, and diffraction contrast CT. This thesis only focuses on absorption contrast CT.

1.2.1.1 Laboratory-CT

Lab-based CT uses X-ray tubes containing the thermionic cathode and anode to produce X-rays. The electric current heats the cathode and causes the thermionic emission of electrons. By switching on the high voltage, a strong electric field is created between the thermionic cathode and anode, which accelerates the electron towards the anode forming an electron beam. The electron beam collides with the anode at high velocity. The anode material slows down

the electrons within a very short distance, this generates the desired X-ray radiations. An electromagnetic lens is used to focus the electron beam at a small spot on the anode surface, called focal spot. The smaller the focal spot the sharper, higher in contrast and high-resolution X-ray image will be [Huda and Abrahams, 2015]. Schematics diagram of an X-ray tube is presented in Figure 1.3a.

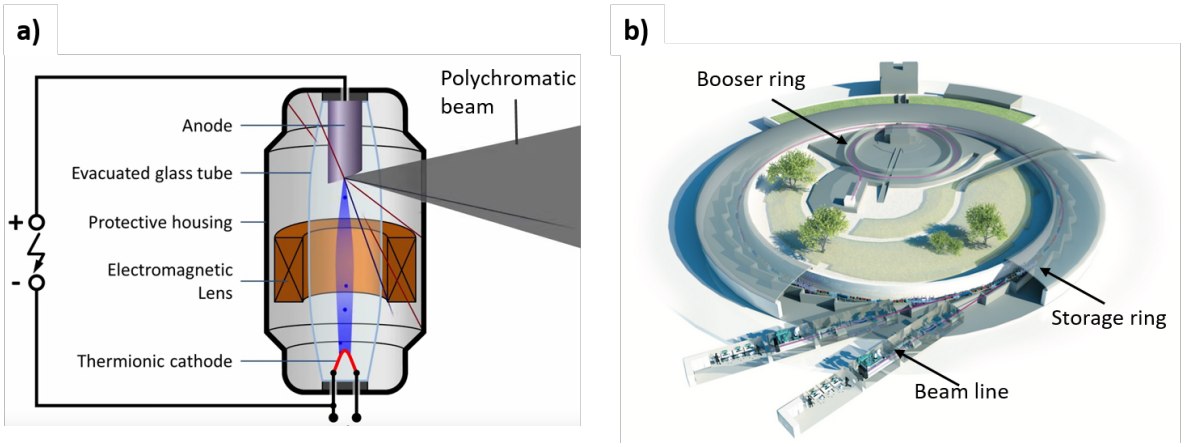

Figure 1.3: Schematics diagram of (a) an X-ray tube: the electrons are emitted from the cathode and collected at the anode releasing X-ray radiation, (b) a synchrotron: high-energy electrons are injected from the booster ring into the storage ring where the synchrotron light is generated using various devices and then transmitted to the beamlines.

The produced X-ray beam is conical and polychromatic with a wide range of energy, usually in 10-150 keV. The conical X-ray beam makes geometrical magnification possible by positioning the object under investigation at any position between the X-ray source and detector, Figure 1.4(a).

Lab sources are limited in the X-ray photons flux, which is usually 10^8 photon/sec/mm^2 and generally offers resolution varying from 0.4 to 500 μm depending on the spot size, CT geometry and the detector used [Plessis et al., 2018]. For example, the achievable source spot size with the EasyTom XL coupled with microfocus reflection source ranges from 5-10 μm and voxel size as low as 4 μm can be achieved whereas, EasyTom XL coupled with nanofocus transmission source allows the spot size below 1 μm and CT scan with voxel size of 0.4 μm can be performed. Advanced tomographs such as ZEISS Xradia 410 Versa offers the high spatial resolution with voxel size down to 100 nm can be achieved. Since last few years new generation X-ray sources such as metal-jet sources based on liquid-metal-jet technology are also being operated in lab-CT. Metal-jet sources can achieve 10 times higher brightness than conventional microfocus tubes [Adibhatla, 2021].

1.2.1.2 Synchrotron-CT

Synchrotron is an extremely powerful source of X-rays and are produced by high energy electrons as they circulate around the synchrotron.

At European Synchrotron Radiation Facility (ESRF), initially, the charge particles are emitted by metal electrode and are guided inside the booster rings. The electrons are then accelerated to an energy of 6 billion electron-volts. These high energy electrons are then injected

into the storage ring which is approximately 800 metres in circumference. Here, the electrons circle for hours without interruption close to the speed of light and their energy remain constant. Synchrotron light is generated in the storage ring. The ring is in-fact an alternation of straight and curved sections. In each curved section, various devices (bending magnet, focusing magnet, insertion devices such as wiggler or undulator) guide the electrons forcing them to deviate from their path and each time they deviate from their path, the electrons emit energy in the form of light. The beams of light tangent to the storage rings are conveyed into the beamlines. Beamlines capture, manipulate and direct this light onto samples for experiments. A schematics diagram of a synchrotron is presented in Figure 1.3b.

X-rays produced can be made quasi-monochromatic by the use of monochromator, Figure 1.4b, and are of specific energy, tightly collimated, parallel, polarized and coherent in nature. X-ray optics are used for geometrical magnification. Compared to lab sources, synchrotron X-ray beam has high flux, nearly 1000 times larger, 10^{12} to 10^{13} photon/sec/mm^2 [Schafers et al., 2008]. Figure 1.4b shows the typical setup of a synchrotron.

High spatial resolution, compared to lab-CT, can be achieved with synchrotron-CT, a voxel size of 50 nm is reported at ESRF ID 16B [Martínez-Criado et al., 2016]. A high brilliance X-ray flux coupled with a fast frame rate detector at synchrotron also makes ultra-fast imaging possible and 1 millisecond scan time has been reported recently [Garcia-Moreno et al., 2021].

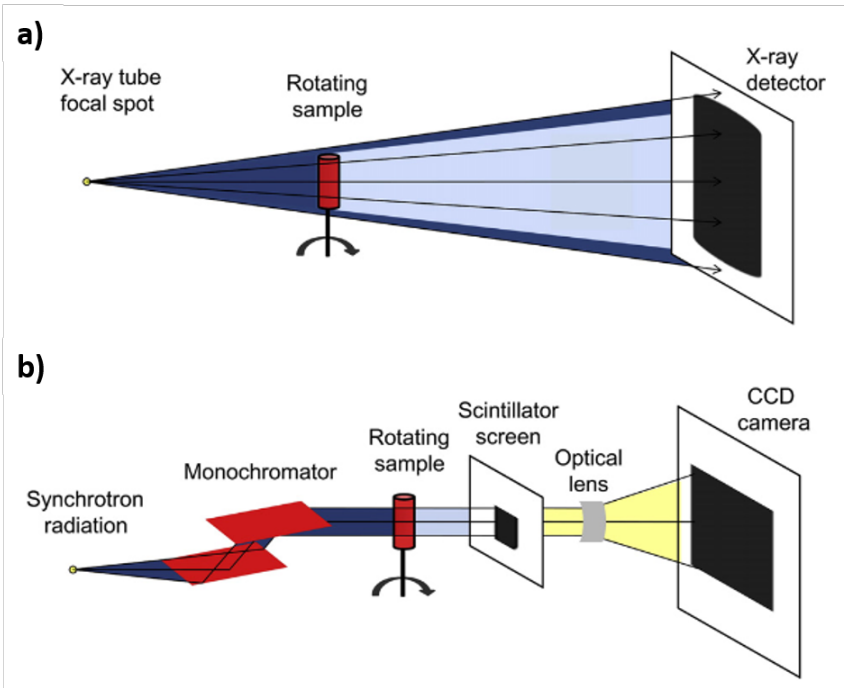

Figure 1.4: Schematic diagram of a (a) typical lab-based micro-CT setup with a conical X-ray beam, (b) synchrotron-based micro-CT setup. [Cnudde and Boone, 2013]

1.2.2 X-ray interaction with matter

When X-ray photons interact with matter, the attenuation of the initial intensity can be measured. Different interacting mechanisms that contribute to the attenuation are photoelectric absorption, Compton scattering, and pair production. In most of the X-ray regimes used in ma-

terials characterization in lab-CT (up to 150 keV), the photoelectric effect is the main process that causes X-ray attenuation. Compton scattering is the dominant process for higher-energy radiations, and for energy higher than 1.02 MeV, pair production occurs.

The probability for a type of interaction between photon and an element is described by cross-sections and attenuation coefficients [Brunetti et al., 2004]. The total mass attenuation coefficient μ/ρ, of an element with atomic number Z is given by the sum of the relevant mass attenuation coefficients, Eq. 1.1, where ρ is the density of the element and E is the energy of the incident photon

$$(\mu/\rho)_{total} = (\mu/\rho)_{photot} + (\mu/\rho)_{compton} + (\mu/\rho)_{pair} \tag{1.1}$$

Figure 1.5 shows the X-ray mass-attenuation coefficient μ/ρ plot for Iodine. The attenuation coefficient is dependent on the photon energy and is based on the respective cross-sections of Compton scattering and the photoelectric effect; however, due to the energy regime, the photoelectric effect is the dominant process that forms the interaction cross-section.

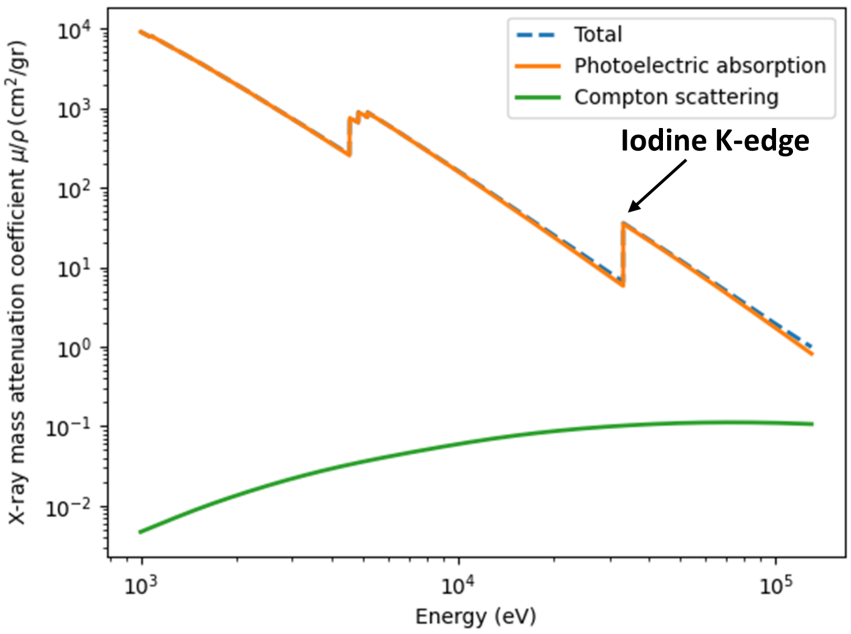

Figure 1.5: X-ray mass-attenuation plot for iodine. The attenuation coefficient for photoelectric absorption, Compton scattering, and total cross-section is plotted, showing the photoelectric effect being the dominant interaction process. The K-edge is located at 33.3 keV.

The photoelectric effect cross-section σ_{pe} is strongly dependent on the beam energy E and the atomic number Z [Darby et al., 2011].

$$\sigma_{pe} \propto \frac{Z^n}{E^4} \tag{1.2}$$

Where n depends on the K-edge of the element and varies from 3 to 5. The linear attenuation coefficient μ of the material can be related to the photoelectric effect cross-section σ_{pe} as follows:

$$\mu = \rho \frac{N_A}{Z} \sigma_{pe} \tag{1.3}$$

where ρ, Z, and N_A are the density, atomic number and Avogadro's constant, respectively. Buzug [Buzug, 2008] uses the following equation, Eq. 1.4, as a rule of thumb for estimating the absorption coefficient μ due to the photoelectric effect, which is a combination of Eq. 1.2 and Eq. 1.3.

$$\mu \propto \rho \frac{Z^n}{E^4} \tag{1.4}$$

Considering a monochromatic beam and a homogeneous sample of thickness d, for absorption CT, the attenuation of the X-ray photons after passing through the sample can be expressed by Beer-Lambert's law

$$I(d) = I_o . e^{(-\mu d)} \tag{1.5}$$

where I_o, is the intensity of the beam before passing through the specimen and $I(d)$ is the intensity after passing through the specimen, μ is the coefficient of the linear absorption and is material dependent as shown in Eq. 1.4. For heterogeneous sample Eq. 1.5 changes to

$$I(d) = I_o . e^{-\int_0^d \mu(s) ds} \tag{1.6}$$

With s is the position along the line. For polychromatic spectra source tubes, Beer-Lambert's law can be formulated as

$$I(d) = \int_0^E I(0, E) . e^{-\int_0^d \mu(E,s) ds} dE \tag{1.7}$$

where E is the energy of the X-ray photons.

1.2.3 X-ray detector

The purpose of the X-ray detector is the detection, quantification, and digitization of the incoming X-ray photons at any given time interval. Every detector has a radiation component that directly interacts with the X-rays, converting them into electrical signals and, an electronics component that processes these signals to create digital images. These two components can be used to classify different detectors according to how they register and process incoming photons [Knoll, 1989]. A large variety of X-ray detectors have been developed. A summary of the most widely used detectors is presented here.

- **Flat-panel detectors (FPDs):** Flat-panel detectors are currently the most widely used detector type in radiography and cone-beam CT [Cowen et al., 2008]. FPDs are indirect detectors that initially convert X-ray photons into visible light using scintillator crystals after the photo-diode layer transforms light into electrical signals. They are also referred to as energy-integration detectors (EIDs) as the output signal of the detector is proportional

to the total energy deposited by all photons. FPDs can be produced with a large detector area, but the readout times are relatively slow, and high dark current and gain, and detector non-linearities can limit the image quality and need consideration [Wischmann et al., 2002, Yu and Wang, 2013]. Pixel size in the flat-panel varies from 50 to 200 µm and frame rate up to 100 frames per second is available. Flat-panel Varian PaxScan 2520V has a pixel pitch of 127 μm containing 1920x1536 pixels and a maximum frame rate of 60 frames per second.

- **Charge-couple devices (CCDs):** Charge-couple devices are EIDs and work on the indirect detection principle. In CCDs, shift registers are used since not every pixel has its own readout circuit. The charge is shifted sequentially to the end of the pixel row and read out serially, resulting in a long readout time. Typical pixel size in the CCDs varies from 2.4 to 15 μm. High efficiency and low noise are usually the advantages of CCDs but their readout speed is very low as compared to flat-panels. Details about the CCDs can be found in [Lesser, 2014, Smith, 2009]

- **CMOS detectors:** A complementary metal oxide semiconductor (CMOS) image sensor has a photodiode and a CMOS transistor switch for each pixel that allow each pixel signals to be amplified individually. An amplifier for each pixel offers a much higher speed than a CCD sensor and reduces the electronic noise [Alle et al., 2016]. Faster and high resolution scans can be performed using CMOS detector. Andor Zyla 5.5 sCMOS has an effective pixel size of 6.5 μm and offers an acquisition speed up to 100 frames per second.

- **Photon counting detectors (PCDs):** Photon counting detectors are innovative detectors that work on direct detection. The X-ray photons are directly converted into electrical charges using a semiconductor material, and each incoming photon is processed individually and independently from the other. Advantages of PCDs are smaller pixel size, high frame rate, spectral imaging capability, and the possibility to suppress dark current [Ballabriga et al., 2016, Taguchi and Iwanczyk, 2013]. Pixirad-Pixie-III has an effective pixel size of 62 μm and has the ability to capture 500 frames per second [Bellazzini et al., 2015]. The detail of PCDs is presented in Chapter 2.

1.2.4 Voxel size

Voxel is a representation of the pixel in 3D and is often confused with spatial resolution of the CT scan. Voxel is the size of the smallest element in a volume (image stack) with an associated grey value. Whereas, Spatial resolution is defined as the size of the smallest observable object that can be measured in a reconstructed volume. It is also refers to the ability of an imaging system to differentiate between two near-by objects.

For lab-CT, the reachable voxel size of a CT scan for a specimen depends on the geometrical magnification determined by the relative position of the specimen with respect to source and detector and the pixel size of the detector. If the specimen is positioned closer to the X-ray source for a given detector position, the higher will be the magnification and the smaller the voxel size, resulting in a higher resolution of CT scan. For synchrotron sources, the optical lenses are used for geometrical magnification of the specimen on the detector. Relatively small

specimens compared to lab-CT are used at synchrotron-CT, and resolutions well below 1 μm can be achieved with high contrast.

1.2.5 3D reconstruction

A series of 2D projections or radiographs at different angular positions of the rotating sample is obtained during the CT scan. After, the mathematical algorithms are used to construct a 3D image from the set of acquired 2D radiographs. This process is called 3D reconstruction.

In 1984, a convolutional-back-projection formula (FDK algorithm) designed for circular cone-beam tomography was proposed by Feldkamp et al. [Feldkamp et al., 1984b]. The FDK algorithm filters the weighted projection data on each ray and then back projects them into the reconstruction space. A simple illustration is shown in Figure 1.6 with an object consisting of five spheres. Three projections (p1, p2, and p3) are acquired, describing the attenuation coefficient distribution for the given X-ray path at three different angles. According to the FBP principle, each acquired projection profile is back-projected along the viewing direction at which it was acquired. In the resulting grid, each contribution is added to each voxel intersecting that ray direction [Carmignato et al., 2017a].

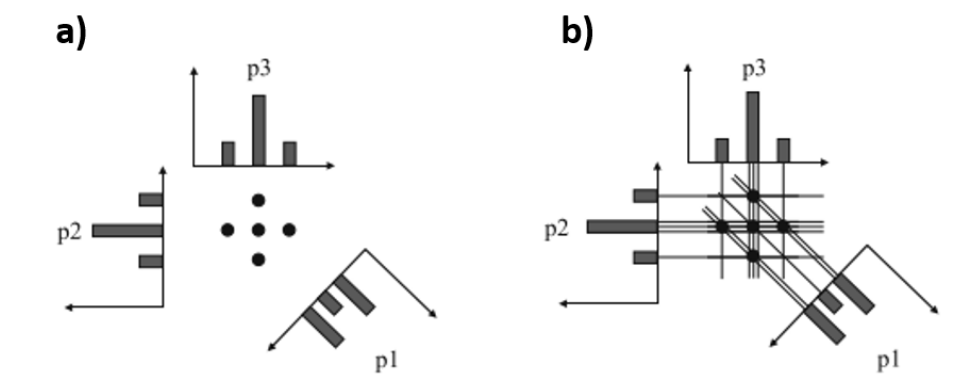

Figure 1.6: Concept of projection and back-projection. (a) Projection: each radiographic projection (p1, p2 and p3) describes the distribution of attenuation coefficients along the captured angle. (b) Back-projection: every radiograph is back-projected along the viewing direction from which it was acquired. The number of lines depicts the amount of absorption. A grid is generated, in which each contribution is added to the voxel intersecting that ray direction. [Carmignato et al., 2017a]

In CT, filtered back projection (FBP), a variant of the FDK algorithm, is the most commonly used reconstruction technique; details can be found in [Hsieh, 2009a]. Besides this, several other reconstruction techniques have been developed, such as iterative reconstruction (IR), 3D Fourier-based reconstruction method, algebraic reconstruction technique (ART). Details and the evolution of reconstruction algorithms from filtered back-projection to artificial intelligence can be found in [Carmignato et al., 2017b, Willemink, 2019].

1.3 X-ray CT as a characterization tool in material science

With the developments and advancements of micro and sub-micro CT devices over the last four decades, X-ray CT has become an essential non-invasive testing technique in material science and in all the disciplines dealing with materials.

The recent increase in the availability of laboratory-scale µ-CT has enabled many researchers to study and characterize the materials in 3D. Generally, two types of material characterization are usually done with the tomography, quasi-static and following process characterization.

1.3.1 Quasi-static characterization

In quasi-static, the specimen remains unchanged during the acquisition of the radiographs. The static analysis of the 3D volumes characterizes the internal and external structure and provides information about the specimen's local geometrical and topological information [Roscoat et al., 2005, 2014, Dadda et al., 2017]. However, it does not provide insight into the dynamics of the processes under investigation.

1.3.2 Following process characterization

X-ray CT technique can be applied to follow the material's structural changes in real-time and under real conditions. Obtaining these 3D images at different timescales is often called time-resolved 3D or 4D images. With the developments of specialized mechanical devices, in-situ acquisitions are now performed on specimens that allow imaging the microstructural evolution during the experiment. Details about the in-situ acquisitions is presented in Section 1.6.

Here the possibilities for characterization go beyond the micro-structural quantification, and dynamic quantities such as flow, damage, and deformation mapping can be quantified. The characterization of these real-time global and local dynamic responses and understanding microstructural level phenomena is also crucial in developing and optimizing material behavior models. Two types of in-situ experiments for dynamic characterizations have been done: mechanical testing (compression and tension) [Viggiani et al., 2004, Otani et al., 2002, Besuelle et al., 2006, Zhao et al., 2014a] and thermal treatment (solidification, sintering, foaming of metal foams) [Lhuissier et al., 2013, 2012, Salvo et al., 2012b, Kumar et al., 2019].

1.3.3 3D image analysis

The reconstructed 3D volumes obtained after the quasi-static or the in-situ CT can be subjected to different types of post-processing analysis depending on the objectives of the study. This post-processing analysis is classified into three different proposed levels L1, L2, and L3.

1.3.3.1 L1: Qualitative analysis

The qualitative analysis, called L1, is the direct observation of the grayscale images by observer perception.

A large number of information can be obtained through observation of the 3D reconstructed images on 2D slices. Once the CT is used as a steady-state characterization, visualization and L1 analysis provide information on the porous phase, location and rough size of the pores, presence of cracks, delamination and on the solid phase, including the location and size estimation of the constituents.
For following processing characterization to monitor the evolving structure, L1 analysis reveals the location, initiation, propagation and evolution of the cracks or a given constituent formation such as dendrites, macro pores or shear bands.

Figure 1.7 presents an example of L1 analysis. A central slice of a quasi-static synchrotron CT to characterize water distribution in compacted soils is presented. In the enlarged view air, water, and sand grains are qualitatively distinguished [Li and Tang, 2019].

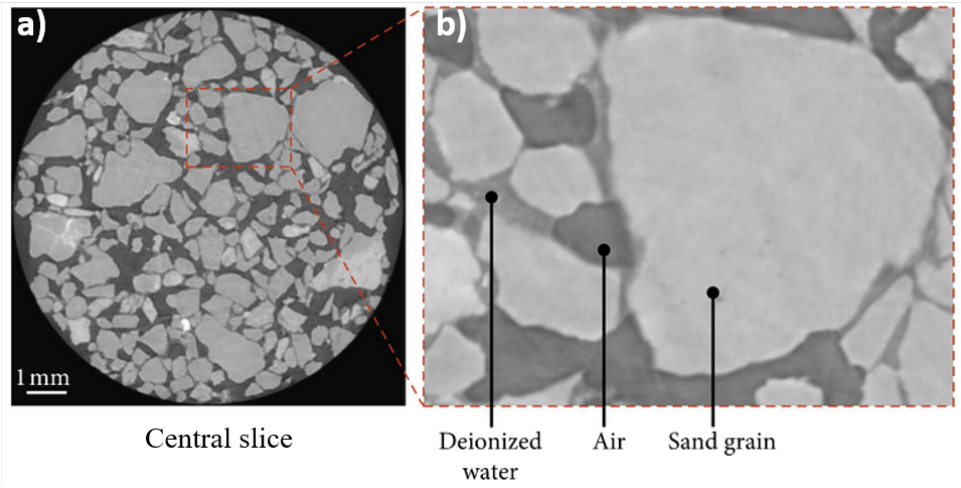

Figure 1.7: L1 analysis. (a) A reconstructed slice showing the water distribution in compacted soil and (b) air, water, and sand grains are qualitatively distinguished [Li and Tang, 2019].

Figure 1.8 shows the qualitative results of nano-mechanical in-situ test to monitor the crack growth in dentin specimen. A cone indenter tip was used to generate and propagate cracks. Figure 1.8(a,b & c) shows reconstructed slices of the sample at different stages of indentation that corresponds to the displacements of 15, 21 and 26 μm. The crack formation can be observed. Figure 1.8(d) shows the loading rate as a function of displacement and three data points correspond to the images (a, b & c) [Patterson et al., 2016].

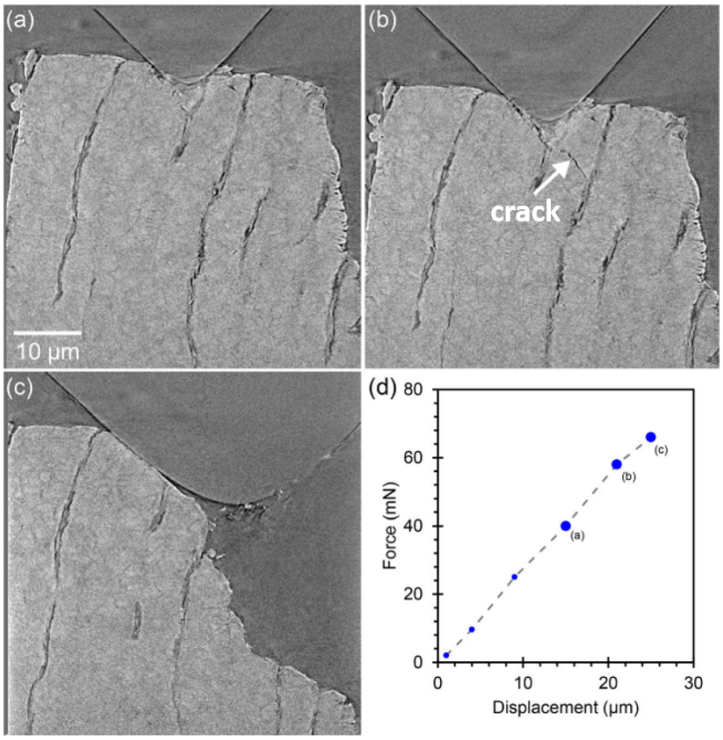

Figure 1.8: L1 analysis. Time-lapse series of reconstructed cross-sections through the dentin sample showing the progress of a crack beneath the indenter as the load and displacement are increased. Slices at different displacements are shown (a) at 15 µm displacement, (b) at 21 µm displacement where a crack has formed and (c) the sample has broken completely by 26 µm displacement. (d) The load and displacement curve of the mechanical test scan, three data points correspond to the images (a,b & c).[Patterson et al., 2016]

1.3.3.2 L2: Low-level quantitative analysis

The low-level quantitative analysis, called L2, concerns the quantification of global microstructural parameters of the specimen such as volume fraction, specific surface area and tortuosity of a phase. Such a characterization requires an accurate segmentation of the phases and the analysis can be performed on steady-state images or on images obtained from in-situ tests.

An example of L2 analysis for quasi-static CT is illustrated in Figure 1.9, where a CT central slice of a concrete core of 200 mm high by 60 mm diameter is shown in Figure 1.9(a). Figure 1.9(b) shows the 3D surface view and 3D crack and porosity view is highlighted in Figure 1.9(c). Crack is distinctly different from porosity and is identified as planar connected features[Plessis and Boshoff, 2019].

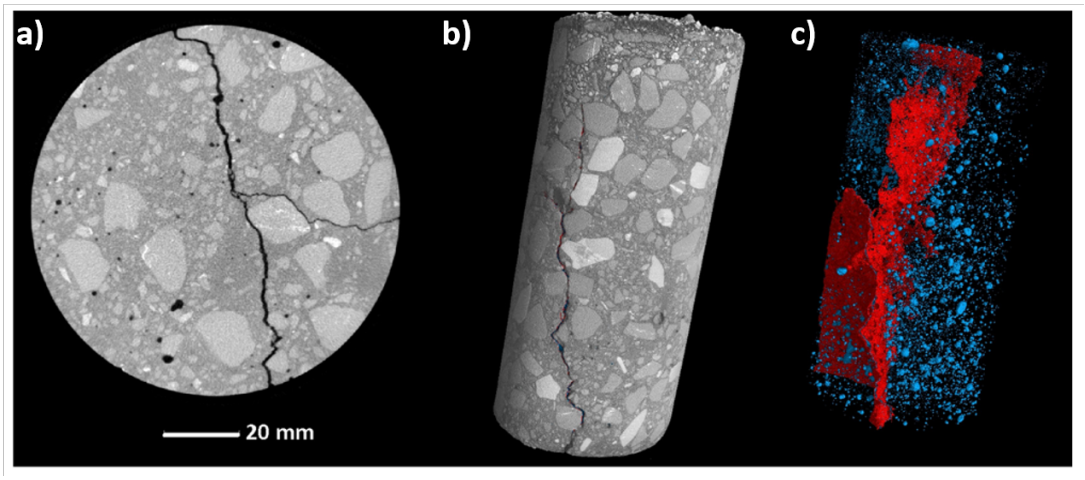

Figure 1.9: L2 analysis. Cracking in concrete core shown as (a) a central reconstructed slice, (b) 3D view of the sample, (c) 3D view of the crack (red) and pores (blue) [Plessis and Boshoff, 2019]

.

Another example for the L2 analysis with in-situ acquisition is shown in Figure 1.10, for the observation of compaction of fibre bundle during a plain stress in-situ test. The evolution of the mean stress as a function of the volume fraction of fibres is shown and the 3D segmented volumes obtained at the five compression steps are represented around the graph [Latil et al., 2011].

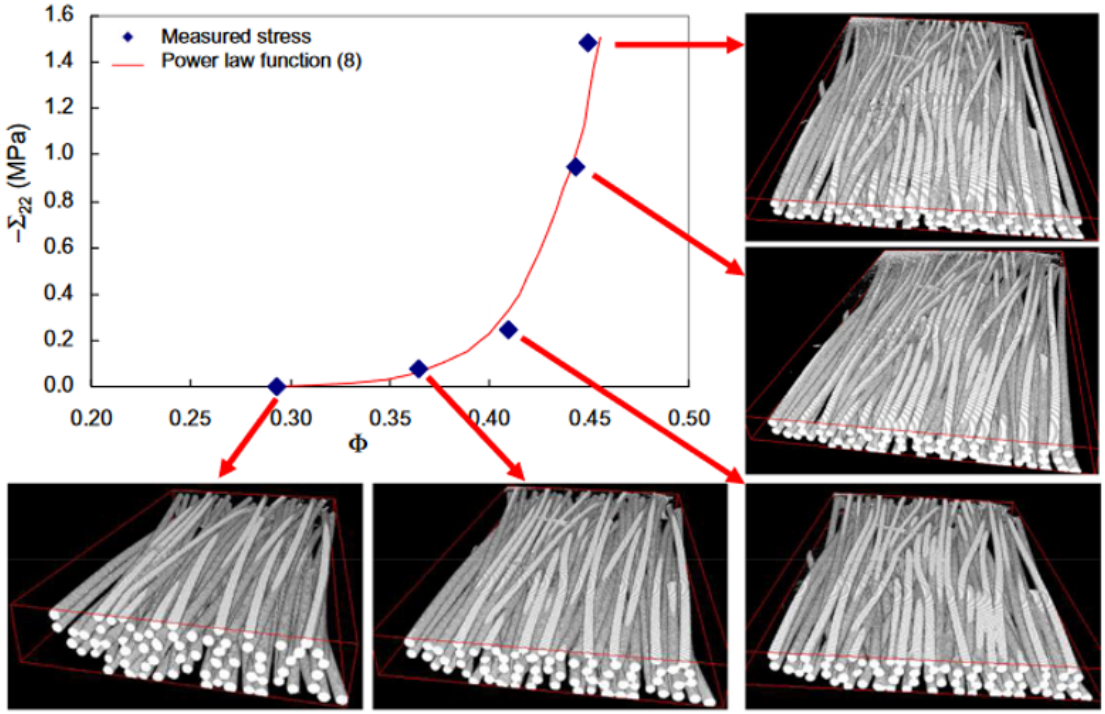

Figure 1.10: L2 analysis. Evolution of the mean stress as a function of the volume fraction of fibers during a plain stress in-situ test. The 3D segmented volumes obtained at the five compression steps are represented around the graphs. [Latil et al., 2011]

.

1.3.3.3 L3: High-level quantitative analysis

The high-level quantitative analysis, called L3, is the object-level quantification and concerns the quantification of local microstructural parameters such as the extraction of individual pore or fiber from the 3D volume.

For in-situ characterization, L3 analysis corresponds to the quantification of dendrites, tracking the growth mechanisms along cavities. Extracting information by full-field measurements, Digital Volume Correlation (DVC), by correlating the deformed volumes with the reference volume to measure displacement and the strain fields is also included in L3 analysis. Figure 1.11 illustrates the high-level quantitative analysis and shows the 3D rendering of one of the dendrites during the first three seconds of solidification of aluminium alloy. The experiment was performed at ESRF ID15 beamline with a scan time of 0.15 seconds [Salvo et al., 2012a].

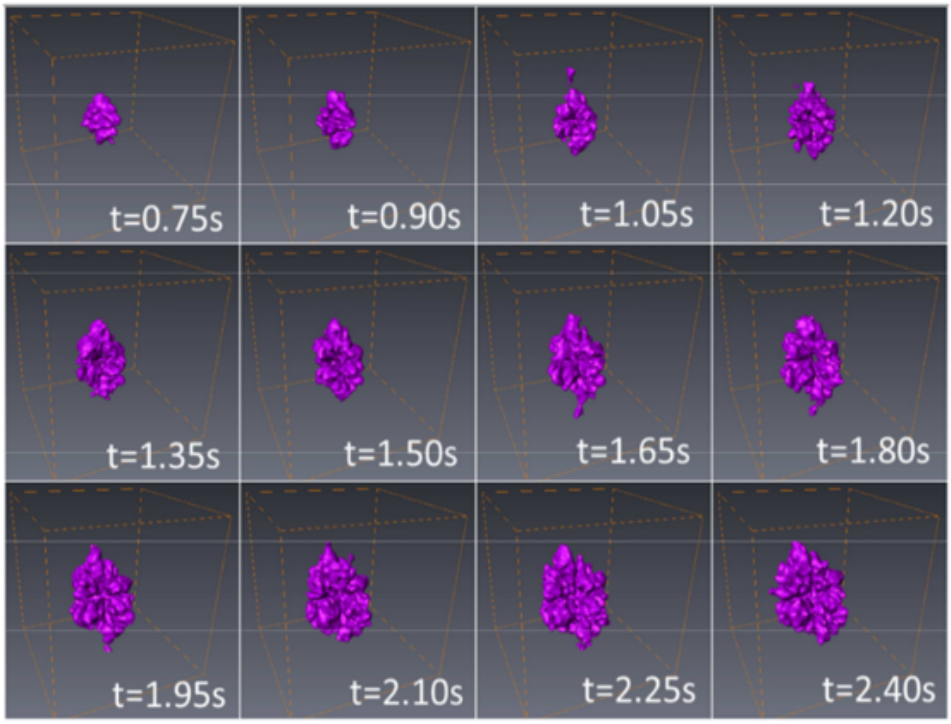

Figure 1.11: L3 analysis. Morphological evolution of one dendrite during the first three seconds of solidification. The size of the box is about 100µm. [Salvo et al., 2012a]

Another example of L3 analysis using the 3D digital volume correlation is shown in Figure 1.12. The vertical displacement field in microns and axial strain field determined by DVC for a volume of interest (VOI) of a wooden sample loaded in three point bending test [Forsberg et al., 2008].

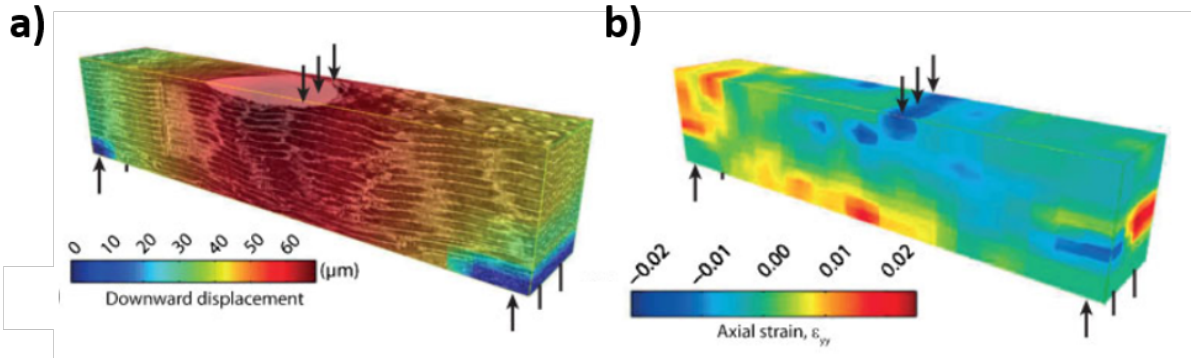

Figure 1.12: L3 analysis. (a) The vertical displacement field determined by digital volume correlation (DVC) for a volume of interest of a wooden sample loaded in three point bending test with the exterior loading points. The 3D microstructure of the wood is overlaid on the displacement field. (b) The corresponding 3D axial strain field. [Forsberg et al., 2008]

1.4 Image quality in 3D X-ray imaging

Generally, image quality in the computed tomographic scan can be described as the usefulness or effectiveness at which an image can be used for its intended purpose in providing accurate analysis. Obtaining good quality images is critical to ensure positive task-based intended post-processing treatment which can be either qualitative, quantitative, or kinetic. This concept is discussed in detail in [Liu et al., 2016].

X-ray CT image quality can be described in terms of contrast, spatial resolution, image noise, and artifacts [Goldman, 2007]. Generally, these factors can be sorted out into three groups: (i) factors affecting image contrast, (ii) factors affecting image spatial resolution, (iii) sources of image noise. However, it is vital to understand that these properties are intrinsically related to each other and further depend on the image-forming process [Martz et al., 2016]. Image forming process which includes X-ray source properties and settings, parameters of the detector, scanning configuration, data reconstruction process, and the post-processing techniques, differ from scan to scan since each CT scan is proposed for its specific objectives, so image quality differences are expected.

Besides, from these image quality variations that can exist due to different scanning configurations and can be minimized and controlled, various other unexpected errors can occur in CT reconstructed images. These unexpected errors are named as artifacts and degrade the image quality, making it sometimes impossible to quantitatively evaluate the obtained dataset. Detail about CT image artifacts can be found in [Carmignato et al., 2017a, Martz et al., 2016, Davis and Elliott, 2006, Hsieh, 2009a, Boas and Fleischmann, 2012]. This section presents the most significant image artifacts in CT and these artifacts are further summarized in Table **1.1**.

1.4.1 Classical artifacts in X-ray imaging

1.4.1.1 Beam hardening artifact

Beam hardening is the phenomenon that occurs when a polychromatic beam passes through an object and results in the selective attenuation of lower-energy photons.

The artifacts of beam hardening come from the difference between what is assumed in the reconstruction algorithm and what actually happens in experiments. The assumption in the reconstruction algorithm is that monochromatic single energy X-rays pass through the sample, are absorbed by the sample and come out as monochromatic single energy X-rays, Figure 1.13(a). But in reality, a polychromatic beam contains a wide range of energy photons (low and high-energy photons), and these different energy photons are not attenuated uniformly when passing through an object. High-energy X-ray photons go through the sample better than the low-energy X-ray photons that can also be completely absorbed, Figure 1.13(b), which means the energy distribution of the X-rays shifts towards the higher side as they pass through the sample. The high-energy X-rays are also called hard X-rays so this means the output beam energy is increased ("hardened") resulting in beam-hardening artifacts.

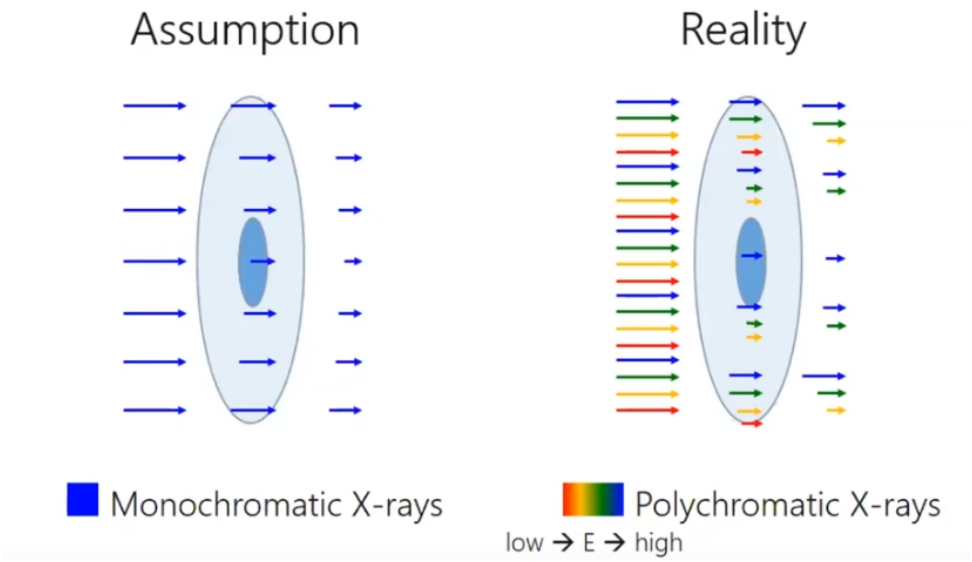

Figure 1.13: (a) Illustration of the assumption in the reconstruction algorithm that a monochromatic single energy X-rays, represented as solid blue color, pass through the sample, are absorbed by the sample and come out as monochromatic single energy X-rays. (b) Systematic representation of the reality during the experiments, a polychromatic X-ray beam having a range of energy is represented as rainbow colors. When it passes through the sample, high-energy X-ray photons go through the sample better than the low-energy X-ray photons resulting in more high-energy photons in the output beam energy.

Two types of beam-hardening artifact are reported: cupping artifact and streaking artifact.

Cupping artifact refers to the appearance of brighter voxels along the uniform cylindrical object's edge in the reconstructed volume. X-rays passing through the central portion of uniform cylindrical object are hardened more than those passing through edges as the central portion of an object is usually the thickest in material. This causes the higher average mean energy along the edges than the mean energy in the identical objects nearby. This phenomena is illustrated in Figure 1.14(a), the beam hardening artifacts which appear as increased intensity, representing false density enhancement, on the margins of an object and decreased intensity at the centre in the cylindrical samples. Figure 1.14(c) represents the variation in gray values along a transect [Abel et al., 2010].

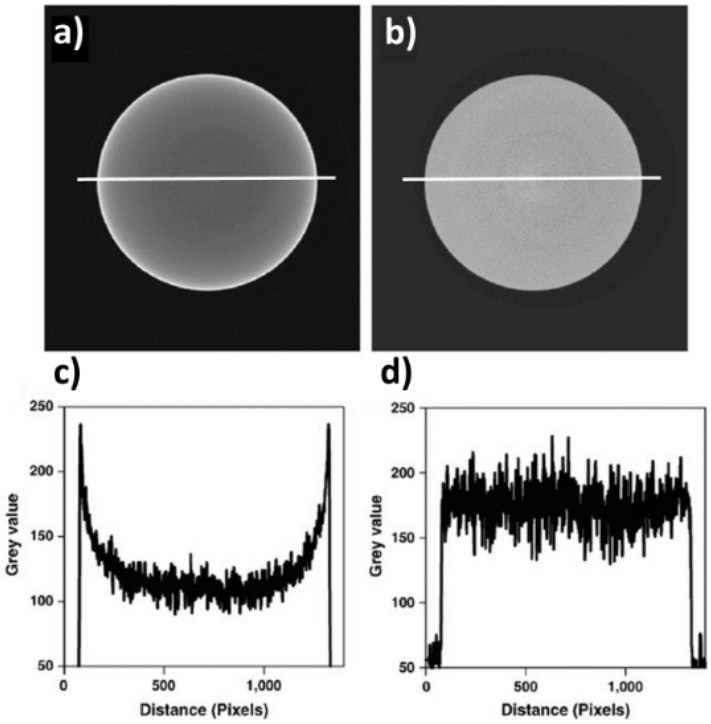

Figure 1.14: Reconstructed CT images of copper cylinder, (a) exhibiting a pronounced cupping artifacts due to beam hardening, (b) after applying correction algorithm. Variation in gray level along the transect (c) for uncorrected image (d) for corrected image. (Modified from [Abel et al., 2010]).

Streaking artifact refers to the appearance of dark bands or streaks between dense objects in the image. It occurs when polychromatic X-ray is being 'hardened' at different rates according to the rotational position of the tube/detector. Figure 1.15 shows an example of a beam hardening streak artifact caused by metal pins on either side of a head phantom [Stowe and Curran, 2016].

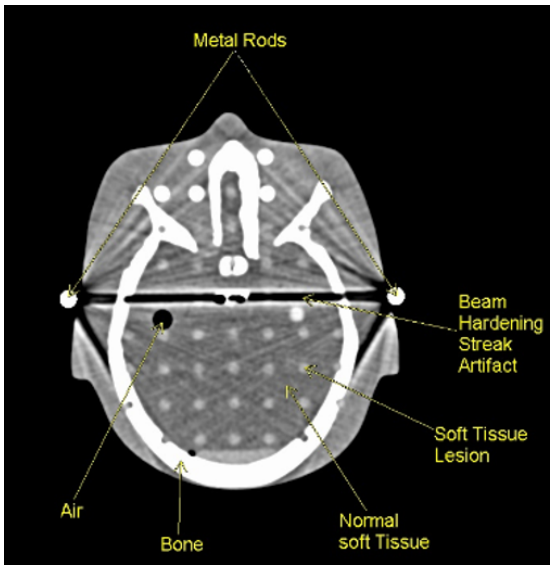

Figure 1.15: Reconstructed 2D slice of a head phantom demonstrating beam hardening streak artifact [Stowe and Curran, 2016].

The mathematical characterization and analysis of beam-hardening artifacts in X-ray CT are highlighted in [Park and Chung, 2015]. Lifton et al. stated that the beam hardening effect could influence larger measurement errors for outer dimensions than for inner dimensions [Lifton et al., 2015]. Various correction techniques were reported. A correction technique based on the use of X-ray beam filtering is suggested in [Meganck et al., 2009]. A hardware filter of different materials and thicknesses is placed on the X-ray source to absorb the low-energy photons and be effective in reducing the beam-hardening artifacts. Linearization of the measured polychromatic attenuation is also an effective technique to minimize the beam hardening artifact. In Figure 1.14(c), the beam hardening artifacts are removed by applying inverse polynomial and the corresponding variation in gray values along a transect is shown in Figure 1.14(d).

Correct calibration and application of iterative reconstruction algorithm during reconstruction also limits the beam hardening artifacts [Barrett and Keat, 2004]. Another effective technique based on signal to equivalent thickness calibration method is discussed in [Jakubek, 2007]. The use of an energy-thresholding photon-counting detector (PCD) with the appropriate setting to only detect high-energy photons from the incoming polychromatic spectrum can also eliminate the beam-hardening artifacts.

1.4.1.2 Ring artifact

Ring artifact occurs due to the detector's miscalibration or due to the defective pixels present in the detector sensor. It can also be referred to as bad pixels artifacts. A dead or saturated pixel with non-linear response results into wrong signal at the same location in each CT projection. During the back-projection step in the reconstruction process, this consistently erroneous reading will form concentric rings centered on the center of rotation in the CT reconstructed volume due to the circular sampling process [Schorner, 2012].

Ring artifacts due to dead or saturated pixels are common with photon-counting detectors in which the pixels inconsistent response and saturation are quite common [Fang et al., 2020]. Various correction techniques exit, correction can be done before or after reconstructing the acquired dataset. A pre-processing method to remove these artifacts is by detecting and removing outliers prior to reconstructing CT data [Motulsky and Brown, 2006]. It works by replacing the specified pixel value with the average of surrounding pixels. A bad pixel map can be applied to the data set to remove the unsaturated pixels. Abnormal pixel detection using projections sum to remove artifact is suggested in [Yang et al., 2012]. Another efficient way is the anti-ring shift in which the detector position is slightly shifted during image acquisition to smear out systematic intensity fluctuations. Proper calibration of the detector before the scan can also reduce ring artifacts. A fast post-processing method proposed by [Sijbers and Postnov, 2004] based on the line artifact subtraction technique can be used for the correction.

A pre-processing method to correct for ring artifacts from variations in scintillator thickness by using a simple method to characterize the local scintillator response is presented by [Vagberg et al., 2017]. The results are depicted in Figure 1.16, the reconstruction from conventionally flat-field corrected images, Figure 1.16(a), suffers from the ring artifacts. And these artifacts are corrected by applying the proposed method, Figure 1.16(b)

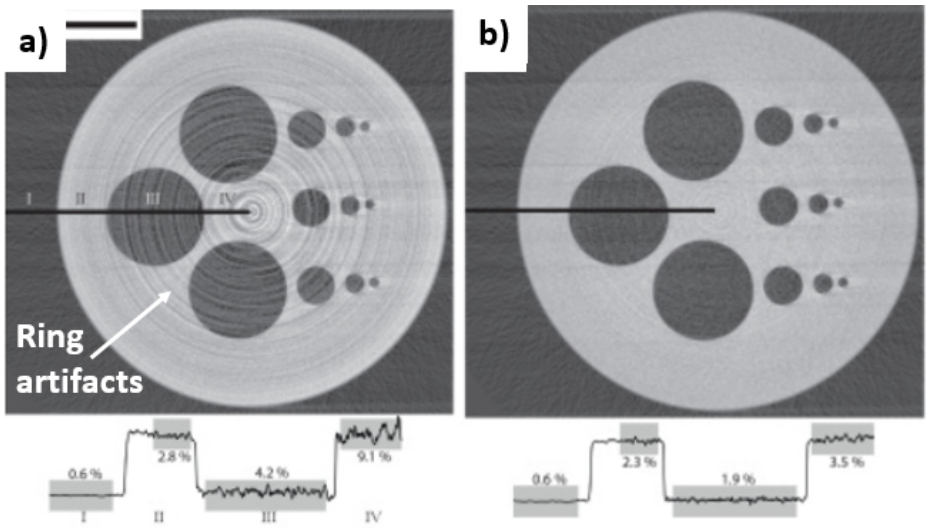

Figure 1.16: A tomography of a PET phantom with air-filled holes, reconstructed (a) after flat-field correction without filter. (b) with the proposed correction method based on characterization of scintillator variations. [Vagberg et al., 2017]

1.4.1.3 Scattered radiation artifact

Scattered radiation artifact occurs due to the scattering of the X-ray photons after interacting with the object.

This phenomenon is prominent with the cone-beam polychromatic X-rays, where a part of the incident X-ray photons is scattered. After interaction with the object, these scattered photons exhibit different travel directions and possibly different energies. Figure 1.17(a & b) shows the ideal and real scenario of the path of photons attenuating the object. In ideal situations, all photons are either absorbed or passing the sample, but in real scenarios, large amounts of photons are scattered and influence the attenuation and detection process.

When scattered photons reach the detector, they give rise to scatter signals, resulting in streaks, inhomogeneities known as cupping artifacts, and result in the reduction of contrast [P.C. Johns and yaffle, 1981, Glover, 2012, Siewerdsen and Jaffray, 2001]. Streaks may lead to misinterpretation, while inhomogeneities cause incorrect readings of attenuation coefficients which serve as the basis for interpretation and quantitative analysis. Scatter radiation correction methods based on the beam-stop array method and temporal modulation of primary signals are proposed [Schorner, 2012].

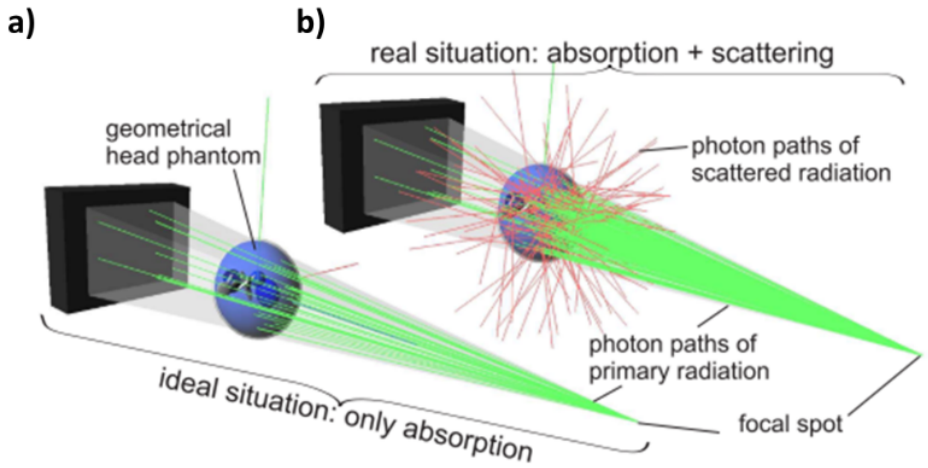

Figure 1.17: Geometry view of paths of the X-ray photons. (a) Ideal case for paths of X-ray photons that are either absorbed or passing the object, thus representing the ideal situation usually assumed for computer tomography reconstructions. (b) The real scenario, where a large number of scattering photons influence the attenuation and are detected as scattered radiations. [Wiegert, 2007]

1.4.1.4 Undersampling artifact

Undersampling artifact occurs when the total number of projections used to reconstruct tomographic reconstruction is relatively low. These artifacts can also occur when a large rotational angle step is used during the tomographic scan. They are referred to as aliasing artifacts since ray aliasing with sharp edges is observed due to undersampling. These artifacts make the segmentation process difficult, which is the primary requirement for quantification. Undersampling artifacts can be minimized by following the Nyquist-Shannon sampling theorem, Eq. 1.8, [Barrett and Keat, 2004], which gives the appropriate number of projections to be acquired for the CT scan for the reasonable reconstruction of the specimen volume.

$$Nb_{proj} = \frac{\pi}{2} * number\ of\ detector\ column\ covered\ by\ sample \tag{1.8}$$

where Nb_{proj} is the number of projections to be acquired. If the total number of radiographs captured gets lower, severe imperfections of the scanned object can be expected [Sause, 2016]. This is illustrated in Figure 1.18 for decreasing number of captured radiographs with the flat-panel detector as the basis for the same reconstruction algorithm. For the full set of 736 radiographs, the rectangular cross-section is well reconstructed. By reducing the number of captured radiographs, the cross-section is hard to reconstruct accurately, and an increasing amount of ray aliases occur that significantly reduces image quality.

However, acquired number of radiographs depends on the expected image quality and level of analysis that need to be performed. Even with 92 radiographs, the cross-section is clearly visible for the L1: qualitative analysis but for the quantitative analysis, higher number of projections need to be recorded. The identified undersampling artifacts can be reduced by using different reconstruction algorithms, such as iterative reconstruction or artificial intelligence based reconstruction algorithms, for a given number of projections.

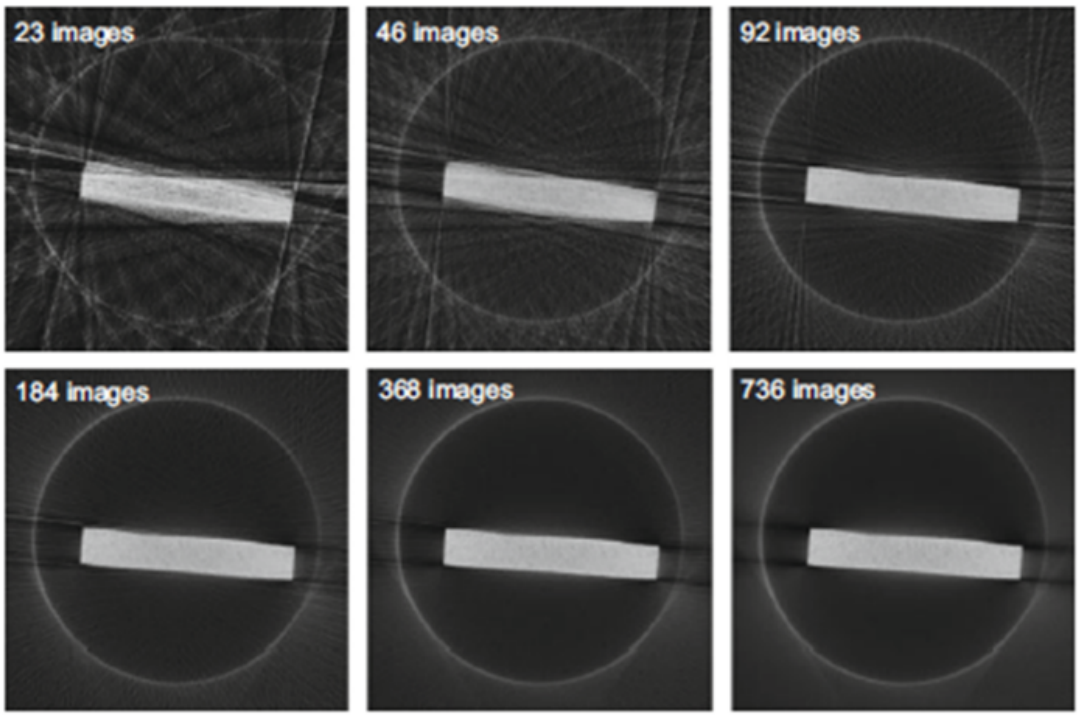

Figure 1.18: Undersampling artifacts in projections reconstructed with reducing number of projections. By reducing the number of captured radiographs, cross-section is hard to reconstruct accurately, and an increasing amount of ray aliases occur. [Sause, 2016]

1.4.1.5 Artifact specific to high density materials

CT scans of high-density materials can result in streak-like artifacts and deteriorate the image quality. Since high-density materials are mostly metals, they are also referred to metal artifacts.

They typically occur because the density of the material may exceed the detector system's measurement range, resulting in incorrect attenuation measurement [Sause, 2016]. These artifacts also arise because of the mismatch between the CT image reconstruction algorithm, filtered back-projection (FBP), and the nonlinear variation in the X-ray attenuation that occurs in the presence of a metallic object [Park et al., 2014].

High atomic number elements with higher mass attenuation coefficients such as iron, steel, and platinum can produce more pronounced artifacts than metals having low atomic numbers and lower mass attenuation coefficient as shown in, Figure 1.19. Artifact is worse with stainless steel, Figure 1.19(a) than with titanium Figure 1.19(b) [Kataoka et al., 2010]. An iterative method called the Metal Deletion Technique (MDT) [Boas and Fleischmann, 2012] which is based on the principle that projection data involving a metal is less accurate due to the assumption explained above, can be used for the correction. It used the forward projection to replace the detector measurements that involve metal.

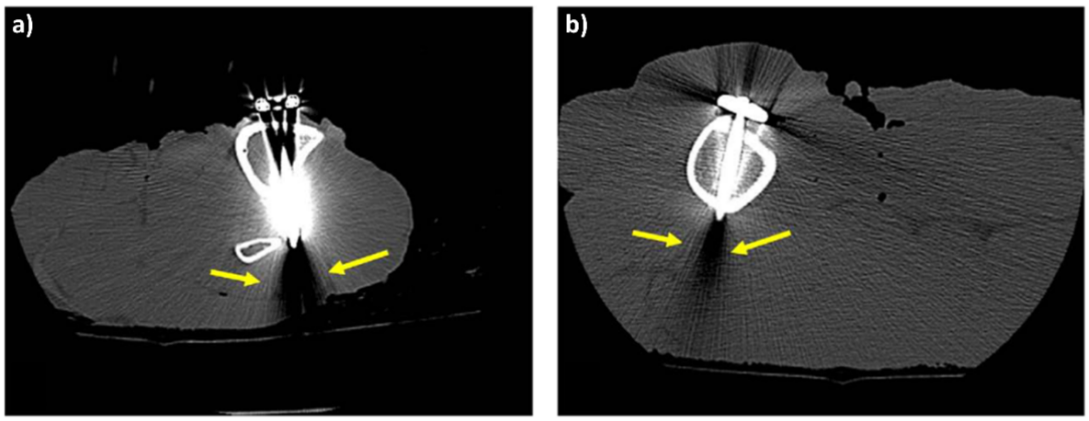

Figure 1.19: Metal artifact is severe with higher mass attenuation coefficient element (a) stainless steel than with lower mass attenuation coefficient (b) titanium. [Kataoka et al., 2010]

1.4.1.6 Motion artifact

Motion artifacts are caused by any structural change within the sample following a dynamic process such as stress-induced internal deformations or temperature related phase changes [Schryver et al., 2018]. It usually happens when the scan is performed at an insufficient temporal resolution. They can also be linked with the rotation stage's inaccuracy or may also result from movement of the X-ray source relative to the specimen.

Motion artifacts result in blurring and double edges. A pixel-specific back-projection method is described in [Ritchie et al., 1996] for the correction of motion artifacts. It reconstructs each pixel in a frame of reference that moves with the in-plane motion in the scanned volume. Motion artifact can also be corrected by correlation of the images before and after the scan.

1.4.1.7 Summary

These various types of artifacts discussed above are summarized in Table 1.1.

Table 1.1: Summary of the various types of artifacts in X-ray CT.

Artifact	Cause	Data treatment
Beam hardening	Selective attenuation of lower-energy photons when passing through a specimen.	Application of beam hardening correction algorithms. Effective filtering by a physical filter or adjusting the X-ray source energy. Linearization of the measured CT data. Use of photon-counting detector.
Ring	Miscalibration of the detector. The presence of defective pixels in the sensor	Re-calibrating the detector. Using pre and post-processing filters. Applying dead pixel mask.
Scattered radiation	Scattering of photons after interacting with the object.	Application of estimated scatter correction during the reconstruction.
High density material	High atomic number materials being scanned.	Metal Deletion Technique (MDT) applied during reconstruction.
Undersampling	Low number of projections.	Follow sampling theorem: Acquiring proper number of projections. Using different reconstruction algorithm type.
Motion	Structural changes within the sample when following a dynamic process. Inaccuracy of the rotation stage.	Correlating images before and after the scan. Pixel specific back-projection method.

1.4.2 Classical quality indexes in X-ray imaging

As described the utility of a CT scan for its intended scientific purpose depends on its ability to resolve and differentiate the objects for which image quality plays an important role. Image quality evaluation in CT images is an ongoing issue as there is no universally relevant and straightforward method to estimate the image quality sufficient for its intended purpose.

Many classical indexes exist to evaluate the objective and subjective image quality of a CT scan. However, these classical indexes do not provide any information about the task-based anticipated quality. Standard quality and similarity indexes are described below, and their limitations are also stated.

The presented quality measure indexes are noise, signal-to-noise ratio, contrast-to-noise ratio, sharpness, quality index and niqe, and the similarity measure indexes are root mean square error, peak signal-to-noise ratio and structural similarity index. These indexes can be used for 2D images (pixel i,j) or 3D images (voxel i,j,k) for the measure of quality of images or similarity between images.

1.4.2.1 Noise

In radiographic imaging, noise refers to unwanted image details that interfere with the visualization of a feature of interest and with the interpretation of an image [Samei et al., 1999]. Noise is classified as quantum noise and system noise [Samei, 2001]. Quantum noise is caused by the limited number of photons forming the image, whereas random and systematic processes cause system noise during image formation.

Noise can be estimated in a Region Of Interest (ROI) in the radiograph or reconstructed projection and measures the standard deviation (SD) of signals in that ROI. Considering the average number of detected photons in an ROI as N, the quantum noise defined as the standard deviation σ is inversely proportional to the square root of the number of photons [Zhao et al., 2014a].

$$\sigma \propto \frac{1}{\sqrt{N}} \tag{1.9}$$

A drawback of using noise as an image quality measurement index is that noise is estimated over an ROI in a single image, employing assumptions of linearity and stationary. The reconstruction process introduces correlation, due to which CT noise is textured and highly non-stationary. Also, it does not contain information about these correlations; therefore, it is not an acceptable metric of image quality [Vaishnav et al., 2014a]. However, it can be used as an objective image quality parameter for comparison between different reconstruction techniques [Willemink et al., 2013]. Due to its quick mean of measurement, many studies use the standard deviation to estimate CT image noise [Zarb et al., 2011, Lubner et al., 2011].

Using standard deviation as a noise measurement index provides a minimal description of noise magnitude and two images with very different noise textures may have identical standard deviations, as illustrated in Figure 1.20 [Friedman et al., 2013].

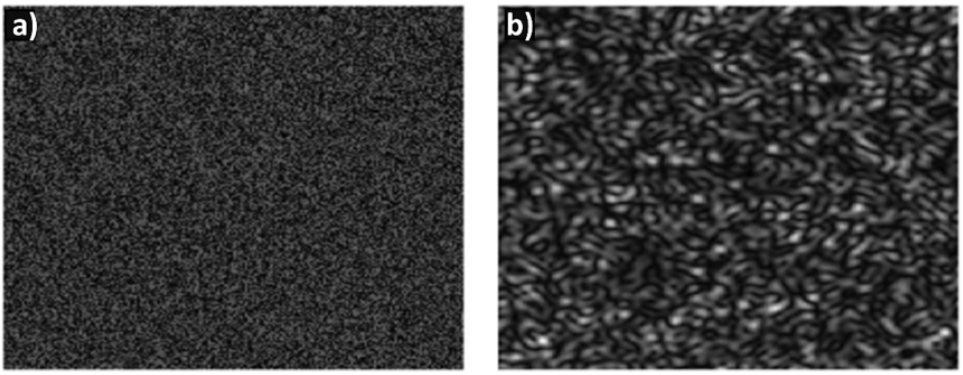

Figure 1.20: Two images with the same standard deviation but show (a) high-frequency noise and (b) low-frequency noise content. The difference between the images demonstrates the limitations of using standard deviation to fully assess image noise. [Friedman et al., 2013]

1.4.2.2 Signal to noise ratio

The Signal-to-Noise Ratio (SNR) is the most commonly used metric to express image quality in CT. SNR measures the intensity of the signals relative to the noise associated with the

signal in an ROI, which can be selected inside or outside the object in the radiograph or in the reconstructed slices.

Considering a given number of detected photons N with an average intensity $\overline{I}_{mean}$, and the standard deviation σ, SNR can be expressed as:

$$SNR \propto \frac{\overline{I}_{mean}}{\sigma} \tag{1.10}$$

In decibel scale (dB), SNR can be calculated as,

$$SNR = 10\log\left(\frac{\overline{I}_{mean}{}^2}{\sigma^2}\right) \tag{1.11}$$

SNR is directly proportional to the image's mean intensity, which makes it directly related to the CT scan parameters (source parameters, detector parameters and acquisition settings). Therefore the SNR will vary depending on the appropriate formulation, properties of the object under study, and the imaging arrangement used. Albert Rose [Rose, 1948] related SNR to the performance of a human observer by demonstrating that an object is detectable by a human observer if the SNR is $\geqslant 5$, and the detection will degrade as SNR approaches zero. SNR does not completely characterize noise as it does not consider the spatial frequency distribution of noise [Boone et al., 2012]. So two images with the same SNR can have different spatial frequency distributions, Figure 1.20. Also, when SNR is estimated in a homogeneous ROI, it does not provide any information if the images are quantifiable or not.

1.4.2.3 Contrast to noise ratio

In radiographic imaging, contrast is usually described in terms of Contrast-to-Noise Ratio (CNR) and gives information about the detectability of an object in the image.

It is usually measured in an ROI in the reconstructed images and is the difference between the average intensity of an ROI in the object $\overline{I}_{object}$ and that in an ROI in the background $\overline{I}_{background}$, with respect to the noise in the background $\sigma_{background}$.

$$CNR = 10\log\left(\frac{\overline{I}_{object} - \overline{I}_{background}}{\sigma_{background}}\right) \tag{1.12}$$

Since the CNR is computed using the difference in mean intensity values between the object and the background, this metric is applicable when objects that generate a homogeneous signal level are used [Bushberg et al., 2012]. In the case of heterogeneous material, CNR is different for each phase of the specimen.

CNR is not a complete description of object detectability as actual signal detectability, besides intensity and noise, also depends on factors including the variance and covariance of measurement noise, spatial resolution, and the observer and detection strategy used [Vaishnav et al., 2014b]. The inability of CNR to give a complete description of detectability of low-contrast object and image quality of CT at different radiation dose levels reconstructed with iterative reconstruction (IR) and filtered back projection (FBP) is shown in [Schindera et al., 2013].

1.4.2.4 Sharpness measures

Image sharpness is the local image quality measure and is used to describe the local contrast of the image. Sharpness, S, of an image is given by the following equation where $\overline{I}_{max}$ and $\overline{I}_{min}$ denote the maximal respectively minimal gray value in the ROI of the reconstructed projection.

$$S = \frac{\overline{I}_{max} - \overline{I}_{min}}{\overline{I}_{max} + \overline{I}_{min}} \tag{1.13}$$

Another objective image sharpness metric by integrating the concept of Just Noticeable Blur (JNB) into a probability summation model [Robson and Graham, 1981] to predict the relative amount of blurriness in images with different content is developed by [Ferzli and Karam, 2009].

A simplified measure of the JNB is used in [Kraemer et al., 2015] and variation of JNB and SNR as a function of the tube current at different source object distances is presented to pre-estimate the image quality. Similarly to SNR and CNR, sharpness is also estimated in a small ROI and no complete information about the image segmentation and the object detectability is provided by this metrics.

1.4.2.5 Quality index

The histogram-based quality metric Q was proposed by Reiter et al. [Reiter et al., 2014]. Q is a measure of the degree of separation of the different material classes in the gray value histogram of the image and is given as.

$$Q = \frac{\left|\overline{I}_A - \overline{I}_B\right|}{\sqrt{{\sigma_A}^2 - {\sigma_B}^2}} \tag{1.14}$$

where $\overline{I}_A$ and $\overline{I}_B$ are the mean values of the material and background in the gray value histogram and σ_A and σ_B are their corresponding standard deviations. Further details regarding the evaluation of Q can be found in [Reiter et al., 2014] where its sensitivity to noise, imaging artifacts, blurring levels and correction techniques is studied.

1.4.2.6 Root mean square error

The RMSE is the full-reference metric and is used where the aim is to compare an image to another image of higher quality. The RMSE is the square root of the mean of the squared signal intensity difference between each pixel in the test image from its equivalent in the reference image and is given by

$$RMSE = \sqrt{\frac{1}{n_x * n_y} \sum_{i=1}^{n_x} \sum_{j=1}^{n_y} \left(x\left(i,j\right) - y\left(i,j\right)\right)^2} \tag{1.15}$$

where $x(i,j)$ and $y(i,j)$ represents the gray level of a specific pixel in the reference and the test image. n_x and n_y are the total number of pixels in the horizontal and vertical directions,

respectively.

If the reference and the test images are identical, RMSE is zero. So a higher value of the RMSE means greater discrepancy. Images with very similar RMSE values can present quite different visual quality, and images with slight geometrical deviations (spatial shifts, rotation) can give large RMSE values but present acceptable image quality to observer [Wang and Bovik, 2006].

1.4.2.7 Peak signal-to-noise ratio

The PSNR is another full-reference metric and is used when the images being compared have different dynamic ranges. PSNR is given by

$$PSNR = 10log\left(\frac{\overline{I}_{max}}{MSE}\right) \tag{1.16}$$

Where, $\overline{I}_{max}$ is the maximum signal value in the test image, and MSE is the mean square error (mean square error is equal to the square of root mean square error). The higher value of PSNR represents the greater similarity between the two images that are being compared. A PSNR value of 100 dB would represent the ideal case, but typically the PSNR lies between 30 and 40 dB [Wang and Bovik, 2006, 2009]. The PSNR metric has the same benefits and limitations as RMSE that images with similar PSNR can present quite different visual quality, and images with slight geometrical deviations can give large PSNR values.

1.4.2.8 Structural similarity index metric

The SSIM represents image quality in terms of similarity index between two images and was proposed by [Kotevski and Mitrevski, 2010]. It represents the image quality by combining three factors: luminance distortion, contrast distortion, and loss of correlation [Ieremeiev et al., 2020], and is given as

$$SSIM = \frac{\left(2\overline{I}_x\overline{I}_y + C1\right)\left(2\sigma_x\sigma_y + C2\right)\left(\sigma_{xy} + C3\right)}{\left(\overline{I}_x^2 + \overline{I}_y^2 + C1\right)\left(\sigma_x^2 + \sigma_y^2 + C1\right)\left(\sigma_x\sigma_y + C3\right)} \tag{1.17}$$

where, $\overline{I}_x$, $\overline{I}_y$ and σ_x, σ_y are the mean values and standard deviations of the two images. σ_{xy} is the covariance between two images. $C1$, $C2$, and $C3$ represent the regularization constants for luminance, contrast, and structural correlation. For an 8-bit grayscale image composed 256 gray levels, C1 = $(K_1L)^2$, C2 = $(K_1L)^2$ and C3 = C2/2, where K1 = 0.01 and K2 = 0.03.

The SSIM is usually evaluated by applying a sliding window that moves pixel by pixel at a time, across an image. At each step, a local SSIM score is calculated. The final score describing the overall image quality is obtained by calculating the simple arithmetic average of each of the local scores. It has been reported that the SSIM is highly sensitive to errors due to alignment (relative translation, scaling and rotation) of images [Wang and Bovik, 2009].

1.4.2.9 NIQE

Natural Image Quality Evaluator (NIQE) [Mittal et al., 2013] is a completely blind image quality analyzer that only makes use of measurable deviations from statistical regularities observed in the natural images and does not require any reference image for the quality estimation. It extracts a set of local features from an image, then fits the feature vectors to a multivariate Gaussian (MVG) model. The local statistical features are derived based on a spatial domain natural scene statistics (NSS) model. The quality of a given test image is then expressed as the distance between a MVG fit of the NSS features extracted from the test image, and a MVG model of the quality aware features extracted from the corpus of natural images [Mittal et al., 2013, Sheikh et al., 2006] . Image quality assessment can be done on a specific ROI and also on a segmented images.

Since NIQE uses a single global MVG model to describe an image, useful local image information which could be used to better predict the image quality is lost [Zhang et al., 2015].

1.4.2.10 Summary

These various X-ray CT quality indexes are summarized in Table 1.2.

Table 1.2: Summary of the various types of image quality indexes used in X-ray CT.

Index	Description	Limitations
Radiographic noise	Measure of the standard deviation of signals in an ROI.	Employ assumptions of noise being linear and stationary in an image. Two images with very different noise textures can have identical standard deviation, SNR and CNR. Estimated in a small ROI. No information about detectability of feature of interest for segmentation. No information about noise in the feature of interest.
SNR	Measure of the intensity of the signals relative to the noise associated with the signal in an ROI.	
CNR	Measure of the contrast of an object in the image ROI with respect to noise.	
Sharpness	Measure of the local contrast of the image in an ROI.	
Quality index	Measure of the degree of separation of different material classes.	Sensitive to image noise, imaging artifacts and blurriness.
RMSE	Compare an image to a reference image of higher quality.	Needs a reference image. Images with very similar RMSE and PSNR values can present quite different visual quality. Slight geometrical deviation between images result in large error.
PSNR	Compare images have different dynamic ranges.	
SSIM	Similarity index between two images.	Needs a reference image. Highly sensitive to alignment errors.
NIQE	Predict image quality based on multivariate Gaussian (MVG) and natural scene statistic (NSS) model. Can be done on specific ROI.	Uses a single global MVG model to describe an image.

1.5 CT acquisitions parameters and image quality

1.5.1 Introduction

As mentioned in section 1.2 and illustrated in Figure 1.4(a), a micro-CT system for non-medical applications is composed of three main components: (i) an X-ray source, (ii) an X-ray detector, and (iii) a positioning system. So the image quality of CT scan depends on these main components and is influenced by several factors, including X-ray parameter settings, reconstruction settings, and image processing techniques [Cantatore and Muller, 2011]. In order to perform a CT scan, an operator has to choose a set of acquisition parameters that determines the quality of the recorded radiographs. The parameters that the user set for a scan are: X-ray source settings (power, current and voltage), the addition of filter, magnification, number of projections, scan mode and the detector parameters that includes binning, exposure time and frame averaging. Understanding the effect of these scanning acquisition parameters on the image quality is essential to find optimal settings for the optimal image quality of a CT scan. Major CT acquisition parameters are grouped in Table 1.2.

There is no developed analytical method to determine the optimal scanning parameters [Buratti et al., 2018] but attempts to optimize the acquisition settings have been made [Reiter et al., 2010, Chahid et al., 2020] focusing on the partial problem. The BSI BS EN ISO 15708 [15708-1:2017, 2019] and VDI/VDE 2630 [VDI, 2010] standards do not provide a protocol for the acquisition parameters selection, leading to differences in acquisition parameters for the same object between operators [Carmignato, 2012]. Similar results are reported by Zabler et al. [Zabler et al., 2020] by comparing quantitative image quality from thirteen different submicrometer CT scans of the polymer microbeads, performed by different experienced operators. Results indicate that operator choices strongly influence scan quality for a given measurement time.

Table 1.3: Major CT acquisition parameters that influence the image quality.

Group	Sub-group	Parameters
Hardware	X-ray source (micro/nano)	Type of source (target material and filament)
	Detector	Type of detector (flat-panel, CCD, PCD)
Operator parameters	Source parameters	Focal spot size X-ray source current Acceleration voltage
	Choice of filter	Material and thickness
	Detector parameters	Frame rate/ Exposure time Acquisition mode of detector (binning) Averaging frame
	Scan setting	Number of projections
	Positioning system	Magnification (SOD,SDD)
Sample properties	–	Size of the sample Material composition
Software	–	Reconstruction Post-processing filters

1.5.2 Hardware

The hardware component of the CT system includes an X-ray source and the detector. Target material used for the production of X-rays and the type of detector used to detect X-rays is the prime influencing parameters for the X-ray source and detector.

1.5.2.1 X-ray source

Many types of X-ray radiation sources exist, such as X-ray tubes and large synchrotrons radiation facilities, discussed in section 1.2.1, summarized in [Martz et al., 2016]. Generally, tube-based micro-focused X-ray sources are commonly used in micro-CT systems.

X-rays are produced when the target material, corresponding to the anode, decelerates an accelerated beam of electrons. The thermionic effect results in the generation of the electrons from the filament referred to as the tube's cathode. These generated electrons are attracted towards the anode target. On hitting the target material, the fast electron beam experiences a sudden deceleration, causing their energy to be converted into heat (more than 99%) and X-ray (less than 1%).

The produced X-rays have a polychromatic spectrum consisting of both bremsstrahlung radiation and characteristic radiation, Figure 1.21. Bremsstrahlung or braking radiation is an X-ray generation process that yields a continuous X-ray spectrum from very low energies up to the maximum voltage applied to the electrons. It occurs when an electron hits an atomic nucleus in the target and gets deflected due to the positive charge of the nucleus and causes an X-ray photon to be emitted. Characteristic radiation mechanism occurs due to the change in the electron's orbit in the atoms that make up the target, and hence it is target material dependent. The X-ray photon energies, in this case, are specific energies characteristic of the

material. Due to these two mechanisms, an X-ray beam is polychromatic.

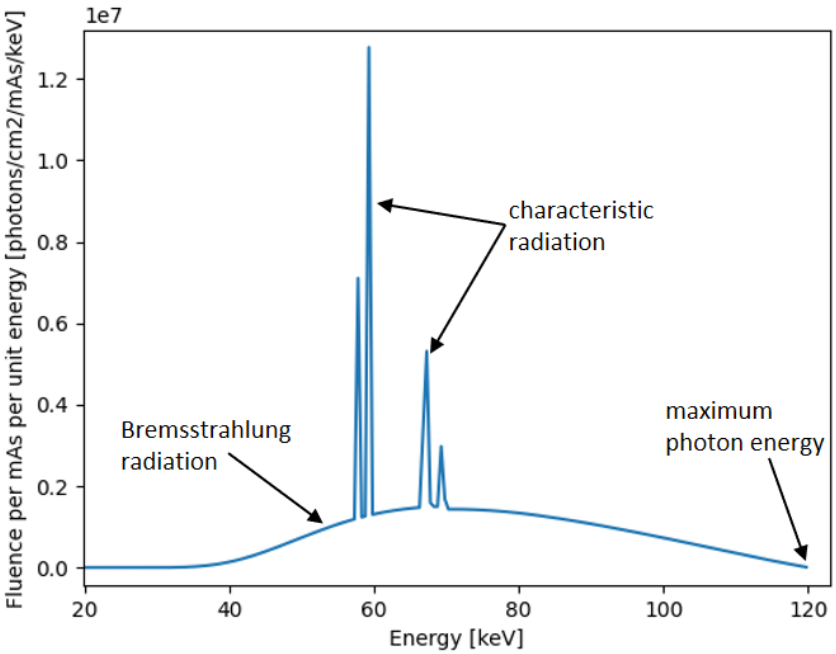

Figure 1.21: X-ray polychromatic spectrum generated using the tungsten W target at an acceleration voltage of 120 kV consists of both Bremsstrahlung radiation and characteristic radiations.

Target material and filament

The generated X-ray spectrum depends upon the target material used in the X-ray source. Tungsten (W) target is the most widely used in laboratory sources which operate in continuous mode with voltages in the range of 20–150 kV and anode currents in the range of 50–1000 µA [P. Russo, 2018]. The filament wire is usually made up of tungsten (W) or lanthanum hexaboride (LaB6). LaB6 offers more brilliant flux but is limited in keV.

The influence of the target material on dimensional measurements and porosity analysis was experimentally investigated in [Tan, 2015]. It was shown that with the same X-ray power, the measured porosity decreases when shifting the target material from copper to tungsten and the choice of target material also has an influence on the dimensional measurement with the tungsten target yields better imaging. The target thickness also influences the intensity of the generated X-rays. Ihsan et al. studied that X-ray intensity increases with the target thickness until a certain point. After, the intensity abruptly decreases due to the increasing X-ray attenuation occurring during the penetration of X-rays through the target [Ihsan et al., 2007].

1.5.2.2 X-ray detector

The type of digital X-ray detector used for CT impacts the image quality since each detector has its detection efficiency and characteristics. Detail about widely used detectors based on indirect and direct detection mechanism is earlier presented in section 1.2.3. Among all the digital detectors, indirect flat-panel detectors are the most commonly used.

The indirect flat-panels are designed to detect X-rays indirectly with the help of a scintillator. They are based on amorphous silicon TFT/photodiode arrays coupled to X-ray scintillators. The scintillator is usually made up of cesium iodide (CsI) or gadolinium oxysulfide (Gd2O2S). Upon interaction with X-ray photons, the scintillator layer converts X-ray photons into visible light. This visible light is captured by the large area photodiodes and generates electrons. The electrons activate the pixels in a layer of amorphous silicon. The activated pixels generate electronic data that is converted into a high-quality projection image of the scanned object. Figure 1.22(a) shows the indirect detection mechanism

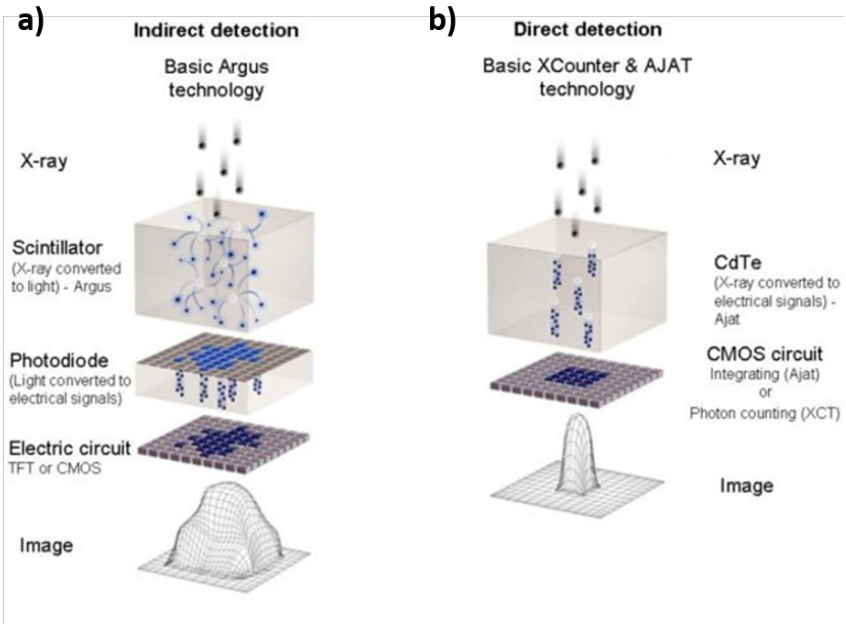

Figure 1.22: General model for indirect and direct detection of X-rays

Indirect flat-panels are available in sizes up to 400 mm × 400 mm and pixel size as small as 100 µm [Oliveira et al., 2019]. The commonly used indirect flat-panels have a pixel size of 127µm. Direct detection flat-panels [Kasap and Rowlands, 2000] and charged-coupled devices (CCDs) combined with scintillator screens are also widely used detectors with the laboratory micro-CT systems. Complementary metal-oxide-semiconductor (CMOS) detectors are also in use for their large area and high frame rates. Detail about CCDs and CMOS detectors can be found in [Kuroda, 2015]. An overview of the key technologies involved in constructing different imaging detectors can be found in [Overdick, 2006].

Earlier this decade, new generation detectors called photon-counting detectors (PCDs), that process each incoming X-ray photon individually, were introduced. PCDs work on a direct detection principle and convert X-ray photons directly into electrical signals with the help of semiconductor material, Figure 1.22(b). In PCDs, each photon contributes to the image formation proportional to its energy resulting in contrast enhancement. These detectors use an energy detection threshold, allowing full noise rejection, leading to higher SNR and image quality.

Detailed information about different radiation detectors used can be found in [Martz et al., 2016]. State of the art of CT detectors and sources can also be found in [Shefer et al., 2013].

1.5.3 Operator parameter

For the CT scan, acquisition parameters selected by the operator according to the scan's objective (aim of analysis: level L1, L2 or L3), largely influence the image quality. These include X-ray source parameters (voltage and current), choice of the filter, detector parameters (exposure time, average frame, acquisition mode of the detector), positioning system (work piece clamping and orientation, magnification, relative position of the rotatory table, and detector) and CT scan setting which include the number of projection to be recorded.

1.5.3.1 Source parameters

X-ray voltage (kV) and current (µA) are the two important source settings that directly influence the quality of the recorded radiographs. Both are user-defined settings; voltage needs to be sufficient to penetrate the scanned specimen and determine the image contrast, whereas current determines the intensity of the X-ray photons.

The tube voltage and current can be adjusted depending on the scanned material absorption coefficient and the objectives of the analysis [Stock, 2009]. The influence of the X-ray power settings and the object size on the accuracy of CT dimensional measurements were evaluated by Kiekens et al. [Kiekens et al., 2011]. It was found that the accuracy of CT dimensional measurement is dependent on both the voltage and current.

1.5.3.1.1 Voltage

X-ray voltage is a source parameter that determines the maximum energy of the X-ray photons. In other words, it determines the penetration ability of the X-ray beam and needs to be high enough to allow good visualization of internal features in the specimen. The change in the voltage is used to optimize the contrast by changing the X-ray spectrum [Orhan, 2019]. For denser samples like metals, higher voltage is required for enough X-ray penetration to get appropriate contrast between materials. If too low voltage is used for dense material, it usually results into more noise and artifacts [Plessis et al., 2018]. Decreasing the voltage leads to an enhanced contrast between low absorption phases [Stock, 2009].

Tang et al. [Tang et al., 2015] investigated the effect of low tube voltage on image quality, radiation dose, and low-contrast detectability (LCD) at abdominal CT. They concluded that reducing the tube voltage from 120 kV to 80 kV at abdominal CT can reduce the radiation dose by 32% to 42% without degradation of CNR and LCD. A study by Plessis et al. [Plessis et al., 2018] gave the guidelines using X-ray tube voltage as starting point for different samples and suggested that for biological samples 30 to 100 kV, for small rocks and light metals 60 to 150 kV, and for large rocks and heavy metals 160 to 240 kV could be suitable voltage.

1.5.3.1.2 Current

The change in the current changes the intensity of the X-ray and does not alters the energy of the X-ray photons. The filament current controls the number of electrons bombarding the target material; thus more current flowing through the filament, the higher the number of electrons emitted. But there is a saturation point at which the emission is at maximum, and increasing

the current even more can shorten the life of filament and can damage it.

For a CT scan, the operator should set up the tube power (multiplication of current and voltage) in such a way that spot size is similar to the voxel size. The focal spot size represents the small area on the anode on which electron beam is focused. A higher power increases the intensity of the electron beam, thus increase the heat in the focal point leading to the increase in spot size. A larger focal spot size increases the Penumbra effect, also known as unsharpness. This effect causes blur at the sample edges in the image which become noticeable when the spot size exceeds the voxel size [Kueh et al., 2016].

Angel and De Chiffre compared the twenty operators' X-ray source settings for two items involving metal and polymer parts, Figure 1.23. It can be seen that, although the items are very different in X-ray absorption and size, very similar power levels were used for both parts [Angel and Chiffre, 2014]. There is also a limitation for maximum current for a given focal spot size of the X-ray source.

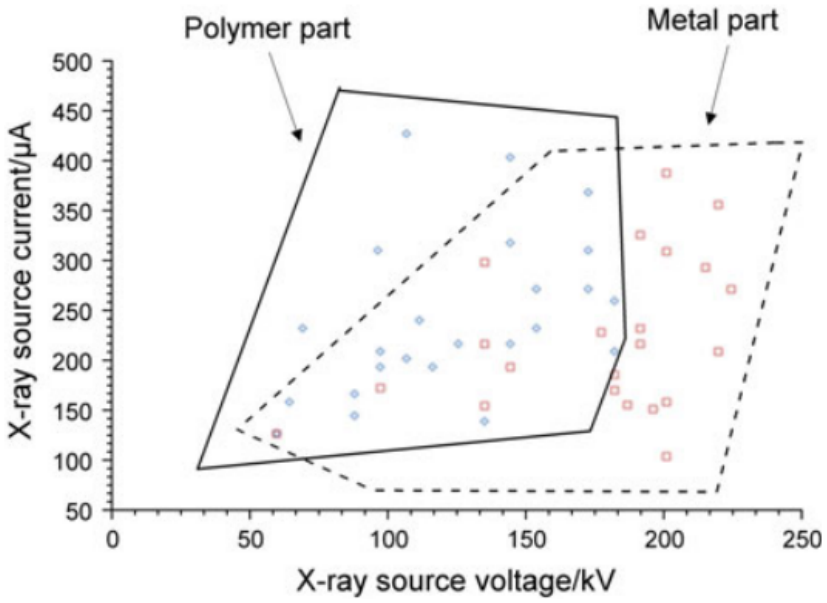

Figure 1.23: Current against voltage for polymer part (blue diamonds) and for a metal part (red square).[Angel and Chiffre, 2014]

1.5.3.2 Choice of the filter

Two different mechanisms associated with hardware filtering exists. (i) The filter is placed between the X-ray source and the sample, (ii) the filter is placed between the X-ray detector and the sample.

The first type of filtering, placed in front of the X-ray source, can be referred to as beam filtering and is useful when high-voltage experiments are performed. A beam filter is added to pre-compensate the expected beam hardening. The second type, referred to as detector filtration, is useful to reduce noise in the recorded radiographs that occur due to the scattering of X-ray photons after passing through the high-density specimen [Plessis et al., 2018]. Hardware filters are not capable of fully eliminating beam-hardening artifacts. They are applied as an initial beam hardening reduction step, often followed by more dedicated beam hardening correction

methods [Tan et al., 2013]. Commonly used X-ray filters include aluminum (Al), copper (Cu), tin (Sn), and steel with variable thicknesses, from 0.1 mm up to several millimeters depending on the application.

Mohd et al. [Mohd et al., 2011] studied the effects of Al, Cu, and AlCu filters of 5 mm thickness in viewing the inner structure of materials, and showed that the images quality with filter is equal or better than those without the filter. The effect of different filters on the X-ray micro-focused source spectrum generated at 50 kV voltage is shown in Figure 1.24(a). Filters absorb the low-energy photons resulting in the increase in the mean energy of the spectrum with the resulting spectrum having an improved penetration. The exposure time, voltage and filters are used to optimise the brightness and contrast of the image [Zwanenburg et al., 2021]. Figure 1.24(b) shows the spectrums with different voltages and filters, the increase in mean energy and decrease in intensity can be seen by using different combinations of voltage and filter thickness. The balancing of voltage and filter influences the mean energy of the spectrum which is responsible for the image contrast; the lower the mean energy the better the contrast. However, it can be difficult task to choose the optimal combination of the voltage and filter for a specific measurement.

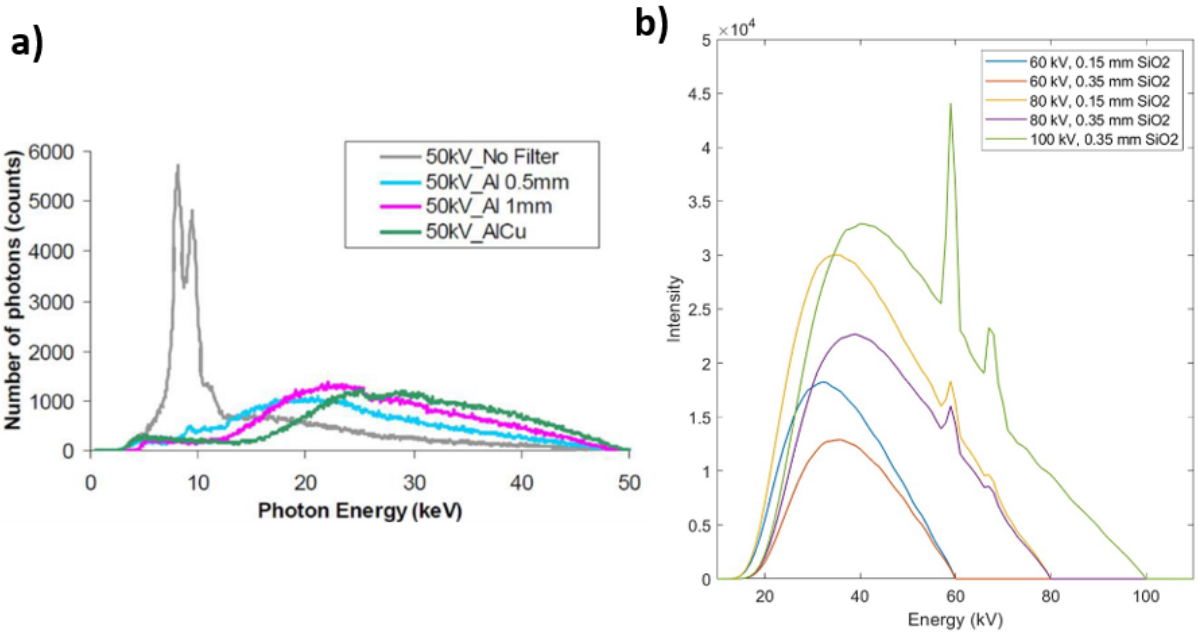

Figure 1.24: (a) Spectrum of a 50 kV X-ray source before and after passing various filters of different thickness. [Tan, 2015]. (b) Example of different spectra to demonstrate the impact of voltage and filter selection [Zwanenburg et al., 2021]

1.5.3.3 Detector parameters

1.5.3.3.1 Exposure time

Exposure time is the time required to capture a single projection during a CT scan and directly influences the total scan time, which refers to the time to record the total number of projections. Increasing the exposure time leads to a higher signal intensity that increases the SNR but at the cost of longer acquisition time. This parameter is important for in-situ tomography, especially

when dynamic processes need to be captured. Generally, the standard tomography exposure time for a single radiograph varies from a few hundred ms to up to several seconds per image resulting in the scan time for laboratory CT systems from few minutes to few hours [Christoph and Neumann, 2012]. Exposure time should be adequate, the low exposure time will result in low SNR, and higher exposure time can result in detector saturation. The combination of exposure time, voltage and filters needs to be optimized for the high quality radiographs.

1.5.3.3.2 Acquisition mode of the detector

Pixel binning is an acquisition mode in the detector that takes a matrix of pixels and combines them to create a larger pixel. Usually, 2x2 or 4x4 binning modes are available in flat-panel detector, in which 2x2 matrix of detector pixels or 4x4 matrix of detector pixels are combined to create a single large pixel prior to the CT scan. Due to the effective increase in pixel size resulting from hardware binning, more signal intensity will be captured, leading to higher contrast sensitivity. Also, data recorded and transferred to the computer is significantly reduced due to the pixel binning, allowing the detector to function at higher frame rates. Flat-panel Varian PaxScan 2520V can operate up to 12 frames per second without any binning, 30 frames per second with 2x2 binning, and 60 frames per second with 4x4 binning. This increase in frame rate with higher signals can be benefit for the high-speed in-situ acquisitions.

The drawback of signal binning is the loss of spatial resolution. Since the effective pixel size of the detector is increased, the detectable feature size of the specimen will be limited. Detector binning is beneficial for scans where faster readout time and improved signal-to-noise ratio are desired at the expense of spatial resolutions.

1.5.3.3.3 Average frame

Image averaging and the total number of projections are two most prominent factors that directly contribute to CT scan time. Averaging more projections, taken at the same angular position, reduces the projections' fluctuations and improves image quality. Generally, the magnitude of fluctuation drops by the square root of the number of images averaged [Carmignato et al., 2017a]. But after a certain number, usually average 6, there is a negligible effect in the noise reduction. Tshibalanganda et al. reported that increasing image averaging from one to three at each rotation step reduced the standard deviation and resulted in a slight increase in edge sharpness of the specimen [Tshibalanganda et al., 2019]. However, increasing the average frame increases the total scan time which can be an issue during fast in-situ acquisitions.

1.5.3.4 Positioning component

1.5.3.4.1 Magnification

In lab-CT, geometrical magnification influences the voxel size of the CT scan. The geometrical magnification M, of an X-ray CT is given as

$$Magnification = M = \frac{SDD}{SOD} \tag{1.18}$$

where SDD is the distance between the focal point of the source and the detector, whereas SOD is the distance between the source focal point and the object, Figure 1.25. Higher magnification can be achieved by positioning the specimen closer to the X-ray source. Eq. 1.18 suggests that same magnification can be achieved using different combinations of SDDs and SODs. The physical dimensions of the lab-CT system restrict the minimum and maximum SOD and SDD distances that can be achieved. For example, EasyTom XL micro-focus tomograph (Rx Solutions) allows the minimum SOD distance of 14 mm and maximum SDD distance of 660 mm. 14 mm is the distance between the X-ray focal spot and the X-ray output window for micro-focus X-ray source, and for nano-focus this distance is 0.5 mm. The user should pay attention while choosing the distances as they directly influence the image quality. A smaller SDD will lead to an increase in the photon intensity on the recorded images as it follows the inverse square law for intensity but it will decrease the magnification for a fixed SOD. From the magnification, voxel size V_{size}, can be deduced.

$$V_{size} = \frac{P_{pitch}}{M} \tag{1.19}$$

where P_{pitch} is the pixel pitch of the detector. Detector with small pixel sizes for a given magnification can result in smaller voxel size which can be beneficial for viewing the small feature of interest in the specimen. A higher magnification yields a better image resolution. But due to the finite focal spot size, the edges of an object are blurred when moving towards the X-ray source for achieving higher magnification [Kruth et al., 2011], as shown in Figure 1.25.

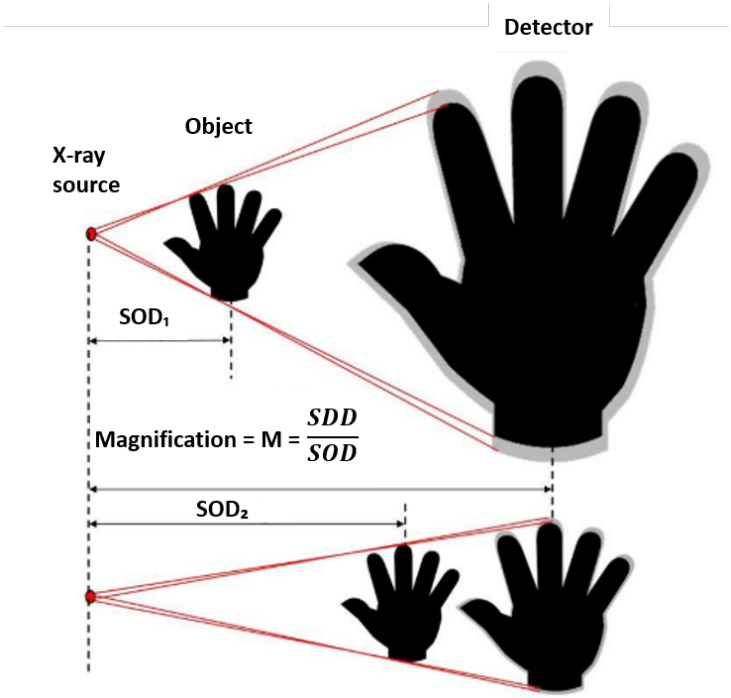

Figure 1.25: Image magnification and blurring by moving part towards the X-ray source. SOD: focal spot – object distance. SDD: focal spot – X-ray detector distance. [Kruth et al., 2011]

1.5.3.5 Scan setting

1.5.3.5.1 Total number of projections Total number of projections or the angular increment between two projections is the most dominant factor describing the CT scan's acquisition time and affects the resultant image quality. The Nyquist-Shannon sampling theorem gives the total number of projections to be acquired, for standard CT tomography, given in Eq. 1.20.

$$Nb_{proj} = \frac{\pi}{2} * \text{number of horizontal pixels in sample width} \tag{1.20}$$

It has been observed that the sampling theorem gives an overestimation of the total projections to be acquired, and half of the projections can be recorded without much affect on the image quality, 1.21.

$$Nb_{proj} = \frac{\pi}{4} * \text{number of horizontal pixels in sample width} \tag{1.21}$$

Acquiring a too small number of projections leads to the undersampling artifacts, explained in section 1.4.1.4. A weak correlation has been reported in the literature between the measurement accuracy and the increase in the number of projections. Weckenmann and Kramer [Weckenmann and Kramer, 2009, 2013] stated that by increasing the number of projections above 800, the measurement's accuracy increases by less than 5%. Gómez and Smith [Gómez and Smith, 2020] studied the effect on size measurements (lengths and diameters) using aluminum and nylon samples by reducing the number of projections and reported that using the Nb_{proj} between 600 and 2000 does not produce major changes in accuracy for lengths and diameters measurements for which absolute deviations between CT and reference data were mainly below 10 µm.

Chighvinadze et al. [Chighvinadze and Pistorius, 2015] investigated the dependence of the reconstructed image quality on the number of projections for multi-projection Compton scatter tomography using a photon-counting detector. By computing CNR and MTF, it was demonstrated that the contrast increases monotonically with the number of projections, while the spatial resolution was independent of the number of projections.

For fast in-situ scans, the recommended number of projections (Eq. 1.20) significantly increases the required acquisition time. In such cases, instead of decreasing the exposure time, the alternative is to reduce the number of projections. Even half, 50% of the recommended number of projections, Eq. 1.21, can be used for adequate image quality for quantification analysis L2 and L3. Many reported studies have even used 10-50% of the recommended projections, such is the case for experimental characterization of the foaming process during glass melting by Luksic et al [Luksic et al., 2020]. Only 10% of the total recommended projections are recorded with a scan time of 58 seconds during the glass melting process. However, it resulted in significant image quality issue as can be seen in Figure 1.26(a), the small features in the specimen is hardly visible but the macro pores are clearly visible and quantifiable, Figure 1.26(c), after repairing the projections to improve the quality of the image, and sufficient to gain insight into the process of glass melting and porosity changes with time.

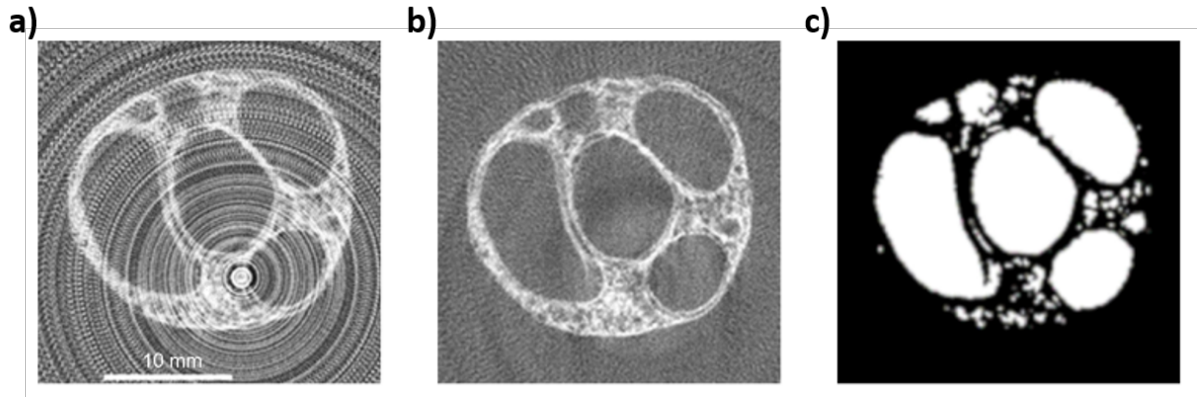

Figure 1.26: Experiment of foaming during glass melting where around 10% of the recommended projections, by Nyquist-Shannon sampling theorem, were used. (a) Initial raw reconstruction with image artefacts, (b) repaired reconstruction, (c) segmented bubbles within foam.[Luksic et al., 2020]

In case of local tomography when the sample diameter is larger the size of the detector and only a part of the sample is being scanned, much larger number of projections compared to Nyquist-Shannon sampling theorem are required for reconstruction with FBP reconstruction algorithm. An estimated value is given in Eq. 1.22.

$$Nb_{proj} = 3 * \text{number of horizontal pixels in sample width} \tag{1.22}$$

The number of projections can be adjusted as a function of level of analysis, L1, L2 and L3, to be performed on the 3D dataset. By using other reconstruction algorithms such as simultaneous iterative reconstruction technique (SIRT), simultaneous algebraic reconstruction technique (SART) and artificial intelligence (AI) based reconstruction algorithm, the number of required projections can be significantly reduced.

1.5.4 Sample properties

X-ray tomographic scans are widely used for inspecting and measuring properties of a wide range of materials ranging from low absorption paper material to high-density metals. The X-ray attenuation coefficient is different for each material, so scanning parameters need to be chosen accordingly. The size and the material composition are important parameters related to work-piece properties.

1.5.4.1 Size of the sample

The size of the workpiece directly defines the attainable spatial resolution of the CT scan. Larger samples are scanned at low resolution; thus, image quality, in this case, will be limited for high-level quantification analysis. Small samples can be scanned at very high resolution. Plessis et al. linked the resolution with the width of the sample and stated that the optimal resolution is a factor 1000 times smaller than the width of the sample. A sample with a width of 100 mm can have an optimal resolution of approximately 100µm [Plessis et al., 2018]. Figure 1.27 shows

the relationship between spatial resolutions and object sizes (diameter) for various CT systems. This relationship is valid only for a 1000 x 1000 pixels detector. Laboratory CT system lies in micro-CT and nano-CT.

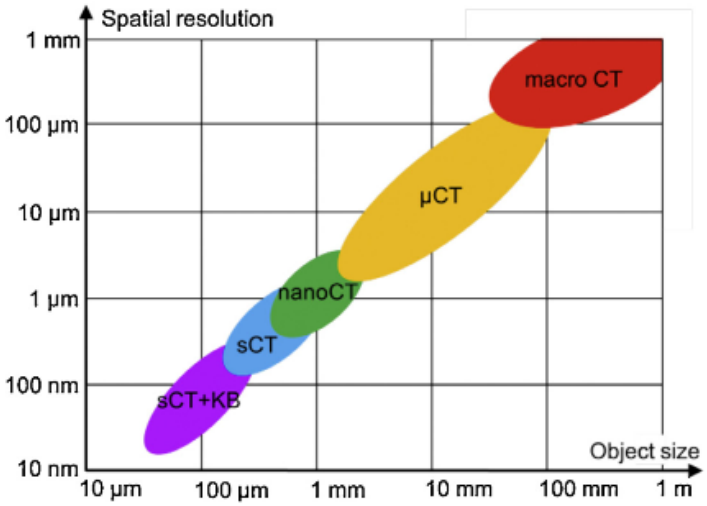

Figure 1.27: Typical spatial resolutions and object sizes (diameter) for macro-CT, micro-CT, nano-CT, synchrotron-CT (sCT) and synchrotron-CT with KB mirrors (sCT+KB) for a 1000 x 1000 pixels detector. [Chiffre et al., 2014]

1.5.4.2 Material thickness and composition

All sort of materials can be scanned with X-ray CT. Typical materials that are scanned belong to polymers, ceramics, biological materials, metals, geomaterials and, composite materials. Material attenuation coefficient and the X-ray photon energy limit the maximum accumulated material thickness that X-rays can penetrate. Before scanning, the object should be oriented to reduce the maximum penetrated material thickness. [Chiffre et al., 2014]. Table 1.4 shows the maximum penetrable material thicknesses for materials at transmission of around 14%.

Table 1.4: Typical maximum penetrable material thicknesses for common industrial materials at 14% transmission. [Chiffre et al., 2014]

X-ray voltage [kV]	**130**	**150**	**190**
Steel/ceramic [mm]	5	8	25
Aluminium [mm]	30	50	90
Plastic [mm]	90	130	200

1.5.4.3 Motion of sample feature

An important parameter that reduces the resultant image quality is the motion of the interested feature present in the sample during the in-situ acquisition. The motion is caused by the structural change of the sample feature following a dynamic process and usually occurs when a dynamic process is imaged at an insufficient temporal resolution [Schryver et al., 2018]. This

motion of the feature during the scan results in motion blurring in the reconstructed datasets. In order to reduce the motion blurring artifacts, the scan time needs to be reduced.

However, for such acquisitions a trade-off is made between the acceptable level of motion, image quality and the temporal resolution.

1.5.5 Software

Data processing is an essential step in CT and influences the resultant image quality. It includes the reconstruction algorithm and post-processing filtering applied to the reconstructed slices prior to quantification. As highlighted briefly in Section 1.2.5, many reconstruction algorithms exist, with filtered back-projection (FBP) being the most commonly used in industrial CT.

Image filtering refers to any operations applied to the pixels in an image to improve the quality of the image. Generally, a median filter of radius 1 or 2 is applied to the reconstructed data to cater for noise. Median filtering is a nonlinear method, which performs better than linear filtering for removing noise in the presence of edges [Castro and Donoho, 2009]. Other common filters for suppressing noise are smoothing and edge enhancement. A number of filtering steps such as ramp filter, Shepp-Logan and Butterworth filter, Hamming filter, and cosine filter typically accompany the filtered back-projection (FBP) algorithm. The main reason for all these filterings in tomographic images is to suppress statistical noise and to preserve spatial resolution and contrast; details can be found in [Lyra and Ploussi, 2011].

1.5.6 Conclusion

The effect of the CT scan acquisition parameters on the image quality is evident. These acquisition parameters need to be optimized for the optimal image quality for a given scan depending on the aim of the analysis to be performed on the 3D images. The selection of these parameters become even more troublesome when fast in-situ acquisitions need to be performed.

Classical approaches to optimize these parameters rely on the empirical choices focusing on a partial problem. No such accepted tool to predict the optimal scanning configuration for a given scan exit and there is a clear need for such optimization tool. The issue is a competition between high SNR and contrast, low motion and high resolution for the selection of suitable parameters for a given scan. A global optimization strategy could lead to improve the quality of images for a scan with optimal configuration in the sense of a reduced error on the quantification of interested feature size.

1.6 Time-resolved CT

As described in section 1.3.2, time-resolved CT (4D images) has become popular for following process characterization of materials. Time-resolved CT is useful to follow the initiation, propagation, and interaction of damage modes inside the specimen as a function of time and environmental conditions. The obtained quantitative information can be used to improve and validate the analytical or numerical models for material behaviors. Other terms such as 4DCT, temporal-CT, time-lapse CT are also used and all refer to the acquisition of volumetric scans over the duration of time period that can be of the order of seconds, minutes, hours or even days.

Salvo et al. [Salvo et al., 2010] described various ways in which X-ray CT is applied in material science to study the microstructural evolution with the thermal treatment or mechanical testing at room or high temperature. These ways include post mortem tomography, ex-situ tomography, and in-situ tomography.

Post mortem tomography: In post mortem tomography, a scan is made at room temperature on a sample after heat treatment or mechanical loading. Several samples are used to study the influence of the thermal or mechanical testing treatment on the microstructure evolution of the material.

Ex-situ tomography: Ex-situ tomography is similar to post mortem tomography as the specimen is deformed outside of the tomograph by heat treatment or mechanical loading. However, the same sample is used for multiple CT scans at room temperature, which requires sample cooling for thermal treatment and stress relaxation for mechanical testing before each scan. The reheating or reloading of stresses can influence the mechanisms to be studied, illustrated in Figure 1.28(a).

In-situ tomography: In-situ temporal CT or in-situ time-resolved CT or in-situ CT is a technique in which specialized testing devices deform material inside the tomograph, and tomographic acquisitions are simultaneously made. Over the last few years, many researchers [Garcea et al., 2018, Gajjar et al., 2018, Dewanckele et al., 2020] further classified In-situ CT according to the testing and scan conditions.

1.6.1 Types of in-situ acquisitions

In-situ CT can further be categorized into three types interrupted acquisitions, uninterrupted acquisitions, and continuous acquisitions.

1.6.1.1 Interrupted in-situ acquisition

Interrupted in situ tomography procedure is similar to ex-situ tomography, except the specimen is deformed inside the tomograph. This technique requires specific testing devices (furnaces, compression–tension machines) mounted directly on the tomograph. The same sample is used, but thermal or mechanical tests need to be interrupted during the scan, affecting the mechanisms to be studied, Figure 1.28(b).

1.6.1.2 Uninterrupted in-situ acquisition

In uninterrupted in-situ, the specimen is deformed under thermal or mechanical tests without any interruptions, and the CT scans are made at regular intervals. Uninterrupted in-situ is done when the kinetic evolution of the specimen is relatively low due to the testing device's slow loading or heating rates, Figure 1.28(c). This acquisition is used to study the material behavior over relatively long times, and scans interval is selected according to the material peak behavior. Usually, the applied deformation rate for uninterrupted time-lapse is slow.

1.6.1.3 Continuous in-situ acquisition

In continuous in-situ, the same specimen is continuously rotated and scanned without interrupting the mechanical test or the thermal treatment. The applied deformation rate for continuous in-situ is relatively faster, and fast scans are often required to capture the rapid microstructural evolution of the deformed specimen, Figure 1.28(d)

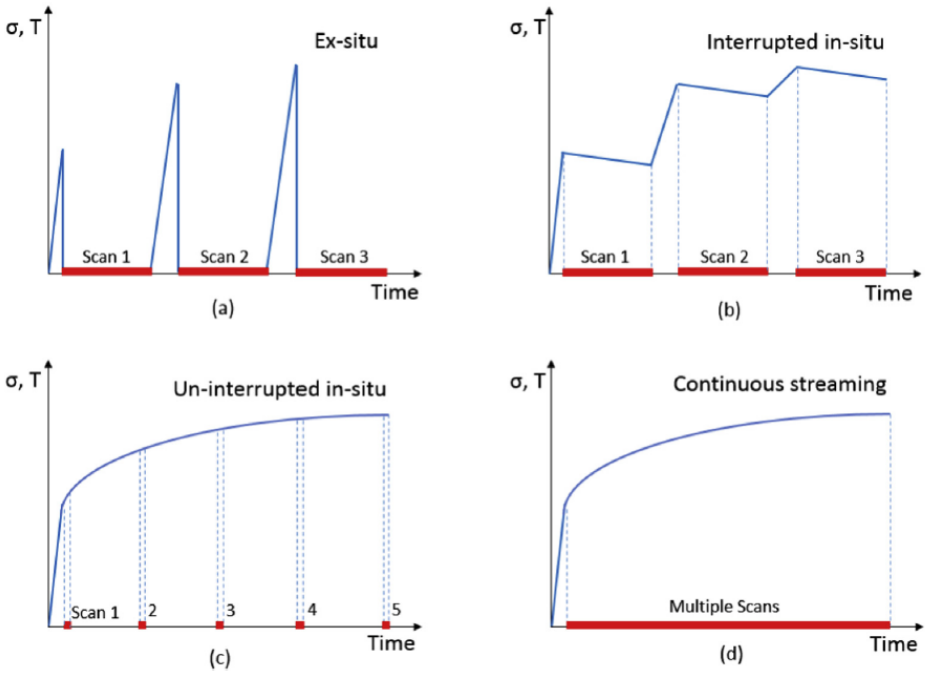

Figure 1.28: Schematics illustrating of various techniques for temporal X-ray CT acquisitions (in red) for mechanical testing σ, and thermal treatment T (in blue). (a) Ex-situ, (b) interrupted in-situ, (c) uninterrupted in-situ, and (d) continuous in-situ tomography. The acquisition times for a single scan depend on the deformation rate and must be compatible to capture the studied phenomena. [Garcea et al., 2018]

1.6.2 Constraints during in-situ tests

Many constraints, practical and tomographic parameters, exist during the in-situ acquisitions and influence the image quality for the desired objectives.

1.6.2.1 Size of the in-situ setup

In-situ CT acquisitions require specialized testing devices that can be mounted inside the tomograph. Thus, the setup size needs to be very specific compared to the standard size of the mechanical devices. For experiments related to small-scale measurements, relatively small devices are required to be placed close to the source to achieve the desired magnification. For bigger setups, the source to object distance is limited, and high spatial resolution cannot be achieved. So, the size of the in-situ setup will typically determine the ultimate spatial resolution of the scan. Figure 1.29 shows the in-situ uniaxial tensile test set-up at laboratory 3SR.

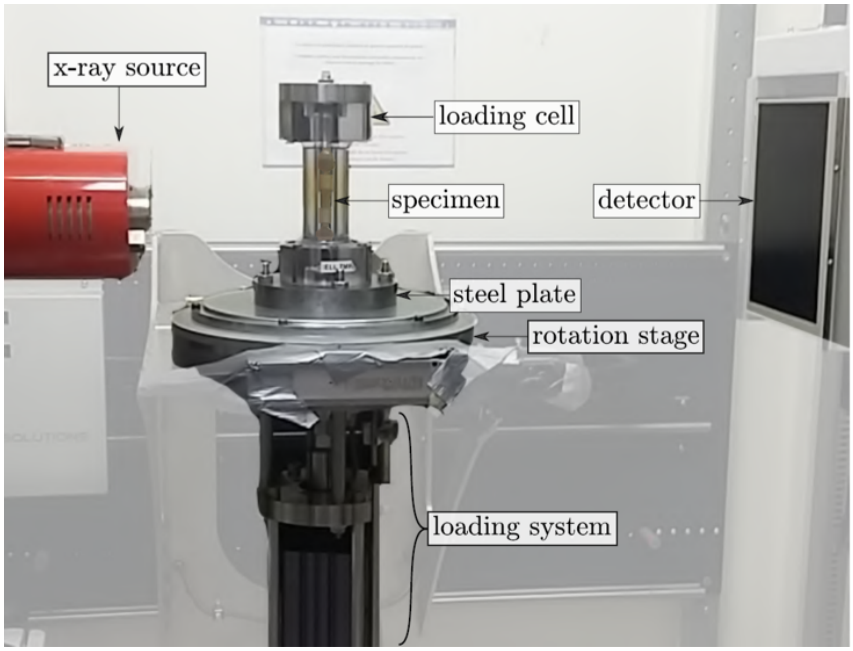

Figure 1.29: Micro-CT setup for in-situ uniaxial tensile test at laboratory 3SR. [Stamati, 2020]

1.6.2.2 Inability to continuously rotate

Another limitation that comes with complex in-situ experimental rigs is the inability to rotate continuously. Complex cables and wires attached to the experimental device restrict the rotation over 360° in standard CT systems. In this case, the setup needs to rotate way and back from 0° to 360° making the acquisition time-lapse and restricting to perform the continuous acquisitions to image the dynamic process.

1.6.2.3 Ultimate resolution

For the laboratory CT systems, the ultimate achievable spatial and temporal resolution is limited compared to the synchrotron facility. The size of the in-situ device along with the cone-beam geometry limits the achievable spatial resolution. With EasyTom XL with a micro-focused X-ray source, considering a specialized in-situ device, furnace, of diameter 50 mm with specimen placed at the center, with 14 mm distance between the X-ray focal spot and output window, the minimum SOD that can be achieved is 24 mm, Figure 1.30. By placing the detector at the farthest position of 660 mm will lead to a voxel size of 7.5 μm with a standard flat-panel

detector of pixel pitch 127 μm in full acquisition mode. Figure 1.30 illustrates the geometry constraints during in-situ lab-CT for EasyTomXL. However, the X-ray flux on the detector with this geometry will depend on the exposure time and X-ray source settings.

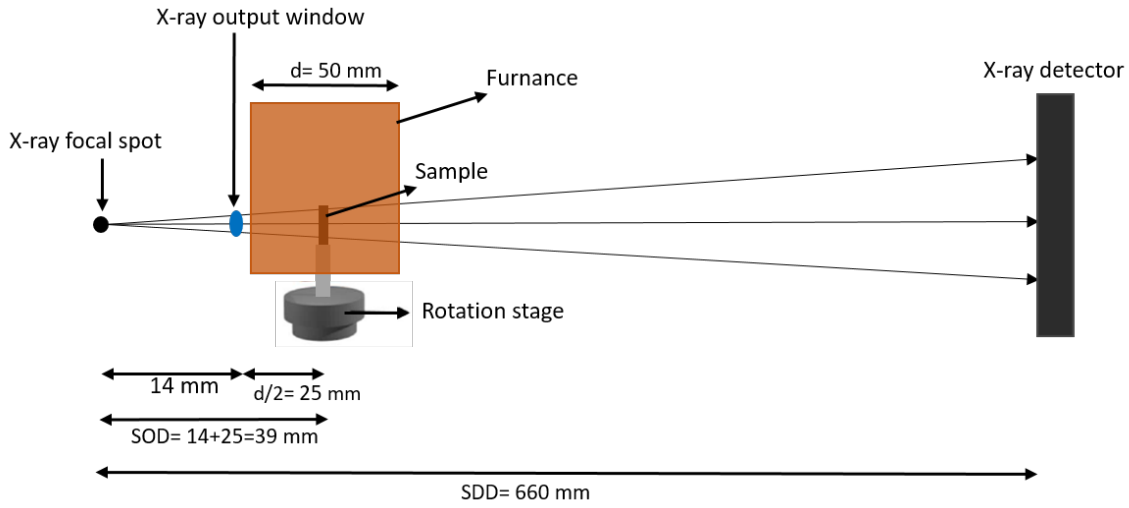

Figure 1.30: Schematic illustration of ultimate spatial resolution constraint during the in-situ acquisitions due to geometry restriction in lab-CT.

The limited photons flux at the lowest possible exposure time of the detector limits the required temporal resolution for dynamic in-situ acquisitions. The intensity received at the detector at this lowest exposure time is significantly low resulting in poor image SNR and contrast. Other key parameters that influence the achievable temporal resolution are various CT acquisition parameters, described earlier in Section 1.5.

1.7 Fast imaging in lab-CT

For in-situ acquisitions, where the sample's microstructure changes relatively fast due to the faster loading or thermal rates, fast continuous acquisitions are needed to capture the rapid microstructural evolution in order to obtain a meaningful tomographic reconstruction. The main parameters affecting the speed of the CT scans are the photon flux, the detector efficiency (exposure time and readout time), and the architecture of the data acquisition system [Michiel et al., 2005], as described earlier in Section 1.5.

Extremely fast imaging has become possible at synchrotrons due to the higher flux, collimated, polarized X-ray beam at high spatial resolutions over the last years. Fast scans with even sub-second time resolution are reported [Rack et al., 2010, Wildenschild and Sheppard, 2013, Salvo et al., 2012a, Mokso et al., 2011, Maire et al., 2016, Garcia-Moreno et al., 2021]. The advantages and use of fast synchrotron imaging can also be found in [Stampanoni et al., 2006, Michiel et al., 2005]. However, restricted access to synchrotrons limit the amount of experiments that can be performed; therefore, the developments in laboratory-scale tomographs have increased drastically since they're easily accessible small scale and inexpensive facilities compared to synchrotrons. For sub-second acquisition times at sub-micron voxel sizes, a synchrotron source is still needed.

In laboratory CT systems where the rotatory stage has the ability to rotate with the complex experimental rigs continuously, and in-situ setup is small enough to achieve the desired spatial resolution, lower X-ray flux limits the time resolution that can be attained with desirable signal-to-noise (SNR) ratio and contrast for quantitative characterization. Although with the improvements in the hardware, the scan time in the order of few minutes is possible but faster acquisitions, comparable with synchrotron, for the imaging of faster dynamic phenomena is still desired.

Generally, with lab-based systems, the maximum attainable resolution for in-situ acquisitions is often in the order of tens of micrometer depending on the size of the in-situ setup and CT parameters, while the acquisition time is generally in the order of few minutes to few hours. Obtaining good quality images with enough SNR and contrast for quantitative analysis under a sub-minute time scale with laboratory-scale tomograph is an ongoing issue. Only a few examples can be found in the literature with the reported acquisition under sub-minute per full rotation [Bultreys et al., 2016, Vavrik et al., 2017], but these scans are mainly qualitatively analyzed, level L1.

Figure 1.31 shows a map depicting the state of the art of the fast scans performed using lab-CT. The map is a scan time versus voxel size of the fast scans. It can be seen that most of the high-resolution works have been done with long acquisition times and only a few scans under sub-minute scan time have been reported.

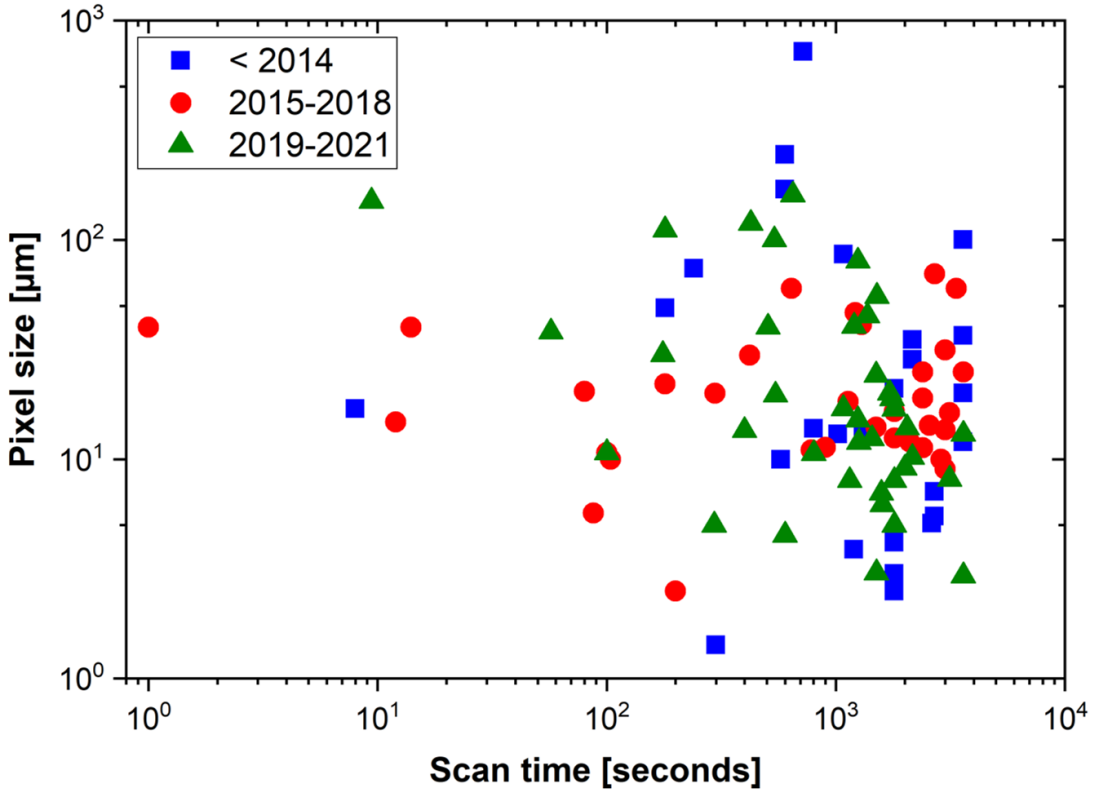

Figure 1.31: State of the art of in situ lab X-ray tomography: pixel size versus scan time for the lab in-situ X-ray CT. Only few scans with sub-minute temporal resolutions are reported due to the limitations of the lab-CT. [Zwanenburg et al., 2021]

Figure 1.32(b) shows a reconstructed slice of a fast scan reported by Bultreys et al. [Bultreys et al., 2016] and compares it with the same scan of high-quality, Figure 1.32(a), for a pore scale experiments using lab µCT. The scan time for the high-quality and fast scans was 21 min and 12 sec with voxel size of 7.4 and 14.8 μm, respectively. It can be seen that image quality is not sufficient for the fast scan to quantitatively analyze the two phases, solid and porous phase. Apart from the few big pores that are visible, many small pores are not even detected. This image quality is the result of the selected scanning parameters that made it possible to reduce the scan time to 12 sec but at the expense of image quality.

The fast scan with the acquisition time of 1 seconds, reported by Vavrik et al. [Vavrik et al., 2017] utilized the new generation photon-counting detector TimePix which allows to reduce the exposure time down to 3.4 ms. However, the scans are only analyzed using the level L1 visual qualitative analysis due to the limited image quality. An overview of these fastest scans parameters performed with the lab-based CT system is presented in Table 1.5.

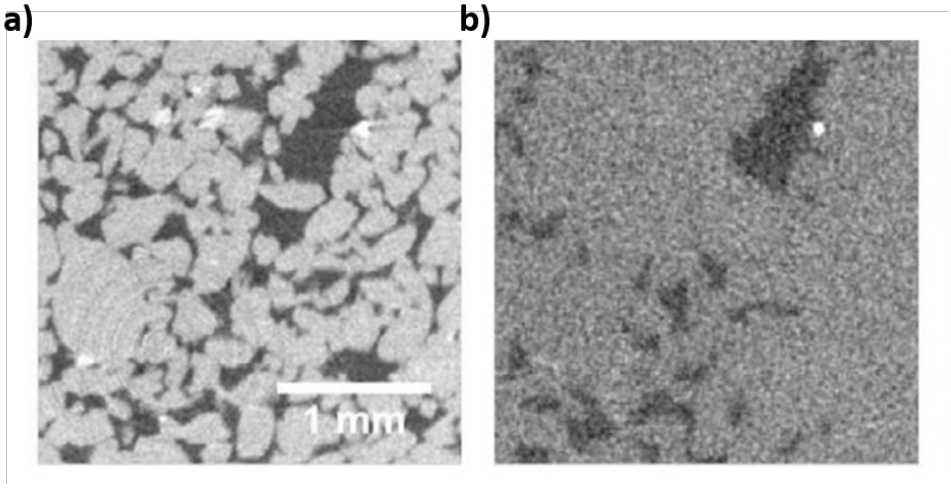

Figure 1.32: The qualitative results of pore scale experiments visualizing two-phase flow and solute transport in real-time with lab-based µCT. A cropped slice from (a) the high-quality scan (7.4 µm voxel size and 21 min scan time), (b) the fast scan (14.8 µm voxel size and scan time 12 s) is shown. [Bultreys et al., 2016]

Table 1.5: Overview of the fastest scans performed on lab-based CT systems, [Bultreys et al., 2016, Vavrik et al., 2017, Eggert et al., 2014, Dewanckele et al., 2020] Adapted from [Zwanenburg et al., 2021].

Year	Author	Scan time (s)	Exposure time (s)	Projections	Voltage	Power	Voxel size	Level of analysis	Type of in-situ
2017	Vavrik et al.	1	0.0034	252	60	50	40	L1	continuous
2014	Eggert at al.	8	0.034	236	60	14.4	17	L1	uninterrupted
2020	Dewanckele at al.	9.4	0.017	550	130	35	150	L1, L2	continuous
2016	Bultreys et al.	12	0.02	600	130	16	14.8	L1, L2	continuous

In most of the cases, users are often limited by the maximum frame rate of the detector which restricts the scan time. The improvements in the detector hardware or by utilizing the new generation fast readout direct detectors can help in achieving the sub-minute scan time. Another aspect to decrease the scan time is to reduce the number of projections. Although for optimal image quality the Nyquist sampling theorem should be followed for filtered back-projection algorithm. But depending on the level of analysis to be performed, Section 1.3.3, the number of projections can be significantly reduced. This is also the case for the fast scans presented in Table 1.5. Also the use of different reconstruction algorithms such as iterative reconstruction method and artificial intelligence based reconstruction algorithms need to be explored.

A number of researches have shown that a fewer number of projections could be sufficient to obtain a suitable image quality and measurement accuracy using iterative reconstruction method [Jorgensen and Sidky, 2015, Coban et al., 2021]. This also applies to the two-phase fluid flow experiment by Myers et al. [Myers et al., 2011]. It uses an iterative reconstruction algorithm that takes advantage of the sample's prior knowledge. This method reduced the number of projections from 720 in case of filtered back-projection to just 72 projections, the time resolution

is increased by a factor of 10.

The developments of new X-ray detectors and sources can also help in reducing the scanning time with quantifiable image quality improving the capabilities of lab-based systems. The possibility to use the new generation photon-counting detectors (PCDs) in lab-CT for improved image quality needs to be explored. The industrial application of new generation laser driven sources is presented by Gruse et al [Gruse et al., 2020] that utilise femtosecond pulses of X-rays and provide micro-scale resolution with fast scanning time. A compacted light source [Hornberger et al., 2019] that provides high-flux, quasi-monochromatic and tunable X-rays in the laboratory can also be used but it is currently very expensive.

1.8 Synthesis of the literature review

In this chapter, brief description of various inter-related aspects of computed tomography is presented. The importance of image quality and the limitation of image quality indexes is presented. The importance of CT various acquisitions parameters and their effect on image quality for both static and in-situ acquisition are explained in detail. Furthermore the time-resolved CT and the fast imaging in lab-CT is also detailed. The synthesis of the chapter is presented below.

- The X-ray CT is widely being used as a characterization tool for materials: proposed classifications L1: qualitative, L2: low-level quantitative and L3: high-level quantitative 3D image analysis are being performed on quasi-static and in-situ CT acquisitions for materials characterization.
- Synchrotron CT offers various advantages over lab-CT. A high flux and monochromatic X-ray beam in synchrotron offers high spatial and temporal resolution with high image quality. Whereas, despite being easily available and cheaper, lab-CT offers polychromatic and limited flux X-ray beam which severely restricts fast in-situ imaging.
- Due to the polychromaticity of the lab X-ray beam, less contrasted images are formed than at synchrotron. This also limits to perform spectral imaging using standard combination of source and detector.
- Image quality of a CT scan plays a vital role for the post-processing characterization. The classical image quality indexes evaluate the objective and subjective image quality of a CT scan but they do not provide any information about the task-based anticipated quality or about the detectability of feature of interest during the segmentation process.
- The effect of scanning acquisition parameters on the image quality is evident, even the parameters selected by experienced operators lead to a difference in scan quality. No analytical method or accepted acquisition protocol exists to determine the suitable scanning parameters for optimal image quality for a given CT scan and there is a clear need for such tools.
- Obtaining good quality images for quantitative analysis with the fast lab in-situ acquisition is an on-going issue. The reported fastest scans are mainly qualitatively analyzed, level

L1, due to the limitation in image quality. A global optimization strategy for the selection of acquisition parameters could help to improve the quality of obtained images allowing both qualitative and quantitative analysis.

- The use of latest hardware components (detectors and sources) could be explored to achieve higher spatial and temporal resolution with improved image quality compared to standard detectors and sources.

1.9 Objectives of the PhD thesis

Improving X-ray imaging in laboratory-scale equipment is the general objective of this PhD thesis. Two different aspects studied in this PhD thesis are as follow.

1.9.1 Methodological aspects

Two possibilities will be investigated in methodological aspects.

1. Hardware strategy: Use of direct photon-counting detector.
   - Quantitative characterization and implementation of energy-discriminating direct photon-counting detector (PCD), Pixirad-2/Pixie-III, in lab X-ray CT using a polychromatic beam.
   - Exploring the potential advantages and possible drawbacks of Pixirad-2/Pixie-III. Accessing the spectral imaging capability of the detector as well.
   - Comparison of the imaging performance of the Pixirad-2/Pixie-III with the standard energy-integration flat-panel detector.
2. Global optimization strategy for the selection of acquisition protocol for fast lab-CT experiments.
   - Developing an optimization model to determine the optimal CT scanning parameters for given sample specifications and based on the level of analysis to be performed.
   - The optimization model will output the scan geometry (SOD, SDD), X-ray source settings (current and voltage), detector parameters (exposure time, frame averaging, binning), scan setting (number of projections) and the estimation of the output image quality.

1.9.2 Application aspects

Performing the real-time fast in-situ application using the developed methodologies, illustrating the potential of fast lab-based CT. An application that is presented in this manuscript is

1. A real-time monitoring of air drying phenomena of 3D cellulose printed parts with fast lab X-ray micro-tomography.

Part I

Methodological aspect

Chapter 2

Characterization of direct photon-counting detectors and preliminary results from lab X-ray imaging

Contents

Abstract

This chapter focuses on the characterization of the imaging performance of the energy discriminating photon-counting detectors for their optimal use in lab-based X-ray computed tomographic applications. Photon-counting detectors offer potential improvements over conventional CT detectors by adding energy discrimination capabilities opening CT to spectral measurements and K-edge subtraction imaging. Moreover, the absence of dark current, small pixel size and high readout frame rate make them attractive for high-resolution CT. To assist in the optimal use of such detectors, different photon-counting detectors were subjected to quantitative characterization. The characterization methods that access the general imaging performance and the spectral capabilities of the detector are proposed, and corresponding results are presented. The results demonstrate the potential of photon-counting detectors for lab-based contrast-enhanced CT applications.

2.1 Introduction

Since the introduction of X-ray computed tomography (CT) as a non-invasive experimental tool in material science, numerous technological developments have been made. One of the primary areas of ongoing research in X-ray CT is spectral imaging [Alvarez and Macovski, 1976], which refers to the use of energy information in polychromatic X-ray spectrum for material differentiation [So and Nicolaou, 2021].

Spectral CT exploits the energy-selective information of materials with different attenuation properties at different energies, enabling differentiation and quantification of different materials [Wang et al., 2011]. Also, the decomposition of the total attenuation into spectral basis enables the possibility to create virtual mono-energetic images which resolve beam-hardening artifacts issue [Sellerer et al., 2019].

Several methods for spectral CT have been proposed in the literature, such as dual-source [Flohr et al., 2006], fast kV-switching [Hsieh, 2009b], dual-layer detector [Altman and Carmi, 2009, Rassouli et al., 2017]. All of these methods use only two energy ranges and have limitations. Two independent source-detector pairs are mounted orthogonally in a dual-source system, and two different scans need to be performed using different tube potentials. Moreover, cross-scattered radiation of X-ray photons is common and needs correction. In fast kV-switching, X-ray tube voltage is changed either within an entire rotation or between successive rotations of the sample. Again, two separate scans need to be performed, and a relatively high overlap of the energy spectra is caused by this method. The dual-layer detector method uses a layered detector (top and bottom layer) made up of two materials with different X-ray attenuation properties resulting in different attenuating power of photons. Thus, low and high-energy photons are collected simultaneously in a single scan. However, this dual-energy acquisition relies on the assumption that all the low-energy photons are attenuated in the top detector layer and that the high-energy photons do not interact with the top layer material during transit to the bottom layer [McCollough, 2020]. Further details about the working and limitations of these methods can be found in [Johnson, 2012, McCollough, 2020, So and Nicolaou, 2021, Boas and Fleischmann, 2012].

New generation detectors called Photon-Counting Detectors (PCDs) or color detectors

have been introduced in recent years and are considered an efficient way to perform spectral imaging [Garini et al., 2006, Shikhaliev and Shannon, 2011]. A variety of such detectors are available, including Pixirad [Bellazzini, 2013], Medipix [Ballabriga et al., 2011], XPAD [Delpierre et al., 2007], and Pilatus [Broennimann et al., 2006]. A comprehensive review of the different types of hardware parameters used in photon-counting detectors is presented by Ballabriga at al., [Ballabriga et al., 2016, 2020].

Due to the fundamental differences in the detection mechanism, PCDs possess many advantages over conventional CT detectors or Energy Integrating Detectors (EIDs). EIDs are indirect detectors relying on a scintillator which converts the incoming X-ray photons into visible light. The visible light is then converted into electrical signals using a photodiode. They are insensitive to the energy of the incoming individual X-ray photons and the output signal is proportional to the total energy of the X-ray beam [Leng et al., 2019].

PCDs, on the other hand, are direct detectors [Prekas et al., 2011], meaning that they directly convert the incoming X-ray photons into electrical charges and provide the possibility to select the energy of the incoming X-ray photons with the help of selectable thresholds. Further, the direct detection mechanism of PCDs enables them to record both the position and energy of the incoming X-ray photons in each pixel of the detector. This results in improved image quality leading to higher signal-to-noise ratio (SNR), and contrast-to-noise ratio (CNR) of the recorded projections [Shikhaliev, 2008a,b, Tumer et al., 2000, Schlomka et al., 2008, Kappler et al., 2010, Taguchi and Iwanczyk, 2013].

The performance of PCDs is not flawless; certain drawbacks such as charge sharing effect [Brunner et al., 2011], pulse-pile up effect [Adam et al., 2011], semiconductor inhomogeneities and unavailability of a large field of view [Llopart et al., 2007, Billoud et al., 2017], limit their performance in X-ray CT. Despite these limitations, PCDs have been used in widespread applications such as micro-CT, mammography, breast CT, clinical CT [Alessio and MacDonald, 2013, Maji et al., 2013, Yu et al., 2015, Ren et al., 2016, Sarno et al., 2016, Brombal et al., 2018, Oliva et al., 2020]. The potential use cases of PCDs in K-edge imaging by optimizing energy thresholds have also been explored [Huang et al., 2019, He et al., 2012, Meng et al., 2016, Brun et al., 2020a,b]. However, their potential use cases in lab-CT are still under exploration.

This chapter aims to explore the potential of PCDs for lab-based contrast-enhanced X-ray CT. The chapter starts by describing the general principle, known drawbacks, and potential benefits of the direct detectors, (Section 2.2). Section 2.3 provides an overview of the characteristics of four different PCDs examined, and a suitable detector (Pixirad-2/Pixie-III) was subjected to detailed quantitative characterization.

The imaging capabilities of the Pixirad-2/Pixie-III were tested by computing signal-to-noise ratio (SNR), contrast-to-noise ratio (CNR), and modulation transfer function (MTF) and compared with flat-panel. These quality indices estimate the magnitude of the signal and contrast present in the image with respect to noise and evaluate the spatial frequency response of the detector. After, the effect of charge sharing correction was investigated by using different operating modes of the detector. Moreover, the static and time-dependent defects of the detector were studied, and suitable correction techniques were proposed. Lastly, the radiographic spectral imaging was performed by creating Iodine, Barium Sulphate, and water phantom (I-$BaSO_4$-H_2O) to estimate the K-edge separation capability and spectral resolution of the Pixirad-2/Pixie-III

detector. These characterization methods and corresponding results are described in Sections 2.4 and 2.5, respectively.

The results capture the imaging performance of the PCD under different characterization techniques using a polychromatic source. In addition, the characteristics of the detector coupled with the imaging performance have demonstrated the potential of the detector to be used in improved X-ray imaging for materials characterizations in lab-CT.

2.2 Photon-counting detectors

2.2.1 Working principle

2.2.1.1 X-ray detection

Photon-counting detectors (PCDs) work on the direct detection mechanism of X-ray photons and use semiconductor sensor material that converts X-ray photons directly into electrical signals. Silicon (Si, $Z = 14$) has been widely used as a sensor material for PCD. However, the low atomic number of Si results in low absorption efficiency for hard X-rays [Chmeissani et al., 2004]. High absorbing materials with high absorption efficiency of X-rays such as cadmium telluride (CdTe, Z = 48/52) have been introduced as the sensor material to exploit the high energy X-ray imaging [Xu et al., 2011, Ballabriga et al., 2011]. Other materials such as Gallium arsenide (GaAs) and Cadmium zinc telluride (CdZnTe) are also used [Amendolia et al., 2009, Shikhaliev, 2008a]. Semiconductor material shares a monolithic electrode (cathode) to receive X-ray photons. The pixelated anode is evenly distributed on the other side connecting to application-specific integrated circuit (ASIC) through bump bonding processing, Figure 2.1(a).

When an incident X-ray photon interacts within the semiconductor material, electron-hole pairs with an amount proportional to the deposited energy of the incident photon are produced. The electrons travel to and are collected by the anode to generate electronic signals upon applying a bias voltage throughout the semiconductor. The pulse height of the signal for each X-ray photon is proportional to the energy of the photon.

Thus, the signal from PCDs carries with it energy information about each individually detected photon. The output signal is processed by the application-specific integrated circuit (ASIC) readout chip. Each detected signal is compared with the energy threshold associated with a counter. When the energy level of a detected photon is equal to or exceeds the specified energy associated with a counter, the photon count is increased by one. Like this, all the photons that have energy equal to or larger than a specified energy level are measured [Leng et al., 2019, Ren et al., 2018]. Figure 2.1(a) shows the direct detection principle of PCDs.

Whereas conventional X-ray CT detectors, called energy integration detectors (EIDs), work on the indirect detection of X-ray photons. They use a layer of the scintillator to convert the incoming X-ray photons into visible light. The scintillator is directly connected to photodiodes that convert the visible light into electric signals, thus forming a digital image, Figure 2.1(b). They are referred to as EIDs as they measure the flux of the incident beam and not the energy of the arriving photons. Thus, the output signal of the detector is proportional to the total energy deposited by all detected X-ray photons. Unlike PCD, the output does not carry any

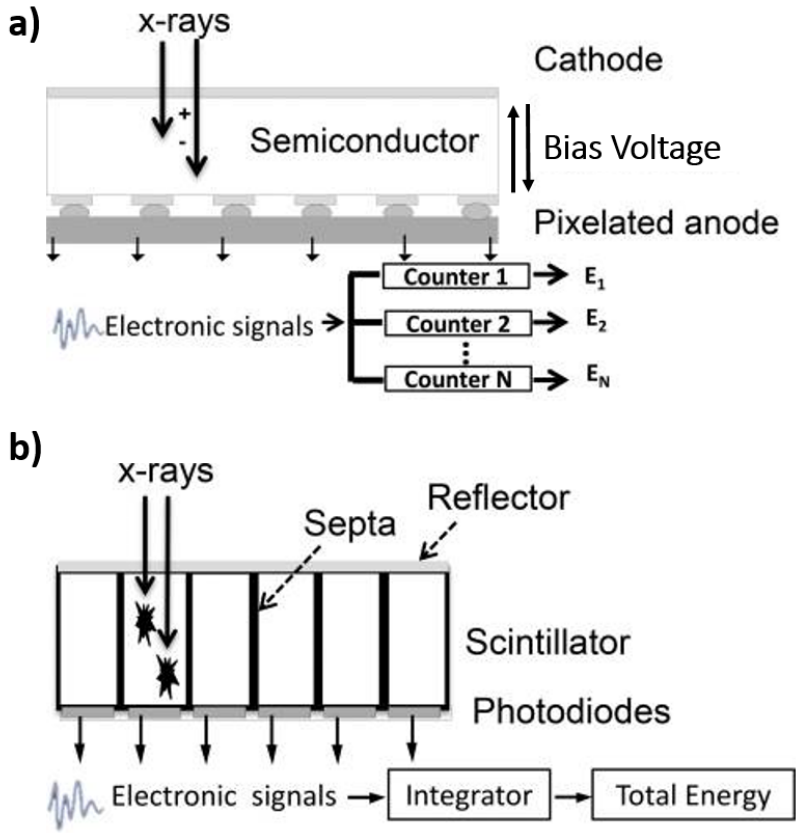

Figure 2.1: Schematic representation of working principles of (a) photon-counting detector (PCD) and (b) energy integration detector (EID). [Leng et al., 2019]

information regarding the energy of individual photons.

2.2.1.2 Tunable energy thresholds

Application-specific integrated circuit (ASIC) of the PCDs is designed in a way that each pixel of the detector is connected with one or more separate imaging counters that are controlled by one or more selectable energy thresholds. PCDs with one or more imaging counters and selectable energy thresholds are available, but two counters and two thresholds are the most common one. The selectable energy thresholds are usually referred as lower E_{th_low} and upper E_{th_high} threshold. These energy thresholds correspond to the energy of the incoming photons and facilitate the creation of two separate images simultaneously with different energy bins.

User sets up both energy thresholds (in keV) prior to data acquisition, depending on the scan objectives. The output events are recorded by the first counter if the energy of the photons falls in-between the defined energy window at E_{th_low} and E_{th_high}, [E_{th_low} - E_{th_high}]. Similarly, the output events are recorded by the second counter if the energy of the photons is greater than the defined energy for E_{th_high}, [E_{th_high} - E_{max}]. Figure 2.2 illustrates the threshold selection phenomenon of PCD. A polychromatic X-ray spectrum generated by the lab source is recorded with two separate binned images by selecting the energy threshold values accordingly. Image 1 contains the photons with energy in between the energy window defined at E_{th_low} and E_{th_high}, represented by red color. Image 2 contains the photons with energy

higher than that is defined at the high-energy threshold E_{th_high}, represented by blue color. The photons of energy lower than E_{th_low} which is represented by gray color are not detected in the output images.

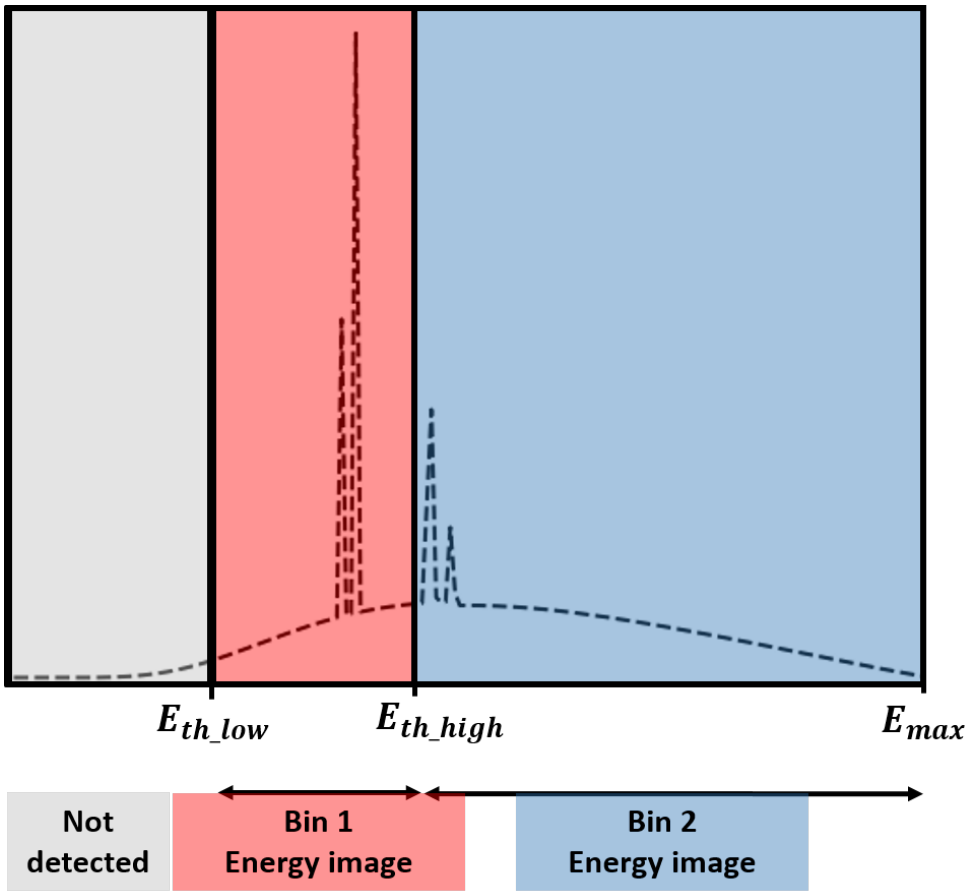

Figure 2.2: Illustration of the energy threshold selection by the PCDs. An X-ray spectrum generated with tube potential E_{max} and two energy thresholds, low-energy E_{th_low} and high-energy E_{th_high}, are defined by the user. Bin 1 image will correspond to the energy of the X-ray photons that is in-between the E_{th_low} and E_{th_high}, represented by red color. Whereas, Bin 2 image will correspond to the energy of the X-ray photons in-between E_{th_high} and E_{max} represented by blue color. The photons of energy lower than E_{th_low}, represented by gray color are not detected.

2.2.2 Possible drawbacks

PCDs are a new emerging technology, and several technical challenges exist that are the performance degradation factors in PCDs and limit their use to full potential. These drawbacks degrade the image quality and energy-resolving ability of the detector. The major drawbacks are listed below.

2.2.2.1 Pulse pile-up

Pulse pile-up is the distortion of the incident photon's measured pulse height, which occurs due to the superposition of the quasi-coincident photons. Two or more events are counted as a single

event which results in the distortion of the energy spectrum.

When the PCDs are in an active state, the first photon incident on the detector pixel will put the detector pixel into the inactive state for a finite period called the dead time τ. There is a significant probability that more than one photon will arrive at the pixel during this dead time. When two or more quasi-coincident photons arrive at the detector pixel during this dead time, these two events are recorded as a single event [Taguchi and Iwanczyk, 2013]. Figure 2.3 shows the pulse pile-up effect; two quasi-coincident events generate a single overlapping pulse which is registered as a single count with wrong energy. It is therefore vital to compensate for this effect.

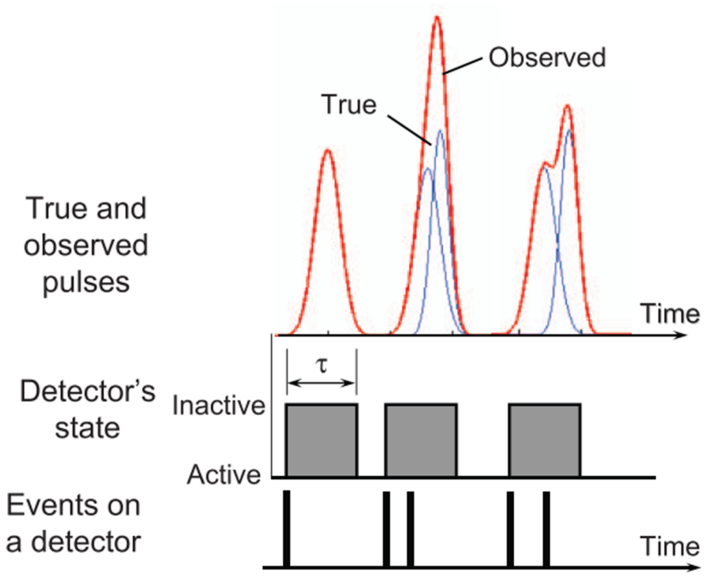

Figure 2.3: Pulse pile-up effect: Quasi-coincident photons that arrive at the detector pixel during the detector resolving time generate a single overlapping pulse and are counted as a single event with the wrong energy. [Taguchi and Iwanczyk, 2013]

An analytical model for the effect of pulse pile-up on the recorded energy spectrum by photon-counting detectors is presented in [Taguchi et al., 2010]. When the pile-up rate increases, a decrease in the output count rate with an increase in the number of photons in the high-energy range is noticed. To compensate for the pulse pile-up effect, PCD with a smaller pixel size is suggested. Small pixels can increase the maximum counting rate of the detector effectively as well and at the same time refine the CT image spatial resolution. A Comparison of different PCDs in terms of their count rate and pixel sizes has been given in [Ballabriga et al., 2016]. However, smaller pixels are more prone to charge sharing effect that results in double counting and spectral degradation [Hsieh et al., 2018].

2.2.2.2 Charge sharing effect

The charge sharing effect is a phenomenon that occurs when a charge cloud generated in the sensor pixel is spread across multiple pixels. Due to this, an event can either be missed or counted more than once, and high-energy photons are detected as low-energy photons, which distort the energy spectra. Charge sharing, unlike the pulse pile-up effect, tends to eliminate

counts from the high-energy region of the spectrum and artificially enhance the low-energy region of the spectrum.

Figure 2.4 illustrates the charge sharing effect; for example a charge of 90 keV photon is split between two pixels (pixel 1 and pixel 2), producing two different counts. One count of 60 keV at pixel 1 and another count of 30 keV at the neighboring pixel 2.

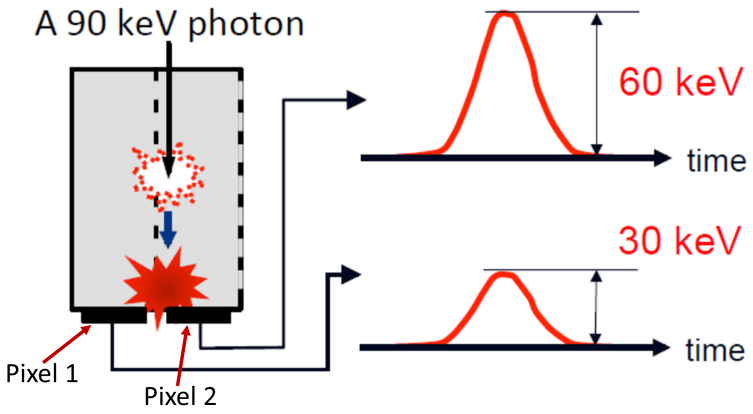

Figure 2.4: Charge sharing effect: A charge of 90 keV photon is split between two pixels and produces two separate counts. One count of 60 keV at pixel 1 and another count of 30 keV at the neighboring pixel 2. [Taguchi, 2020]

The pixel size of the detector has a direct effect on the charge sharing effect: the smaller the pixel size, the more dominant the charge sharing effect will be. Figure 2.5 shows the comparison between the charge sharing effect in different detectors with varying pixel sizes. For example, the charge sharing effect is dominant in the spectrum measured with PCD of a pixel pitch 55μm, and no characteristics peaks are visible compared to the spectrum measured with PCDs of pixel pitch of 110μm and 165μm where the peaks are clearly identifiable [Koenig et al., 2012].

A study by Xu et al. [Xu et al., 2011] suggested that the charge sharing effects should be taken into account when the pixel size is smaller than 1 mm. To compensate for the charge sharing effect, PCD with a larger pixel size is suggested. However, larger pixels increase the X-ray photon's incoming rate per pixel, causing the pulse pile-up effect [Taguchi and Iwanczyk, 2013]. So a trade-off is made in the pixel size of the PCD to minimize either the pulse pile-up or charge sharing effect. The smaller pixel size of the detector, despite having a charge sharing issue, can be beneficial for high-resolution imaging.

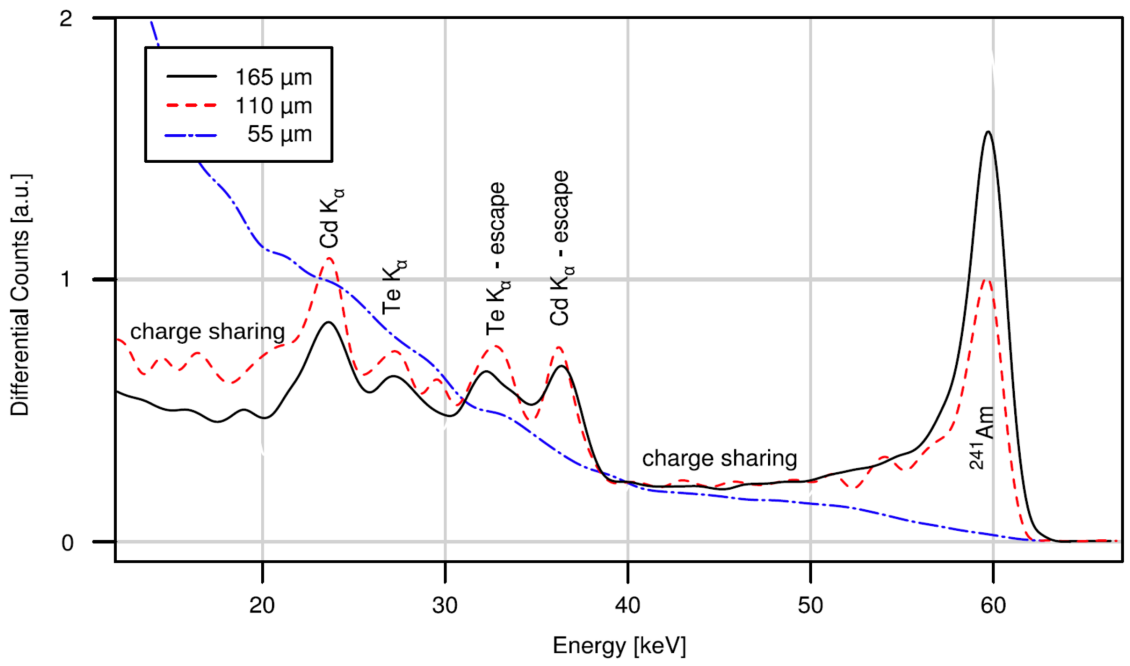

Figure 2.5: Effect of charge sharing. A spectrum measured with a PCD of a pixel pitch of 55μm and no visible characteristic peaks of Cadmium (Cd), Tellurium(Te), and Americium (Am) are visible due to the charge sharing effect compared to the spectrum measured with PCDs of pixel pitch of 110 μm and 165 μm where the peaks are clearly identifiable. [Koenig et al., 2012]

2.2.2.3 Defects

At present, PCDs come with a large number of static and time-dependent defects, also called dynamic or time-dependent dynamic defects.

Static defects mainly correspond to the dead pixels present on the detector sensor and central spacing between different modules of the detector which is also referred to as gap pixels. Dead pixels on the detector sensor are due to the CdTe crystal's production difficulties and its bonding with the ASIC chip [Lindstrom et al., 2015]. The surface area of a single sensor is limited (typically a few cm^2), so a large field of view is obtained by combing different sensors together. These arrangements lead to the presence of a non-negligible gap between the sensors, which is called the central spacing or gap pixels.

Time-dependent dynamic defects are due to the polarization of the CdTe crystals. Polarization arises from the trapping and de-trapping of ionized deep-level acceptors inside the semiconductor crystal, affecting the space-charge and electric field distribution [Niraula et al., 2002]. In addition, the polarization rate is influenced by operational conditions such as temperature, radiation flux, and exposure time. Detail about the polarization can be found in [Malm and Martini, 1974, Bell et al., 1974, Astromskas et al., 2016].

Time-dependent defects due to polarization are of two types: grain boundaries and dark spots. A time-dependent increase in the count rate is observed at the grain boundaries whereas, a time-dependent decrease in the count rate and charge collection deficiency is observed at dark spots. The phenomenon of polarization is a critical issue for CdTe detectors because it determines its time instability [Sordo et al., 2009]. Polarization causes severe degradation

of detector performance over time and limits the application of PCDs to relatively short time operations. Figure 2.6 highlights the static and time-dependent defects in a flat radiograph taken with Pixirad-2/Pixie-II detector at 100 kV with 1 s exposure time.

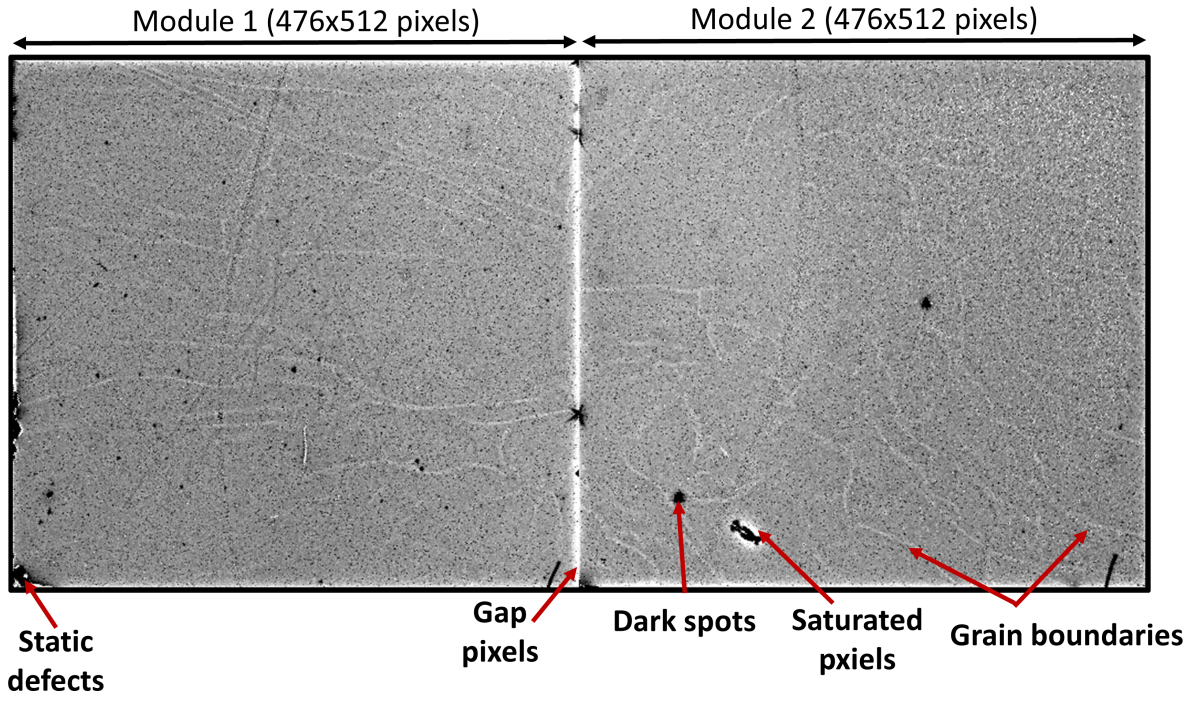

Figure 2.6: Flat radiograph taken with Pixirad-2/Pixie-II detector highlighting the static (dead pixels and gap pixels) and time-dependent inhomogeneities (grain boundaries and dark spots).

Both static and time-dependent defects degrade the image quality and create artifacts in the reconstructed CT slices. Also, the presence of these defects within the scanned sample leads to missing small specimen features. These defects need to be corrected to improve the quality of recorded radiographs to be reconstructable. The application of a dead-pixel map can compensate for the static defects. It replaces the values of the misbehaving pixels with averaged obtained from the surrounding pixels. For dynamic defects, solutions such as dynamic flat-field [Delogu et al., 2017] and refreshing the sensor by resetting the bias voltage at frequent intervals [Chen et al., 2020] have been proposed.

The major drawbacks are summarized in Table 2.1.

Table 2.1: Summary of major drawbacks of the photon-counting detector.

Current drawbacks	**Origin**	**Effect on the image**	**Possible Correction**
Pulse pile-up	Superposition of quasi-coincident photons occurs, and two events are counted as a single event.	Distortion of the energy spectrum with a shift towards high-energy.	Smaller pixel size of the detector.
Charge sharing effect	Charge clouds generated in the sensor pixel are spread across multiple pixels.	Distortion of the energy spectrum with a shift towards low-energy.	Larger pixel size of the detector.
Static defects	Production difficulties of CdTe crystals and bonding of it with ASIC chip Multiple small area sensor modules are joined together to increase the field of view of the detector	Poor image quality. Creates artifacts in the reconstructed CT scan. Missing small features of the specimen in the image	Dead pixel map Post-processing image filtration Bias voltage reset
Dynamic defects	The time-dependent polarization phenomenon of the CdTe crystals.		Dynamic flat-field

2.2.3 Potential advantages

2.2.3.1 Spectral imaging

A significant advantage of the energy-resolving PCDs is spectral or K-edge subtraction imaging. The ability of the PCDs to monochromatize the polychromatic X-ray source spectrum with the help of selectable energy thresholds makes possible the monochromatic measurements. The high-energy binned images are much less affected by the beam-hardening artifact that is common with the conventional EID measurements.

By selecting different energies of photons in the lower and upper thresholds, contrast of the image can be modified. Figure 2.7 shows the energy sensitivity of the Pixirad sensor for spectral imaging. Images of a jasmine flower, which is a deficient contrast object, are taken using the energy of photons in between 1 and 6 keV (Figure 2.7(a)) and by using the energy of photons only higher than 6 keV energy, Figure 2.7(b) [Bellazzini, 2013]. It can be seen that by selecting the different energy of the selectable thresholds, different features of the specimen can be visualized with increased contrast which makes the identification of different materials easy.

This energy discrimination property of the PCDs makes them suitable to perform K-edge subtraction (KES) imaging using a lab polychromatic source to exploit the sharp rise of the absorption coefficient at the K-edge energy of a specific element. The acquisition of two digital images at different energies at either side of the K-edge of the element can be made simultaneously and by post-processing the dataset, KES image can be obtained from which absorbance of the specific material can be computed. This technique can be applied to

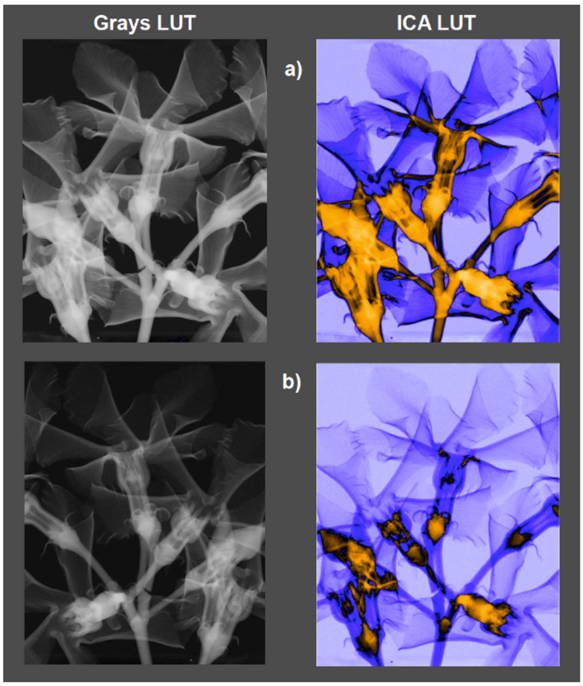

Figure 2.7: Images of a jasmine flower are taken using (a) energy of photons in between 1 and 6 keV and (b) energy of photons only higher than 6 keV energy. [Bellazzini, 2013]

radiography as well as to computed tomography. The potential applications of spectral or KES imaging can be found in [Fredenberg, 2018].

2.2.3.2 Improved resolution

Another major advantage of the PCD is the improved spatial and temporal resolution as compared to standard energy-integrating detectors such as flat-panel. The pixel size of the PCD is typically smaller as compared to flat-panel detectors. Conventional CT detectors, flat-panels, have pixels typically in the range of 90 μm to 127 μm, whereas PCDs with a pixel size as small as 55 μm are available. With these small pixel size detectors, small voxel size can be achieved resulting in improved spatial resolution of the CT scan, Eq. 1.19, (chapter 1). Thus PCD detector can overcome the achievable spatial resolution problem in lab-CT.

PCDs are equipped with a high acquisition frame rate, making high-speed imaging possible. A frame rate of 500 frames per second can be achieved with Pixirad/Pixie-III detector [Bellazzini et al., 2015]. And an exposure time of 3.4 ms has been reported by using the WidePix detector consisting of TimePix readout chip [Vavrik et al., 2017]

A small pixel size of the detector along with the availability of high frame rate can result in improved spatial and temporal resolution of the CT scan.

2.2.3.3 Efficiency

PCDs are direct detectors with fundamentally different photons detection mechanism than conventional EIDs, they directly convert X-ray photons into electrical signals. This results in

improved detection efficiency of the detector. Moreover, all photon energy levels receive uniform weighting, allowing improved contrast between soft materials and sharper images.

PCDs have a particular advantage for imaging with low dose levels, because of their ability to reduce the impact of electronic noise. With the help of selectable energy thresholds, noise due to low-energy photons can be excluded from the measured signal by selecting an energy threshold higher than the noise floor, typically higher than 10 keV, prior to imaging. This also results in improved image quality, higher contrast and SNR, of the images. Figure 2.8 compares the high-resolution micro-CT measurement of cylindrical nanoparticulate bioactive glass-reinforced gelan-gum (GG-BAG) sample using a large area flat-panel detector and a large area PCD WidePix detector, consiting of 10×10 Timepix devices. The voxel size for both measurements was comparable, being 5.0^3 μm^3 for flat panel and 6.0^3 μm^3 for WidePix. The tomographic reconstruction from the WidePix provides significantly sharper images, and the thinnest cell walls are clearly visible, Figure 2.8(b), whereas numerous walls are unidentifiable in the reconstruction based on the flat-panel data, Figure 2.8(a) [Kumpová et al., 2016].

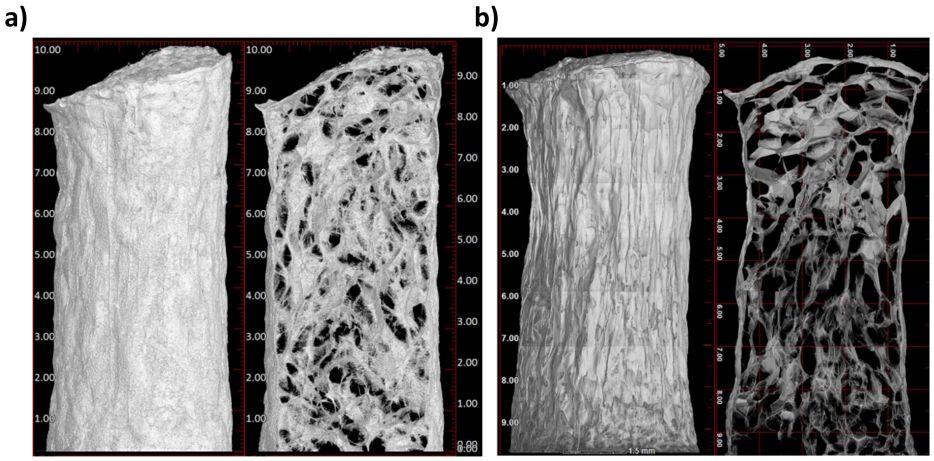

Figure 2.8: 3D visualizations of the reconstructed volumes of the high-resolution µ-CT scan of cylindrical nanoparticulate bioactive glass-reinforced gelan-gum sample using (a) flat panel detector and (b) photon-counting detector. [Kumpová et al., 2016]

The presented advantages of PCDs are summarized in Table 2.2.

Table 2.2: Summary of potential advantages of photon-counting detector.

Potential advantages	**Origin**	**Expected imaging capabilities**
Spectral imaging	Energy thresholds discriminate incoming X-ray photons by energy.	Monochromatic measurements or Color images: material identification using spectral signals. Higher contrast KES imaging Reduced beam-hardening artifacts
Improved resolution	Small pixel sizes, 55μm. Availability of high fast read speed.	Possibility to achieve very high spatial resolution. High-speed imaging.
Efficiency	Direct detection of X-ray photons. Energy threshold selection above the noise floor.	High X-ray conversion efficiency. Higher image quality with high SNR and sharpness. No electronic noise Low signal acquisitions possible such as diffraction contrast tomography (DCT)

2.2.4 Summary

PCDs are emerging technology with multiple advantages compared to conventional EIDs, owing to their unique interaction physics, energy-discrimination abilities, small detector pixels, and higher noise efficiency. However, drawbacks such as pulse pile-up, charge sharing effect, and sensor inhomogeneities limit their use to its full potential. Extensive research activities are being done to find the solutions for these drawbacks and to characterize the performance of PCDs to make them suitable for improved X-ray CT imaging.

2.3 Characteristics of the studied detectors

During the PhD thesis, four photon-counting detectors were studied and characterized as illustrated in Figure 2.9(a). Two of them were provided as a loan for one week each by ADVACAM (WidePix and TimePix3) and the other two by PIXIRAD Imaging counters s.r.l., Pixirad-2/Pixie-II and Pixirad-2/Pixie-III.

Pixirad-2/Pixie-III detector is the primary detector that was characterized and installed in laboratory SIMAP. Since it is not easy to produce the CdTe, we first worked on an old version of the Pixirad-2 detector (Pixirad-2/Pixie-II) before the actual delivery of Pixirad-2/Pixie-III. Other two loaned detectors, WidePix and TimePix3, were briefly examined for their features and potential use cases in lab-CT. Figure 2.9(b) shows the characterization timeline of these detectors during the three years of Ph.D. thesis.

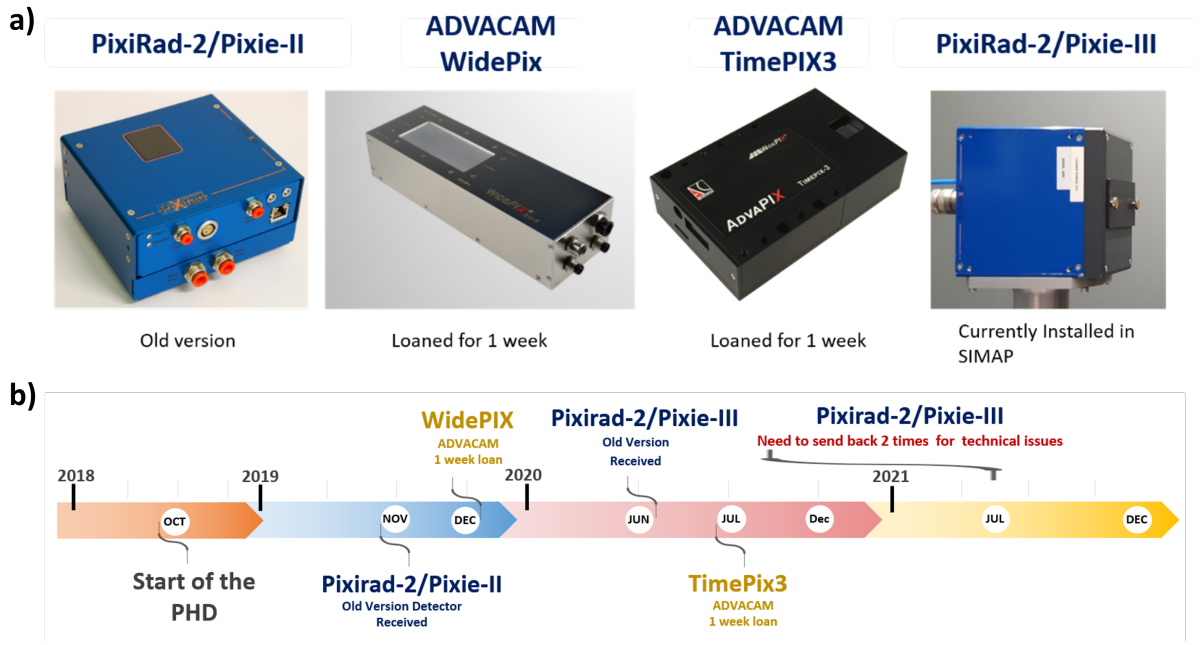

Figure 2.9: (a) Four direct photon-counting direct detector that were examined during the PhD thesis. (b) Timeline of the four detectors during the PhD thesis.

2.3.1 Pixirad detectors

2.3.1.1 Characteristics

The Pixirad detector is a pixel array detector with a 650 μm thick cadmium telluride (CdTe) sensor. There are two versions of the ASIC readout chip, the older Pixie-II and the newer Pixie-III. A single module Pixirad-1, two modules Pixirad-2, and eight modules Pixirad-8 with Pixie-II or Pixie-III readout chips are available.

Pixie-II module-based Pixirad-2 sensor (Pixirad-2/Pixie-II) has a pixel pitch of 60 μm hexagonally arranged. The total sensitive area is 62 x 25 mm^2 containing a total of 476x1024 pixels. Cadmium telluride (CdTe) of 650 μm thickness is used as a sensor material. The sensor comes with a large number of static and dynamic defects due to the poor quality of CdTe used

as earlier described in, Section 2.2.2.3 and Figure 2.6. No hardware feature to correct these polarization defects is present. Charge sharing correction is not implemented in the detector hardware.

Pixie-III module-based Pixirad-2 sensor (Pixirad-2/Pixie-III) has a pixel pitch of 62 μm and in squared arrangement. The total sensitive area of the sensor is 64 x 25 mm^2 containing a total of 402x1024 pixels. Cadmium telluride (CdTe) of 650 μm thickness is used as a sensor material. Charge sharing correction is implemented in the detector hardware.

2.3.1.2 Operating modes and charge sharing effect

The charge sharing correction is implemented in the Pixirad-2/Pixie-III detector hardware using three different acquisition modes:

- **No Neighbour Pixel Inhibit mode (NONPI):** In NONPI mode, each pixel is counted independently from the other. No correction is performed on the charge received by each pixel resulting in distorted energy spectra. Figure 2.10(a) explains the procedure. A photon of 90 keV energy (red circle) is received, near the boundary of the four pixels, by the detector, and the charge is spread over four pixels (P1, P2, P3, and P4) (grey colors) with 15, 5, 50 and 20 keV energy respectively. For NONPI mode, all four grey color pixels will be counted as separate events resulting in four counts. This results in a distorted energy spectrum in the output image containing a higher number of low-energy photons.

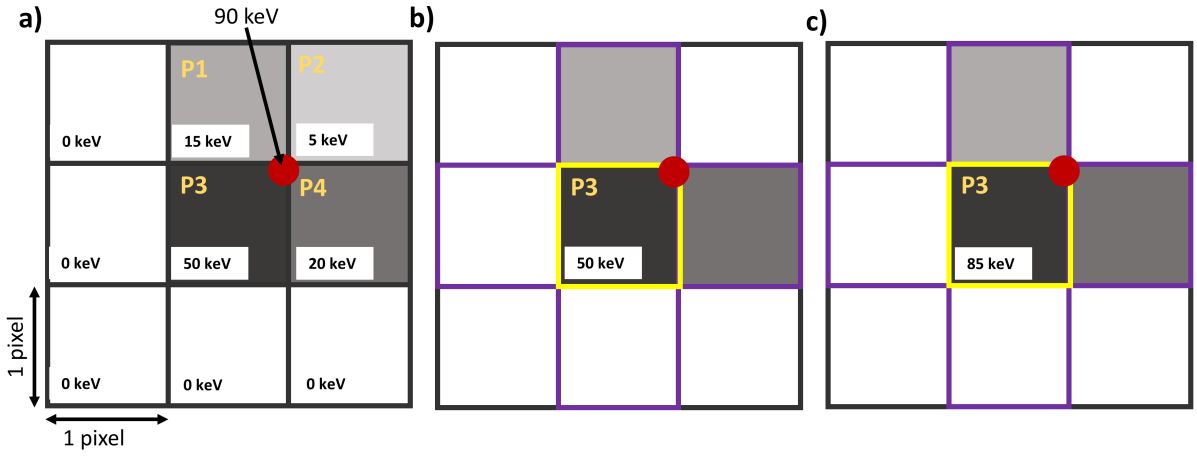

Figure 2.10: Working of three different acquisition modes of Pixie-III module in terms of charge sharing correction phenomenon.

- **Neighbour Pixel Inhibit mode (NPI):** In NPI mode, only one pixel per event is allowed to count. When an event spreads over multiple pixels, the count is assigned to the pixel receiving the highest fraction of the charge. For NPI mode, Figure 2.10(b), the detector will reconstruct the charge based on the purple box, and the count is assigned to pixel 3 (yellow box) since it contains the highest charge of 50 keV as compared to its surrounding pixels. However, charge sharing is not completely solved in this mode.
- **Neighbour Pixel Inhibit and Pixel Summing Mode (NPISUM):** In NPISUM mode, only one pixel per event is allowed to count. The hit event is allocated to the pixel

receiving the highest fraction of the total deposited energy, and after that, the signals of 4 neighbour pixels are summed together to evaluate the total energy correctly. For NPISUM mode, Figure 2.10(c), hit event is allocated to the pixel 3 (P3, yellow box), and after the sum of charges of the purple box will be added to the yellow box. Charge sharing is corrected in this mode, but correction is limited to only four neighbouring pixels (purple box, pixels sharing one face). Further detail on the Pixie-III module detector and acquisition modes can be found in [Bellazzini et al., 2015].

2.3.1.3 Energy selection

In the Pixirad detector, each pixel has two 15-bit counters (Counter 0 and counter 1) and two independent discriminators with tunable thresholds that capture two color images simultaneously in a single exposure. For the selection of energy, two selectable thresholds, lower threshold E_{th_low}, and upper threshold E_{th_high} are present. The events are counted into the counter 0 when the energy of the photons is in-between the energy window defined by E_{th_low} and E_{th_high}, [E_{th_low} - E_{th_high}]. The events are counted using the counter 1 when the energy of the photons is higher than the energy selected in E_{th_high}, [E_{th_high}, E_{max}]. Pixirad detectors have a broad energy range from 2 to 100 keV. Figure 2.11 shows the flat radiographs captured by counter 0 and counter 1.

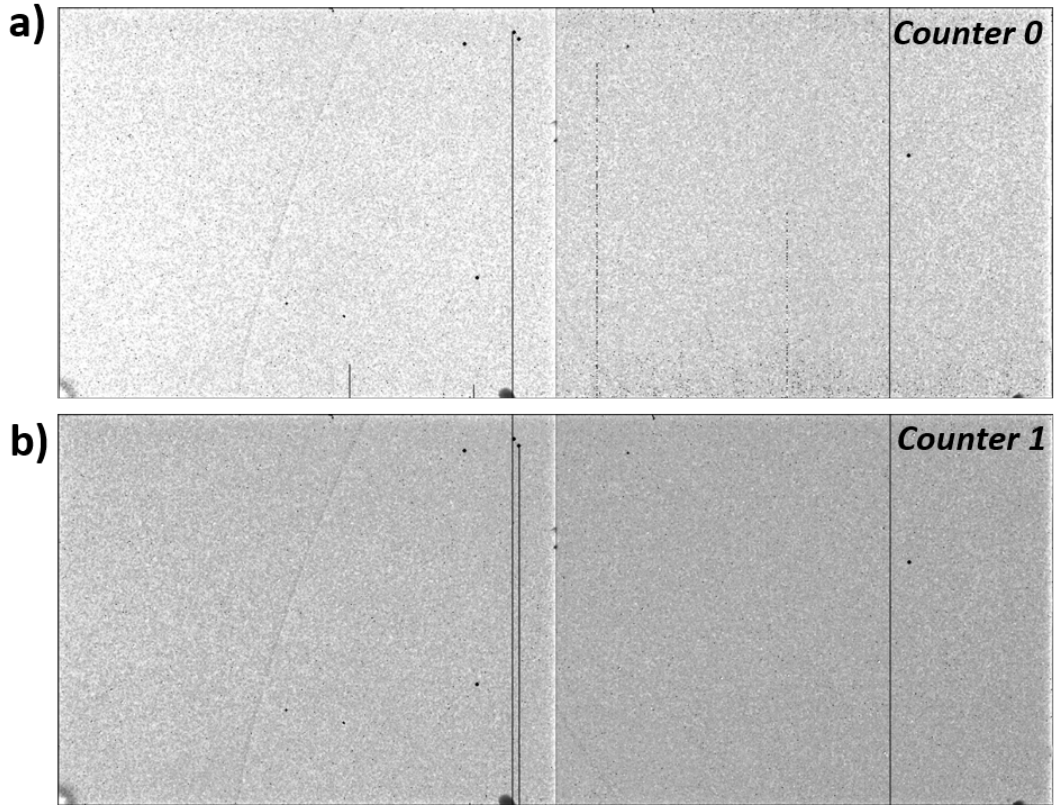

Figure 2.11: Flat radiographs captured by Pixirad-2/Pixie-III detector using (a) counter 0 having photons of energy in in-between the energy window defined by the lower and upper threshold, [E_{th_low} - E_{th_high}], (b) counter 1 having photons of energy higher than defined in the upper threshold, [E_{th_high}, E_{max}]. Static defects are visible in both radiographs.

2.3.1.4 Other functionalities

Pixie-III module also has a bias voltage reset option. By resetting (turning off and on) the bias voltage, the defects due to polarization can be discarded, and detector performance is recovered.

2.3.2 ADVACAM detectors

Two ADVACAM detectors, WidePix and TimePix3, were briefly examined for their potential use cases.

2.3.2.1 WidePix

The WidePix detector contains five Medipix3 [Ballabriga et al., 2011] readout chips, of 256 x 256 pixels, connected together. Figure 2.12 shows a flat radiograph taken with the WidePix detector. The detector provides a very large field of view with 256 x 1280 pixels with a sensitive area of 70.4x14 mm^2 with a pixel pitch of 55 μm in the squared arrangement. The sensor material is made up of 1 mm thick CdTe. The WidePix works with low threshold mode and has only a single imaging counter, which means that all the photons with energy higher than the selected threshold are detected. And all photons with energies below the set value are cut off. It is impossible to acquire two images with different energy bins with WidePix. WidePix does no charge sharing correction, and no hardware feature to correct polarization defects is present.

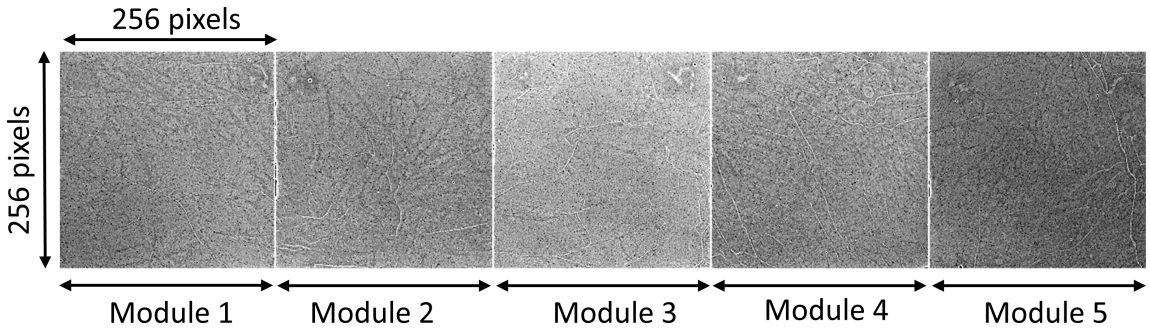

Figure 2.12: Flat radiograph captured by WidePix. 5 readout chips are connected together, giving the large field of view of 256x1280 pixels.

2.3.2.2 TimePix3

ADVACAM TimePix3 (TPX3) is recognized as the world's first radiation imaging that uses the TimePix3 [Poikela et al., 2014] readout chip and has an event-based readout. Contrary to the frame-based readout where the whole pixel matrix is read out at once, in the event-based readout, values recorded by pixels are read out immediately after the hit. Thus, every single hit of radiation is recorded as a continuous stream of data, including the position, energy, and detection time of each detected quanta at each pixel. The event base output can be recorded using the time-of-arrival (ToA) and time-over-threshold (ToT) mode of the detector.

The detector has a sensitive area of 14 x 14 mm^2 with a single chip of TimePix3 containing 256 x 256 pixels, (Figure 2.13), with a pixel size of 55 μm. 1 mm thick CdTe is used as a sensor material. TPX3 detector also operates in low threshold mode with a single imaging counter in frame-based output. The minimum detectable energy is 5 keV. Charge sharing correction is implemented in the software Pixet Pro, which is used to control the detector. Thus the acquired data can be subjected to the charge sharing correction in the post-processing. No hardware feature to correct polarization defects is present.

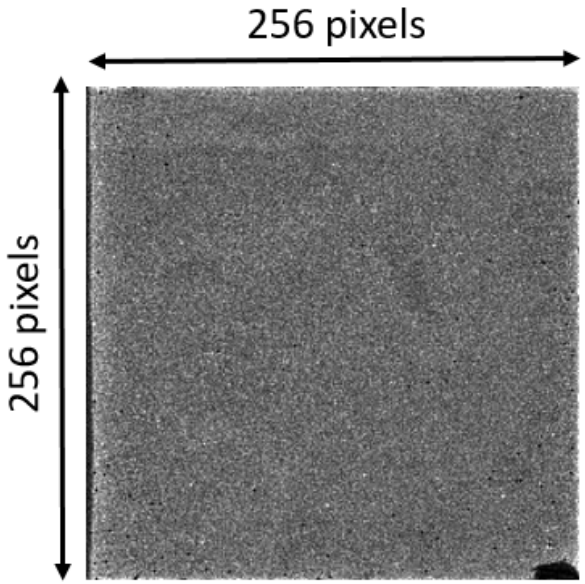

Figure 2.13: Flat radiograph captured by TimePix3, consisting of a single readout chips with 256 x 256 pixels.

2.3.3 Summary and synthesis

The main characteristic of the tested detectors are presented in a comparable way in Table 2.3, and the distinguishing features of each detector are highlighted in bold green color and the bad feature is highlighted in bold red color. Both Pixirad2/Pixie-II and WidePix detectors do not have any charge sharing correction feature or option to deal with the sensor polarization issue, so their use for longer scan time CT and spectral imaging is not recommended. TimePix3 on the other hand has a very small active pixel area, limiting its use for standard lab-based CT, although it offers the software solution to deal with charge sharing effect. Both WidePix and TimePix3 also have only a single imaging counter compatible with a low threshold in frame-based readout mode, so it is also not possible to acquire two images with different energy bins with a single acquisition.

From the characteristics of the presented detectors, Pixirad-2/Pixie-III appears to be a promising candidate since charge sharing correction, and detector bias reset option are implemented in the detector hardware. The active pixel area of the sensor is also large enough to be used for laboratory CT with a standard sample size. Also, the possibility to acquire two images simultaneously by using the two imaging counters of the detector makes it suitable for spectral K-edge imaging.

Table 2.3: The main characteristic of four detectors, their distinguishing features are highlighted in bold green color and bad features are highlighted in bold red color.

Characteristics	**Pixrad-2/Pixie-II**	**WidePix ADVACAM**	**TimePix3 ADVACAM**	**Pixrad-2/Pixie-III**
Thickness of CdTe sensor (mm)	0.650	1.000	1.000	0.650
Sensitive area (mm^2)	62 x 25	70.4 x 14	14 x 14	64 x 25
Readout chip	Pixie-II	Medipix3	TimePix3	Pixie-III
Readout speed (Frame/sec)	**100**	50	–	**100**
Number of pixels	**1024 x 476 (2 chips of 512x476 pixels mounted)**	**256x1280 (5 chips of 256x256 pixels mounted)**	**256 x 256 (1 chips of 256x256 pixels mounted)**	**1024 x 402 (2 chips of 512x402 pixels mounted)**
Pixel pitch (μm) arrangement	60, hexagonal	55, squared	55, squared	62, squared
Imaging counters	**2**	**1**	**1**	**2**
Minimum detectable energy (keV)	2	5	5	2
Output modes	Frame-based	Frame-based	**Frame-based, Time-over-Threshold (ToT), Time-of-Arrival (ToA)**	Frame-based
Charge sharing correction	**No**	**No**	**Yes, implemented in the software**	**Yes, implemented in the hardware**
Sensor refresh feature	**No**	**No**	**No**	**Yes, implemented in the hardware**
Dimensions (LxWxH) (mm)	92 x 134 x 135	213 x 60 x 40	125 x 79 x 25.5	92 x 134 x 135
Software	XAct	Pixet Pro	Pixet Pro	XAct
Condition	Owned: Received Nov 2019	1-week loan	1-week loan	Owned: Received July 2020

2.4 Characterization procedures

Based on the comparison presented in Section 2.3.3, the characteristics of the Pixirad-2/Pixie-III appear to be suitable to be used for lab-CT, so the imaging performance and the spectral response of the Pixirad-2/Pixie-III detector were characterized using the lab polychromatic sources. The imaging performance of the Pixirad-2/Pixie-III was also compared with a standard CT detector, flat-panel.

Flat-panel that was used as reference is an indirect amorphous silicon (a-Si) detector (Varian PaxScan 2520DX). It consists of a 700 μm thick layer of caesium iodide (high X-ray absorption) scintillator to convert in-coming X-ray photons into visible light, which later are converted into electrical signals. The total pixel area of the detector has dimensions 244 $\times$195 mm consisting of 1920 $\times$1536 pixels, with each pixel of 127 x 127 μm.

The behaviour of static and time-dependent defects present in the sensor was also studied, and suitable solutions were proposed. Spectral response for the ADVACAM detectors was also studied briefly.

2.4.1 X-ray source and experiment configurations

Radiographs were acquired using one of the following configurations for characterization.

Configuration 1: Configuration 1 was used to characterize the static and dynamic defects in the Pixirad-2/Pixie-III and Pixirad-2/Pixie-II.

A time series using an exposure time of 1 s and 100 kV acceleration voltage was recorded using the micro-focus (Hamamatsu L12161-07 Reflection, sealed) X-ray source, with Tungsten (W) target and W as filament. Time series consists of flat radiographs and each radiograph was recorded every minute, for 60 minutes, using the old version Pixirad-2/Pixie-II sensor. No threshold limit was applied on the photons energy, and full range of energy photons were detected by setting lower threshold E_{th_low} to 2 keV and upper thresholds E_{th_high} to 186 keV.

Configuration 2: Configuration 2 was used to evaluate the charge sharing correction performance of the different operating modes of the Pixirad-2/Pixie-III detector.

Flat acquisitions were recorded using an exposure time of 4 s at an acceleration voltage of 100 kV using the nano-focus (Hamamatsu L10711-03 Transmission, open) X-ray source with W target and Lanthanum hexaboride (LaB6) as filament. 1 mm thick Aluminium (Al) filter was placed in front of the X-ray source to discard low-energy photons. Pixirad-2/Pixie-III detector was operated in low threshold mode, and counter 0 was used for acquisitions. For each operating mode (NONPI, NPI, NPISUM), programmable thresholds, E_{th_low} was initially set to 5 keV and was incremented by 1 keV after recording each flat radiograph. E_{th_high} was fixed at 100 keV. So counter 0 was set to record the flat radiographs by increasing the low-energy threshold by 1. [E_{th_low}, E_{th_high}]=[i,100],i=5,6,7,... 70.

Configuration 3: Configuration 3 was used for the estimation of the contrast, noise, and spatial resolution response of the Pixirad-2/Pixie-III and flat-panel detector.

Acquisitions were made using an exposure time of 1s and 0.5 s at an acceleration voltage of 50 kV and 100 kV using the nano-focus (Hamamatsu L10711-03 Transmission, open) X-ray source with W target and LaB6 as filament. A total of 10 projections were acquired and then averaged together before computing the SNR, CNR, and MTF. For Pixirad-2/Pixie-III, images were acquired using counter 0 under NPISUM configuration and programmable thresholds, E_{th_low} and E_{th_high}, were set to 5 and 100 keV, respectively. 5 keV was used for E_{th_low} to disregard the noise, so images were captured using photons with energy ranging between 5 to 100 keV. The voxel size for both acquisitions was 13 μm.

Configuration 4: Configuration 4 was used to investigate the single-shot K-edge subtraction (KES) imaging capability and the spectral resolution of the Pixirad-2/Pixie-III detector.

Both acquisitions were acquired using the exposure time of 5 s at 50 kV voltage using the nano-focus (Hamamatsu L10711-03 Transmission, open) X-ray source with Tungsten (W) target and LaB6 as filament. The Pixirad-2/Pixie-III detector was configured in NPISUM mode.

For the KES imaging, both imaging counter 0 and 1 were used for the acquisitions. The programmable energy threshold E_{th_high} and E_{th_low} were set to 28 and 38 keV, respectively and two images with the photon of energies ranging from [28,38] and [38,50] keV were recorded. For the spectral resolution, imaging counter 0 was used for the acquisitions. The programmable energy threshold E_{th_high} was set to 50 keV and E_{th_low} was changed from 15 to 50 keV with an increment of 1. In this manner counter 0 was set to record the phantom projections and flat images by increasing the lower threshold by 1. [E_{th_low}, E_{high}]=[i,50], i=15,16,17...50. Before changing the lower threshold value, a bias reset was done to correct the detector polarization behaviour.

Configuration 5: Configuration 5 was used to evaluate the energy characterization performance of the ADVACAM, WidePix detector.

Flat acquisitions were recorded using an exposure time of 1 s at an acceleration voltage of 50 kV using the nano-focus (Hamamatsu L10711-03 Transmission, open) X-ray source. Molybdenum (Mo) target was used as an anode to produce X-rays. The detector's low-energy threshold was set to 5 keV, and it was incremented by 1 keV after recording each projection till 30 keV. The energy threshold increment was reduced to 0.2 keV between the energies 16 to 20 keV to observe the characteristic peaks of Molybdenum.

2.4.2 Defects characterization and solution

2.4.2.1 Static defects

To estimate the total number of static pixels in a radiograph captured by Pixirad-2/Pixie-III detector, a bad pixels map was created. To create a bad pixel map, initially, a filtered image with conditional median filtering (by a pattern 3x3) was created, and then the absolute difference between the original and filtered image was made. From this absolute difference image, based on the suitable threshold value, these bad pixels can be detected. A threshold of 200 was chosen for the bad pixel map.

Figure 2.14 shows the bad pixel map from the radiograph captured by Pixirad-2/Pixie-III detector. Red color corresponds to the bad pixels, which are about 2% of the total number of pixels in an image.

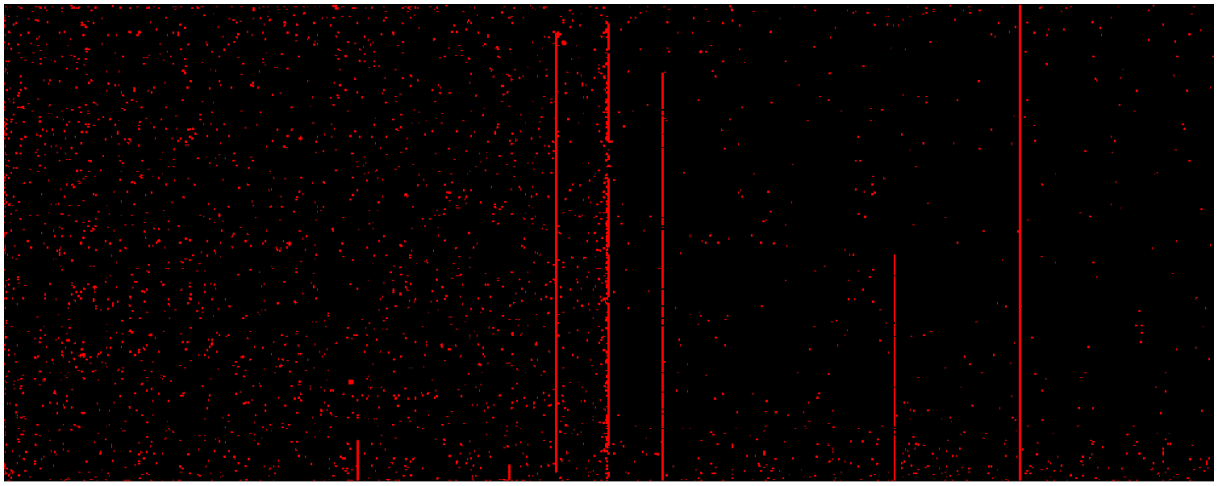

Figure 2.14: Bad pixel map of the radiograph captured by Pixirad-2/Pixie-III. 2% of the total pixels are detected as bad pixels.

These bad pixels can be corrected by the application of a local median filter of radius 2x2 or 3x3 pixels. The local median filter replaces a pixel with the median of nearby pixels, determined by the radius if it deviates from the median by a specified value determined by the threshold. A bad pixel map can also be imported during the acquisitions to remove these static defects automatically.

2.4.2.2 Dynamic defects

As described earlier in the (Section 2.2.2.3), two types of time-dependent dynamic defects exit, grain boundaries and dark spots. These defects start to appear on the detector sensor and thus in the recorded radiographs after the detector has been running for some time. To characterize these dynamic defects, radiographs captured by the old version detector Pixirad-2/Pixie-II were used since Pixirad-2/Pixie-II exhibits more prominent dynamic defects than Pixirad-2/Pixie-III due to the poor quality of CdTe. Figure 2.15(a) shows a cropped flat radiograph from the Pixirad-2/Pixie-II (old version detector) highlighting dark spots and grain boundaries. The contrast value is enhanced to show the dynamic defects.

Dark spots: To understand the evolution of dark spots, the evolution of pixels profile from the center of the dark spots to the distance of 20 pixels were plotted for initial 20 minutes, captured by the time series. Figure 2.15(b) shows the pixel profile in grayscale values as a function of the distance from the defect center for the two highlighted dark spots. The solid and dotted lines represent the measured and exponentially fitted curves. It can be seen that the dark spots start to appear roughly 7-10 minutes after the operating time of the detector. Their magnitude (radius) increase with the operating time and the average intensity in the dark spots decrease.

Grain boundaries: To understand the evolution of grain boundaries behaviour, the temporal evolution of each pixel profile present in an ROI containing the grain boundaries, Figure 2.15(a), was plotted. Figure 2.15(c) shows the pixel's values as a function of time, and each color

corresponds to a single pixel value. It can be noted that the values of pixels inside the grain boundaries increase linearly with time. The width of the region affected by the grain boundary was measured to be 3 pixels, and it remains constant with time. Similar to the dark spots, grain boundaries also start to appear roughly 7-10 minutes after the operating time of the detector. However, some pixels values start to increase from the beginning of the acquisition.

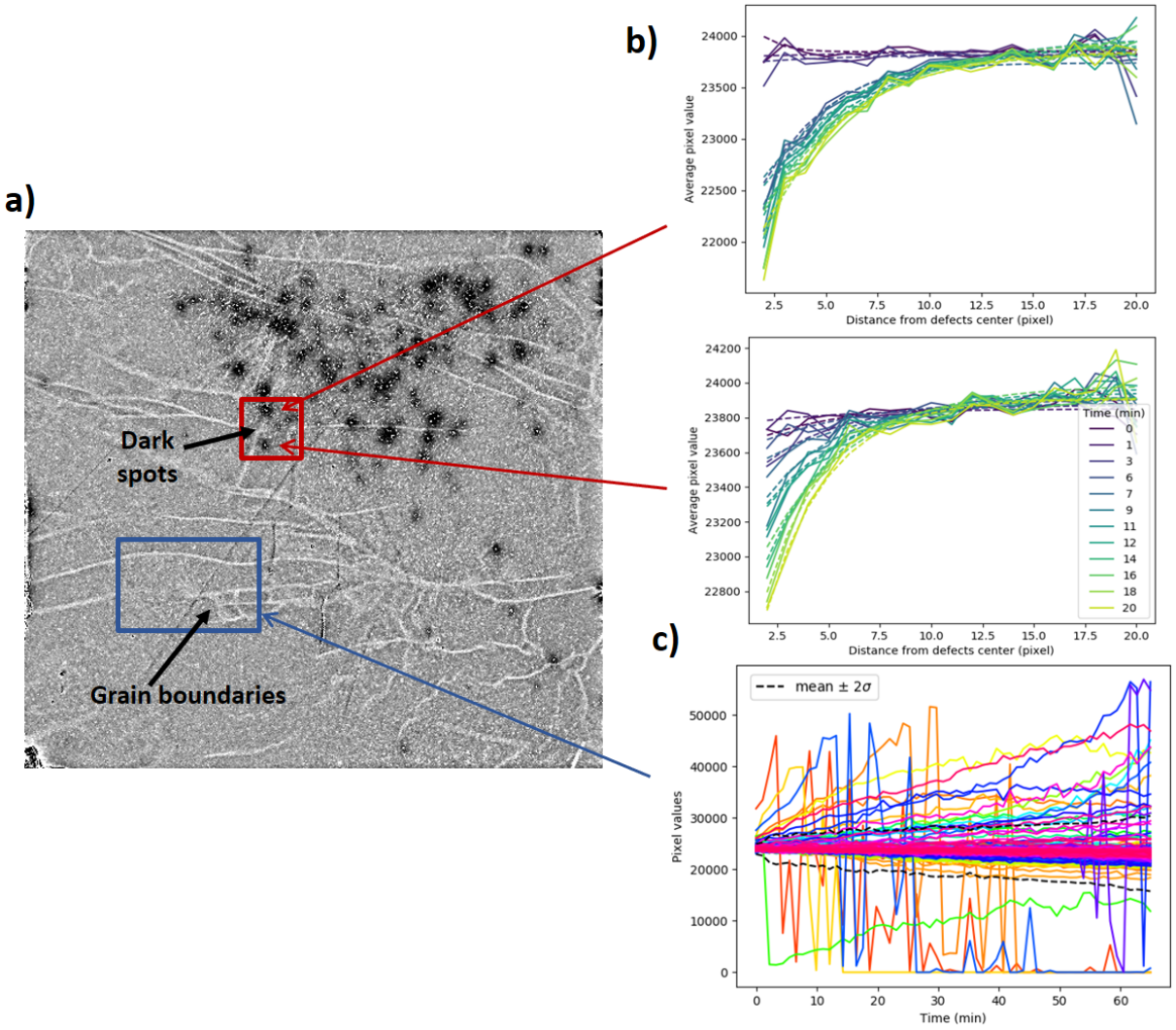

Figure 2.15: (a) Contrast-enhanced radiograph captured by Pixirad-2/Pixie-II highlighting time-dependent defects, dark spots, and grain boundaries. (b) Evolution of the pixel profile in grayscale values as a function of the distance from the defect center to 20 pixels in the two highlighted dark spots. (c) Evolution of the pixels profile as a function of time in an ROI containing the grain boundaries. Each color corresponds to a single pixel value.

Multiple solutions were tested in order to correct these time-dependent dynamic defects, such as linear and temporal interpolation methods, and their transposability from one scan to another was also tested. These solutions take the radiographs recorded at t=0 min as a reference and correct the radiographs affected by the dynamic defects using the reference radiographs. However, an efficient method that was used during the characterization of the detector is refreshing the sensor after a certain time span.

Sensor refresh:

Pixirad-2/Pixie-III sensor has a hardware feature to refresh the sensor by resetting the bias voltage. This turning off and on the bias voltage reset the detector to its initial stage and all time-dependent defects are discarded. This sensor refreshing is really an efficient way to decrease the magnitude of the time-dependent defects and to recover the detector's performance.

Dynamic flat-field:

The time-dependent dynamic defects can also be compensated by using the dynamic flat-field method proposed by [Delogu et al., 2017], which requires the capturing of flat images for each sample projection.

Considering N_{proj} as projection with sample and N_{flat} as flat radiograph, the corrected flat-field projection can be given as N_{corr} as

$$N_{corr} = \frac{N_{proj,\ i}}{N_{flat,\ i}},\ i = 1, 2, 3, \ldots\ N_{View} \tag{2.1}$$

where N_{View} represents the total number of recorded radiographs. Dynamic flat-field correction is usually needed when the PCDs are radiated for longer time scans. For shorter time scans, time-dependent defects are not prominent; hence projections can be corrected by the classical flat-field correction method.

2.4.3 Flat-field correction

Images acquired using both flat-panel and photon-counting detectors for all the characterization techniques were subjected to flat-field correction. Due to the variations in the X-ray field, detector inhomogeneity, and variations in detector electronics, the counting rate of the pixels may differ; thus, a flat-field correction is necessary to match the counting rates of all pixels under X-ray radiation in order to obtain a homogeneous image.

A flat-field correction consists of two steps: An acquisition of flat image N_{flat} that is made with detector irradiation (bright field) to achieve an effective pixel gain map, another acquisition of dark image N_{dark} that is captured without irradiation (dark field) to achieve the dark current of each pixel. N_{flat} and N_{dark} are set of images that are acquired prior to or after the scan. After the sample projections N_{proj}, are recorded using the same setup of the detector. Based on the acquired flat and dark images, the measured projection images with the sample are then normalized to corrected images N_{corr} as

$$N_{corr} = \frac{N_{proj} - N_{dark}}{N_{flat} - N_{dark}} \tag{2.2}$$

Since PCDs do not exhibit any dark current $N_{dark} = 0$, so Eq. (2.2) becomes

$$N_{corr} = \frac{N_{proj}}{N_{flat}} \tag{2.3}$$

2.4.4 Classical imaging capabilities

2.4.4.1 Noise and contrast measurement

Noise characteristics of both detectors, Pixirad-2/Pixie-III and flat-panel, were compared on the basis of SNR and CNR. SNR (respectively CNR) compares the level of the signal (respectively the contrast) of the image to the level of background noise. To evaluate the SNR and CNR, a test phantom made from a carbon tube of diameter 5 mm with a 2 mm diameter steel bead inside was used. Two rectangular Regions Of Interest (ROI) of 100x120 pixels, representing 15% of the total image, were selected both inside the circular bead region and in the image background for both detector images.

Acquired radiographs from both detectors were initially subjected to flat-field correction. The averaged projections of the sample and flat (without the sample), obtained by averaging of acquired 10 projections for each acquisition condition, were used according to the method explained in Section 2.4.3.

Selecting the ROI is quite troublesome for Pixirad-2/Pixie-III detector due to the presence of random defective pixels. A local median filter of radius 3 and threshold 100 was applied in order to remove these defective pixels and correct the images. It selects the pixels that deviate from the median of the surrounding pixels, determined by radius, by more than a certain value, determined by a threshold, and replaces them with the median value. This operation was applied to remove both darker and brighter pixels that deviate more than the surrounding pixels median value. Figure 2.16 shows the phantom radiographs taken with Pixirad-2/Pixie-III, Figure 2.16(a) and flat-panel detector, Figure 2.16(b). The red boxes highlight the ROI in which SNR and CNR were computed.

As described earlier in (Chapter 1, Section 1.4.2), considering average signal $\overline{I}_{mean}$, and standard deviation σ_{mean} of the measured signal in the homogeneous ROI in the background, SNR and CNR can be computed as

$$SNR = 10\log\left(\frac{\overline{I}_{mean}{}^2}{\sigma_{mean}{}^2}\right) \tag{2.4}$$

$$CNR = 10\log\left(\frac{\overline{I}_{object} - \overline{I}_{mean}}{\sigma_{mean}}\right) \tag{2.5}$$

where, $\overline{I}_{object}$ represents the average signal in the rectangular ROI inside the circular steel bead.

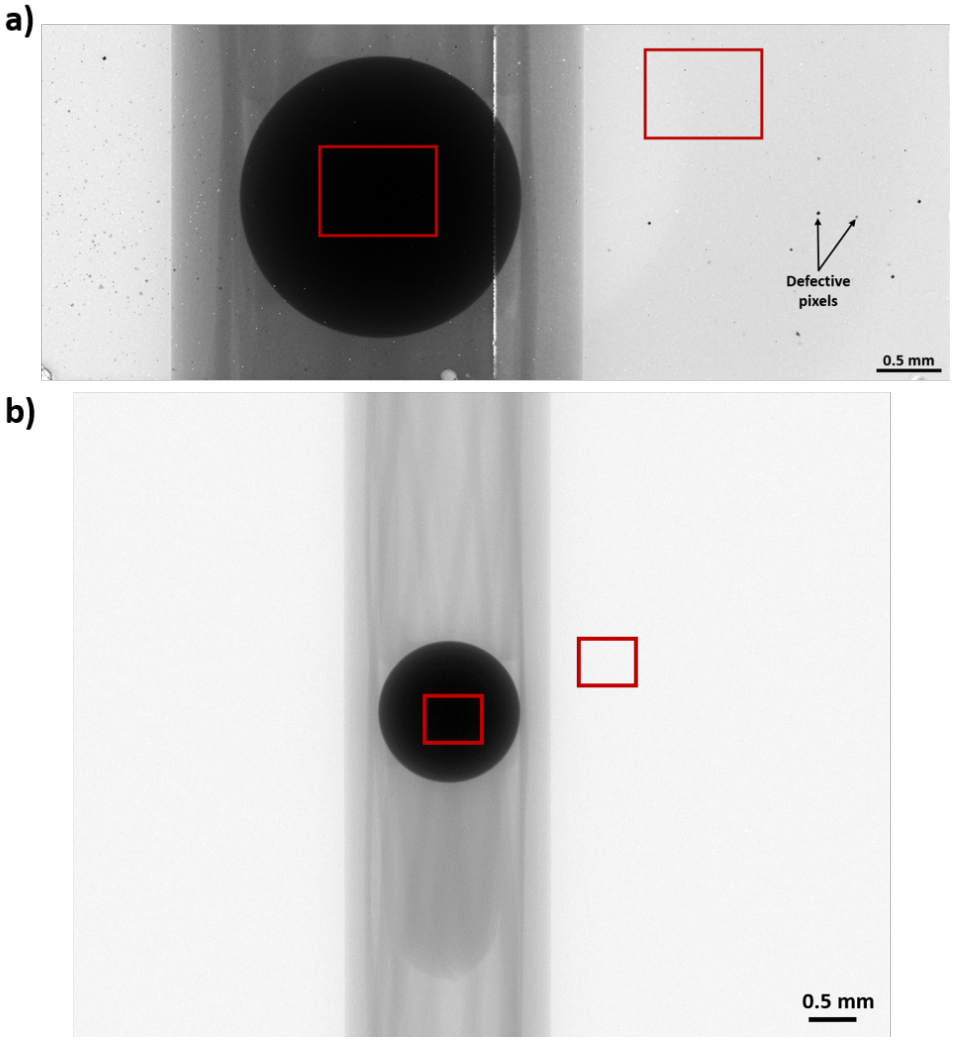

Figure 2.16: Radiographs of the test phantom for the computation of SNR and CNR at 100 kV and 1s exposure time taken with (a) Pixirad-2/Pixie-III detector (b) flat-panel detector. Rectangular red boxes represent the ROI in which SNR and CNR were computed.

2.4.4.2 Spatial resolution

The spatial resolution of detectors was compared with MTF. The MTF was evaluated using 1mm thick Copper (Cu) plate with a sharp edge as attenuating edge phantom. The phantom was attached against the detector window in a slightly tilted position relative to the pixel matrix. Acquired radiographs from both detectors were initially subjected to flat-field correction, and a local median filter of radius 3x3 was applied to Pixirad-2/Pixie-III detector images. Figure 2.17 shows a flat-field corrected radiograph captured using attenuating edge phantom with Pixirad-2/Pixie-III detector.

The MTF was computed according to the method described in [Samei et al., 1998]. The computation of MTF involves three steps. In the first step, the position and orientation of the edge line in the image are estimated. The gray scale image is binarized by applying a threshold value computed as the average of the signals from the two sides of the edge image. A gradient operation is performed to detect the line at the edge transition along with the angle and position of the edge transition using Hough transformation feature extraction technique.

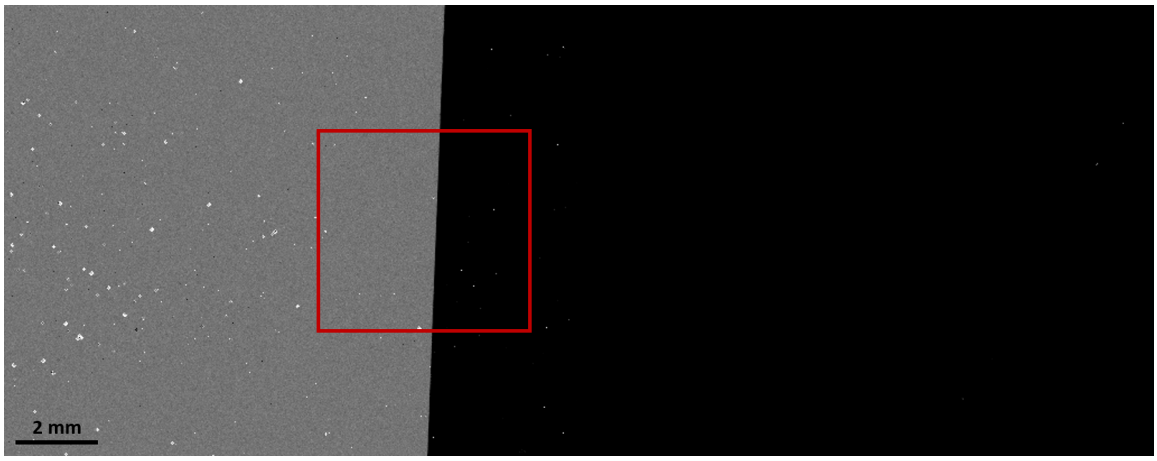

Figure 2.17: Flat-field corrected radiograph of 1 mm Copper (Cu) edge phantom captured using Pixirad-2/Pixie-III detector. A sub ROI of 200x200 pixels is highlighted in the red box used to compute the MTF.

The second step involves determination of the presampled edge spread function (ESF), which is obtained by reprojecting the grey level data of the original image along the direction of the estimated angle into a one-dimensional array of sub-pixel elements by using a sub-pixel bin width of 0.5 pixels. The ESF is then smoothed by utilizing a fourth-order, Gaussian-weighted, moving polynomial fit using window width 11 bins. After, in the third step, the smoothed ESF array is numerically differentiated to obtain the line spread function (LSF). The presampled MTF is then obtained by a fast Fourier transform (FFT) of the LSF.

2.4.5 K-edge subtraction radiographic imaging and spectral resolution

To access the single-shot K-edge subtraction (KES) imaging capability and the spectral resolution of the Pixirad-2/Pixie-III detector, Iodine (I) and Barium (Ba) elements were selected. Both I and Ba are easily available and their K-edge values are close to each other, being 33.2 keV for I and 37.4 keV for Ba, respectively. The relatively close K-edge values can also help to efficiently access the energy resolution of the detector.

For the experiment, a phantom (I-$BaSO_4$-H_2O) was prepared, consisting of three capillary tubes with the outer and inner diameter of 1.55 and 1.15 mm respectively. One tube was filled with Iodine solution (300 g in 1 L of water), the second tube was filled with barium sulphate solution (333 g in 1L of water) and the third one was filled with distilled water. Figure 2.18 shows the phantom.

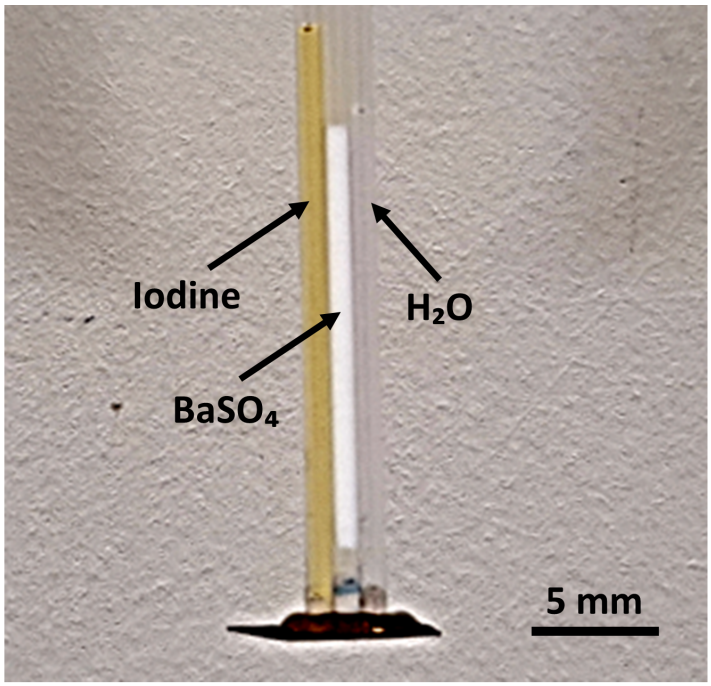

Figure 2.18: A phantom consisting of three capillary tubes consisting of iodine solution, barium sulphate solution, and distilled water.

2.4.5.1 K-edge subtraction radiographic imaging

A single-shot KES image was obtained by separating the polychromatic spectrum into two parts (below and above the K-edge of the elements, Iodine and $BaSO_4$) using the programmable energy thresholds.

For the acquisition, both imaging counter 0 and 1 were used and the lower threshold E_{th_low} and E_{th_high} were set to 28 and 38 keV, respectively. With this setup, two sample and flat images were recorded in a single exposure with energy ranging from 28 to 38 keV (with imaging counter 0) and 38 to 50 keV (with imaging counter 1). These images can be referred to "low" and "high" image.

For the post-processing, first the flat-field correction is applied and then the logarithmic digital subtraction of the two flat-field corrected sample images is performed to get the KES image N_{KES} using the Eq. 2.6, i.e. an image where only the desired elements are supposed to be observed.

$$N_{KES} = \log(N_{K+}) - \log(N_{K-}) \tag{2.6}$$

where, (N_{K+}) and (N_{K-}) are the flat-field corrected "high" and "low" images, respectively.

2.4.5.2 Spectral resolution

The spectral capabilities of the Pixirad-2/Pixie-III detector was illustrated by measuring the absorption spectra of Iodine and $BaSO_4$ sample. The acquisitions were performed using configuration 4 by sweeping E_{th_low} from 15 keV to 50 keV by steps of 1 keV. After this threshold scan, the digital subtraction was performed on consecutive images in order to get the image with an energy bin of 1 keV. This procedure was done on sample projections and flat radiographs to get the images with counts for energy bins of width 1 keV.

Noting $N_{E,sample}$ the image for bin of energy E with the sample, and $N_{E,flat}$ the image for bin of energy E without the sample, the corresponding image of absorbance was obtained by the following equation:

$$Absorbance = A_E = -\log \frac{N_{E,sample}}{N_{E,flat}} \tag{2.7}$$

Then, averaged spectra of absorbance were calculated as the averaged value of A_E over a ROI of 150x150 pixels in each tube of the phantom. Figure 2.19 shows the radiograph of the (I-$BaSO_4$-H_2O) phantom. ROI of 150x150 pixels was shown in white, blue and orange squares for water, Iodine, and Barium sulphate solutions, respectively.

Finally, the spectrum measured in the ROI containing only the water sample, white ROI in Figure 2.19, was subtracted from the spectra obtained from the ROI containing only Iodine or $BaSO_4$ in order to account for absorbance of the capillary tube and water to get the absorbance of I and $BaSO_4$.

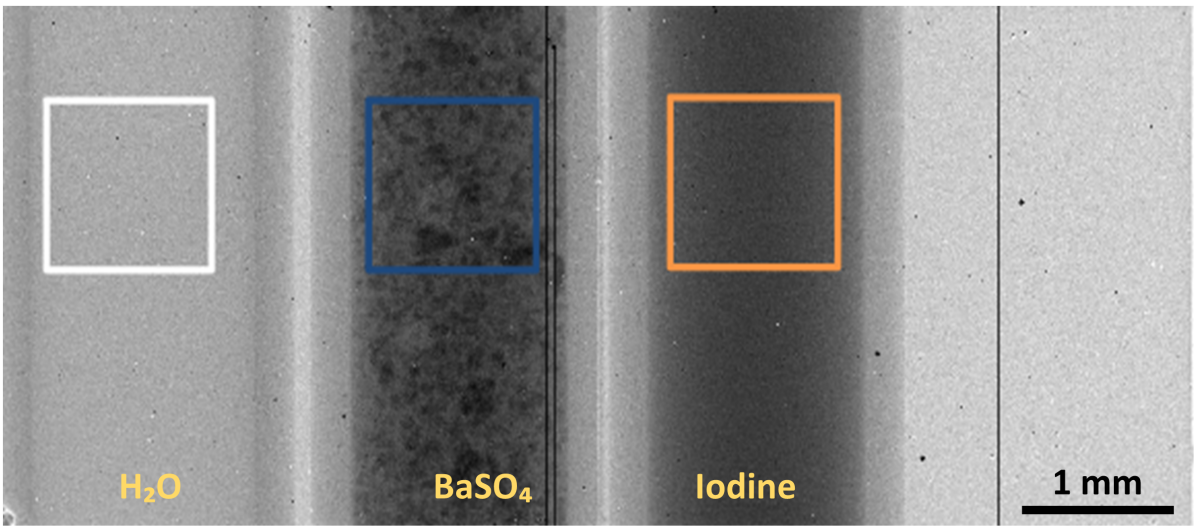

Figure 2.19: Flat-field corrected radiograph of the (I-$BaSO_4$-H_2O) phantom consisting of three capillary tubes. ROI of 150x150 pixels was shown in white, blue and orange squares for water, Barium sulphate, and Iodine solutions, respectively.

2.5 Characterization results of the Pixirad-2/Pixie-III detector

2.5.1 Introduction

The characterization results of only the new version Pixirad-2/Pixie-III detector are presented in this section. Although a significant amount of time was spent in characterizing the old version Pixirad-2/Pixie-II detector before the delivery of the Pixie-III module detector, characteristics of Pixirad-2/Pixie-III are significantly better than the Pixirad-2/Pixie-II, so it was chosen as a potential candidate for lab-based imaging.

Initially, in Section 2.5.2, the correction results for the dead and bad pixels and dynamic defects are presented, and some recommendations to efficiently operate the detector with minimum defects are suggested as well. Section 2.5.3 presents the spectrum measurements for charge sharing correction by using different acquisition modes of the detector. The results for the classical imaging capabilities of the Pixirad-2/Pixie-III detector in terms of SNR, CNR and MTF is presented in Section 2.5.4 and are compared with the measurements done with the standard flat-panel detector. Lastly, in Section 2.5.5, the qualitative and the quantitative results for the K-edge subtraction (KES) imaging and absorption spectral measurements are presented.

2.5.2 Defects

An application of a local median filter to correct the radiographs from static defects and bad pixels is illustrated in Figure 2.20. A local median filter of radius 3x3 with threshold 100 is applied to replace both brighter and darker pixels to the raw projection of AlCu sample, Figure 2.20(a) captured by Pixirad-2/Pixie-III detector. Figure 2.20(b) shows the corrected projection. It can be seen that the quality of the radiograph has improved significantly and most of the defects were replaced by the median value of surrounding pixels. However, few bad pixels are still visible in the corrected projection which can be further removed by refining the parameters of local median filter or by applying further post-processing correction.

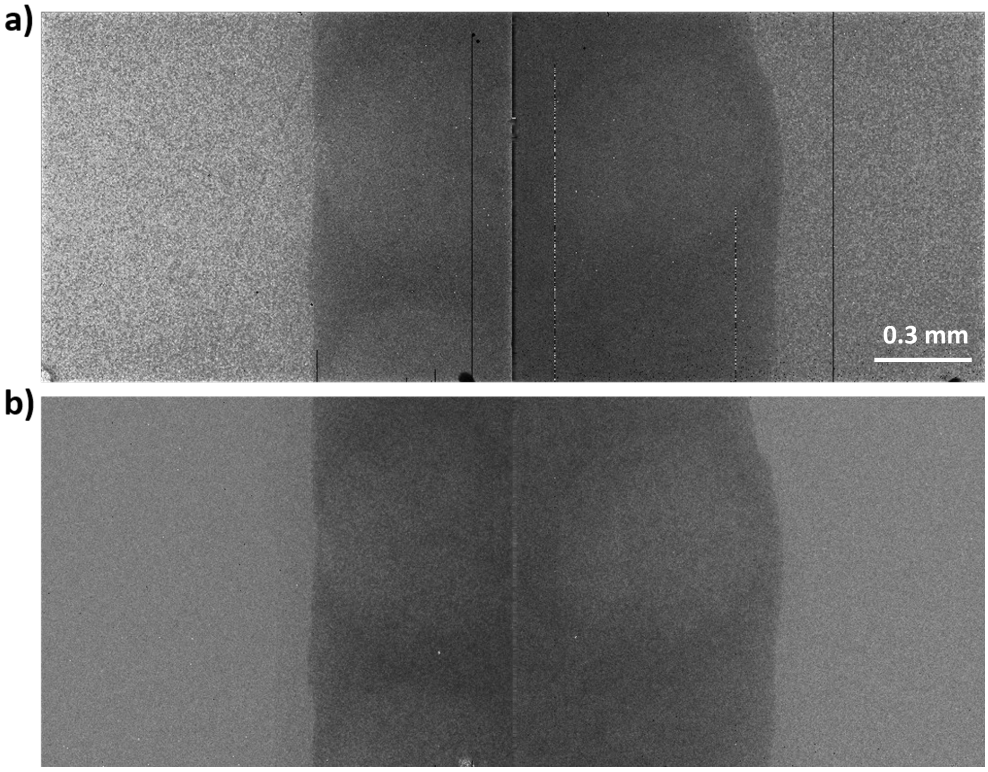

Figure 2.20: Example of radiograph correction by a local median filter. (a) Radiograph captured by the Pixirad-2/Pixie-III detector with static defects and bad pixels visible. (b) After the application of local median filter, most of the static defects and bad pixels are removed.

Figure 2.21(a) shows the cropped radiograph captured by the Pixirad-2/Pixie-III after 20 minutes of operation with the time-dependent defects visible. Figure 2.21(b) shows the same radiograph after performing the sensor refresh using the hardware bias reset feature present in the detector. The bias reset roughly takes 3-4 seconds, eliminating most of the time-dependent instabilities of the sensor and restoring sensor performance.

It is concluded that bias reset or sensor refresh is the most simple and efficient way to remove the time-dependent defects. However, post-processing filtering can be performed to further improve the quality of the radiographs.

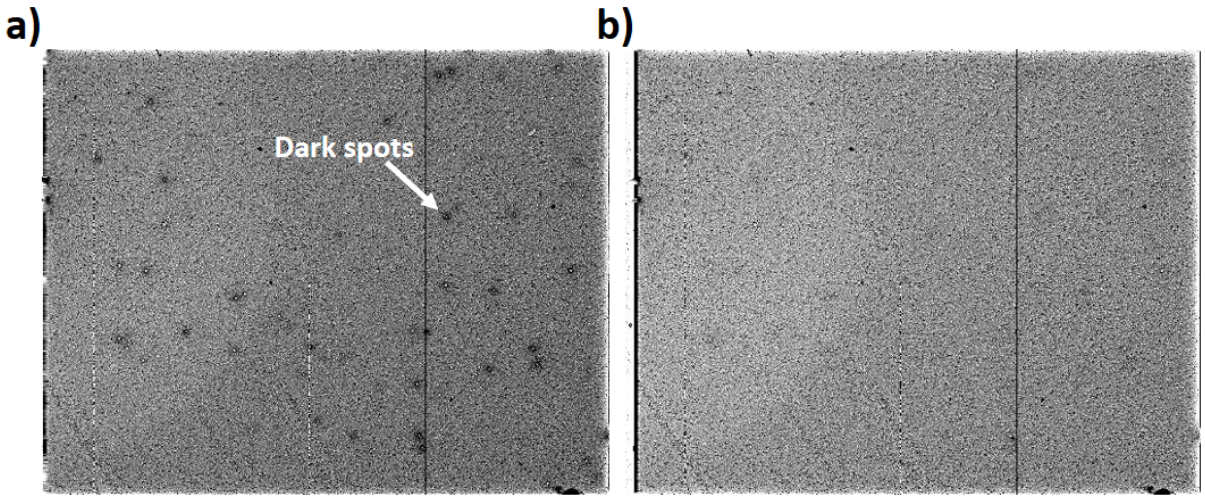

Figure 2.21: Radiographs captured by the Pixirad-2/Pixie-III detector (a) before and (b) after the sensor refresh. It takes 3-4 seconds to turn on and off the bias voltage and it recovers the detector performance eliminating the time-dependent instabilities.

As mentioned earlier in Section 2.4.2 that time-dependent instabilities start appearing on the sensor 7-10 minutes after activation. The following scheme was concluded, Figure 2.22, for the bias refreshing strategy during the CT scans. If the scan time is less than 1-2 minutes, then no sensor refresh is needed as there will be no time-dependent instabilities. It is recommended to refresh the sensor every 4-5 minutes if the scan time exceeds 7-10 minutes. This will stop the data acquisition for only 3-4 seconds and restore the sensor performance.

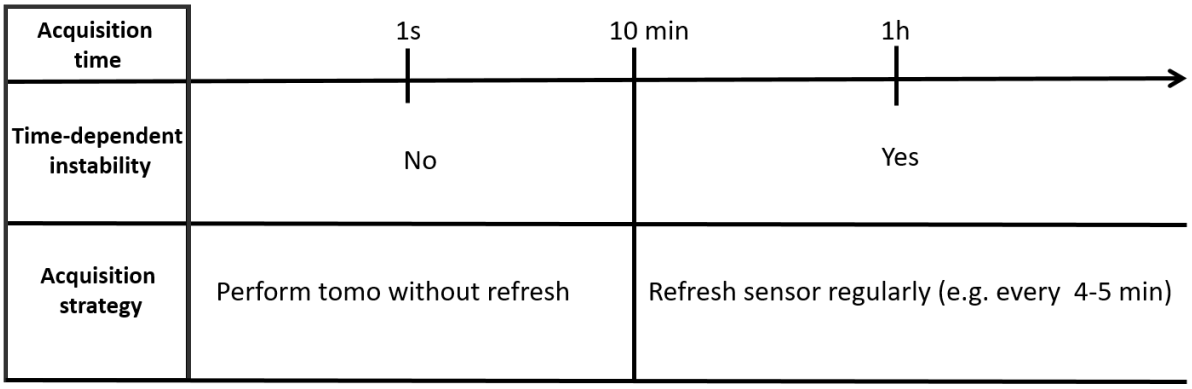

Figure 2.22: Scheme for managing the sensor refresh time depending on the acquisition time of tomography. It is recommended to regularly refresh the sensor every 4-5 minutes if the acquisition time of the scan exceeds 10 minutes.

2.5.3 Charge sharing effect correction

Charge sharing correction measurements for the Pixirad-2/Pixie-III detector were carried out using configuration 2, (section 2.4.1). After the acquisitions with imaging counter 0 for each operating mode (NONPI, NPI, NPISUM), the digital subtraction was performed on consecutive images to get images with 1 keV energy bin. Then, the average signal intensity of the image was measured, which represents the differential counts. The differential counts, representing

photons per keV per second, as the function of energy are plotted in Figure 2.23 for three operating modes. In the Figure 2.23 we can observe that

- NONPI mode does not correct the charge shared from the high-energy photons. These shared charges into two or more neighbouring pixels are counted as separate events; hence the integral spectrum overestimates the low-energy photons and underestimates the high-energy photons indicating the sharp increase at low energies as seen in the black curve of the Figure 2.23.

- In NPI mode, only one pixel per event is allowed to count and recover the shared signals by allocating the count to the pixel receiving the highest fraction of the charge. So it does not account for the low-energy photons shared in the neighbouring pixels, and there is still an issue of underestimation of high-energy photons. It can be seen in the red curve of the Figure 2.23 that low-energy photons below 20 keV have been recovered to some extent, but total energy is underestimated due to charge sharing.

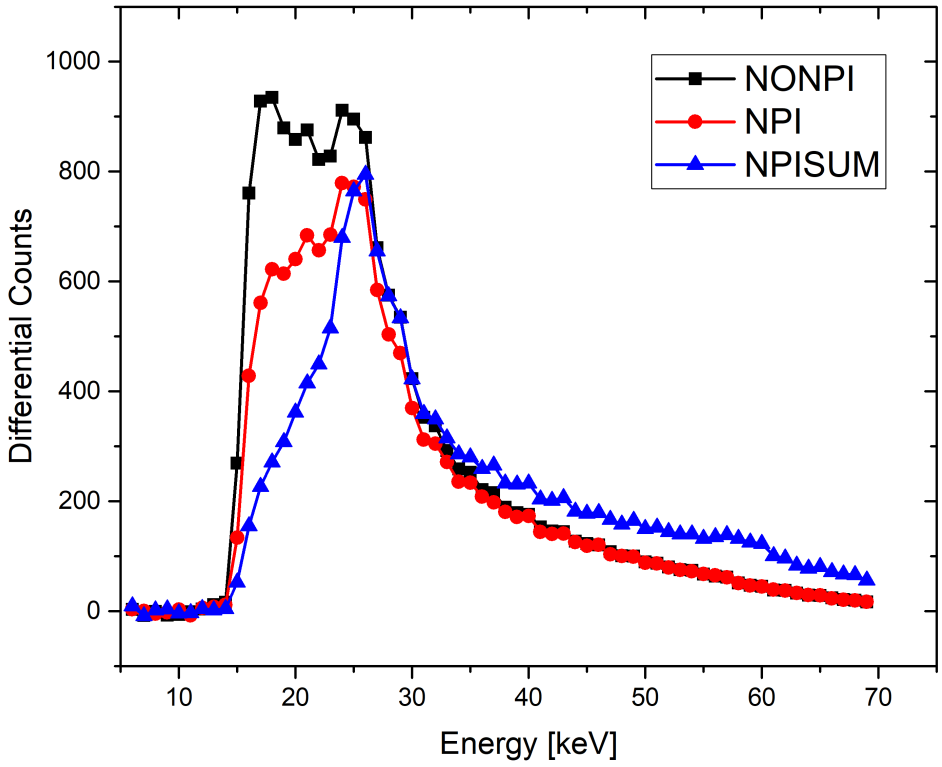

Figure 2.23: Energy characterization of different operating modes of the Pixirad-2/Pixie-III detector. Differential counts against the threshold energy.

- NPISUM mode recovers the shared charge up to four neighbouring pixels (horizontal and vertical) by summing the shared charges together to evaluate the total energy correctly. Thus the charge sharing is corrected to some extent, as seen in the blue curve in Figure 2.23. Low-energy photons detected in NONPI and NPI mode are now corrected to their original photon and are represented as a single high-energy photon. However, no correction is applied on the neighbouring diagonal shared charges. Also, since the pixel size of the

detector is small, 62 μm, the charge of the incoming photon can spread over more than four pixels in horizontal, vertical and diagonal directions. The limitation of the NPISUM mode to correct the shared charges up to only four neighbouring pixels can still result in distorted measured spectrum.

The differential spectra obtained with monochromatic beam of energy E = 26 keV indicating the similar observations that spectra depend on the operating mode NONPI, NPI and NPISUM were previously reported in [Di Trapani et al., 2020]. The imaging performance and noise characterization for different combinations of operating modes in terms of the SNR, presampling MTF, the normalized noise-power spectra (NPS) and the assessment of noise equivalent number of quanta (NEQ) using the synchrotron source have been previously presented [Di Trapani et al., 2020].

2.5.4 Classical imaging capabilities

SNR and CNR acquisitions for both Pixirad-2/Pixie-III and flat-panel detector were performed using the Configuration 3, (Section 2.4.1), and computed using the method described earlier in Section 2.4.4. Radiographs acquired from both detectors were subjected to flat-field correction as described in Section 2.4.3. A local median filter of radius 3 and threshold 100 was applied, to the Pixirad-2/Pixie-III projections, to correct the defects due to static pixels and polarization. Removal of these defects significantly lowers the standard deviation of the detector. The plot of SNR and CNR against the acquisition conditions (voltage and exposure time) is shown in Figure 2.24.

Before the correction of Pixirad-2/Pixie-III radiographs with local median filter, SNR values of Pixirad-2/Pixie-III is significantly lower than flat-panel against all acquisition conditions. The lower SNR for the Pixirad-2/Pixie-III is due to the high standard deviation of the mean gray value of pixels. The high standard deviation is due to the presence of bad pixels in the region of interest. However, after the correction of these bad pixels, SNR for Pixirad-2/Pixie-III improves significantly, around 25%, but it is still lower than the flat-panel of about 15%.
This improvement in SNR is primarily due to the decrease in the standard deviation value. However, the standard deviation can be further reduced by tuning the parameters of the local median filter or by applying image quality filters which in turns will result in an increase in SNR. Moreover, as stated earlier in Chapter 1 that SNR is not a very useful image quality index as it does not provide any information about the detectability of feature of interest for the segmentation process.

CNR in both conditions (before and after removal of the detectors inhomogeneities) is higher for Pixirad-2/Pixie-III. CNR in the corrected radiographs is around 12% higher than flat-panel detector for all acquisition conditions.

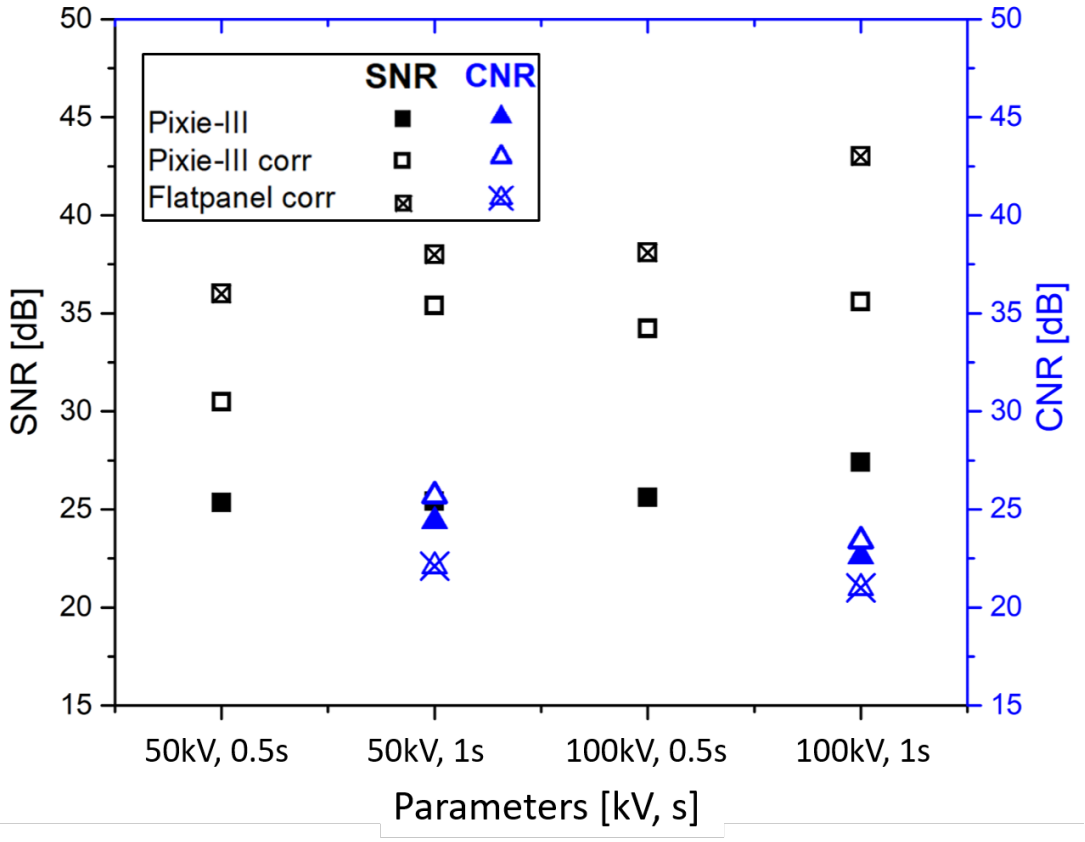

Figure 2.24: Comparison of Pixirad-2/Pixi-III and Flat-panel detector in terms of SNR and CNR at different acquisition conditions.

Figure 2.25 compares the presampling MTF obtained using the attenuating edge object, (section 2.4.4.2), for both Pixirad-2/Pixie-III and flat-panel detector. The MTF curve from the photon-counting detector shows a higher spatial resolution than the flat-panel detector. The spatial frequency at 0.5 MTF lines is 0.43 and 0.17 cycle/pixels for Pixirad-2/Pixie-III and flat-panel, respectively. The high spatial frequency at 0.5 MTF of Pixirad-2/Pixie-III detector corresponds to fine image detail and sharper image. The Nyquist frequency (0.5 cycles/pixels) estimates the MTF value of 9% for flat-panel and 38% for Pixirad-2/Pixie-III detector, indicating the improved MTF of Pixirad-2/Pixie-III detector.

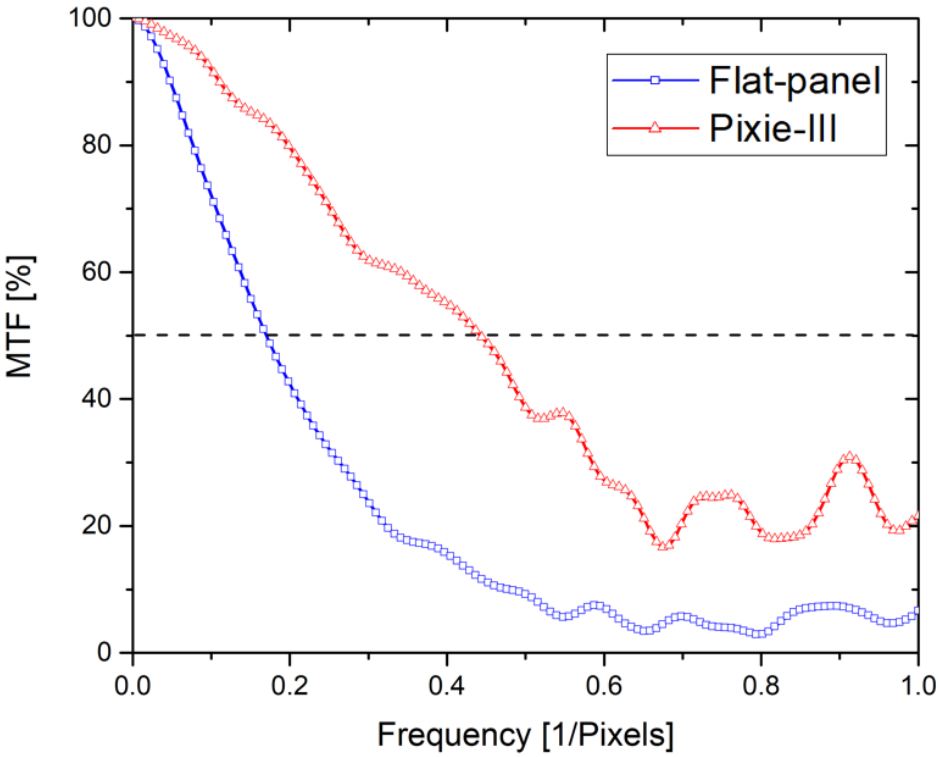

Figure 2.25: Comparison of MTF for Pixirad-2/Pixie-III and Flat-panel detector.

2.5.5 K-edge subtraction imaging and spectral resolution

KES imaging and spectral resolution experiments were carried out using configuration 4, (section 2.4.1) and computations were done using the methods described in section 2.4.5. The obtained results are presented in this section.

2.5.5.1 KES imaging: qualitative results

Figure 2.26 shows the qualitative results of the KES radiographic experiment. Flat-field corrected standard and KES radiograph of (I-$BaSO_4$-H_2O) phantom at two distinct energy ranges are shown. It can be noticed that different settings of the detector programmable thresholds produce different images with the same input X-ray spectrum. In Figure 2.26(a) a standard radiograph captured using photons of energy between 5 to 50 keV using the imaging counter 0 is shown.

Figure 2.26(b) presents the processed KES image using photons of energy between 28 to 38 keV. Since the K-edge of Iodine and Barium lies at 33.2 keV and 37.4 keV so only, Iodine and Barium Sulphate solutions are visible in Figure 2.26(b) while water and glass tubes are completely removed. The obtained KES image is similar to the observations recently reported in [Brun et al., 2020b] for Iodine and Barium with the same energy range.

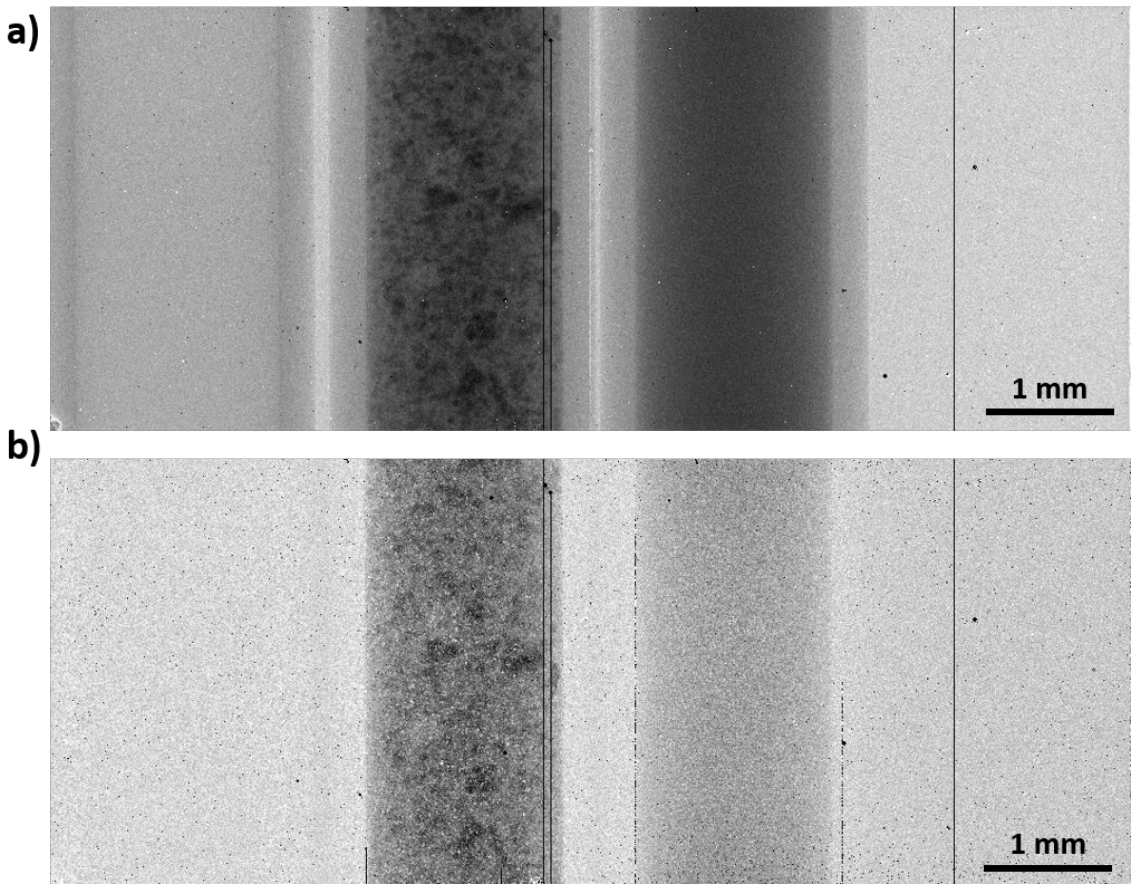

Figure 2.26: (a) Standard flat-field corrected radiograph of the (I-$BaSO_4$-H_2O) phantom recorded with E_{th_low} = 5.0 keV. (b) KES flat-field corrected radiograph of the (I-$BaSO_4$-H_2O) phantom recorded with using E_{th_low} = 28 keV and E_{th_high} =38 keV.

2.5.5.2 Absorbance measurement: quantitative results

Figure 2.27 shows the computed absorbance spectra for both Iodine and Barium and compares them with the tabulated value.

The obtained spectra are displayed in solid blue lines. The bin width of 1 keV energy was used for the experimental dataset. Experimentally computed absorbance peaks for Iodine and Barium are well visible around 35 keV and 39 keV, respectively. In orange dashed lines are theoretical spectra for I and Ba respectively, accounting for the pure sample and same thickness obtained with Xraylib [Schoonjans et al., 2011].

The first observation that can be made is that the K absorption edges of Iodine (33.2keV) and Barium (37.4 keV) are well visible and correctly quantitatively placed. Additionally, the measured spectrums are quantitatively consistent with the tabulated values. The tabulated curve was further smoothed using the Gaussian smoothing with the standard deviation of 1.8 keV to match it with the experimental curve. The magnitude of smoothing is consistent with the energy sensitivity of the Pixirad-2/Pixie-III detector reported in the literature [Bellazzini et al., 2015]. The theoretical values for Iodine and Barium are of pure elements while, for the experiment, the solution of Iodine and Barium Sulphate with 33% concentration was used, due to which the difference is expected.

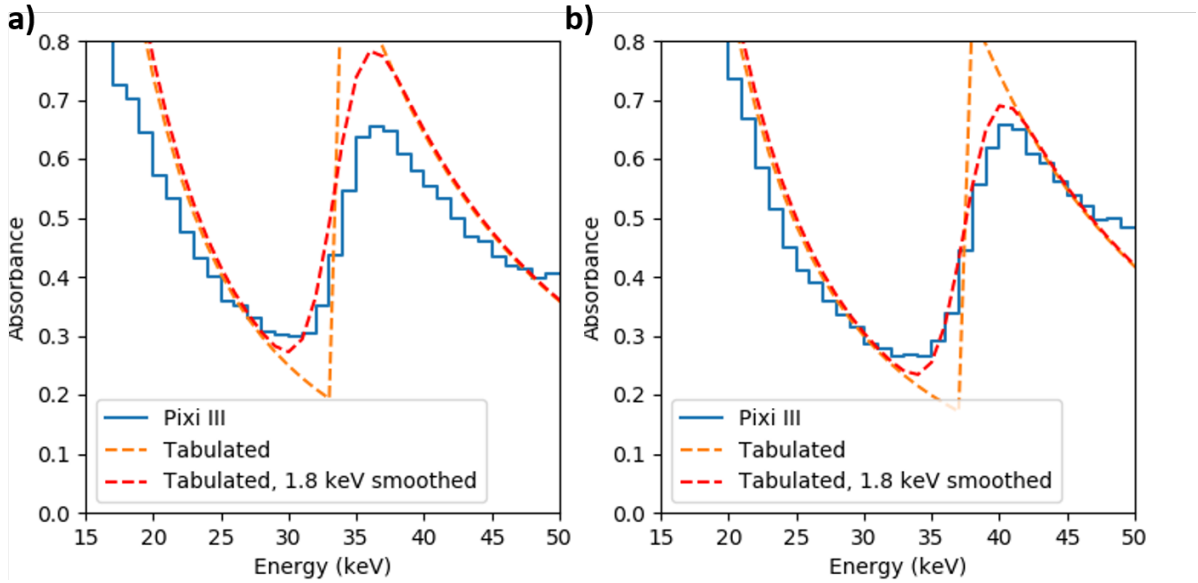

Figure 2.27: Comparison of the experimentally computed absorbance spectra with the tabulated values for (a) Iodine (b) Barium. The tabulated curve was Gaussian smoothed by 1.8 keV to match with the experimental curve.

2.6 Characterization results of the ADVACAM detector

The characterization results for ADVACAM detectors, WidePix and TimePix3 are presented in this section. Since both detectors were loaned for only one week, only few of their characteristics were examined.

2.6.1 WidePix spectrum measurement

The ADVACAM detectors were loaned for only 1 week, so only the energy characterizations were performed and some results from the WidePix detector are presented here. Energy characterization measurements for the WidePix detector were carried out using configuration 5, (section 2.4.1). After the acquisitions, the digital subtraction was performed on consecutive images to get the image with 1 keV energy bin. Then the average signal intensity of the binned images representing differential counts was measured.

The differential counts as the function of energy are reported in Figure 2.28. Each point corresponds to a single energy bin. The characteristic peaks of Molybdenum are at 17.5 keV and 19.6 keV, so the refined energy bins with 0.2 keV are plotted as the secondary axis between 16 to 20 keV in red color to visualize the characteristic peaks of Molybdenum clearly. However, no characteristic peaks are visible in the measured spectrum using the WidePix detector. It can be explained due to the charge sharing effect. No hardware or software feature for the correction of the charge sharing effect was present in the WidePix detector, resulting in the distorted recorded energy response. Thus the WidePix detector appears not to be suitable for spectral imaging.

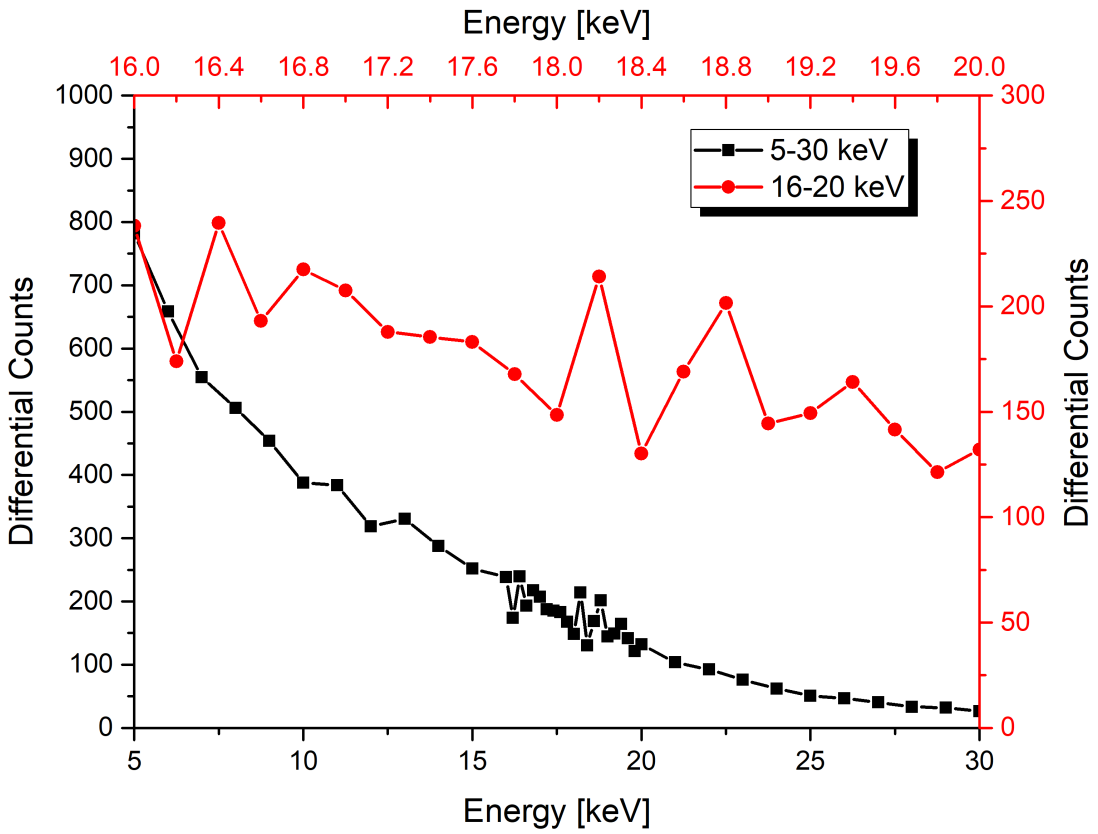

Figure 2.28: Energy characterization of WidePIX detector using the nano-focus X-ray source with Molybdenum target. Differential counts are plotted against the 1 keV energy bin. The characteristic peaks of Molybdenum are at 17.5 keV, and 19.6 keV, the refined spectrum with 0.2 keV energy bin is plotted in red color between 16 to 20 keV.

2.6.2 TimePix3 measurement

No specific characterization was done for the TimePix3 detector. Detector saturation was a major issue in most of the measurements even at very low values of the input current.

When the detector was operated in time-over-threshold ToT and time-of-arrival ToA mode to record the time, position, and energy of each X-ray photon, significantly large output data files in .t3r (time-tagged time-resolved data) format were generated, usually, 10 of a gigabyte (GB) and in some cases 100 GB depending on the input parameters (exposure time, energy). This large .t3r file also takes a couple of minutes to transfer to the hard drive. The large readout time of the detector couple with a very small area of the detector and the detector saturation at the standard value of current does not make it suitable for the intended in-situ acquisitions in lab-based CT systems.

However, many potential features of this detector exist which need to be explored. The output .t3r file contains information on the energy, position, and time of arrival for each X-ray photon. The time of arrival information enables the possibility to identify clusters of events belonging to the single-photon interaction. These cluster of pixels is used for the charge sharing correction in the post-processing. After identifying the clusters of pixels, the TOT information can be used, and the weighted mean of the energy distribution in the pixel cluster can be

calculated, which is further used to localize the sub-pixel position of the photon interaction [Khalil et al., 2018]. The details about the pixel clustering and sub-pixel resolution can be found in [Khalil et al., 2018, Dreier et al., 2019].

Using Advacam developed interface software Pixet Pro, sub-pixel resolution images were obtained using an Cu edge phantom placed on the detector. Figure 2.29(a) shows the original frame-based output of the detector containing 256 x 256 pixels. Figure 2.29(b) shows the 2 x 2 sub-pixel resolution image obtained during the post-processing and contains 512 x 512 pixels. Figure 2.29(c) shows the 4 x 4 sub-pixel resolution image containing 1024 x 1024 pixels.

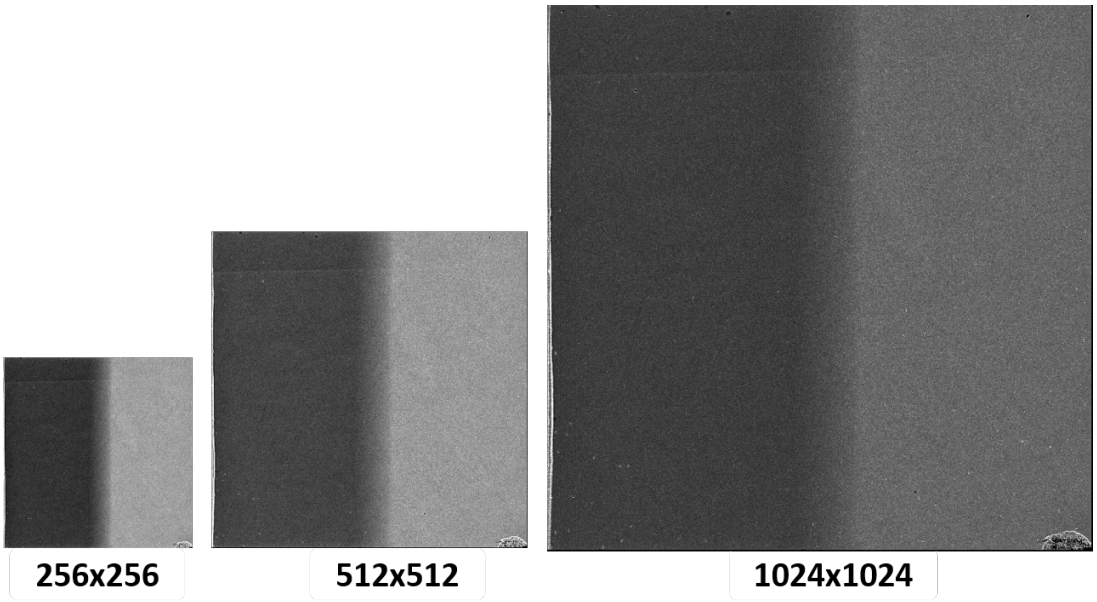

Figure 2.29: Sub-pixel resolution with TimePix3 detector. (a) Standard acquisition with the output frame containing 256 x 256 pixels. (b) 2 x 2 sub-pixel resolution image obtained during the post-processing containing 512 x 512 pixels. (c) 4 x 4 sub-pixel resolution image obtained during the post-processing containing 1021 x 1024 pixels.

2.7 Synthesis of the detectors results

The characterization results presented in section 2.5 and 2.6 can be synthesized as:

- The old version Pixirad detector, Pixirad-2/Pixie-II, was not a suitable detector, and no characterization results of the detector were presented in this chapter, although a significant amount of time was spent to characterize the detector performance. The major issue with the detector was the presence of a large number of static and dynamic defects, and no hardware features to correct the dynamic defects due to polarization were present. Moreover, no charge sharing correction was implemented, making this detector unsuitable for spectral measurements.

- The presence of noise, bad pixels, is a major issue in the Pixirad-2/Pixie-III detector, however, the standard local median filter can significantly improve the image quality and makes the radiographic measurements possible, but these noisy pixels will create ring artifacts during the reconstruction process for tomographic measurements. An automatic dedicated post-processing procedure needs to be developed in order to remove these bad pixels from the recorded projections prior to reconstruction.

- The energy characterization of the three operating modes of the Pixirad-2/Pixie-III was done to evaluate the charge sharing correction performance. NPISUM mode recovers the shared charges compared to NONPI and NPI mode but the efficiency of the correction is only limited to four neighbouring pixels in the horizontal and vertical direction.

- The radiographic characterization results of Pixirad-2/Pixie-III in terms of its imaging performance were presented using the polychromatic beam. The classical imaging capabilities of the Pixirad-2/Pixie-III in terms of SNR, CNR and MTF were tested and compared to the standard flat-panel detector. The results indicated lower SNR but improved CNR and MTF of Pixirad-2/Pixie-III detector compared to flat-panel.

  The spectral imaging ability of the Pixirad-2/Pixie-III detector was evaluated by accessing the single-shot KES imaging and by measuring its spectral resolution. The detector is quite efficient for single-shot KES imaging to distinguish the materials on the basis of their K-edges using the programmable energy thresholds. Moreover, the energy resolution of the detector was measured to be within 2 keV range which is adequate for practical applications such as monochromatic measurements and spectral CT using the laboratory CT.

- To fully understand the performance of the Pixirad-2/Pixie-III detector and to build guidelines for its use in tomographic imaging, other characterizations such as detector linearity and saturation behaviour as a function of input flux, source-to-detector distance, and energy threshold also need to be studied. The effect on the image quality in terms of SNR and CNR as a function of the energy threshold value and the effect on the energy spectrum due to the pulse pile-up effect of the detector also needs to be quantified. The potential of the detector to correct the beam-hardening effect in the CT reconstructed images by selecting only the high-energy photons during the acquisition also needs to be quantified.

- ADVACAM WidePix detector consisting of Medipix readout chips does not include any feature for charge sharing correction, resulting in distorted spectrum measurements underestimating high-energy photons. But since the detector was only available for a one-week loan time period, the potentials of the detector were not explored.
- ADVACAM TimePix3 was also available for only one-week time period. This detector has many potential benefits which were not explored. The pixel clustering, charge sharing correction, and the possibility of achieving sub-pixel resolution during post-processing can make this detector suitable for many applications. Although the active pixel area of the detector is quite small for standard CT with standard sample size, the implementation of multiple TimePix3 readout chip in WidePix detector can solve this problem. The potential benefits of this detector need to be explored in-depth to conclude something concrete.

2.8 Conclusions

The introduction of photon-counting detectors is expected to be one of the next major breakthrough in X-ray computed tomography (CT). Over the last few years, significant research has been conducted in the fields of photon-counting detectors in terms of the hardware design, detector performance, drawbacks, factors affecting the image quality, and potential applications in micro-CT. This chapter presented the quantitative characterization of the imaging performance of a photon-counting detector Pixirad-2/Pixie-III, using a lab polychromatic X-ray source. Pixirad-2/Pixie-III exhibits improved CNR and MTF but lower SNR compared to the standard flat-panel detector.

The energy thresholding feature of the detector allows to limit the polychromaticity of the lab X-ray spectrum and makes possible the monochromatic measurements. This energy discriminating ability of the Pixirad-2/Pixie-III detector was investigated by performing the single-shot K-edge subtraction radiographic imaging. The spectral resolution of the detector was investigated by measuring the absorption spectra of Iodine and Barium sulphate and was found to be adequate for practical spectral measurement applications such as material identification spectral tomography and contrast-enhanced CT using the laboratory X-ray sources. Moreover, the improved characteristics of the detector, smaller pixel size and faster readout frame, compared to the standard flat-panel detector, can also improve the spatial and temporal resolution of the CT scan. However, to fully understand the performance of the detector and to use it for tomographic scans, other factors such as detector linearity and the saturation behaviour as a function of acquisition parameters and the effect of pulse pile-up on the output spectrum also need to be characterized.

Chapter 3

Towards optimization of the acquisition parameters

Contents

Nomenclature

Definitions of some *Key Words* used in this chapter.

Feature size or feature of interest (FOI): It is defined as the smallest size of the spherical feature (pore, particle) present in the scanned specimen that needs to be quantified from the reconstructed datasets.

Segmented volume: Segmented volume is the estimated volume of the feature of interest of specific size after thresholding using the mean gray value.

Error and weighted average error: Error is defined as the relative change in the estimated thresholded volume of the spherical feature using the volume of an ideal sphere as reference. The probability distribution curve is represented as a function of estimated error for a specific radius feature.
Weighted average error is the single absolute weighted value of the error distribution.

Constraints: Constraints are limitations or restrictions on the optimization model that the model needs to take into account and are given as input parameters.

Interface velocity: It is defined as the kinetic evolution of the feature of interest (FOI) during a single CT scan and is expressed in physical units (μm/sec).

Motion: Motion is defined as the change in the diameter of the feature (in pixels) during a single CT scan.

Integrated transmitted intensity: It is defined as the output X-ray photons flux after passing through the specimen towards the detector pixel. It is computed by integrating the Beer-Lambert law by taking into account the penetration lengths of the different materials constituting the specimen.

Contrast: Contrast is defined as the ratio between transmitted intensity after passing from two constituent materials of the specimen in case of a heterogeneous specimen, and ratio between the transmitted intensity after passing from the specimen and background intensity in case of a homogeneous specimen.

Abstract

This chapter details the attempt towards the optimization of the CT acquisition parameters. An optimization model is developed to estimate the optimal CT scan configuration using the prior information of the sample, sample environment, and the objectives of the CT scan.
The optimization model is based on the weighted average error estimation criteria in the segmented volume of the feature of interest present in the specimen. The global workflow of the model is based on three modules: modelling noise in the feature of interest, X-ray absorption simulation tool, and a screening algorithm. The screening algorithm loops over all the possible scanning parameters and outputs the different possible scanning configurations along with the estimation of the probability of detection of the interested feature size for each configuration taking into account the resultant image contrast, resolution and motion of the feature of interest. The output scanning configurations include the X-ray source parameters, geometry settings, and detector parameters. After a cost function is used to select the most optimal scan setting according to the weighted average error in the feature of interest criteria, taking into account the level of the analysis to be performed on the 3D images.

3.1 Introduction

X-ray computed tomography (CT) is a powerful imaging technique that provides non-destructive access to the three-dimensional morphology of the scanned specimens. The obtained information from the reconstructed 3D images is used to characterize the specimen. The characterization goal is to perform qualitative or quantitative image analysis on a certain feature of interest (FOI) present in the specimen.

The possible levels of 3D image analysis (L1, L2 and L3, Chapter 1 Section 1.3.3) that can be carried out for specimen characterization entirely depend on the image quality obtained from the X-ray CT scan. Generally, in laboratory X-ray CT setups, the achievable image quality is significantly lower than the one provided by synchrotrons, due to the limited X-ray flux produced by the micro-focused X-ray tubes. This subsequently limits the temporal resolution due to a lack of photon statistics at the lowest detector exposure times [Schryver et al., 2018]. The achievable image quality depends on many factors such as specimen's material composition and geometry, CT setup, and especially on the user-defined scan acquisition parameters. These acquisition parameters include X-ray source voltage and current, positioning and the orientation of the specimen in the X-ray beam, detector exposure time, number of projections, and the measurement conditions [Reiter et al., 2010]. Since the achievable image quality depends on the selected acquisition parameters, the optimization of these parameters is required.

Many studies have been reported in the literature quantifying the effect of a specific scanning parameter on the image quality and thus focus on the partial problem. Gomez and Smith [Gómez and Smith, 2020] examined the effect of decreasing number of projections on the image quality and concluded that with the decrease in the number of projections the image quality decreases but without having a significant effect on the dimensional measurements, although this was not the case for form measurements such as flatness and cylindricity. The guidelines for the selection of voltage for light and heavy materials are presented in [Plessis et al.,

2018]. Hilleret al [Hiller et al., 2012] investigated the physical characterization and performance of the X-ray tube and detector. However, no global optimization strategy exists to determine the suitable scan acquisition parameters for a CT scan.

Nowadays, the selection and optimization of these scan acquisition parameters are usually made by an experienced operator which leads to subjective image quality differences since setting up a CT scan with optimal parameters is a highly complex task. Zabler et al. [Zabler et al., 2020] recently compared the quantitative image quality from thirteen different sub-micrometer CT scans of a simple test phantom made of polymer micro-beads performed by different experienced operators. Results indicate that operator choices strongly influence scan quality for a given measurement time. A similar observation was concluded by Moroni and Petro [Moroni and Petro, 2018] and highlighted the need for more procedures for the selection of scanning parameters. Moreover, there is no standard holistic quality metric in X-ray CT to estimate the quantitative image quality [Sanchez et al., 2020].

The selection of the scan acquisition parameters becomes even more complex when fast in-situ acquisitions with high temporal/spatial resolution need to be performed because the image quality, in such cases, is further reduced due to the motion blurring artifacts. This motion blurring is caused by the structural change within the specimen following a dynamic process and usually occurs when a dynamic process is imaged at an insufficient temporal resolution [Schryver et al., 2018]. For such acquisitions, a trade-off has to be made between the acceptable level of motion, image quality, and resolution. Optimization of the acquisition parameters can be achieved by experimentally varying different acquisition settings and choosing the set of parameters that produces the best possible radiographs. However, the large dimensionality of the scanning parameters makes the process of manually changing the acquisition settings and examining the quality of radiographs and reconstructed dataset not an easy task.

A global optimization strategy such as an X-ray CT optimization model could help to automatically optimize the different scan acquisition parameters for given sample specifications, and according to the objective of the scan and can output the possible scanning configurations. The model would also predict the quality of the recorded images that would be produced for a particular set of acquisition configurations, and the suitable scanning configuration can be selected by establishing a trade-off between image contrast, resolution, and motion during the scan.

This chapter contributes towards building an optimization model for the CT acquisition parameters. The developed optimization model described in Section 3.2 uses the knowledge of the sample, sample environment, and scan objectives as the input parameters. The optimization tool includes a noise model to predict the probability of detection of the interested feature size, X-ray absorption spectrum simulation tool to compute the output image contrast, and a screening algorithm based on screening over all the possible scanning parameters. After, a cost function is used to select the suitable configuration on the weighted average error in the feature size criteria.
The working of the model is illustrated with the user-defined case study, Section 3.3.1. The validation for some parameters is done and strengths, limitations, and recommendations for the improvement of the optimization model are presented in Section 3.3.

3.2 Model description

The global workflow proposed for the optimization model is presented in Figure 3.1.

Model inputs the preliminary knowledge of the sample, the in-situ process, and the objective of the CT scan. The input parameters are described in Section (3.2.1). After, based on the hypothesis and knowledge of the tomograph system, it loops over all acquisition parameter space and computes the different possible configurations. For each configuration, it predicts the image quality based on the output image contrast and weighted average error estimation criteria in the feature of interest using the developed X-ray absorption simulation tool and noise model. Then, a cost function is used to get the optimal configuration according to the given aim of analysis. The development of the optimization tool and its different modules are detailed in Section (3.2.2). The model outputs the tabular with all possible scanning configurations including the CT scan geometry settings, detector parameters, expected image quality and indicates the optimal configuration based on cost function, (Section 3.2.3).

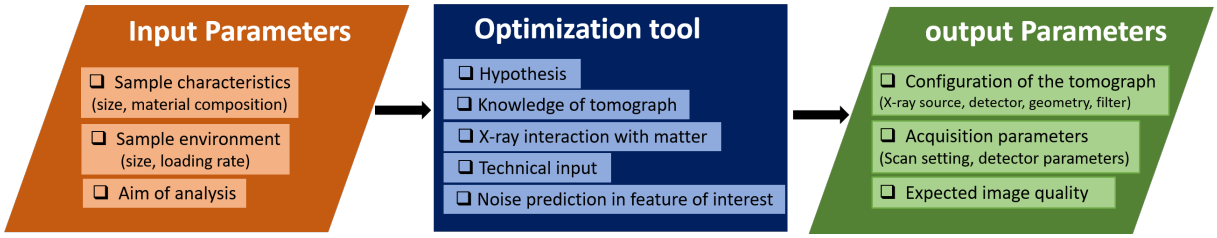

Figure 3.1: Overview of the optimization model.

3.2.1 Input parameters

The input parameters of the optimization model were chosen to correspond to the user's point of view about

- the nature of the sample (physical and chemical composition)
- the type of measurement (post-mortem, ex-situ, or in-situ)
- the aim of analysis (L1, L2, and L3).

This leads to define 5 main categories of the user-defined input parameters that are geometrical, absorption, temporal, and technical constraints and the aim of the analysis. These constraints also define the boundary conditions for the screening algorithm. Figure 3.2 shows these constraints along with their parameters used as an input for the screening model.

Geometrical constraints consist of the size of the sample and sample environment to be placed inside the tomograph and the size of the feature of interest to visualize.

Absorption constraints include the physical and chemical composition, density, and the representative volume fraction of the specimen.

Temporal constraints include the kinetic evolution of the features during the in-situ investigation and the total duration of the process. For steady-state scanning, interface velocity can be set to zero.

Technical constraints incorporate mechanical or system constraints such as minimum and maximum source-object-distance (sod) and source-detector distance (SDD). It also includes the detector characteristics such as the total number of horizontal and vertical pixels and the pixel pitch, and the limitation of the minimum and maximum exposure time.

Aim of analysis describes the objective of the tomographic study and is classified into three levels: L1: qualitative analysis, L2: low-level quantitative analysis, and L3: high-level quantitative analysis. Details about these analyses are previously presented in Chapter 1, Section (1.3.3).

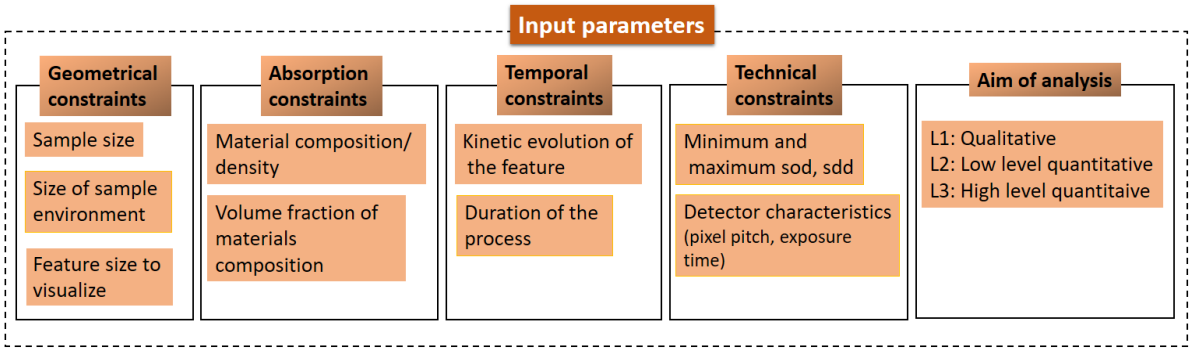

Figure 3.2: Overview of the input parameters for the optimization model.

3.2.2 Optimization tool development

This section introduces the development and the different modules of the optimization tool. The overview of the different parameters that are optimized in the optimization model and the technical inputs for the screening algorithm are presented in Figure 3.3.

The structure of the developed model consists of three modules: (i) modelling noise in feature of interest, (ii) X-ray absorption contrast simulation, and (iii) screening algorithm. The hypotheses used in these modules are presented in Section (3.2.2.1).

Initially, a noise model detailed in Section (3.2.2.2) was developed that estimates the weighted average error in the segmented volume of the feature size. It considers the feature to be spherical. Different model grayscale spheres of varying radius were generated, and statistical computations were performed to compute the weighted average error.

Section (3.2.2.3) describes the procedure to simulate the X-ray absorption spectrum for the computation of contrast in the output image. It includes the generation of X-ray polychromatic spectrum, the interaction with the object and the computation of output integrated transmitted intensity towards the detector pixel. This integrated transmitted intensity towards the detector pixel is used to compute the contrast in the output image. The detector response is not included in the model.

Section (3.2.2.4) details the screening algorithm that loops over the whole parameter space and computes the possible scanning configurations based on the technical inputs. For each configuration, it estimates the image quality in the sense of weighted average error in the segmented volume of the FOI using the noise model taking into account the image contrast, resolution, noise and the motion of the FOI. After a cost function is used based on the aim of analysis to select the optimal configuration.

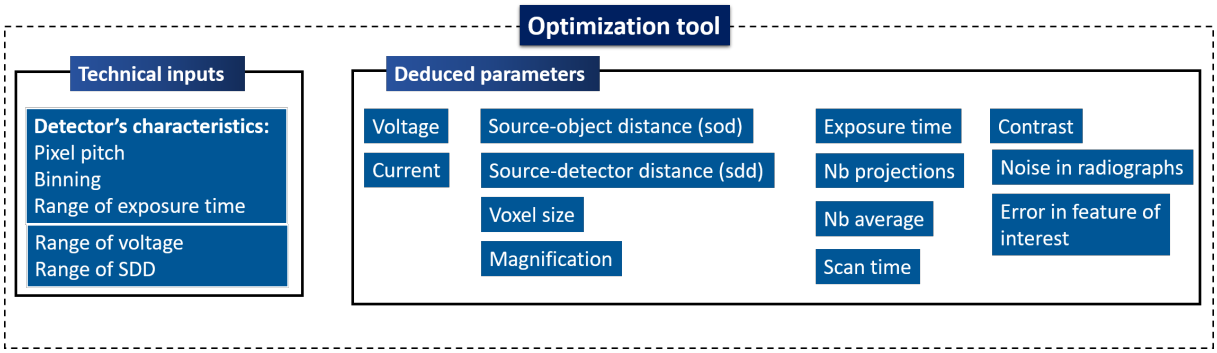

Figure 3.3: Overview of the optimized parameters and technical input to the optimization model.

3.2.2.1 Hypothesis

The hypotheses used in the different modules of the optimization tool are listed below.

- The criteria for the optimization is based on the estimation of weighted average error in the segmented volume of the feature size in the reconstructed dataset.

- The feature of interest (FOI) is considered spherical, so 3D simulated spheres were used to perform statistical computations for the estimation of weighted average error in the thresholded volume.
- For the computation of weighted average error, threshold is defined as the mean gray value of two phases. Considering $\bar{I}_{background}$ and $\bar{I}_{sample}$ being the intensity in the background and sample with grayscale value 0 and 255, respectively, the defined threshold is at 128.
- The predicted noise on the radiographs is used for the computation of weighted average error on the reconstructed datasets. No additional noise regarding the reconstruction algorithm is added.
- For the computation of the image contrast, the transmitted intensity towards the detector pixel was used. The detector response is not accounted for in the model.

3.2.2.2 Noise model (Modelling noise in feature of interest)

The purpose of the noise model is to estimate the weighted average error in the segmented volume of the feature size based on the global image noise. The feature size is considered a sphere and is represented by 3D simulated grayscale sphere of varying radius ranging from 1 to 10 pixels. Moreover, the motion is induced in the spheres ranging from 1 to 10 pixels to incorporate the motion blurring artifacts that occurs during the dynamic acquisitions performed at an insufficient temporal resolution.

The image noise is represented by Gaussian standard deviation. Probability density and chi-squared distribution computations were performed to get the cumulative distribution curve of thresholded voxels for a given radius sphere based on the global image noise using the threshold value of 128. From this distribution curve, the weighted average error is estimated using the volume of an ideal sphere as a reference. This operation is detailed in this section.

3.2.2.2.1 Sphere's generation

A 3D grayscale image of a sphere is made of three types of voxels: full voxels that are wholly inside the sphere, empty voxels that are wholly outside the sphere, and intermediate voxels that are on the boundary of the two.

For the generation of 3D grayscale spheres, a script was built that takes as an input the size of the image, the size of the sphere in terms of radius, and the central position of the sphere within the image. Initially, 3D 8-bit binarized spheres with ten times larger radius were generated centered on the center of the image. Binarized spheres were then down-scaled by averaging to convert into the grayscale values. Full voxels and empty voxels were assigned the values 255 and 0, respectively. Gray values of the intermediate voxels varies between 0 to 255. For gray value 0, only the voxels that touch the boundary of the sphere were taken into account. Using this operation, series of the spheres with radii varying from 1 to 10 pixels and their corresponding histograms representing the number of voxels for each gray level were generated.

Figure 3.4(a) shows the central slice of grayscale sphere of radius 7-pixel highlighting the full, empty and intermediate pixels. The corresponding histogram of the 3D sphere, Figure

3.4(b), represents the gray levels and the number of times they occur in the sphere. It can be noted that the histogram contains a large number of full voxels with gray value 255.

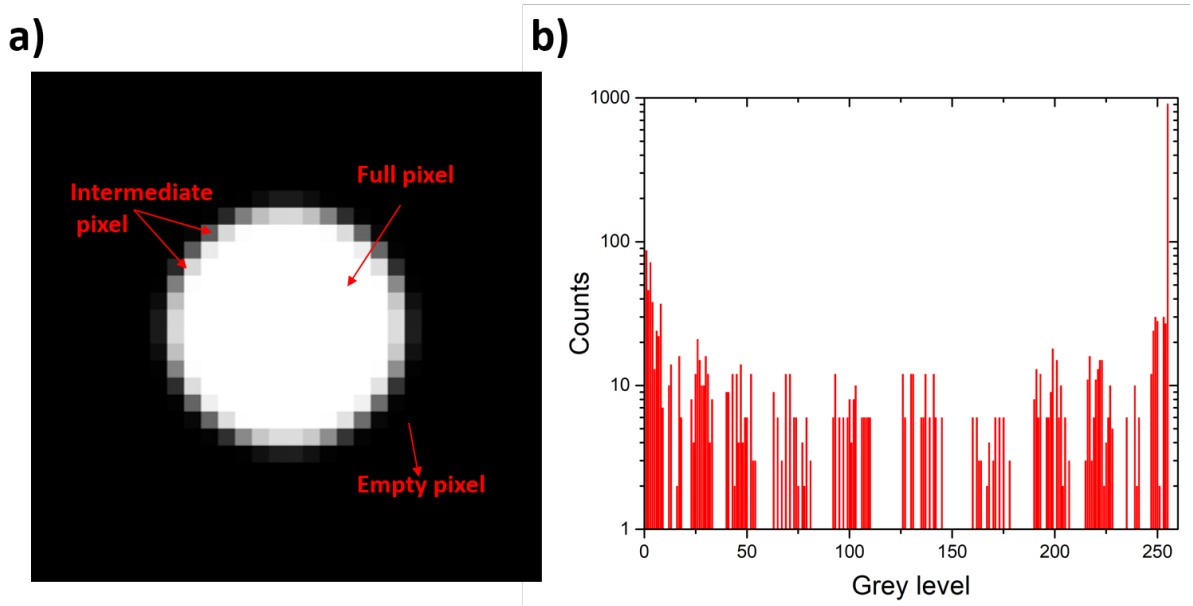

Figure 3.4: (a) The central slice of the grayscale sphere of radius 7-pixel highlighting different types of pixels present in it and (b) the corresponding histogram of the 3D volume. For gray level 0, only the voxels touching the boundary of the sphere were taken into account.

Motion incorporation

To incorporate the motion of the feature of interest that usually occurs during the dynamic acquisitions and results in blurring, series of spheres of a specific radius were generated by varying their x-directional central position according to the intended pixel motion and then averaged together to simulate a single motion-induced sphere. A motion-induced sphere has more intermediate gray value voxels at the boundary representing blurring and less full voxels at the center. For each radius, spheres with motion ranging from one to ten pixels were generated.

Figure 3.5(a and b) shows the central slice of the 7-pixel radius sphere with 3-pixel motion and the corresponding histogram, respectively. It can be noted that with the motion of 3 pixels, more intermediate grey voxels, and fewer full voxels exist in the histogram than without motion, as presented in Figure 3.4(b). Similarly, the central slice of 7-pixel radius sphere with 7-pixel motion is shown in Figure 3.5(c and d), and even more intermediate voxels and fewer full voxels can be observed in the grayscale image and in the histogram.

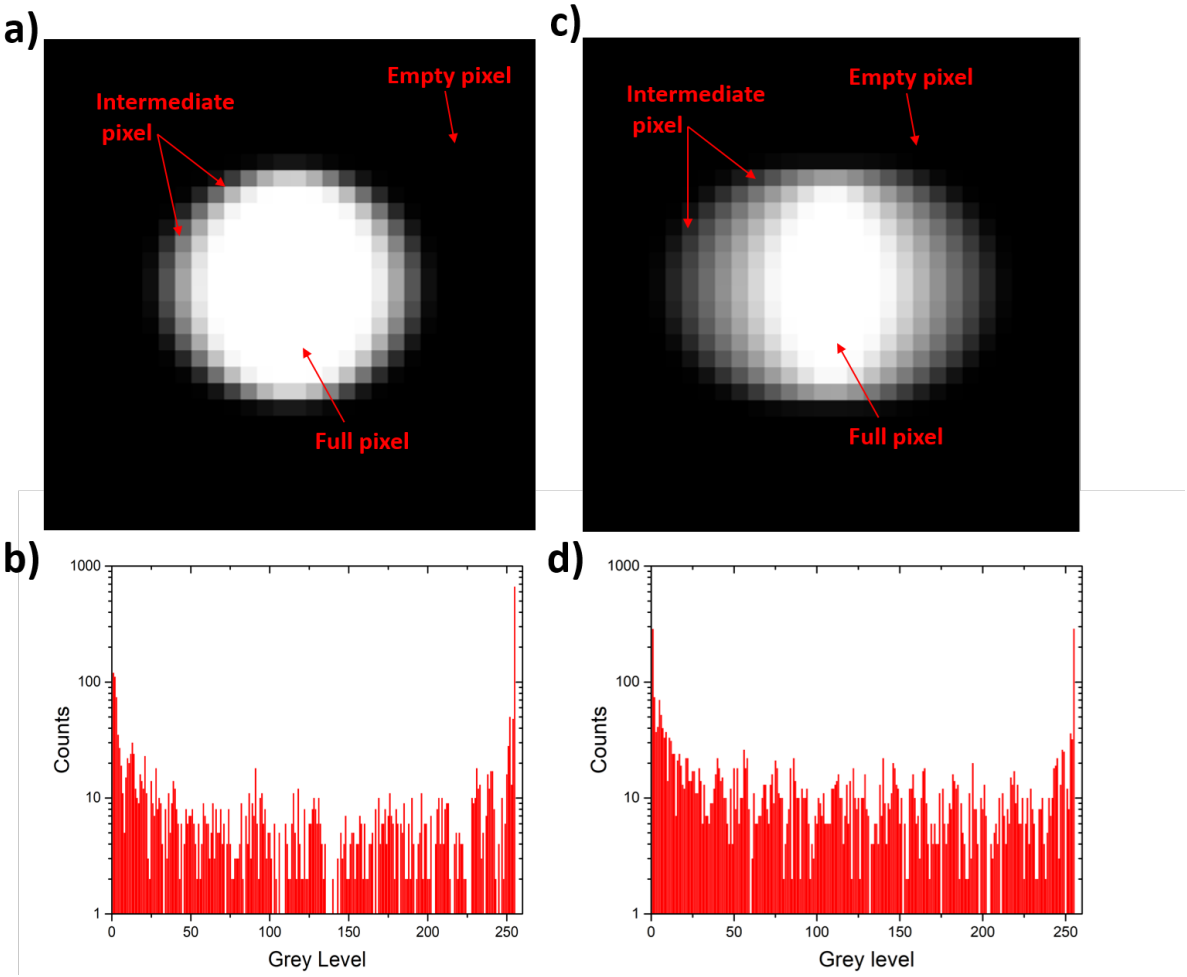

Figure 3.5: (a & b) The central slice of the grayscale sphere of radius 7 pixels with 3-pixel motion highlighting different types of pixels present in it and the corresponding histogram of the 3D volume. (c & d) The central slice of the 7-pixel radius sphere with 7-pixel compensated motion and the corresponding histogram of the 3D volume. For gray value 0, only the voxels touching the boundary of the sphere were taken into account.

3.2.2.2.2 Statistical computations

The histogram of the sphere was used as an input for the statistical computations. The purpose of the statistical computations was to determine the global probability distribution curve of the thresholded voxels present in the 3D sphere. For this purpose, an estimation of the gray level distribution of a sample of voxels was done from which the global distribution of the number of thresholded voxels was computed.

The probability of each single gray level (sample) present in the histogram of the sphere to be thresholded (i.e., assigned a gray value higher than 128) was estimated using the three-step statistical computations operation. This three-step operation is illustrated in Figure 3.6 and is explained below. For the demonstration of these steps, a single gray level $\mu = 180$ with count n = 9, in the radius-7 3D grayscale sphere is considered.

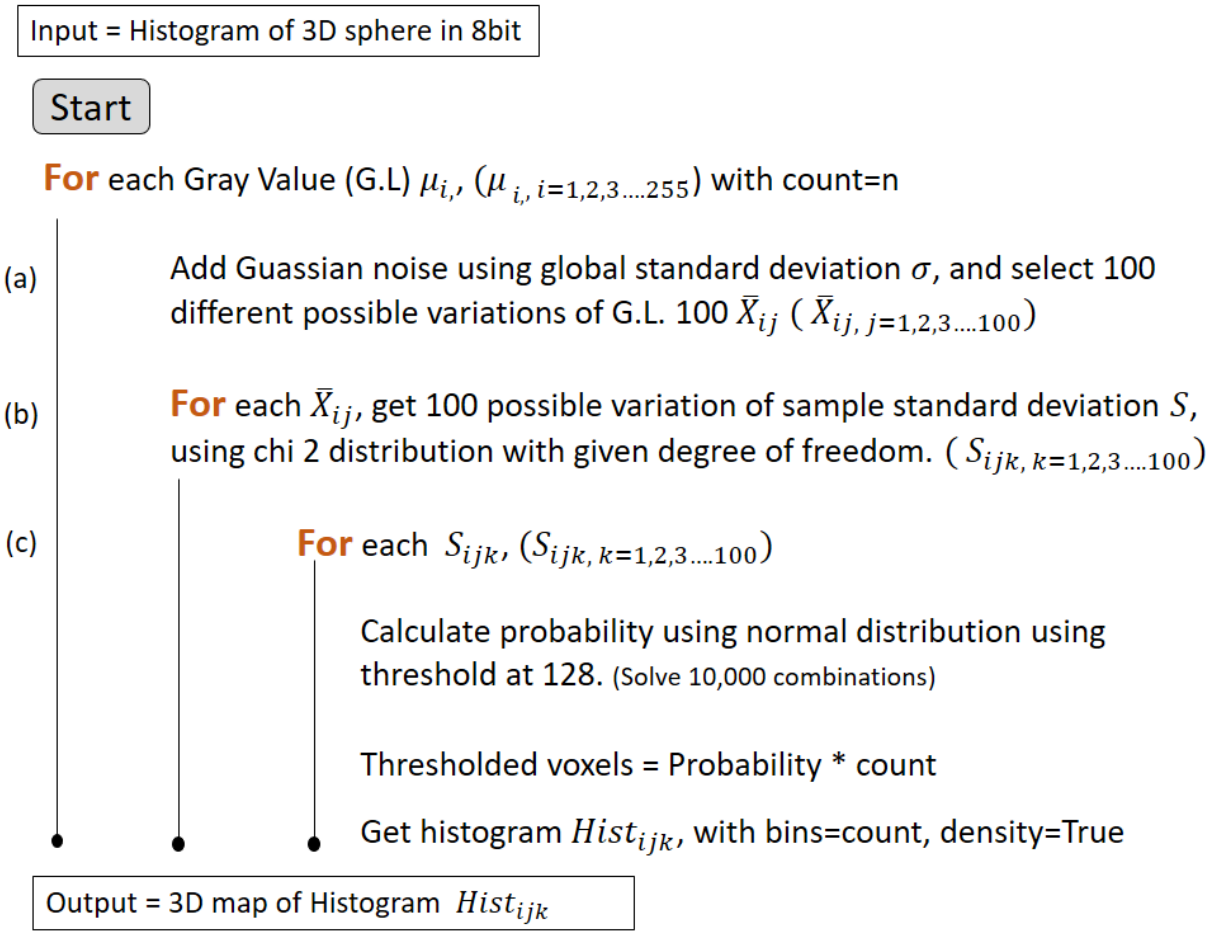

Figure 3.6: Flowchart showing how the probability distribution histogram of a single gray value voxel, present in the 3D sphere, is obtained.

First step: Initially, each gray level in the histogram was statistically noised by a Gaussian noise to get the different variations of the mean gray level. A Gaussian noise is a statistical noise that has a probability density function (PDF) equal to the normal distribution. The PDF of a Gaussian random variable x is given as

$$f(x) = \frac{1}{\sigma\sqrt{2\pi}} e^{-\frac{1}{2}(\frac{x-\mu}{\sigma})^2} \tag{3.1}$$

where x and μ represent the gray level and the mean gray level, respectively, and σ represents the standard deviation. From the distribution curve of a given gray level for a global standard deviation, hundred different equally spaced possible variations of the mean grey value were selected, Figure 3.6(a). Figure 3.7(a & b) shows the probability density distribution (PDF) and commutative density distribution (CDF) curves for a gray value $\mu = 180$ and count n = 9, using global noise $\sigma = 20$.

Second step: In the second step, the possible variations of the global standard deviation were computed by plotting the chi-squared χ^2 distribution with a degree of freedom k, using sample standard deviation S. The PDF of the χ^2 distribution of random variable x with k degree of freedom is given as

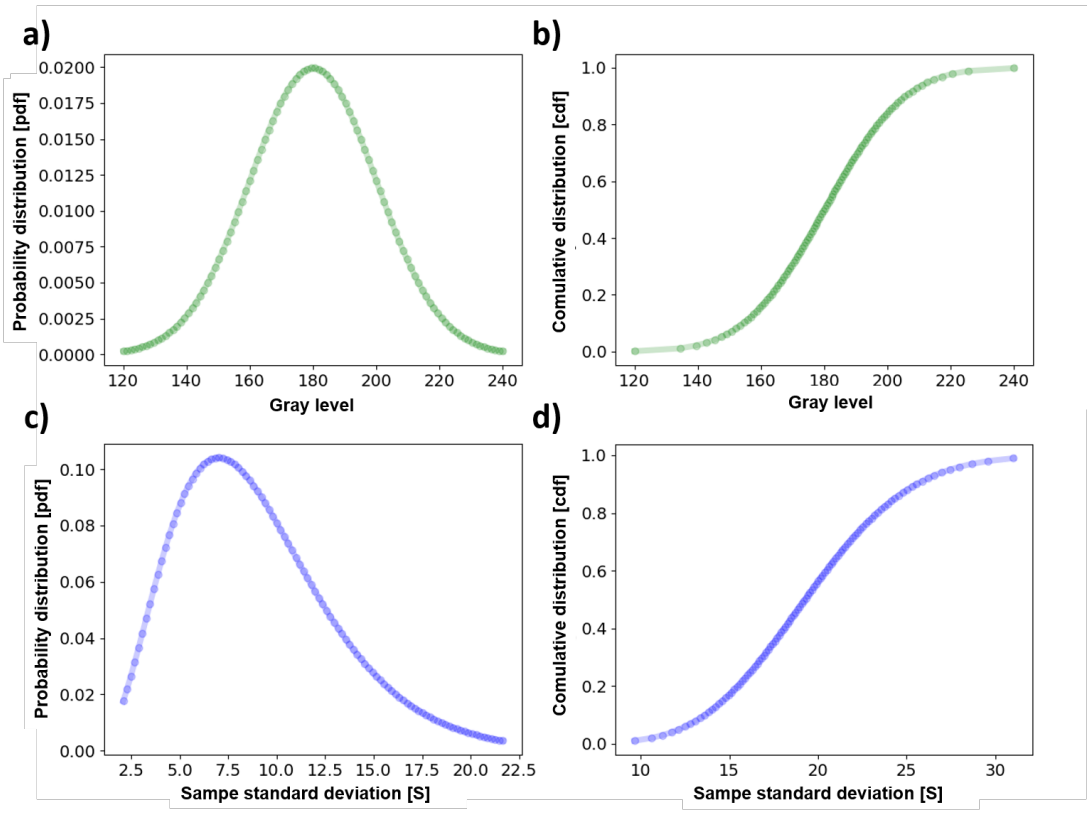

Figure 3.7: The probability density distribution and cumulative density distribution curves for single gray level with gray value $\mu = 180$ which occurs nine times in the image, count n = 9, using global $\sigma = 20$ using (a & b) normal distribution, (c & d) chi-squared distribution with degree of freedom 8 (DF=n=9-1) using sample standard deviation S.

$$f(x) = \frac{1}{2^{k/2}\Gamma(k/2)} x^{k/2-1} e^{-x/2} \tag{3.2}$$

where Γ represents the Gamma function. The degree of freedom k is linked to the sample size n, that is in our case, using the following relationship

$$DF = k = n - 1 \tag{3.3}$$

The global image noise (global standard deviation) σ can be linked with the sample standard deviation S as, Eq. 3.4, where χ^2 is the chi-squared value.

$$\chi^2 = \frac{(n-1)S^2}{\sigma^2} \tag{3.4}$$

From the distribution curve, hundred different equally spaced sample standard deviation S values were selected, Figure 3.6(b). Figure 3.7(c & d) shows the PDF and CDF curves of chi-squared distribution for degree of freedom k=9-1=8, using sample standard deviation S.

Third step: After selecting the hundred different possible variations of mean gray level and sample standard deviation, the probability of thresholded voxels was calculated using the normal distribution. The cut-off threshold was set to 128, and all possible 10,000, combinations

were computed. Figure 3.6(c) shows the iterative loop for the computation. The output of this operation is the histogram of the probability of the thresholded voxels with bins equal to the total count of the gray level (which in the current example is 9).

Figure 3.8 shows the probability distribution histogram of the thresholded voxels for gray level $\mu = 180$, with count n=9, at different values of the global noise level. It can be noted that, at noise=20, there is more than 90% probability that all nine voxels will be thresholded. But as the noise increases to 50 and 70, Figure 3.8(b & c), the probability of thresholding all nine voxels starts to decrease (42% at noise = 50 and 32% at noise =70) while the probability to threshold fewer voxels increases.

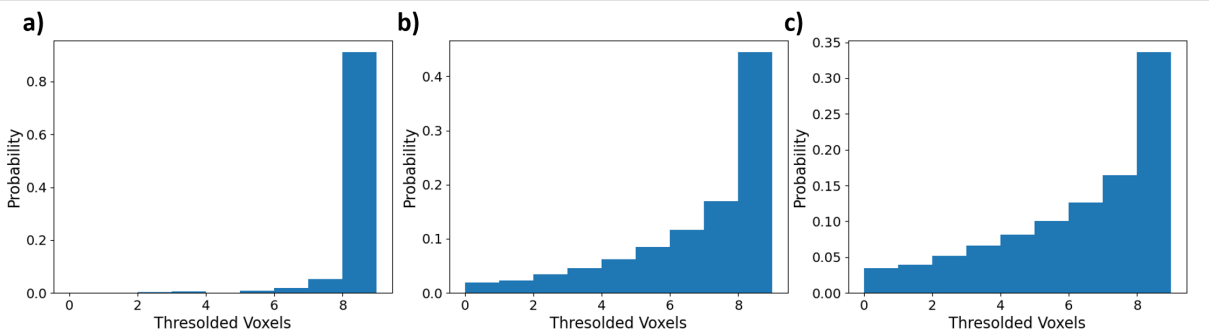

Figure 3.8: Probability of thresholded voxels for gray level 180 with count=9 at (a) noise =20 (b) noise=50 (c) noise=70.

This three-step operation to compute the probability distribution histogram was repeated for all 255 gray levels present in the histogram of the sphere to get the 255 different probability distribution histograms. The total bins of a histogram of a specific gray level is equal to the count of the gray level. After the resultant histogram combining all 255 histograms was computed by sequencing addition of all histograms.

Figure 3.9(a) shows the flowchart illustrating the iterative operation to compute the resultant histogram by combining all 255 histograms, while Figure 3.9(b) shows the procedure of obtaining the cumulative of two histograms, and this procedure is used iteratively to get the resultant of all 255 histograms.

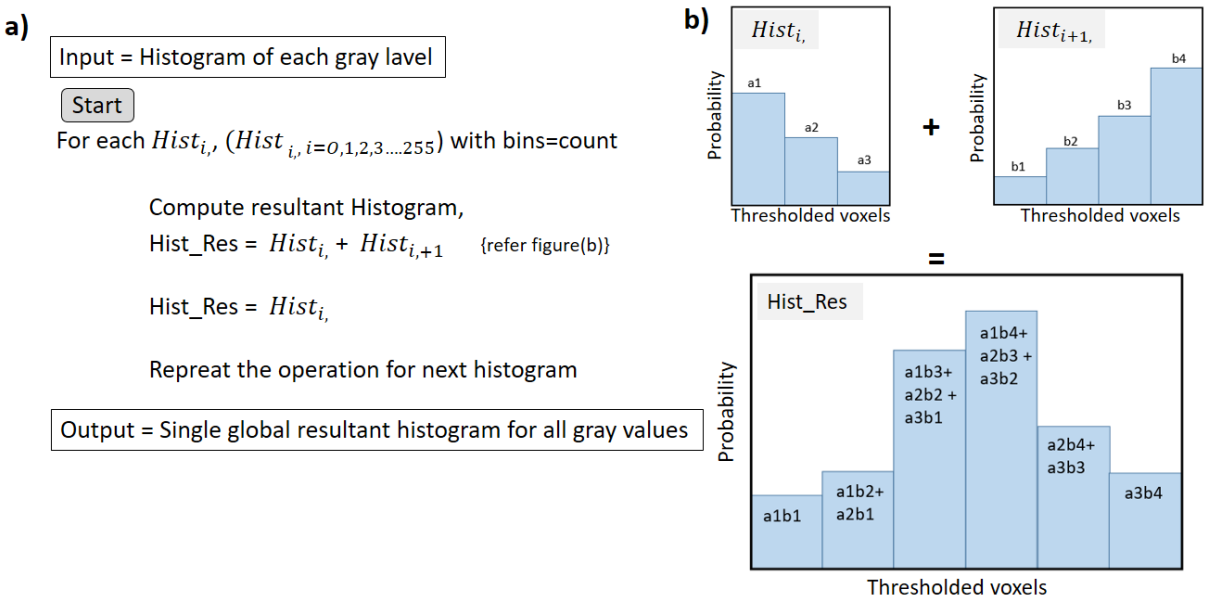

Figure 3.9: (a) Flowchart showing the procedure to obtain the cumulative histogram combining all 255 histograms. (b) Illustration of how two histograms can be combined together to get the resultant histogram.

Figure 3.10 shows the resultant probability distribution curve as a function of thresholded voxels after the iterative summation operation for a sphere of radius 7 at different global noise value. Total of 3147 voxels are present in the 3D simulated grayscale sphere of radius 7 pixels having gray levels ranging from 0 to 255 with 1450 voxels having gray levels higher than 128, which was set as a threshold value. At global noise=20, Figure 3.10(a), the probability to threshold high number of voxels close to the actual volume is higher with very little curve dispersion. But as the noise value increases to 50 and 70, Figure 3.10(b & c), the shape of the curve starts to deviate more from the mean and the probability to threshold fewer and higher voxels increases as represented in the graph.

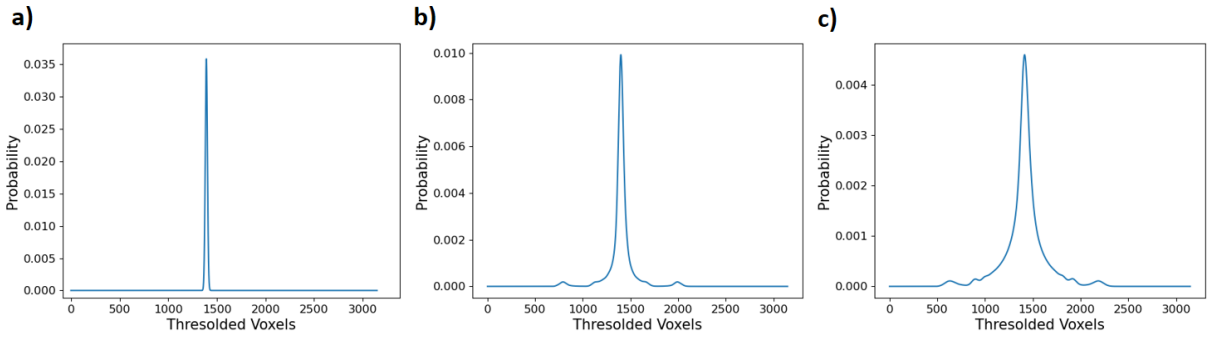

Figure 3.10: Resultant probability distribution curve of thresholded voxels for radius 7 sphere with (a) noise =20, (b) noise=50 (c) noise=70.

3.2.2.2.3 Error in the volume of feature of interest

To estimate the error, the relative change in the thresholded voxels, the x-axis of Figure 3.10, was computed using the volume of an ideal sphere as reference using the following expression, Eq. 3.5. The volume of an ideal sphere is given in Eq. 3.6.

$$Error_i = \frac{\text{Thresholded voxels - Ideal volume}}{\text{Ideal volume}} \tag{3.5}$$

$$\text{Ideal volume} = \frac{4}{3} * \pi r^3 \tag{3.6}$$

Figure 3.11 shows the resultant probability distribution curve as a function of error in the segmented volume of the radius 7 feature size. The horizontal axis of Figure 3.10 is just changed to the error (relative change in volume) and shows the different probabilities of error at different value of image noise.

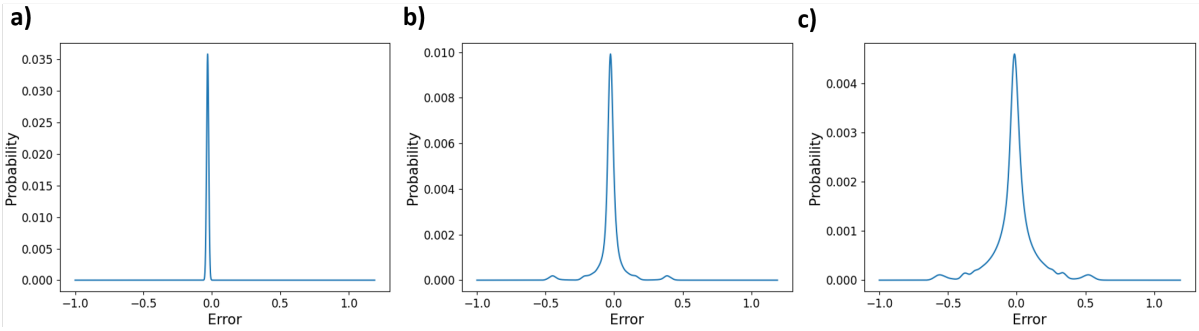

Figure 3.11: Resultant probability distribution as a function of estimated error for radius 7 sphere with (a) noise =20, (b) noise=50 (c) noise=70.

To estimate a single value of the error, the absolute weighted average error from the resultant probability distribution curve, Figure 3.11, was deduced using the Eq. 3.7 with $Error_W$ represents the absolute weighted average error.

$$Error_W = \left| \frac{\sum_{i=1}^{n} Probability_i Error_i}{\sum_{i=1}^{n} Probability_i} \right| \tag{3.7}$$

The weighted average error from the probability distribution curve, Figure 3.11, was calculated to be 3% at noise =20, 5.8% at noise =50, and 9.85% at noise =70. The standard deviation of the weighted average error was deduced as well.

This whole three-step statistical computations operation till the estimation of weighted average error was performed for all spheres of radius 1 to 10 pixel using different values of global image noise ranging from 1 to 200. The results are summarized in Figure 3.12, which presents the weighted average error as a function of image noise. Sphere radius is represented by different symbols of different colors. In the graph, Figure 3.12, we can observe that:

- The weighted average error in the segmented volume of the feature size increases as a function of the standard deviation. This is consistent with the general observation that the noisier the image, the worst precision of the quantification.
- Two regimes depending on the size of the feature can be seen. When the radius is larger or equal to 4 (diameter of at least 8-pixel sphere), the weighted average error remains less than 10% for the image noise smaller than 75. Moreover, the weighted average error remains limited to 20% for the radius equal and greater than 5 even at a higher value of

the standard deviation while for radius 4 it can reach up to 30%.

- For sphere radius smaller than 3 pixels, the weighted average error is significantly high even at the lower values of image noise, especially for radius 1 sphere. This is due to the presence of very few full voxels (255 gray level) in the sphere's 3D volume, leading to the measurement error. With the increase in noise, the weighted average error further increases in the segmented volume.
- This output curve from the noise model can be used to pre-estimate the image quality in terms of measurement error in the volume of a specific size of the feature based on the global image noise. Moreover, it can also help to estimate the number of pixels required in the diameter of the feature of interest according to the required measurement accuracy for estimated image noise.

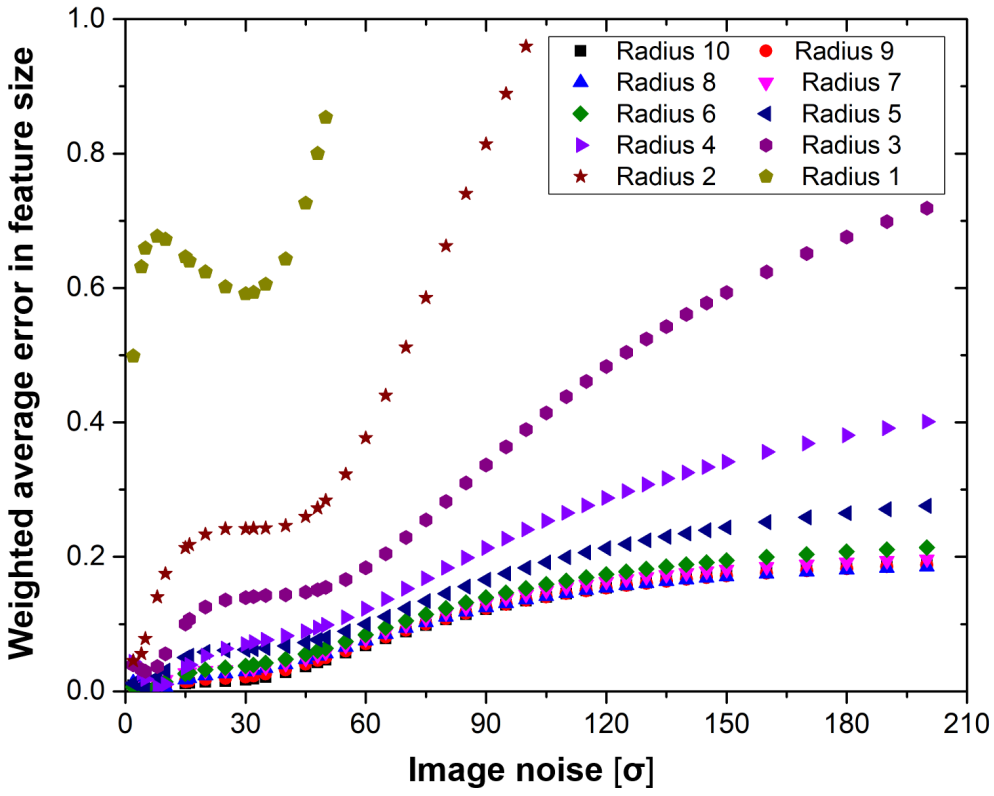

Figure 3.12: Weighted average error in the segmented volume of the feature of different radius sphere, centered on the central axis, as a function of global image noise.

Figure 3.13 presents the simulation results of the weighted average error as a function of image noise for the spheres of radius 7 with motion ranging from 1 to 10 pixels. Motion is represented by different symbols of different colors. It can be seen that for the radius 7 sphere, the weighted average error increases with the motion. Due to the presence of less number of full voxels (255 gray level) and more intermediate voxels (1 to 254 grey levels, more voxels in the below 128 grey level) in the 3D grayscale image of the sphere, with the increase in the motion the probability of thresholding number of voxels close to the actual volume of sphere decreases and the dispersion (standard deviation) of the cumulative probability distribution curve increases.

The dispersion of the curve continues to increase with the increase in global image noise and leads to the increase in weighted average error as can be seen in Figure 3.13.

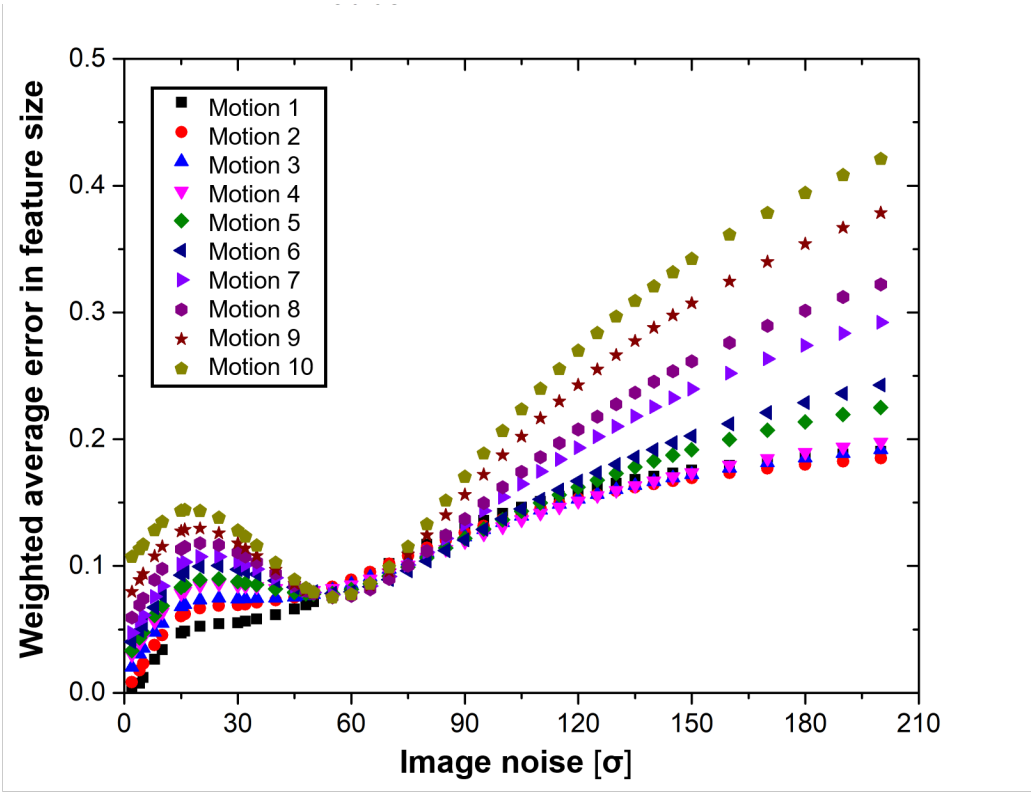

Figure 3.13: Weighted average error in feature size of radius 7 sphere simulated with motion ranging from 1 to 10 pixels as a function of the global image noise.

However, some artifacts can be seen in the curve mainly for larger motion-induced sphere, and with the increase in image noise, till the noise equal to 50, the weighted average error decreases. These artifacts simply come from the fact that without the noise, the discretization leads to an underestimation of the sphere volume (more voxels with gray level below 128). Since we use saturated values (0 and 255), an addition of noise can only increase the sphere volume and thus reduce the weighted average error.

To further understand this initial decrease, the cumulative probability distribution curve as a function of error for the radius 7-pixel sphere with 7-pixel motion simulated using different values of image noise is presented in Figure 3.14. It can be seen that at noise=20, Figure 3.14(a), the dispersion (standard deviation) of the curve is small and the computed weighted average error is 0.10. At noise=50, Figure 3.14(a), the computed weighted average error decreases to 0.08 which shows a decrease of 25%. Although the dispersion of the curve increases but there is a small probability to have a high value of error close to 0.5 which causes the decrease in the weighted average error. Whereas, at noise=90 the dispersion of the curve is increasing uniformly till the high value of error, and this causes the correct estimation of weighted average error of 0.132.

It can be noted that at noise=50 and noise=90, the dispersion of the curve only increases towards the right; this is due to the presence of a large number of intermediate voxels with gray values less than 128 in the 3D grayscale images of the sphere. With the increase in noise,

the probability to threshold these lower gray value voxels increase leading to the overestimation of the thresholded volume.

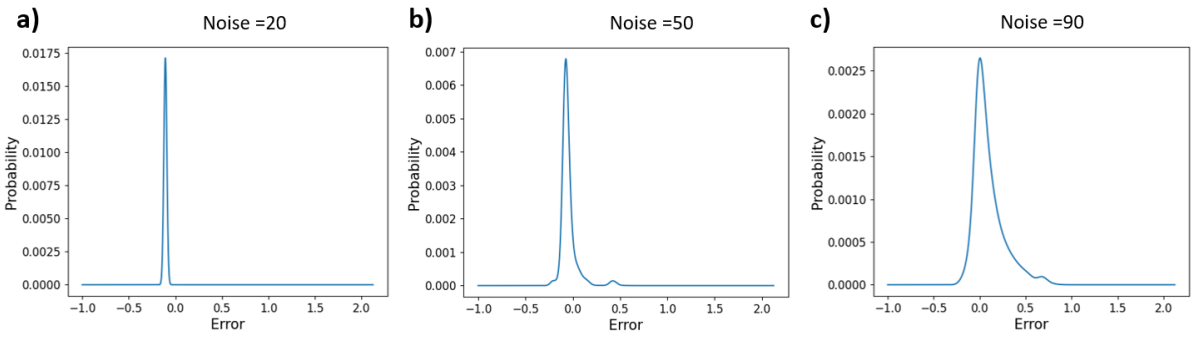

Figure 3.14: Cumulative probability distribution as a function of estimated error for radius 7 sphere with 7 pixel motion at (a) noise =20, (b) noise=50 (c) noise=90.

The standard deviation of the weighted average error in Figure 3.13 for radius 7 spheres with varying motion is presented in Figure 3.15. It can be seen that even with the decrease in weighted average error with the initial increase in image noise, the standard deviation of the weighted average error increases.

Three different regimes of the increase in standard deviation of the weighted average error can be seen in the curve. (i) an linear increase in the standard deviation till noise = 25. (ii) a sharp increase in the standard deviation from noise = 25 till noise = 90. (iii) a slow increase in the standard deviation after noise = 90. Moreover, the standard deviation of the weighted average error is relatively larger for a high value of image noise indicating the more spread or variation in weighted average error.

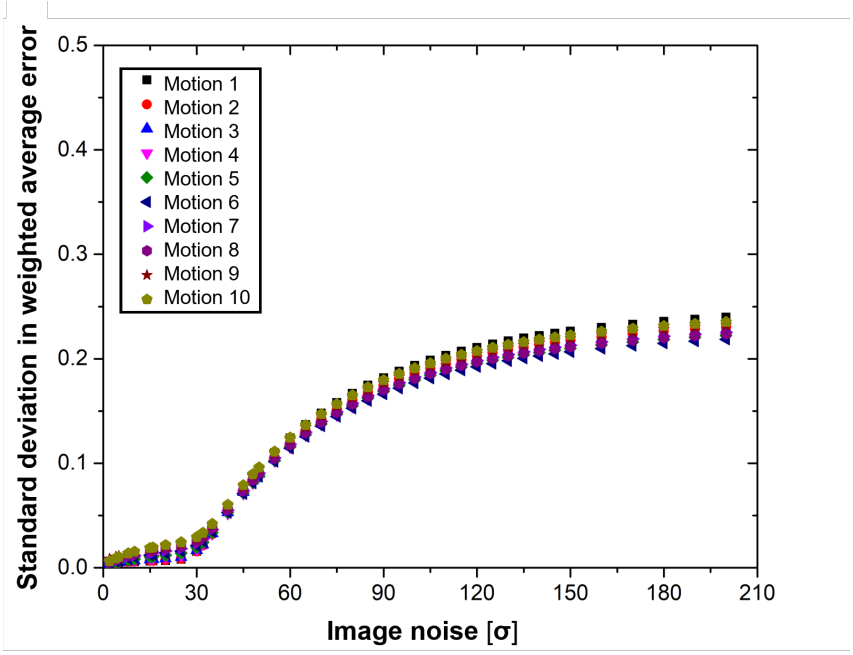

Figure 3.15: Standard deviation in weighted average error in feature size of radius 7 sphere with motion ranging from 1 to 10 pixels as a function of the global image noise.

3.2.2.3 X-ray absorption simulation

As mentioned in Chapter 1, the contrast of an image is an important parameter for the image quality. X-ray absorption spectrum was simulated in order to compute the image contrast. The output transmitted intensity after passing from the specimen towards the detector pixel is used for the estimation of the contrast. The computation of contrast involves three steps: first is to simulate X-ray tube spectra, second is the calculation of X-ray mass attenuation coefficient for a given specimen and third is the computation of the integrated transmitted intensity on the detector pixel by Beer Lambert's law.

A model AlCu specimen of 2mm diameter consisting of 95% Al matrix and 5% Cu inclusion is considered for the demonstration.

3.2.2.3.1 X-ray polychromatic spectrum simulation

X-ray tube spectra was simulated using SpekPy [Poludniowski et al., 2021] which is an open-source toolkit for modelling polychromatic X-ray spectra and allows the calculation of X-ray polychromatic spectra consisting of bremsstrahlung and characteristic radiation. The selectable parameters for SpekPy are (i) target material, (ii) anode angle, (iii) accelerating voltage, (iv) source-detection distance, and (v) anode current. Furthermore, the shape of the X-ray spectra can be modified by adding any filtering of arbitrary material of arbitrary thickness.

Figure 3.16 shows the emitted X-ray spectra from the tungsten W target at an anode angle of 43 degree with a source to detection distance of 100 cm using 1 mAs current at different acceleration voltages. No filtering material was used to modify the spectrum and the mean energy at each voltage is listed in caption. It can be noted that both voltage and mean energy of the spectrum are linked to each other meaning that with the increase in applied acceleration voltage the mean energy of the spectrum increases. The peaks correspond to the characteristic radiation and the continuous part of the spectrum represents the Bremsstrahlung radiation.

Figure 3.17 shows the emitted spectrum with same conditions but using of 1 mm Aluminium (Al) filter, Figure 3.17(a), and 1 mm Copper (Cu) filter, Figure 3.17(b). A filter is typically used to pre-harden the X-ray emission spectrum to prevent artifacts due to the low-energy photons in CT scans. By comparing these different spectrum, it can be noticed that a 1 mm Al or Cu filter completely absorbs photons below 18 and 40 keV, respectively. Also the intensity of photons in the energy range of 18 to 130 keV for Al and 40–130 keV for Cu is heavily reduced as well. The use of filters also influences the mean energy of the spectrum which is also largely responsible for the image contrast; the lower the mean energy the better the contrast. But at the same time the exposure time and the power should be adequate to have a reasonable SNR in the images.

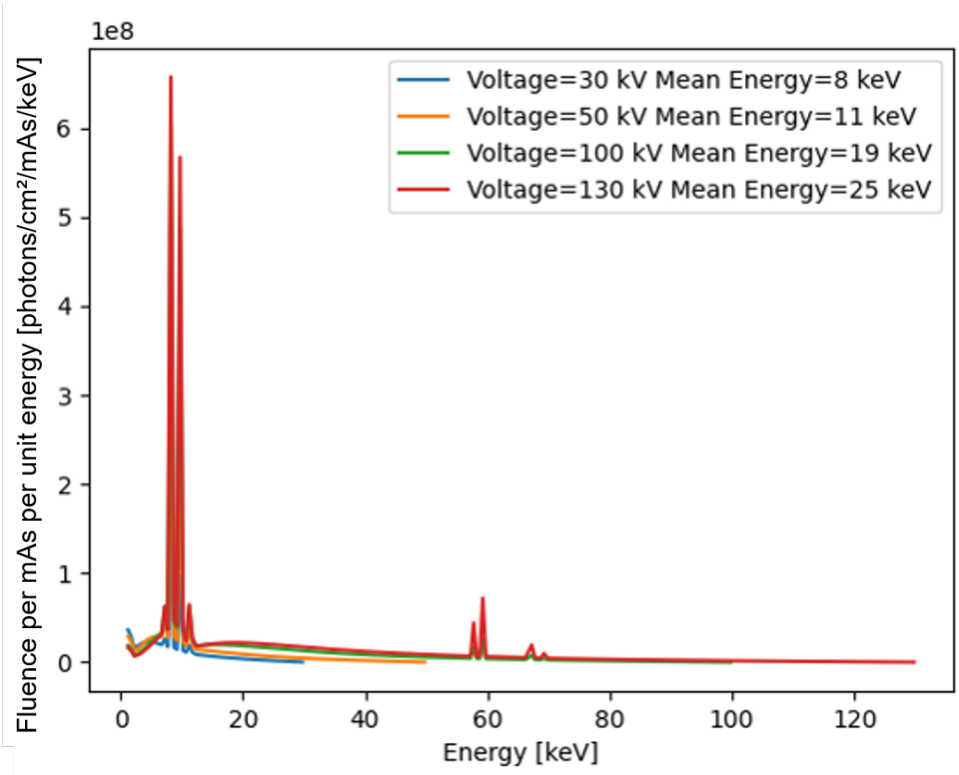

Figure 3.16: Simulations of emitted X-ray spectra from the tungsten W target at anode angle of 43 degree at 100 cm detector distance and 1 mAs current at different acceleration voltages. The bin width for the calculations is 0.5 keV.

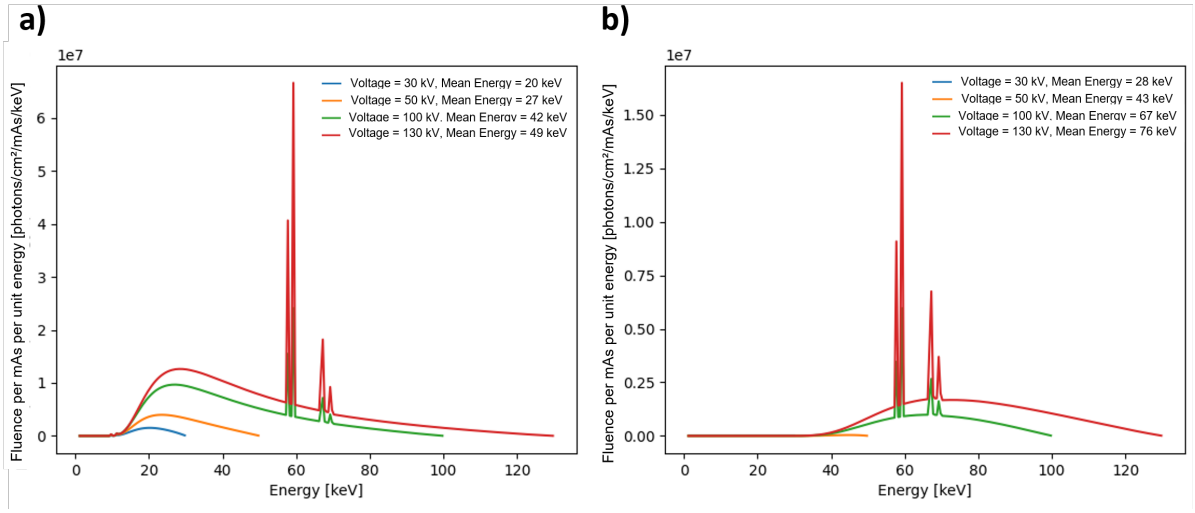

Figure 3.17: Simulations of emitted X-ray spectra from the tungsten W target at anode angle of 43 degree at 100 cm detector distance and 1 mAs current using different acceleration voltages using 1mm (a) Al filter (b) Cu filter. The bin width for the calculations is 0.5 keV.

3.2.2.3.2 X-ray mass attenuation coefficient

X-ray mass attenuation coefficient μ/ρ, for different materials was tabulated using the XrayDB python library, which uses the database from [Elam et al., 2002]. For the X-ray energies up to 150 keV, the photoelectric effect is the dominant process that causes the X-ray attenuation, thus X-ray mass attenuation coefficient μ/ρ strongly depends on the element's atomic number

and on the X-ray energy. In addition to these, sharp increases, so-called K-edges, will be seen at the energy level just beyond the binding energy of the k-shell electrons of the absorbing atom.

The required parameters for the XrayDB function to calculate the mass attenuation coefficient are the energy range and the atomic symbol of the element. Moreover, calculation of mass attenuation coefficient for multi-element material can also be done by using the chemical formula of the material, it's density and the energy range. Figure 3.18 shows the X-ray mass attenuation coefficient for Al and Cu with K-edge effect visible at the binding energy. The K-edge of Al and Cu is at 1.56 keV and 8.97 keV, respectively.

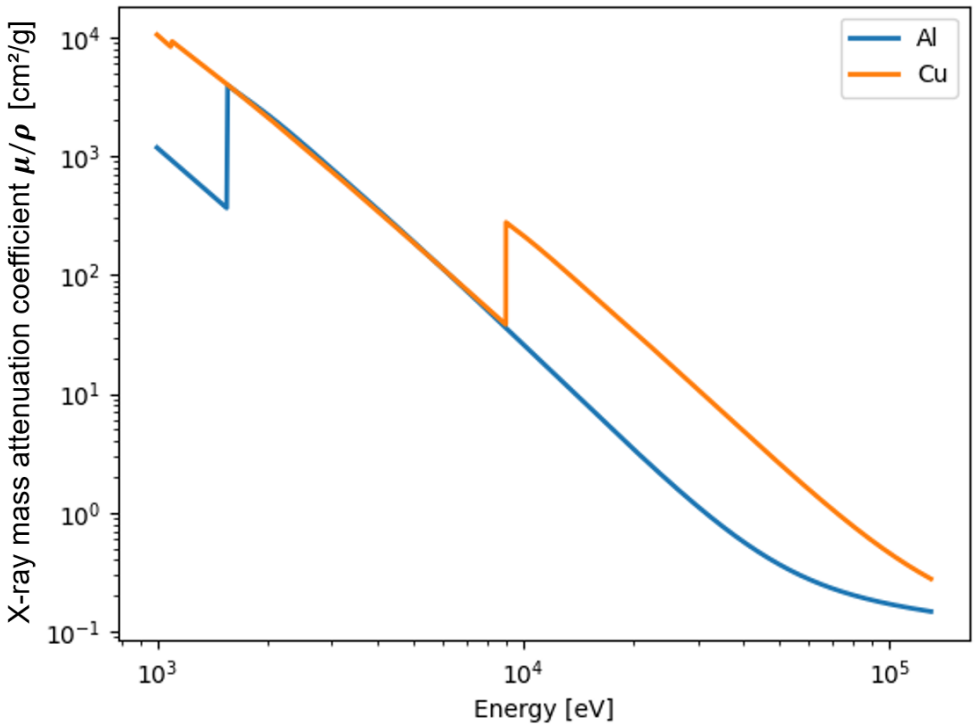

Figure 3.18: X-ray mass attenuation coefficient μ/ρ, for Al and Cu over range of X-ray photons energy. The bin width for the calculations is 0.5 keV.

3.2.2.3.3 Integrated intensity and contrast computation

As described earlier in, Chapter 1 (Section 1.2.2), the X-ray absorption along a ray path from the source, after passing through an heterogeneous material towards a detector pixel can be described by Beer-Lambert law for polychromatic radiation, Eq. 3.8. Along the X-ray path, different materials contribute to the absorption depending on their mass attenuation coefficient and penetration lengths.

$$I(d) = \int_0^E I(0,E).e^{-\int_0^d \mu(E,s)ds} dE \tag{3.8}$$

Where I is the intensity of the beam before passing through the specimen and $I(d)$ the transmitted intensity after passing through the specimen, μ is the coefficient of the linear absorption and is material dependent, and s is the thickness of materials composing the specimen.

To compute the output transmitted intensity $I(d)$, towards a detector pixel after pass-

ing through 95-5% AlCu specimen, the emitted X-ray tube spectra, Figure 3.16, and X-ray mass attenuation coefficient, Figure 3.18, were integrated using, Eq. 3.8, by taking into account the penetration lengths of both Al and Cu that are 1.9 mm and 0.1 mm respectively.

Figure 3.19(a) shows the resultant integrated transmitted intensity $I(d)$, after passing from model specimens over range of voltage 30-130kV. Blue curve represents the 95-5% AlCu specimen with thickness 1.9 mm and 0.1 mm and black curve represents the 100% Al specimen of 2 mm thickness. It can be seen that number of photons per unit area on the detector pixel increases with the voltage and its higher for a less absorbing specimen (100% Al). The presence of 5% Cu which is a high absorbing element, in the blue curve, decrease the transmitted flux. Figure 3.19(b) displays the normalized intensity for the same model specimens after dividing it by background intensity. Background intensity was computed by integrating only the first part of the Eq. 3.8 without considering the specimen.

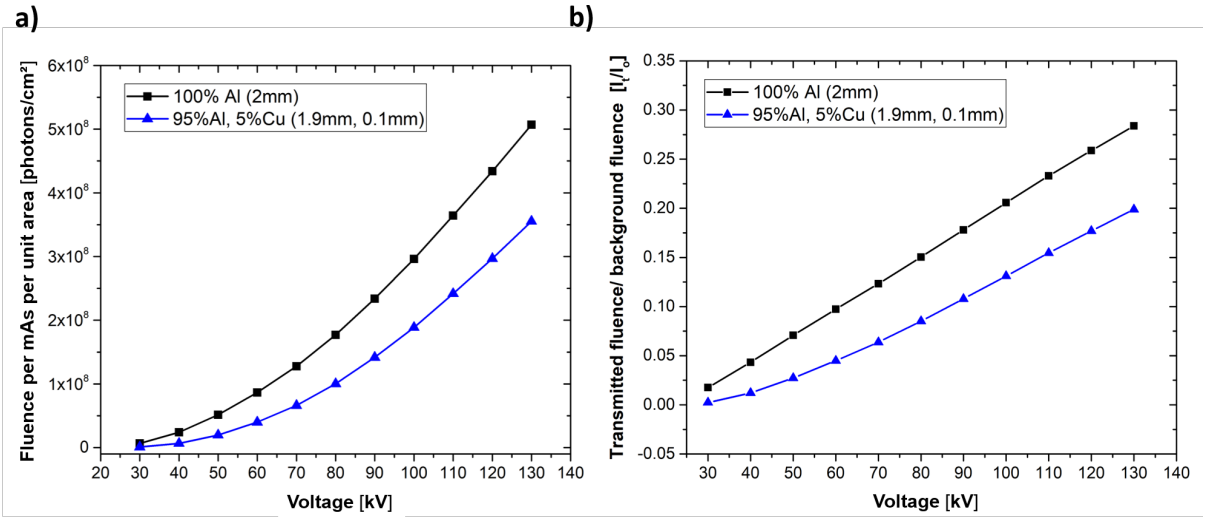

Figure 3.19: Integrated X-ray spectra, using Eq. 3.5, after passing from 100% Al, and 95-5% AlCu model specimens without any filter over range of voltage 30-130kV. (a) Total photon fluence per unit area, (b) Transmitted fluence normalized by background fluence.

From this transmitted intensity curve, the contrast C, can be computed by using the following equation, Eq. 3.9, where $I(d)_{Al}$ and $I(d)_{AlCu}$ correspond to the transmitted intensity after passing from 100% Al specimen and 95-5% AlCu specimen at a given acceleration voltage.

$$C = \frac{I(d)_{Al} - I(d)_{AlCu}}{I(d)_{Al} + I(d)_{AlCu}} \tag{3.9}$$

Figure 3.20 shows the integrated intensity for the 95-5% AlCu model specimen and the corresponding contrast over range of voltages. As expected the contrast starts to decrease as the acceleration voltage increases. The higher contrast resulted with the low voltage values but at the same time the photon flux is significantly low which will result in poor SNR and brightness in the images. At higher voltage the mean energy of the spectrum increases leading to the decrease in contrast. So a trade-off between the output image contrast and brightness is made for the selection of optimal source parameters. For the homogeneous specimen, the contrast can be computed by taking the intensity difference using the background transmitted intensity $I(d)_{background}$ as the reference value.

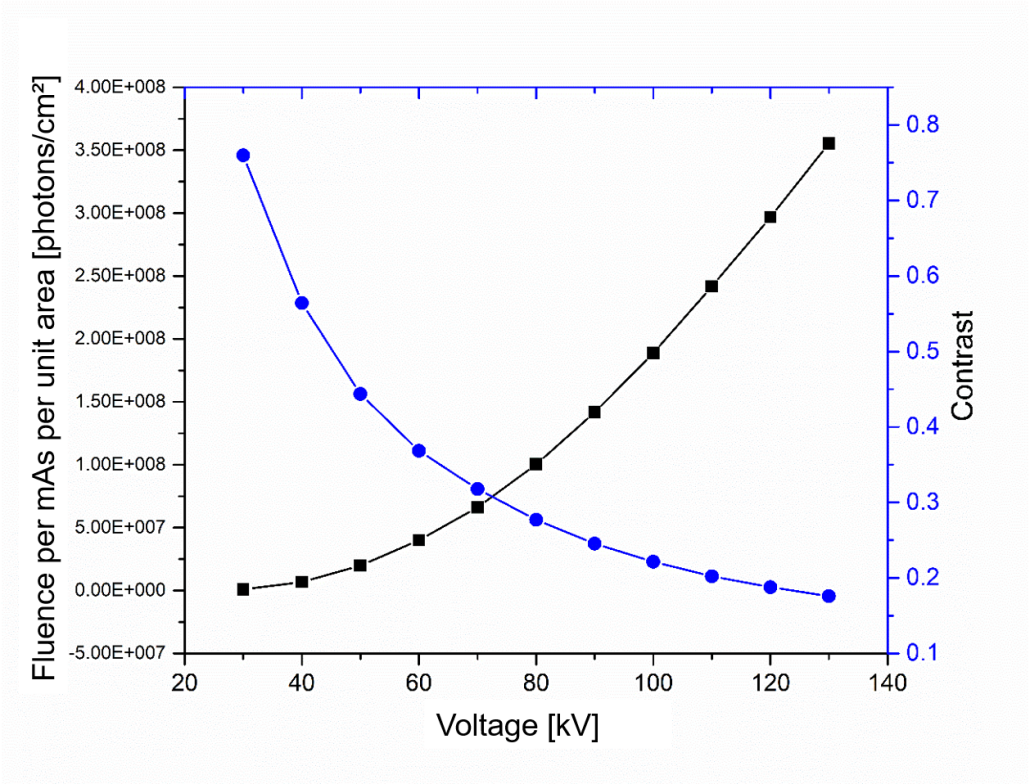

Figure 3.20: Integrated X-ray spectra, using Eq. 3.5, after passing from 95-5% AlCu specimen and corresponding contrast without any filter over range of voltage 30-130kV.

Figure 3.21 shows the integrated intensity after passing from the 95-5% AlCu model specimen and by using different filtering materials of 1 mm thickness over the range of voltages. The effect of the different filtering materials on the transmitted spectrum is clearly visible, the total number of photons per unit area significantly reduced as we use the filter of higher atomic number with higher absorption power. With the increase in the thickness of the filters, the photon flux is further reduced.

The purpose of this X-ray absorption simulation in the optimization model is to compute the contrast and the photon flux in the output image for a given specimen specifications (thickness and constituent materials) and for a given acceleration voltage.
The suitable voltage depending on the required contrast in the output image need to be selected for a given CT scan. Filter can be placed on the X-ray tube to modify the generated spectrum. The combination of voltage, current and filter affects the total photon flux and the mean energy of the spectrum for a given exposure time, which contributes to the source noise in the recorded radiographs.

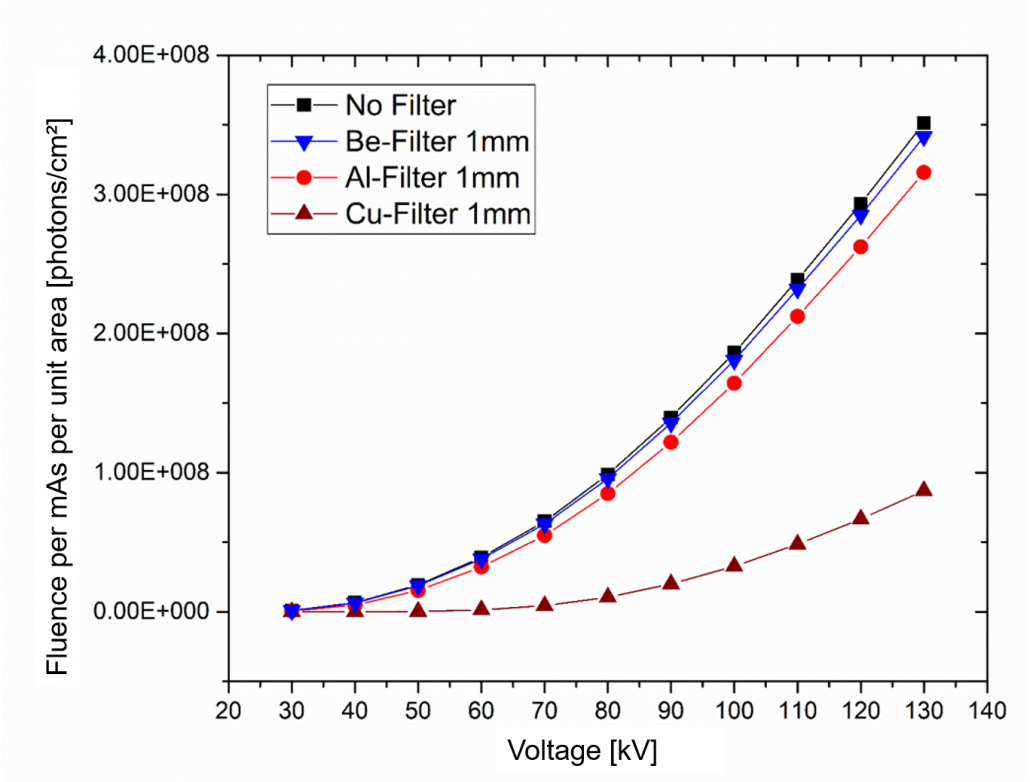

Figure 3.21: Influence of various filters on the integrated transmitted beam over range of voltage 30-130 kV.

However, the detector response is not implemented in the simulation tool so some difference can be expected for the computed contrast and the actual output image contrast. The detector response can be implemented in the Eq. 3.8 to estimate the photon flux received by the detector and furthermore the received photon flux can be approximated to the grayscale value on the radiographs from which the image contrast and SNR can be estimated accurately.

3.2.2.4 Screening algorithm

The next module of the proposed model is the screening algorithm that loops over all possible scanning parameters and estimate the all possible scanning configurations for a CT scan. It uses the X-ray absorption simulation tool and noise model, presented in Section 3.2.2.2 and 3.2.2.3, to estimate output image contrast and the weighted average error in the segmented feature size (probability of detection) for each configuration. The simplified form of the screening algorithm is presented in a flow chart in Figure 3.22. The nested loop operations implemented in the screening algorithm is also illustrated in Figure 3.23.

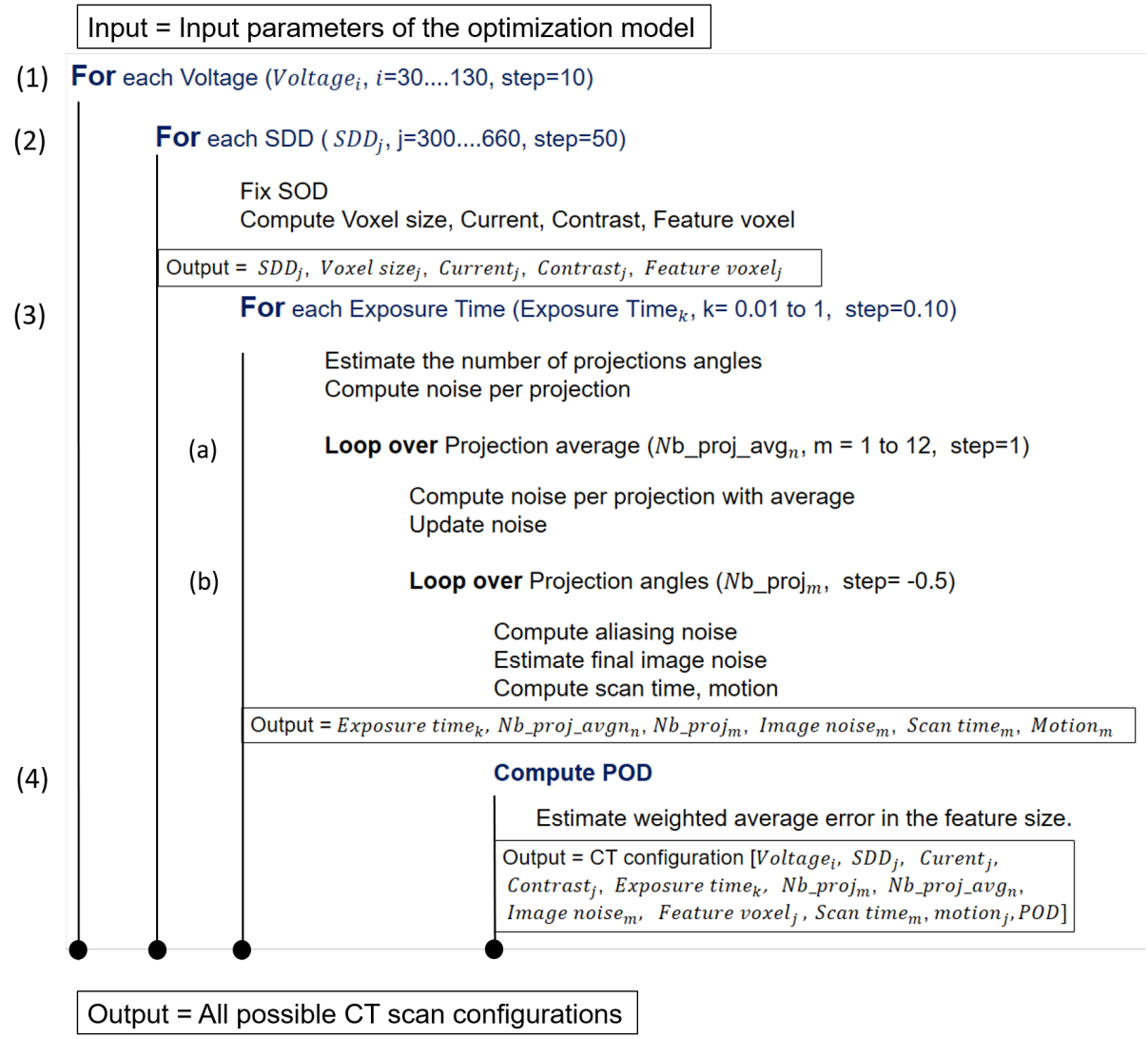

Figure 3.22: Flowchart of the work flow of the screening algorithm.

Four major nested loops functions are implemented in the screening algorithm and each major loop function contains sub-loops as can be seen in Figure 3.22 and 3.23.

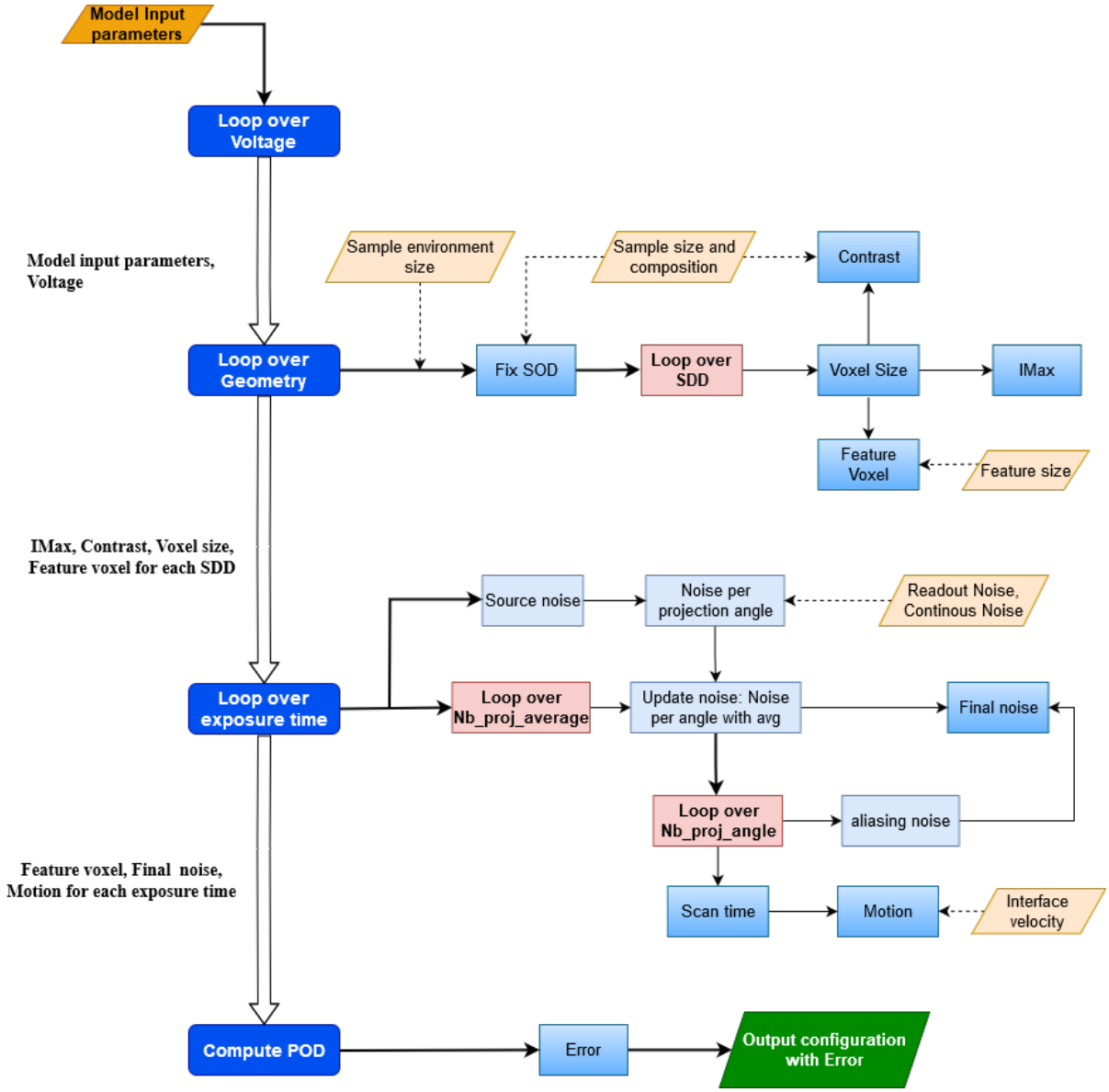

Figure 3.23: Flowchart of the work flow of the screening algorithm illustrating the implemented nested loops.

The screening algorithm starts with **the first major loop** over the range of voltage that is provided as a technical input to the model.

It then fix the source-object-distance (SOD) based on the closet possible distance by taking into account the size of the sample environment from the input parameters. Eq. 3.10 can be used to estimate the closet position of SOD, where ϕ_d is the distance between the X-ray source focal point and the output window, which is 14 mm for the EasyTomXL coupled with micro-focus X-ray source. τ is the thickness of the filter and d is the diameter of the sample environment for a in-situ scan or the diameter of the sample/sample holder for a static scan.

$$SOD = \phi_d + \tau + d/2 + \text{few mm for rotation if the sample is misaligned} \tag{3.10}$$

Once the SOD is fixed, **the second major loop** is based on the range of source-detector-distance (SDD). The minimum and maximum possible position of detector for a given CT system is provided as a technical input to the model and step defines the increment for each iteration. For each SDD, geometrical parameters such as voxel size and magnification are calculated using the Eq. 3.11:

$$\frac{SDD}{SOD} = \frac{P_{pitch}}{V_{size}} \tag{3.11}$$

where V_{size} is the voxel size of the scan and P_{pitch} represents the pixel pitch of the detector. The number of voxels in the diameter of the feature of interest (FOI) in the specimen is computed based on the calculated voxel size and the size of the FOI provided as an input parameter. Following equation can be used:

$$\text{feature voxels (number of voxels in diameter of feature)} = \frac{\text{feature size}}{\text{voxel size}} \tag{3.12}$$

Half of the feature voxels represents the radius of the feature size and this radius will be used as an input parameter to the noise model as radius of the sphere (feature) to compute the weighted average error in the segmented volume of the feature.

After, the maximum current is estimated for a given voltage to get the maximum power. The maximum reachable current depends on the focal spot mode of the source. For each focal spot mode, the maximum current is limited in order to prevent damage to the anode and the size of the focal mode restricts the attainable resolution. For the micro-focus source (Hamamatsu L12161-07 Reflection) installed in the EasyTomXL, the curve presented in Figure 3.24, was used to estimate the maximum current for a given spot size and voltage.

Three different focus modes are available associated with the restraint on the maximum power. The operational range of the source is 40 to 150 kV for the applied voltage and 10 to 500 µA for the applied current depending on the focus mode. The focus mode is usually decided depending on the desirable pixel size, small focus mode if voxel size is less than 10 μm and maximum reachable power is limited to 10 W, middle focus mode if voxel size is less than 30 μm and maximum reachable power is limited to 30 W, and large focus mode for the voxel size higher than 30 μm and maximum reachable power is limited to 75 W. Usually in a CT scan, the voxel size is larger than the focal spot size.

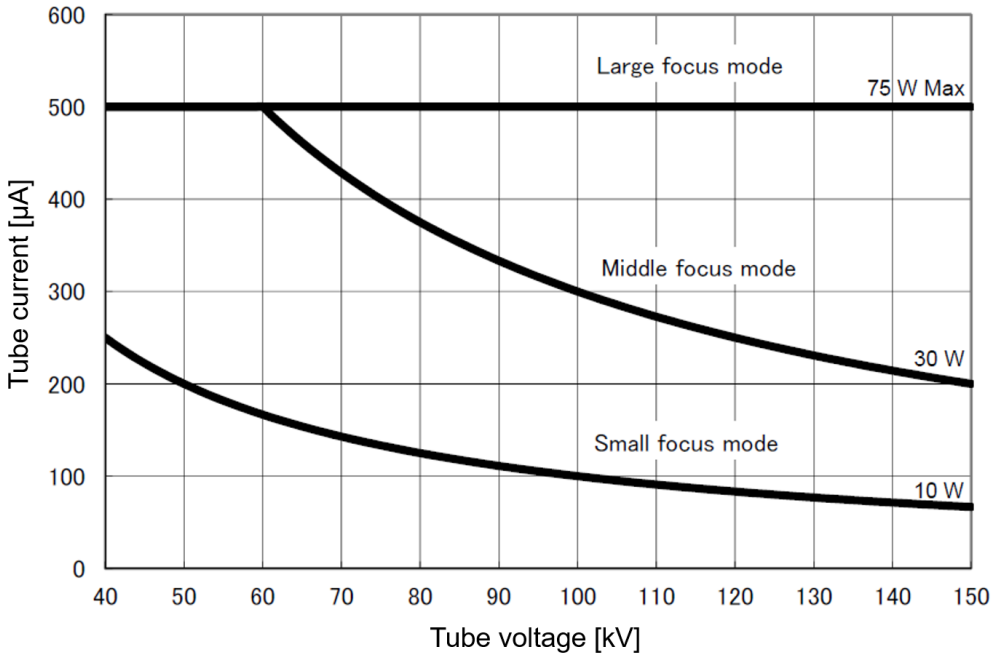

Figure 3.24: X-ray tube voltage and the current operation range according to the focus mode of the micro-focus X-ray source.

After computing the maximum current for a given voltage, X-ray absorption simulations are performed in order to compute the output photon flux and the contrast according to the procedure detailed in Section 3.2.2.3. The sample size and the composition of the different materials that constitute the sample given as input parameters, and already estimated X-ray source and geometrical parameters (voltage, current and SDD) are used for the contrast computation.

The third major loop in the screening algorithm is based on the range of exposure time. The minimum and maximum value of the exposure time is provided as technical input to the model based on the detector binning and the step defines the increment after each iteration. Two additional loops, one on the projections average and another on the number of projections are implemented inside the exposure time loop. The number of projections or number of projection angles for a scan is initially estimated based on the Nyquist–Shannon sampling theorem found in signal processing [Herman, 2010], Eq. 3.13.

$$Nb_{proj} = \frac{\pi}{2} * \text{number of horizontal detector pixels covered by sample} \tag{3.13}$$

After estimating the number of projection angles for an iteration configuration, the noise on the radiograph can be estimated. The three type of noise, source noise, readout noise and continuous noise are summed together to compute the noise per angle, Eq. 3.14

$$\text{noise per angle} = \text{source noise} + \text{readout noise} + \text{continuous noise} \tag{3.14}$$

The source noise is the dominant noise for a given configuration which can be estimated based on the Eq. 3.15 and is inversely proportional to the detected X-ray photon flux [Verdun et al., 2015].

$$\text{source noise} = \frac{255}{\sqrt{contrast * \text{photon flux} * \text{exposure time}}} \tag{3.15}$$

The photon flux given by the X-ray spectrum simulations tool is in per unit area (cm^2) per second exposure time units for an input voltage, current and SDD. Prior to the computation of source noise, some basic calculations were performed in order to convert this photon flux in the physical units, i.e. per unit detector pixel area (μm^2) per exposure time. The source noise is estimated based on the photon flux towards the detector pixel, it underestimates the noise since the detector response is not implemented in the X-ray absorption simulations.

Noise per projection angle ranges between 0 to 255 and is computed without any projection average. A loop on the projection average $Nb_{proj-average}$, is implemented and noise per projection angle is updated accordingly, using the following equation, Eq. 3.16 that the magnitude of noise reduces by the square root of the number of projections averaged [Carmignato et al., 2017a].

$$\text{noise per angle with average} = \frac{\text{noise per angle}}{\sqrt{Nb_{proj-average}}} \tag{3.16}$$

The projection average was increased from 1 to 12 with an increment of 1 after each iteration. With the increase in the projection average, the noise per angle will decrease according to the inverse square law.
Another loop is implemented on the required number of projection angles. Eq. 3.13 overestimates the required number of projections and they can be reduced without much affecting the image quality. However by reducing the projections, aliasing noise will increase the noise per angle with average. The Nb_{proj} was reduced to half after reach iteration and the corresponding aliasing noise was estimated according to Eq. 3.17 and was added in the noise per angle with average.

$$\text{noise aliasing} = \frac{\alpha}{(Nb_{proj})^{\beta}} \tag{3.17}$$

With the decrease in the number of projections, aliasing noise will increase and this increase depends on the value of coefficients α and β [Zhao et al., 2014b]. The values of α and β were derived from the experimental dataset in which scans with the decreasing number of projection were recorded and the standard deviation was measured on the projections. The estimated values were 336 for α and -0.606 for β.

In the loop for Nb_{proj}, the number of projections were reduced by a factor of two in each iteration and corresponding aliasing noise was estimated accordingly. The noise per angle with average was updated using Eq. 3.18:

$$\text{Image noise} = \text{noise per angle with average} + \text{noise aliasing} \tag{3.18}$$

The scan time can be estimated by the multiplication of the exposure time, number of projections and projection average as:

$$\text{Scan time} = Nb_{proj} * Nb_{proj-average} * (\text{exposure time} + \text{readout time}) \tag{3.19}$$

For the continuous in-situ acquisition, using the estimated scan time and kinetic evolution of the feature provided as an input temporal parameter, the motion of the feature size during a scan can be estimated according to the Eq. 3.20.

$$Motion = \frac{\text{velocity interface} * \text{scan time}}{\text{voxel size}} \tag{3.20}$$

The final loop, fourth, for the screening algorithm is based on computing the probability of detection (weighted average error) in the segmented volume of the feature according to the radius of the feature and noise in the radiograph. The number of voxels in the diameter of the feature size is already computed using Eq. 3.12 from which radius can be deduced, half of the diameter. The final image noise and motion of the feature size are estimated with Eq. 3.18 and Eq. 3.20, respectively. It should be noted that photon flux and the contrast has already been used to estimate the final image noise. Using these as input parameters (image noise, motion, feature voxels) to the noise model, the weighted average error can be estimated as explained in Section (3.2.2.2).

The output of the screening algorithm is a tabular file containing all the possible configuration for a CT scan and estimated image quality based on probability of detection and contrast for each configuration.

3.2.2.5 Cost function

After getting the set of different scanning configurations for a CT scan, a cost function is defined to select the optimal configuration.

Different strategies can be used to implement the cost function. In the optimization model, the parameters that are usually used to make the trade-off in choosing the optimal configuration such as image contrast, resolution including the number of pixels in the diameter of FOI and motion were already implemented, so we implemented the cost function only based on the weighted average error in the interested feature size.

Three different categories for the level of analysis were defined in the input parameters: L1: qualitative analysis, L2: low-level quantitative analysis and L3: high-level quantitative analysis. According to the level of analysis, the maximum limit values of the weighted average error were set in the cost function as follow:

- **For L1 analysis:** Maximum weighted average error in the FOI of 20 percent.

  (Classically for L1 analysis, a minimum of 6 voxels in the diameter of the feature of interest, image contrast of 0.3 to 0.5 are expected, but for the implemented cost function these parameters were not constraint.)

- **For L2 analysis:** Maximum weighted average error in the FOI of 10 percent.

  (Classically for L2 analysis, a minimum of 8 to 10 voxels in the diameter of the feature of interest, image contrast of 0.3 to 0.5, and minimum motion in the FOI are expected).

- **For L3 analysis:** Maximum weighted average error in the FOI of 5 percent.

  (Classically for L3 analysis, a minimum of 16 voxels in the diameter of the feature of interest, image contrast of 0.3 to 0.5, and no motion in the FOI during the scan are expected.)

3.2.3 Output parameters

As mentioned earlier, the output of the optimization model is a tabular file containing the possible scan configurations for a CT scan and the optimal configuration is selected based on the cost function that is designed according to the objective of analysis to be performed on the 3D dataset. Scan parameters that are optimized by the model and given as an output is shown in Figure 3.25.

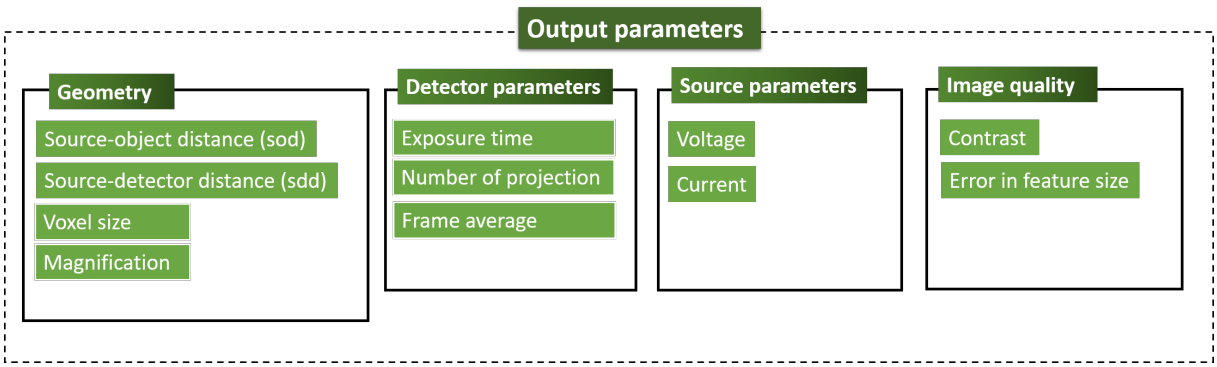

Figure 3.25: Overview of the output parameters.

3.3 Validation and discussion

In this chapter, an attempt towards the optimizing of the CT acquisition parameters is presented by developing an optimization model. The model estimates the suitable scanning configurations for a given CT scan based on specimen's specifications. After, the optimal configuration is chosen by using the cost function. In this section the validation and the discussions regarding the strengths, limitations and further improvement of the optimization model is presented.

Initially in Section 3.3.1, the functionality and the efficiency of the optimization model to estimate the optimal configuration is illustrated with the help of an real-time CT scan case study. The input and output parameters and the sensitivity of the cost function to the various acquisition parameters are discussed. In Section 3.3.2 and 3.3.3, the validations of the different predicted parameters of the model is confronted with the experimental values. Further discussion about the strengths, limitations and improvements needed for the optimization model is detailed in the Section 3.3.4.

3.3.1 Validation 1: case study

3.3.1.1 Problem statement

A 1 mm diameter Al specimen with 5% Cu inclusions needs to be scanned with a scan time of less than 1 minutes. This constraint on the scan time comes from the loading conditions of the in-situ environment. The interested feature to be quantified is a small Cu inclusion of 100 μm diameter. 3D reconstructed images need to be quantified with the level 3 (high-level quantitative) analysis. The EasyTom XL coupled with micro-focus source and flat-panel detector located in laboratory SIMAP will be used for the CT scan.

What should be the suitable parameters of the CT scan?

3.3.1.2 Model input parameters

According to the given information (sample size and the size of the feature of interest FOI), a high resolution scan is needed in order to quantify the interested feature so the detector's parameters in full acquisition mode (no binning) was directly used in the optimization model which gives the detector size of 1840 x 1456 with pixel pitch of 127 μm. Binning 2 and binning 4 mode of the detector will result in lower scan resolution making it difficult to quantify the 100 μm feature.

The geometrical and absorption constraints and the aim of analysis, detailed in Section 3.2.1, were given to the model as input parameters and are listed in Table 3.1.

The farthest position of the detector in EasyTom XL is 668 mm so the reasonable range of source-detector-distance (SDD) from 300 to 660 mm was added as an technical input to the model. Moreover, the full acquisition mode of the detector limits the minimum exposure time to 0.08 seconds (12.5 frames per second), so a range of exposure time from 0.08 to 1 seconds was given as technical input. All these input parameters along with the technical inputs given to the model are listed in Table 3.1.

Table 3.1: Input parameters to the optimization model.

Input parameters	**Value**
Sample diameter [cm]	0.1
Matrix material	Aluminium [Al]
Matrix material diameter [cm]	0.095
Matrix material density [g/cm^3]	2.7
Inclusion material	Copper [Cu]
Inclusion material diameter [cm]	0.005
Inclusion material density [g/cm^3]	8.96
Feature of interest [μm]	100
Sample environment diameter [mm]	40
Level of analysis	L3: high-level quantitative
Technical input	**Value**
Range of SDD [mm]	300 to 660, step = 30
Range of voltage [kV]	30 to 100, step = 10
Range of exposure time [s]	0.08 to 1, step = 0.2
Range of projection average	1 to 6, step = 1
Detector size	1840 x 1536
Detector pixel pitch [μm]	127

3.3.1.3 Model output parameters

Based on the input parameters, the optimization model predicted the different possible configurations of the scan and a suitable configuration presented in Table 3.2(a) was chosen by using the cost function that outputs the scan configuration with the minimum error in the segmented volume of the feature of interest and satisfies the constraint on the scan time. This selected configuration results in a scan time of 58 seconds with 240 number of projections with an average of 3 using exposure time 0.08 seconds at 70 kV voltage and 142 μA current.

The 40 mm diameter sample environment and the 14 mm distance between the source focus point and the output window limit the SOD to 34 mm and combined with a SDD of 660 mm results in voxel size of 6.5 μm with binning 1 configuration. With this geometry, a total of 16 voxels are estimated in the diameter of the interested feature of size 100 μm resulting in an estimated weighted average error of 2.2% in the thresholded volume. The exposure time of 0.08 seconds (minimum limit with no binning mode) was chosen which results in weighted average error of 2.2% with the sub-minute scan time combined with other parameters. Although longer exposure time can further increase the measurement accuracy of the feature but it will significantly increase the required scan time.

However, different other scanning configurations output by the optimization model, in the output tabular file, can also result in the weighted average error within the range of 2.3 to 3% which can be used for CT scan as well. One possibility can be to use half of the number of projection (120 projections), it will increase the weighted average error in the feature size to 3.7% but it can help to reduce the total scan time from 58 seconds to 28 seconds with keeping the all other parameters constant as per selected optimal configuration. Such possibilities are addressed in the following section.

Table 3.2: CT configuration predicted by optimization model.

Scanning parameters	**Model estimated value for scan time ≈ 1 minute**
SOD [mm]	34
SDD [mm]	660
Voxel size [μm]	6.54
Magnification	19.4
X-ray voltage [kV]	70
X-ray current [μA]	142
Contrast	0.26
Number of projections	240
Projection average	3
Exposure time	0.08
Scan time [s]	58
Number of pixels in the diameter of the feature of interest	16
Weighted average error in the feature of interest	≈ 2.2%

3.3.1.4 Accessing the efficiency of the model

In order to see the assess the efficiency of the model it is important to understand the sensitiveness of the cost function to the various acquisition parameters. For this purpose, for the selected optimal set of parameters defined in Table 3.2(a), the evolution of the cost function in terms of weighted average error in the segmented volume of the feature size is plotted as a function of each parameter.

Figure 3.26(a) shows the evolution of weighted average error as a function of the number of projections with average 1 and 3 with keeping all other parameters at their optimal value. The evolution of the standard deviation in weighted average error is plotted as a secondary y-axis in red color. An increase in the weighted average error is observed with decreasing the number of projections for both average 1 and 3. 240 projections, estimated by Nyquist sampling theorem, were selected as an optimal value since it produces the minimum weighted average error. However, 50% of the initial projections result in good order of measurement accuracy which is consistent with the previously reported study [Gómez and Smith, 2020].

By decreasing the number of projections, only the aliasing noise is added in the model, but the noise will change as a function of feature size and the position (near the axis of rotation or far away). The decrease in number of projections with average 1 result in significantly high value of standard deviation in weighted average error due to the high image noise whereas the increasing tendency of the standard deviation with average 3 seems to be in good order. Moreover, it should be noted that by reducing the number of projections, dimensional measurement such as the volume of the feature is not significantly affected but it can have an significant effect on the form measurement such as sphericity or cylindricity. No such criteria on the error estimation for the form measurement is currently implemented in the optimization model.

The evolution of weighted average error and the standard deviation in weighted average error (in secondary y-axis in red color) as a function of average of the number of projection is presented in Figure 3.26(b). A decreasing trend in weighted average error and the standard deviation in weighted average error can be observed with the increase in the averaging at each projection angle. This decrease is due to the reduced estimated image noise which increases the measurement accuracy for a 16 pixel diameter feature.

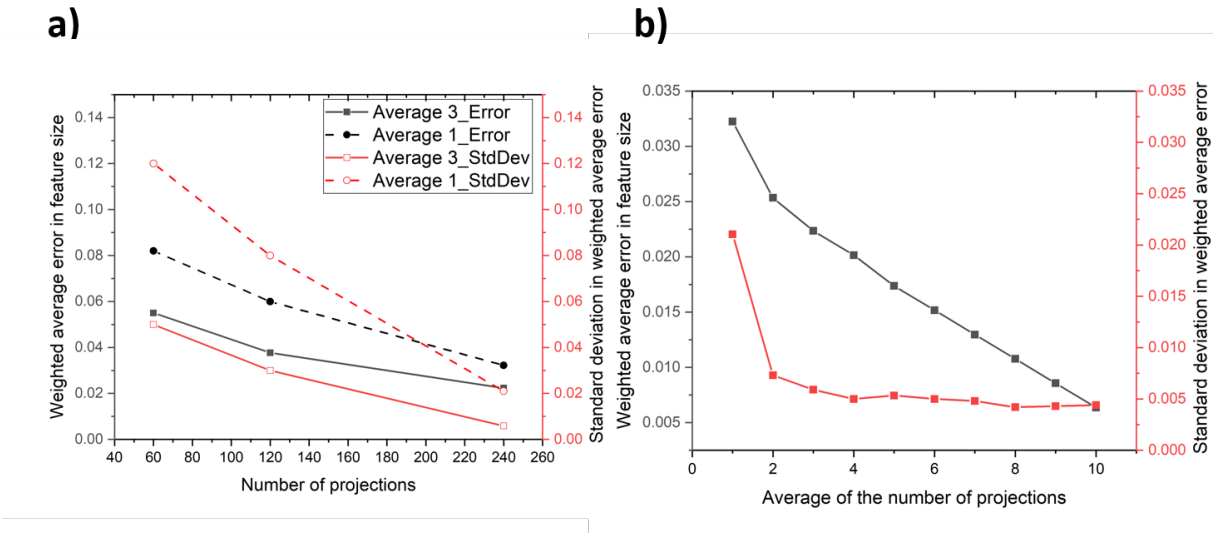

Figure 3.26: The evolution of the weighted average error and the standard deviation in weighted average error (in secondary y-axis in red color) in the feature size as a function of (a) the number of projections (b) average of the number of projections, keeping all other parameters at optimal value.

Figure 3.27(a) presents the evolution of weighted average error and the standard deviation in weighted average error (in secondary y-axis in red color) as a function of source-detector distance (SDD) for both projection average 1 and 3. No significant variations in the weighted average error with the change in SDD is observed expect for the SDD of 300 mm which results in higher error. In order to understand this behaviour, the effect of SDD on the parameters that are directly related to the estimation of the weighted average error is investigated.
Although all other acquisition parameters are at their optimal value but changing SDD automatically change certain parameters that are presented in Figure 3.27(b, c & d). With the increase in SDD from 300 mm to 660 mm the voxel size of the scan decreases from 14.3 μm to 6.45 μm resulting in higher resolution of the scan, Figure 3.27(b). Similarly increase in SDD results in larger feature size (more number of pixels in the diameter of the 100 μm feature) as indicated in Figure 3.27(c). However, at the same time, the photon flux received on the detector pixel decreases as per inverse square. This decrease in photon flux at larger SDD results into higher estimated image noise. High image noise for a large SDD combined with a large feature size and low image noise for a small SDD combined with a small feature size yields similar estimation of weighted average error.

It is concluded that within the SDD range from 300 to 660 mm with other acquisition parameters at their optimal values, 100 μm feature size seems quantifiable but feature size smaller than 50 μm would be difficult to visualize and quantified as size of the feature in pixels would be smaller and it'll result in significantly high weighted average error even at low values

of image noise, as previously explained in Figure 3.12. Moreover, a further criteria on the weighted average error with changing SDD and correspondingly estimated feature size need to be implemented in the model.

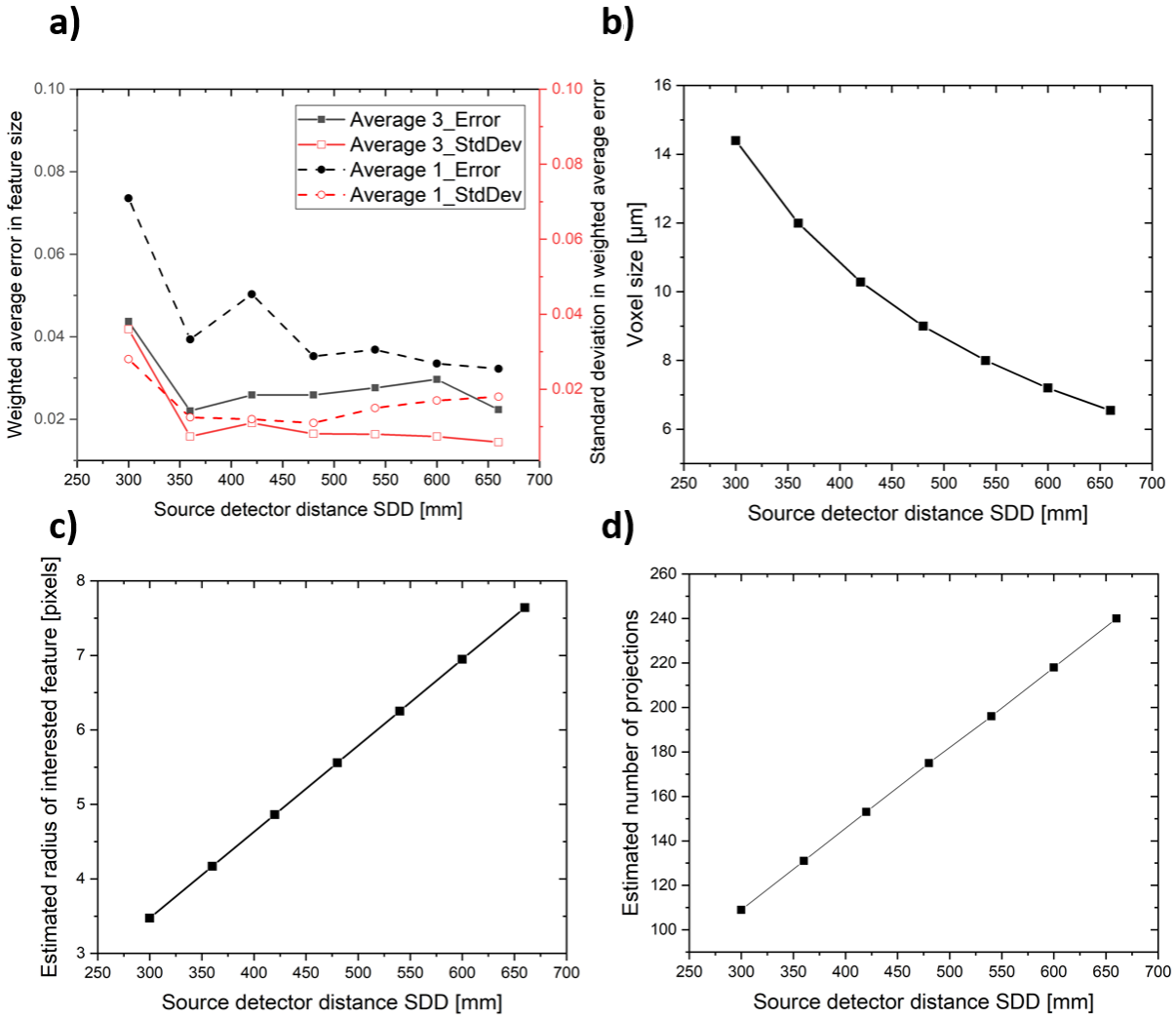

Figure 3.27: (a) The evolution of the weighted average error and the standard deviation in weighted average error (in secondary y-axis in red color) in the feature size (b) voxel size, (c) estimated radius of feature size and (d) estimated number of projections, as a function of SDD.

Similarly Figure 3.27(d) shows the evolution of estimated number of projections with the change in SDD. With the increase in SDD, the number of detector pixels covered by the sample increases (window size) resulting in increase in estimated number of projections as per Eq. 3.13. However, this estimated number of projection is the maximum number estimated by Nyquist sampling theorem for the reasonable reconstruction with FBP algorithm. In practice, it can be reduced to half without much affecting the measurement accuracy.

The sensitively of the weighted average error and the standard deviation in weighted average error (in secondary y-axis in red color) as a function of the exposure time is presented in Figure 3.28(a). The decreasing tendency of the weighted average error with an increase in exposure time is consistent with the general observation that the longer the exposure time, the better the image quality. Longer exposure times increase the photon flux received by the

detector leading to the higher image quality and higher measurement accuracy of the feature but at an expense of the total scan time.
Similarly, the evolution of the weighted average error and the standard deviation in weighted average error (in secondary y-axis in red color) as a function of the acceleration voltage is shown in Figure 3.28(b). No effect on the weighted average error is seen with the change in voltage. This is due to the fact that in the screening algorithm the power is always kept constant according to the spot size as per Figure 3.24. In the current case-study, the small spot size is used for the voxel size of 6.45 μm which limits the maximum power to 10 W. In order to get the power of 10 W for each configuration of voltage, the corresponding current is changed accordingly. For example, the estimated current at 50 kV is 200 μA and at 100 kV is 100 μA. Since no variation in the measurement accuracy with the change in voltage is observed, it is concluded that a criteria on the weighted average error with the change in voltage also needs to be implemented.

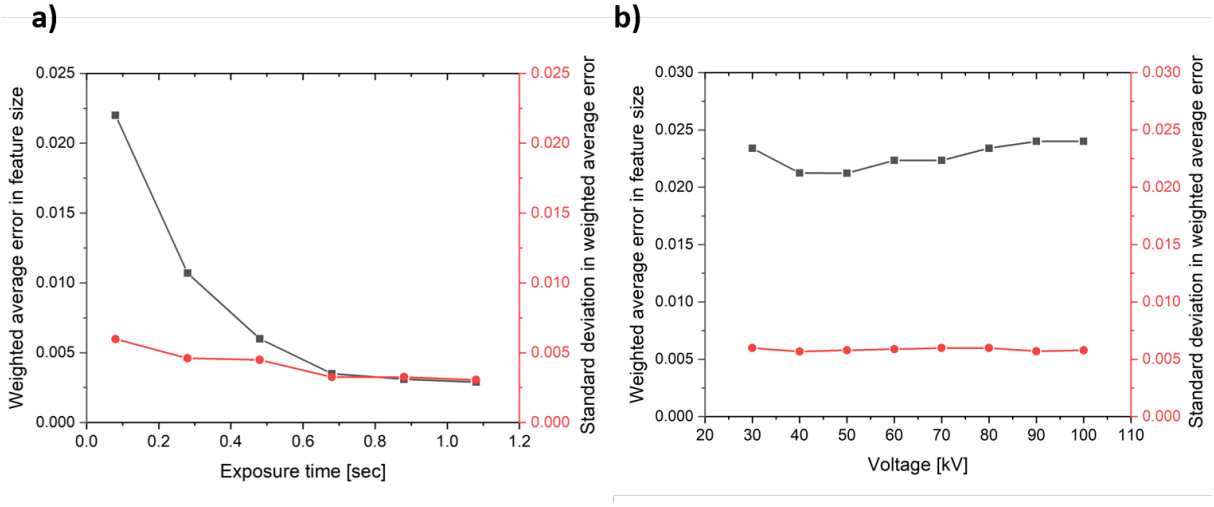

Figure 3.28: (a) The evolution of the weighted average error and the standard deviation in weighted average error (in secondary y-axis in red color) in the feature size as a function of (a) exposure time, (b) voltage.

Figure 3.29 and 3.30 present the other possible configurations for the scan from the output tabular file illustrating the potential of the model. Figures show the contour plots illustrating the effect on weighted average error as a function of number of projections and exposure time with average 3 and average 1, respectively. Number of projections range from 240 (maximum estimated number) to 60 projections and exposure time ranges from 0.08 (minimum possible with flat-panel no binning mode) to 1 seconds with all other parameters constant as per Table 3.2(a).

Different configurations can be used resulting in almost similar measurement accuracy. It is interesting to note that, in case of ultra-fast scan, an exposure time of 0.08 second combined with only 60 projections with average 1 can be used, Figure 3.30. It would help in reducing the scan time to 5 seconds, although at an expense of the measurement accuracy. Such compromise can be acceptable for in situ condition where ultra-fast dynamic process need to be imaged. Moreover, using the 60 projections results in high value of image noise by reconstructing with filtered back-projection algorithm. In such cases, the possibility of using different reconstruction algorithm needs to be explored that can accurately reconstruct the datasets with significantly

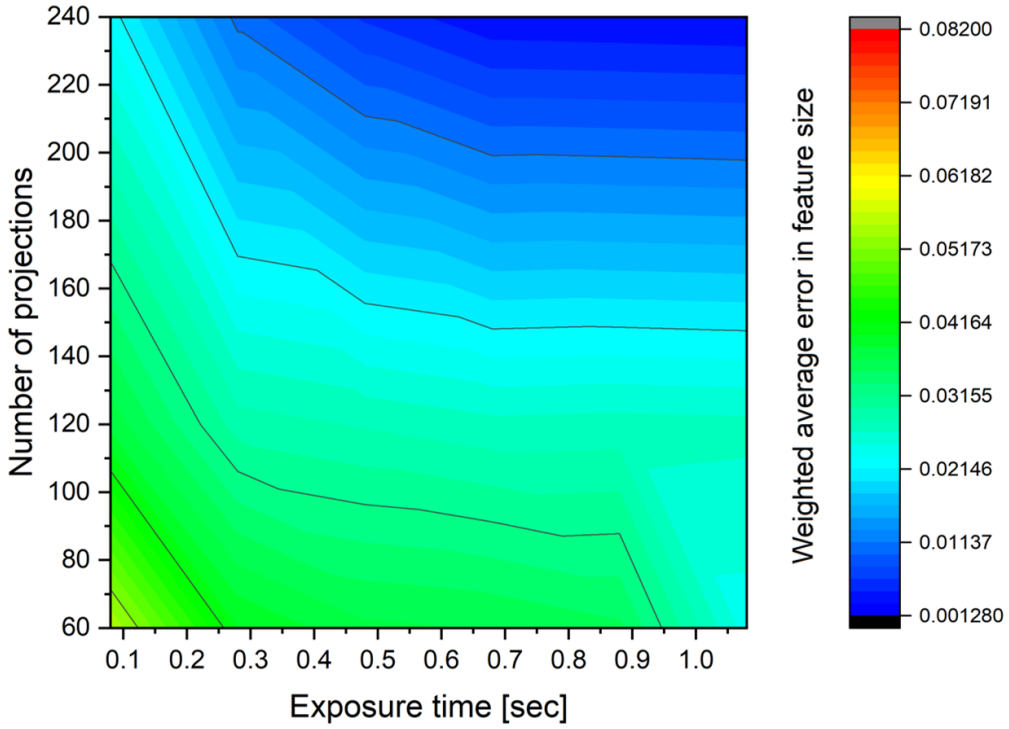

Figure 3.29: The contour plot showing the effect on weighted average error as a function of the number of projections and exposure time with average 3.

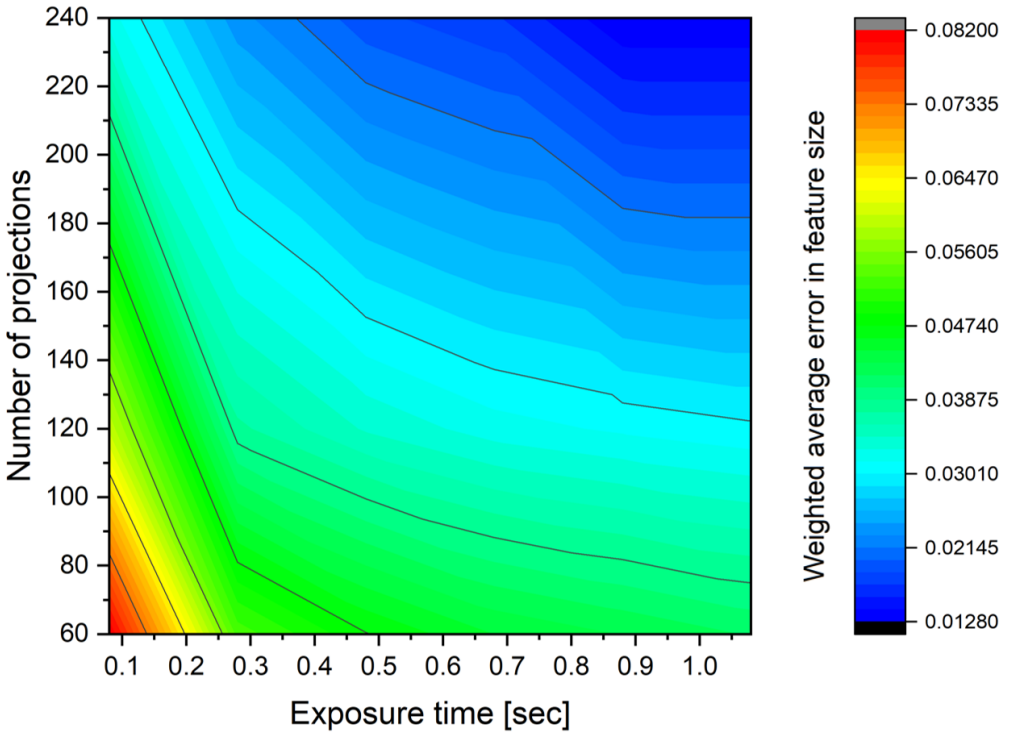

Figure 3.30: The contour plot showing the effect on weighted average error as a function of the number of projections and exposure time with average 1.

reduced projections such as iterative reconstruction algorithm and artificial intelligence and machine learning based reconstruction algorithms [Hendriksen et al., 2019, Pelt et al., 2018,

Weigang and Jinxiao, 2021].

3.3.2 Validation 2

As detailed in Section 3.2.2.2, the noise model estimates the probability of detection for a given size of the spherical feature of interest based on the global image noise. The global image noise is defined in-terms of Gaussian standard deviation. Feature size of radius 1 to 10 pixels are currently implemented in the noise model. In order to validate the estimated weighted average error from the noise model, a tomography with a phantom consisting of spherical object was performed.

Phantom that was used is a carbon rod with 2 mm diameter consisting of circular steel bead of diameter 1 mm. The steel bead was used as a feature of interest. The geometry of the scan was initially optimized using the model in order to get the maximum of 20 pixels in the diameter of the steel bead to compare with the model. The optimized geometry resulted in SOD of 30 mm, SDD of 285 mm with a voxel size of 53.44 μm using the binning 4 mode of the detector. This resulted in approximately 18.7 voxels in the diameter of the bead (radius 9.35 pixels). The scan was recorded using the Voltage of 140 kV and 70 μA current using 0.5 mm Cu filter. 100 radiographs were taken with an average of 3 using exposure time of 0.0167 seconds. The recorded radiographs were reconstructed with the filtered-back-projection algorithm implemented in the tomograph reconstruction software.

Figure 3.31(a & c) represents the reconstructed central slice of the steel bead consisting of approximately 18.7 pixels in the diameter and corresponding histogram. Due to the high absorption coefficient of the material, cupping artifacts are clearly visible which will affect the thresholding operation leading to the measurement error. Figure 3.31(b & d) shows the corresponding 10 pixel radius simulated sphere by the sphere generation script and the corresponding histogram.

The reconstructed sphere was thresholded using the threshold value 128 which was used in the noise model and the corresponding sphere volume was estimated by counting the total number of white voxels. After, the relative error in the sphere volume was computed using the volume of ideal sphere of radius 9.35 pixels, Eq. 3.6, as reference. The error is estimated to be around 3.3% whereas the weighted average error predicted by the optimization model for radius 10 pixel sphere is around 1%. This difference of 2.3% in the volume measurement can be explained by the following facts:

- The noise model predicts the error on the basis of noise measured in the radiographs. The noise in the reconstructed projections is significantly increased which is not included in the model. Moreover no further noise based on the image artifacts (cupping artifacts) is included in the noise model. These artifacts do not necessarily affect the standard deviation of the image but can highly affect the feature of interest as seen in Figure 3.31(a) leading to the difficulty in segmentation.

- The threshold of 128 was used in the noise model for the computation of weighted average error assuming the saturated gray value 0 and 255 in the image background and in the sample, respectively. However, in the actual this assumption is not true, the threshold value

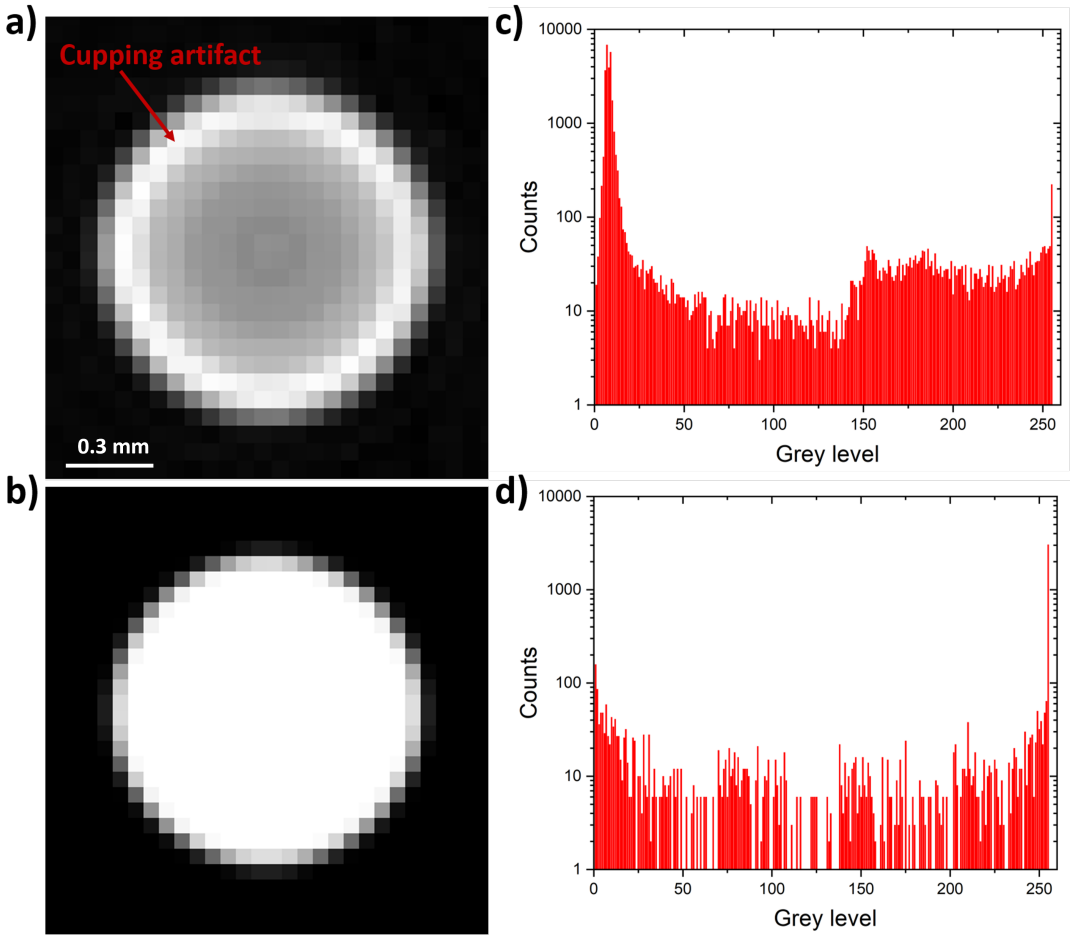

Figure 3.31: (a) A reconstructed slice of a steel bead with 20 pixels in the diameter. (a) A slice from the 3D simulated sphere with the radius of 10 pixels.

in the reconstructed volume depends on the histogram and it is generally not exactly 128 as can be noted in the Figure 3.31(c).

- Moreover the error is compared with the radius 10 simulated sphere and the actual size of the reconstructed sphere is radius 9.35, as predicted by the optimization model, due to which some error can be expected.

3.3.3 Validation 3

Figure 3.32 shows the comparison between the image noise in terms of standard deviation predicted by the model on the experimentally recorded radiographs as a function of the average of the number of projections keeping the total number of projections and other CT detector parameter constant. A cellulose cube 9 mm^3 was used as a phantom and its dimensions and material properties were inserted in the model for computing X-ray photon flux using X-ray absorption spectrum simulations and then estimating noise.

The voltage of 100 kV and 300 μA were used as X-ray source parameters and SDD = 757 mm and SOD = 42 mm as geometrical parameter. An aluminium filter of 0.5 mm thickness was placed on the X-ray source to discard the low-energy photons. 12 different scans

consisting of 720 radiographs were recorded at frame rate of 60 per second varying number of projection averaging in each scan. The dataset was reconstructed using classical filtered back-projection algorithm. The resultant noise on the radiographs, on the reconstructed projections and predicted by the optimization model is shown in Figure 3.32.

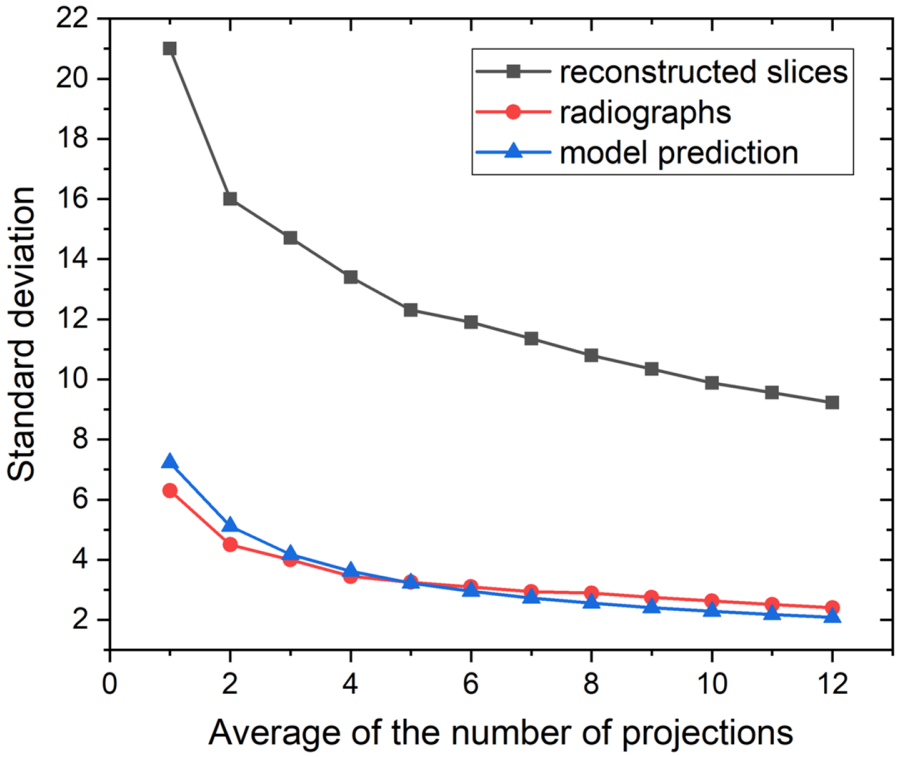

Figure 3.32: Comparison of the standard deviation on the radiographs from optimization model and from experimental dataset as a function of average of the number of projections. Noise on the reconstructed slices is presented as well.

It can be seen that developed model efficiently predicts the noise in the radiographic images, and tendency of the decrease in the image noise with the increase in image is consistent with the experimental measurement, Figure 3.32. However the noise in the reconstructed slices is measured to be three times higher. In the model, the probability of detection is computed based on the noise in radiograph and not in reconstructed slices due to which difference in the error measurements is expected. The predicted noise on the radiograph with decreasing number of recorded projections was also found to be consistent with the experimental dataset, as the experimental curve for aliasing noise was implemented in the screening algorithm.

3.3.4 Strengths, limitations and recommendation for the improvement of the model

The strengths and limitations of the model along with the recommendation that can be implemented for better estimation of the optimized CT configuration are discussed below.

- The model is quite efficiently able to estimate all the geometrical parameters by taking into account the dimensions of the sample and the sample environment. Moreover the modules to compute the detector pixels covered by the sample to estimate the number of projections and number of pixels in the diameter of the interested feature are also well modelled by implementing the physical laws.
- In the noise model, the spherical feature of interest of radius 1 to 10 pixels are currently implemented. The histograms of the 3D simulated spheres were used for the statistical computations. Moreover the criteria on the motion of the feature is also implemented that usually occurs during the dynamic acquisitions. The feature size can be extended to larger radius and to different shapes as well.
- The criteria for the optimization is based on the estimation of weighted average error in the thresholded volume of the interested feature. The computation of thresholded volume comes under the dimensional measurements. Moreover nested loops implemented on the number of projections and projection averaging updates the image noise for the measurement of thresholded volume of the interested feature. It was noted that the decrease in number of projections to half or one third of the initial estimated projection do not have a significant effect on the thresholded volume. However, it can have an effect on the form measurements such as sphericity, flatness and cylindricity. The criteria on the weighted average error on the basis of form measurements is not currently implemented in the noise model. To improve efficiency of the optimization, such criteria can be implemented.
- The statistical computations for the estimation of the weighted average error in the segmented volume of the FOI is well implemented. Initially, this operation estimates the probability of the thresholded voxels for each single gray level present in the histogram separately, for a specified noise, and then a cumulative probability distribution histogram for all gray values is generated from which weighted average error is deduced. However the threshold limit was selected at 128, based on an ideal case senior with grayscale value in the background and sample being 0 and 255. The threshold limit value can be adjusted based on the experimental dataset.
- The motion of the feature was incorporated by inducing blurring in the simulated 3D grayscale sphere. This was done by generating the series of 3D spheres with varying their x-directional central position according to the pixel motion and then computing the single averaged sphere. This averaged sphere has more intermediate gray values along the boundary representing blurring but the size of the sphere remains constant. However, a detailed experimental validation is needed to validate the motion-induced simulation results for spherical object.
- The methodology for the X-ray absorption spectrum simulation tool is well built and it takes into account the spectrum generation using X-ray tube parameters, and it's interac-

tion with the sample using sample thickness and constituent materials for the computation of integrated transmitted intensity towards the detector pixel at a given detection distance. However, the detector response is not modelled in the tool. The image contrast is estimated based on the photon flux towards the detector pixel without considering the detector response which might leads to the overestimation of the image contrast.

- For the estimation of weighted average error, the estimated noise on the radiograph for a given configuration is used in the noise model. However, in an actual case, image quality is further reduced due to the reconstruction algorithm and due to the artifacts. Only the noise due to undersampling (aliasing) artifacts was taken into account. Noise per projection needs to be updated by introducing the noise for the reconstruction algorithm and for the image artifacts for further refining the error measurements in the FOI. Currently the image quality is estimated as a function of the Gaussian noise. Other image quality indexes such as signal-to-noise ratio and contrast-to-noise ratio can be implemented as well to estimate the weighted average error in the interested feature.

- The screening algorithm is based on the nested loop function that loops over the all possible scanning parameters in sequential order and outputs the possible scanning configurations. In the workflow of the screening algorithm the order of the looping is defined as: the first major loop is implemented on the range of voltage, the second major loop over the range of source-detector distance (SDD) and the third major loop on the range of exposure time. Each major loop contains nested sub-loops for other acquisition parameters as illustrated in the flowchart in Figure 3.23. The output configurations are quite inline with the experimental configurations and the trade-off between different output configurations can be made according to the scan constraints.

- The implemented cost function is based on the weighted average error criteria in the segmented volume of feature of interest. The maximum limits for the weighted average error were set in the cost function by taking into account the three levels of analysis to be performed on the images. No other constraints based on the image contrast, resolution, and motion that are classically expected depending on the level of analysis are implemented in the cost function. In the optimization model, these constraints were already taken into account while computing the weighted average error. However, these constraints can be implemented in the cost function according to the user's requirement. Other metrics such as SNR can also be implemented in the cost function for a trade-off after they are introduced in the noise model.

- The sensitivity of the cost function in terms of weighted average error as a function of acquisition parameters is presented in the case study example. It was observed that the fluctuation in the cost function with different parameters is inline with the general observations expect for the SDD and voltage. With changing SDD and voltage no significant change in the cost function was observed, this is due to the fact that parameters such as feature size, current and image noise change with the change in SDD and voltage resulting in similar weighted average error. So in order to improve the optimization efficiency, further criteria on the weighted average error with changing voltage and SDD needs to be implemented in the model.

3.4 Conclusions

In this chapter, we propose a model-based approach to determine the suitable X-ray laboratory tomography configurations to perform in-situ or steady state CT acquisitions.

The proposed optimization model is based on three modules. A noise model that estimates resultant image quality in the sense of weighted average error in the segmented volume of the feature of interest. An X-ray absorption simulation tool for the computation of contrast in the output image. And an screening algorithm that loops over the all possible scanning parameters and outputs the different possible scanning configurations. For each output configurations, the image quality in the sense of weighted average error in the segmented volume of the feature of interest is estimated by taking into account the criterion such as image contrast, resolution, motion of the feature size and image noise. After, a cost function is used to select the optimal configuration for a CT scan by taking into account the level of analysis to be performed on the output images. The model efficiency to predict the parameters was accessed by comparing it with the experimental values and were found to be consistent. The strengths, limitations and recommendations of the optimization model are detailed as well.

Part II

Application aspect

Chapter 4

3D real-time monitoring of air-drying of 3D printed part made up of cellulose by fast laboratory X-ray microtomography

Contents

Abstract

This chapter presents the fast in-situ application preformed with the optimized setup of laboratory tomograph. The objective was to image and quantify in real-time the 3D printed part made up of cellulose paste. For this purpose an optimized image acquisition and analysis protocol was developed to perform the fast in-situ test coupled with a qualitative and quantitative analysis. First an experimental screening was performed to optimize the CT acquisition protocol to perform the in-situ test. The experimental screening results were compared to the predicted configurations by the optimization model and they were found to be in-line with each other. The experiment was performed with one of suitable optimized configuration that allows to perform L1, L2 and L3 level analysis on the acquired 4D datasets. The quantified differential drying within the structure explains the sequence of defects evolution. Moreover, the quantified micro-scale deformation mechanism explains the observed macroscopic behaviour over time. Part of the drying was performed in collaboration with laboratory LGP2 and corresponds to an article submitted to Carbohydrate Polymers.

4.1 Introduction

In the last decade, additive manufacturing (AM) technologies, commonly named 3D printing, of cellulose-based polymer have been increasingly developed for various applications such as medical or electronical because cellulose is a very promising candidate to produce cheap, lightweight, robust, and recyclable 3D structures by 3D printing [Wang et al., 2018, Dai et al., 2019, Firmanda et al., 2022]. Despite the fact that cellulose fibres represent the most abundant bio-based polymer on earth and present excellent mechanical properties [Dufresne, 2012], the use of cellulose in the form of short fiber or microfibril or nanofibril in the specific case of additive manufacturing by material extrusion is still in its infancy [Markstedt et al., 2014, Wang et al., 2018]. Namely, when paste made up of short fibers are considered, the paste contains a large amount of water (larger than 50% in weight, [Thibaut et al., 2019]. This huge proportion of water in the paste implies a deformation larger than 30% upon air-drying [Klar et al., 2017] during the 24h of drying. In such processes, the huge deformations undergone by the part come from an interplay between gravity, evaporation effects and capillary effects which mainly occurs during the first hours of drying [Rémond et al., 2010, Sampson and Yamamoto, 2011].

In general, three temporal phases are identified during the drying phenomena of such structures. Phase I corresponds to the constant drying rate period during which the water evaporation at the surface of the sample is replaced by water diffusion i.e. the rate of evaporation is of the same order of magnitude as the rate of water diffusion inside the sample. Phase II corresponds to the falling rate period during which the surface water evaporation is not fast enough to maintain a continuous film on the surface. Phase III corresponds to a steady-state where an equilibrium is reached and a constant drying rate is observed [Scherer, 1990, Thiery et al., 2017, Zhou et al., 2019, Tang and Min, 2018]. These drying phenomena affect the geometry and the inner structure of the extruded filaments themselves as well as their contacts created during the printing process and therefore affect the final geometry of the dried final part. In order to understand the macroscopic shrinkage of such structures, there is a need to visualize the 3D structure at the filament scale during drying [Metzger, 2018].

Among the tools that can be used to visualize and quantify the printed structure, X-ray microtomography, which gives access to the inner structure of such parts, have been successfully used to visualize [Huan et al., 2019, Pfister et al., 2004] and characterize the final shape of such 3D structures [Klar et al., 2019]. However, none of these works proposed a temporal characterization of the samples during their air-drying process. Such a monitoring is commonly performed using synchrotron tomography in the case of thermo-hydro-mechanical tests on cellulose materials [Joffre et al., 2016, Viguie et al., 2011] or during 3D printing of metallic part [Lhuissier et al., 2020] where 3D images can be achieved in a second or less. Such monitoring of microstructural evolutions is then qualitatively or quantitatively analyzed, which requires a high-level quality of images in term of signal to noise ratio and shape fidelity. In general, such image quality necessary to perform a quantitative analysis is achieved in lab tomographs with images acquired in 1h, which is not compatible with the characteristic time of the drying process investigated in this study.

For this purpose, we performed an experimental screening for the optimization of acquisition protocol to perform the fast in-situ test with quantifiable image quality. The experimental screening is detailed in Section 4.2, and the optimal configuration was chosen by making the trade-off between the spatial and temporal resolution and image quality in accordance with the objective of the scan. In Section 4.3, the configurations predicted by the optimization model are confronted with the experimental configuration. Section 4.4 details the advanced image analysis protocol applied to analyze qualitatively and quantitatively the evolution of the macroscopic shrinkage of the part and of the changes that occur at the filament scale in order to identify the microstructural changes that occur during two main phases of the drying process. This section is based on an article submitted to Carbohydrate Polymers.

4.2 Experimental screening for the optimization of acquisition parameters

In this section, the experimental screening for the optimization of the CT acquisition parameters for the intended in-situ tests is detailed. Initially, the choice of the 3D printed sample according to the objectives of the study is presented. After, the influence of the different CT screened parameters on the image quality and the reasons for their selection is presented.

4.2.1 Sample characteristics

Camille Thibaut, in her recent PhD thesis [Thibaut, 2020], developed an optimized aqueous paste based on short natural cellulose fibers as a bio-based material for 3D printing by extrusion. This optimized aqueous paste was extruded to build simple and complex 3D parts. Figure 4.1 shows the 3D printed parts on which we worked during the PhD.

The mean diameter of the filament was 720 μm. The aqueous cellulose paste contains more than 50% water by weight which causes the 3D printed samples to undergo a nearly 50% reduction in weight during the air-drying phenomena.

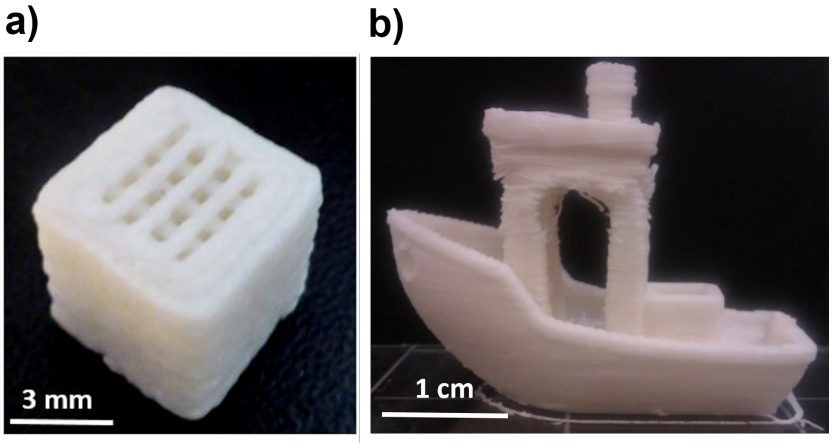

Figure 4.1: 3D printed parts made up of aqueous cellulose based paste, (a) a 3D cube and (b) a 3D boat. [Thibaut, 2020]

4.2.2 Aim of the analysis

The objective of the study was to quantify the macroscopic shrinkage behaviour during the air-drying phenomena of the 3D printed sample and explain the micro-mechanics occurring at the filament scale.

All three proposed image analysis levels L1, L2 and L3 were decided to be performed on intended in-situ drying application. L1 analysis was performed on the 3D rendered cross-sectional view of reconstructed X-ray tomographic scans at different drying times. For L2 analysis, the quantification of the solid and porous phase volume was done. For L3 analysis, the identification and characterization of pores present in the sample were done. Moreover, the kinematic analysis was performed by applying digital volume correlation (DVC) to compute

the displacement and corresponding strain fields at the local filament scale. This also allowed the tracking of the individual pores to monitor their morphological evolution during the drying phenomena.

For such study, a simple 9^3 mm^3 3D printed cube, Figure 4.1(a), was selected for the monitoring of air-drying phenomena. The printing speed was 10 mm/s leading to a printing time of about 3 minutes. For the in-situ observation, the whole sample needed to be in the field of view to monitor the macroscopic deformation, and the resolution of the scan (temporal and spatial resolution) needs to be adequate enough (compatible with the drying time) to quantify the microstructure evolution at the filament scale.

4.2.3 Technical constraints

4.2.3.1 Fixed parameters of the tomograph

The 3D cellulose printed cube air-drying monitoring application was performed using the CT facility in laboratory 3SR. The CT system is equipped with micro-focus X-ray tube (Hamamatsu Corporation L8121-03 X-ray sealed source) and an "indirect" flat-panel Varian PaxScan® 2520.

In the tomograph setup, the detector flat-panel position is fixed at a distance of 766 mm from the source focal point. Therefore, higher magnification can only be achieved by placing the sample close to the X-ray source.

4.2.3.2 Detector capacity

The flat-panel detector can be operated in 3 operating modes: (i) No binning: the detector is operated in full pixel mode, and the pixel size of the detector is 127 μm. The maximum frame rate in this mode is 12.5 frames per second. (ii) Binning 2: 2x2 pixels of the detector are grouped together to create larger pixels with a pixel pitch of 254 μm and a maximum frame rate of 30 frames per second can be achieved. (iii) Binning 4: 4x4 pixels of the detector are grouped together to create larger pixels with a pixel pitch of 508 μm and a maximum frame rate of 60 frames per second can be achieved.

4.2.4 Methods and results

4.2.4.1 Influence of CT geometry

The specimen position was selected by moving it close to the X-ray source, and the effect on the field of view, magnification and voxel size was observed with all three binning modes of the detector. The source-object distance of 42 mm was selected as the optimal position. The SOD of 42 mm results in the magnification of 18 and the full field of view of the specimen at the voxel size of 7, 14 and 28 μm with no binning, binning 2 and binning 4 modes of the flat-panel combined with small and middle focal mode of the X-ray source (small focal mode for voxel size of 7 μm and middle focal mode for voxel size 14 and 28 μm). Moreover, no binning, binning 2 and binning 4 modes result in almost 100, 50 and 25 pixels in the diameter of the filament. These number of pixels are sufficient to perform high-level quantitative analysis as explained in

Chapter 1, Section 1.3.

4.2.4.2 Influence of source parameter

The X-ray source was operated using the middle focal spot mode, based on the voxel size, at the maximum power of 30 W. An acceleration voltage of 100 kV and a filament current of 300 μA was selected in order to get the maximum flux of the X-ray photons. Although high energy (kV) results in the reduction of image contrast, the specimen, in our case, is of homogeneous material, so these parameters still result in good image contrast. An Aluminum Al filter of the thickness 0.5 mm was placed in front of the X-ray source to eliminate the lowest energy photons.

4.2.4.3 Influence of the number of projections

In order to understand the effect of the number of projections on the resultant quantitative measurements, several studies were carried out during the first year of the thesis. The image quality indexes such as a relative change in solid volume, root-mean-square error (RMSE), signal-to-noise ratio (SNR) and contrast-to-noise ratio (CNR) were estimated on the reconstructed datasets as a function of decreasing number of projections to quantify the effect of undersampling artifacts. One of the studies is briefly presented here.

A 3D printed boat, Figure 4.1(c) was scanned using the micro-focus X-ray source and flat-panel detector at a source-object distance (SOD) of 229 mm and source-detector distance (SDD) of 766 mm. Combined with the detector pixel pitch of 127 μm, this results in a voxel size of 38 μm. X-ray source was operated at 100 kV voltage and 300 μA current. A total of 1440 projections were recorded with an average of 6 at a frame rate of 12.5 frames per second. The reconstruction was performed by using the conventional filtered back-projection algorithm. The number of projections used for the reconstruction was reduced to half, equally distributed over 360°, after each iteration.

Figure 4.2 shows the 2D reconstructed horizontal slices of a 3D boat with decreasing number of projections from 1440 to 23 projections. The corresponding vertical slices reconstructed with three different numbers of projections (1440, 360 and 23) are shown in Figure 4.3. The boat is well reconstructed for a full set of 1440 projections and by reducing the projections to 720 and 360, no significant artifacts are visible on the images. The undersampling artifacts can be observed in the images reconstructed with 180 and lower number of projections significantly affecting the images quality. However, the 3D boat specimen is still clearly identifiable in the image.

In order to quantify the effect of decreasing number of projections, all reconstructed datasets were segmented using the same threshold value, computed by the inter-mean method implemented in ImageJ, and the resultant solid volumes were computed using the thresholded datasets. After, the relative change in solid volume was computed using the solid volume for 1440 projections as reference. It is plotted as a function of the number of projections, presented in Figure 4.4.

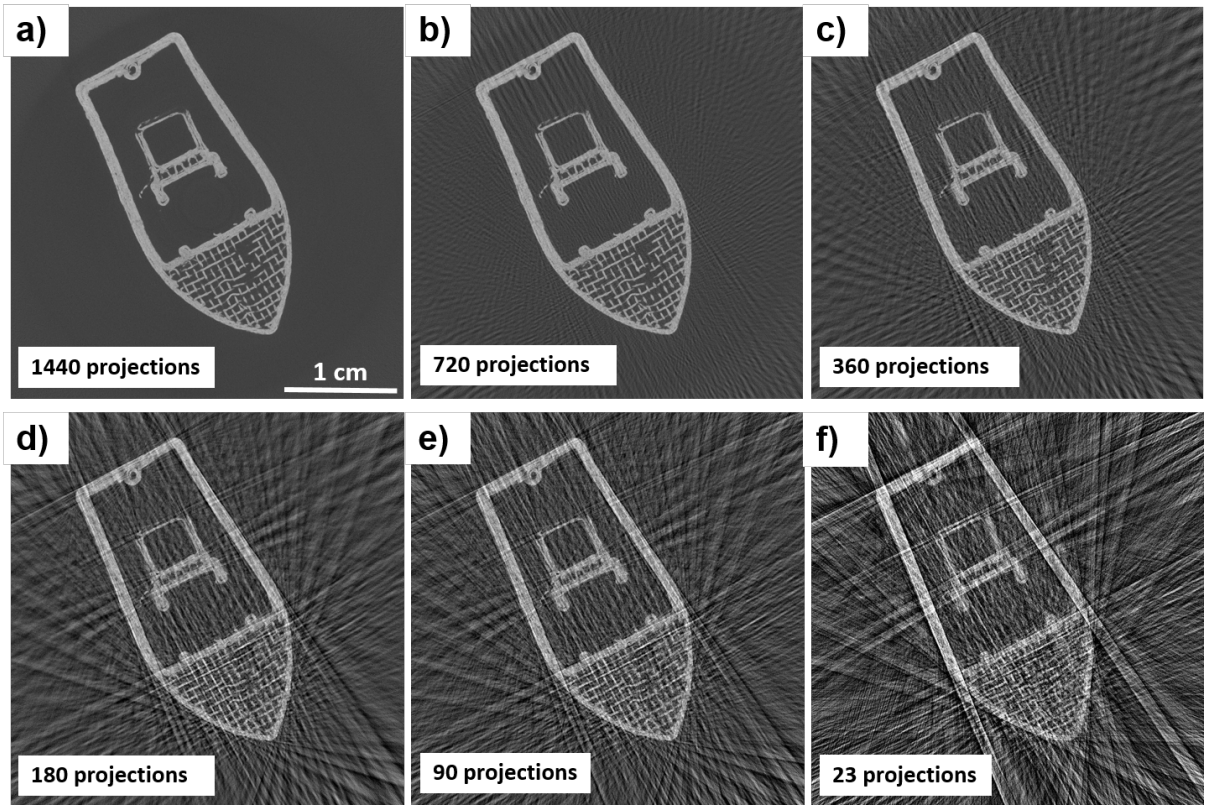

Figure 4.2: 2D reconstructed horizontal slices of a 3D printed boat by using a decreasing number of projections from (a) 1440 to (f) 23 projections.

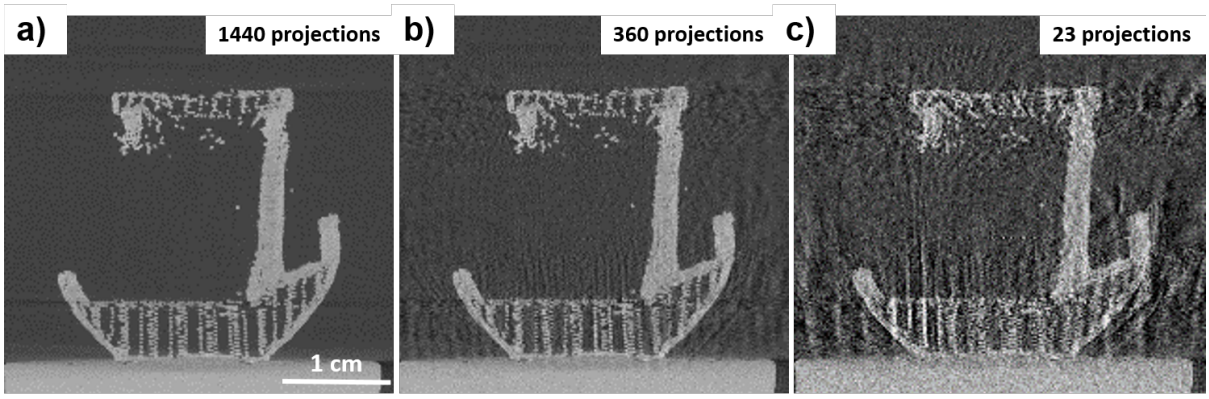

Figure 4.3: 2D reconstructed vertical slices of a 3D printed boat by using a decreasing number of projections from (a) 1440 to (c) 23 projections.

It can be observed in Figure 4.4, that the relative change in the solid volume is close to 0 for a number of projections larger or equal to 360. Reducing the number of projections below 360 resulted in a higher deviation in the relative change in the solid volume, which is about 12% for 180 projections and 32% for 90 projections. Therefore, it can be noted that by decreasing the number of projections, global parameters such as solid volume categorized into L2 level (low-level quantitative) analysis can be measured with good accuracy, but the presence of ray aliasing artifacts (undersampling) visible on the images in Figure 4.2 can significantly effect the measurement accuracy of local parameters that comes under L3 level (high-level quantitative) analysis.

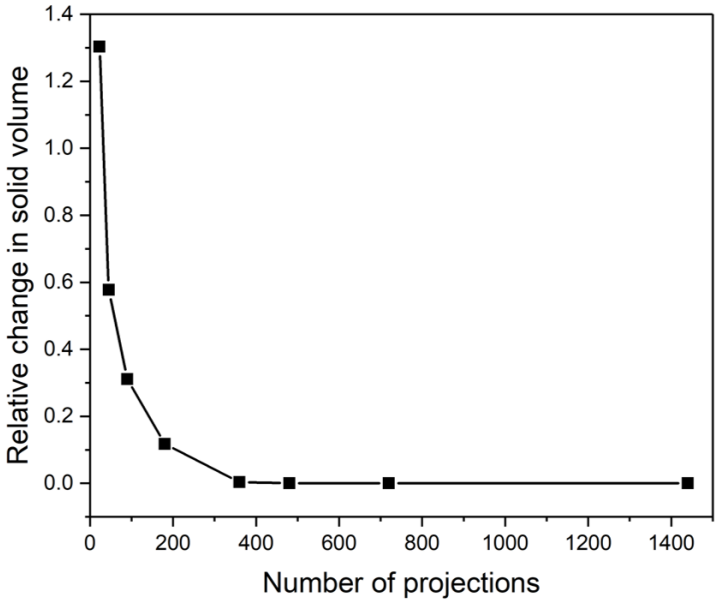

Figure 4.4: Relative change in solid volume of a 3D printed boat as a function of number of projections.

4.2.4.4 Influence of the detector parameters

Each operating mode of the flat-panel detector has limitations in the maximum number of frames that can be captured per second, which limits the acquisition time of a scan. The air-drying of the 3D printed cellulose specimen occurs relatively fast in the initial stage of drying [Thibaut, 2020] and in order to capture the macroscopic and microscopic deformation behaviour during this stage, a sub-minute scan time was required.

Using no binning and binning 2 modes of the detector and acquiring the suitable number of projections (Nyquist sampling theorem) with suitable projection averaging (3 or 6) combined with the maximum frame rate (12.5 and 30 frames per second), result in the scan time in the order of minutes. Even with reducing the number of projections or reducing the projection averaging to half still results in the scan time of few minutes which was not suitable for intended objectives. Figure 4.5 shows the reconstructed 2D slices and the corresponding histograms from the three different scans performed using the three operating mode of the detector keeping the SOD 42 mm, SDD 766 mm, X-ray source parameter 100 kV and 300 μA, and 6 number of projection averaged constant. It can be noted that all images are of good contrast but a clear difference in the resolution can be observed (zoomed section of the images).

Figure 4.5(a) presents a reconstructed 2D slice from the scan acquired with the no binning mode of the detector resulting in a voxel size of 7 μm. 1440 radiographs with an average 6 were recorded at 2 frames per second, resulting in a scan time of 72 minutes. It can be seen that the slice exhibit a good quality and resolution: the small intra-filament pores are visible. However, the scan time is significantly large which limits to capture the deformation mechanism during drying. Increasing the frame rate to 12.5 frames per second with the same number of projections and projection average, resulted in 12 minutes scan time which still did not solve the issue.

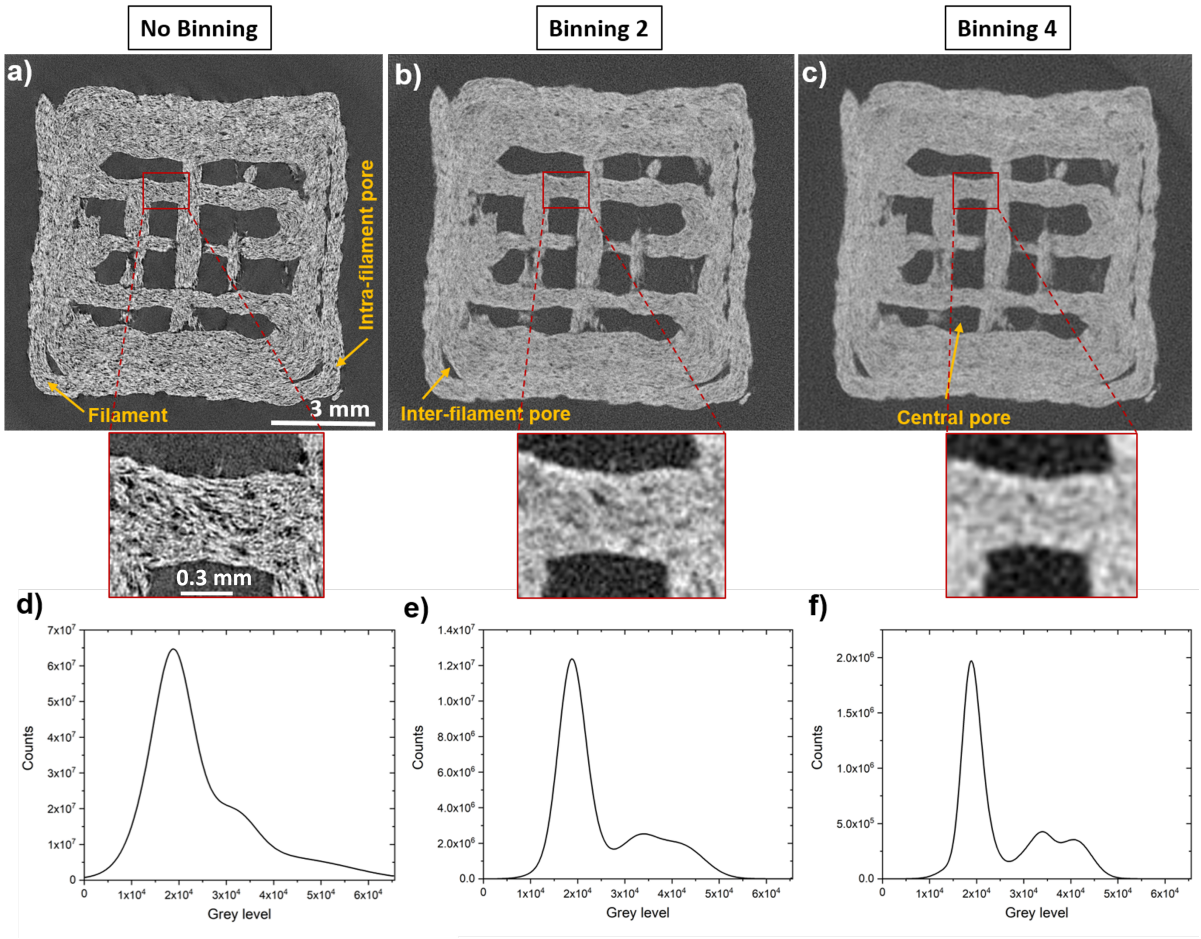

Figure 4.5: 2D reconstructed slice and the corresponding histogram of a 3D printed cube using different operating modes of the flat-panel detector. (a & d) Binning 1 mode containing 1840 x 1456 pixels and at a voxel size of 7 μm (b & e) Binning 2 mode containing 920 x 728 pixels and at a voxel size of 14 μm, (c & f) Binning 4 mode containing 460 x 364 pixels and at a voxel size of 28 μm.

Figure 4.5(b) presents a reconstructed 2D slice from the scan acquired using the binning 2 mode of the detector at a voxel size of 14 μm. 940 radiographs with an average 6 at 9 frames per second were recorded resulting in a scan time of 10 minutes. Using the maximum frame rate of 30 can reduce the scan time to 3 minutes which is still significantly larger than the required sub-minute scan time. It can be noted that most of the small intra-filament pores visible in Figure 4.5(a) are not clearly visible due to decrease in the resolution of the scan but the larger inter-filament and intra-filament pores are clearly distinguishable. The zoomed section of Figure 4.5(b) illustrate the decreased resolution compared to Figure 4.5(a).

Figure 4.5(c) shows a reconstructed 2D slice captured using the binning 4 mode of the detector at the maximum possible frame rate of 60 per second. 720 projections with an average 6 were recorded resulting in scan time of 72 seconds at a voxel size of 28 μm. At such pixel size and the induced resolution, smaller intra-filament pores are not clearly visible, but their texture can be identified in the zoomed section of Figure 4.5(c). The larger central, inter-filament and intra-filament pores can be identified in the image.

The decreased resolution of the scan is further illustrated in Figure 4.6 in which the

volume fraction of the cube as a function of binning mode is presented. A 25% increase in the volume fraction is observed using binning 4 mode compared to no binning mode. The increase is due to the over estimation of the solid volume in binning 4 mode. Due to the decreased resolution of the scan the small pores are not visible in the 3D images and they're thresholded as solid volume leading to over estimation of the volume. Moreover, a relative change of 10% in volume fraction is observed with using binning 4 mode compared to binning 2 mode.

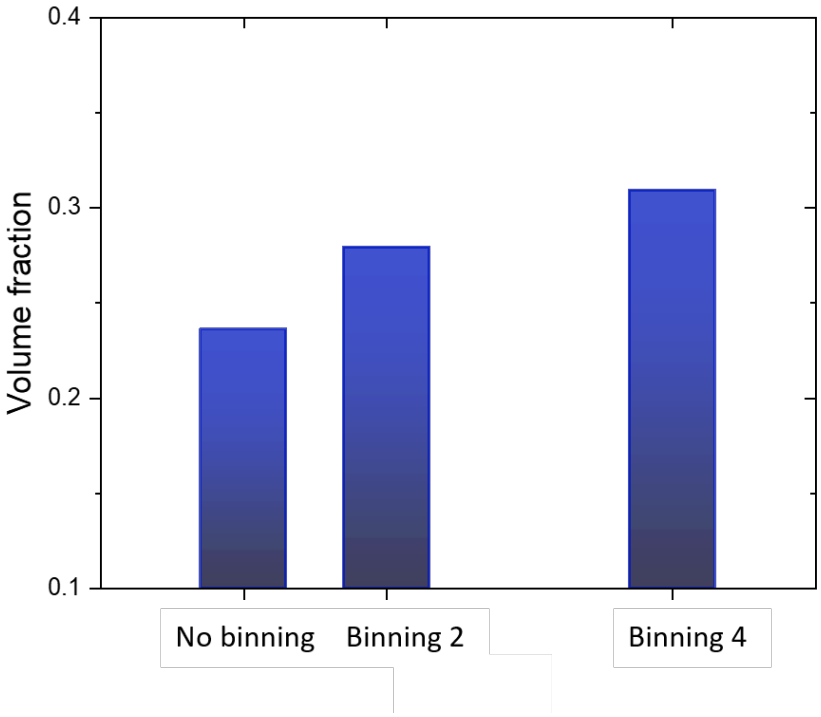

Figure 4.6: Volume fraction of the 3D printed cube using different operating modes of the detector.

However, despite the limitation in spatial resolution with binning 4, the acquisition conditions resulted in the scan time in the order of a minute which can be further reduced by reducing the frame average and the number of projections. Based on the presented analysis, we selected the binning 4 mode of the detector and frame rate of 60 frames per second for the drying application as these conditions can result in scan time fast enough to capture the macroscopic deformation behaviour of the specimen as well as the behaviour of the larger pores.

4.2.4.5 Influence of number of projections averaging

In order to optimize the number of projections averaging, different scans with a varying number of projections averaging were recorded using the already optimized parameters (binning 4 mode with frame rate 60 frames per second, voxel size of 28 μm, 100 kV voltage and 300 μA current). The effect on the image quality of the radiographs and projections was studied. Figure 4.7 shows the 2D reconstructed slices and the corresponding histograms of the 3D printed cube with varying projection averaging 1, 3 and 6. The artifacts seen on Figure 4.7(a) come from the speed of the rotation stage and not from the average 1. No clear visible difference can be seen in Figure 4.7(b) and Figure 4.7(c) with average 3 and average 6, however the histogram of the average 6 shows slight improvement, Figure 4.7(f). The scan time for the three scans were 12,

36, and 72 seconds.

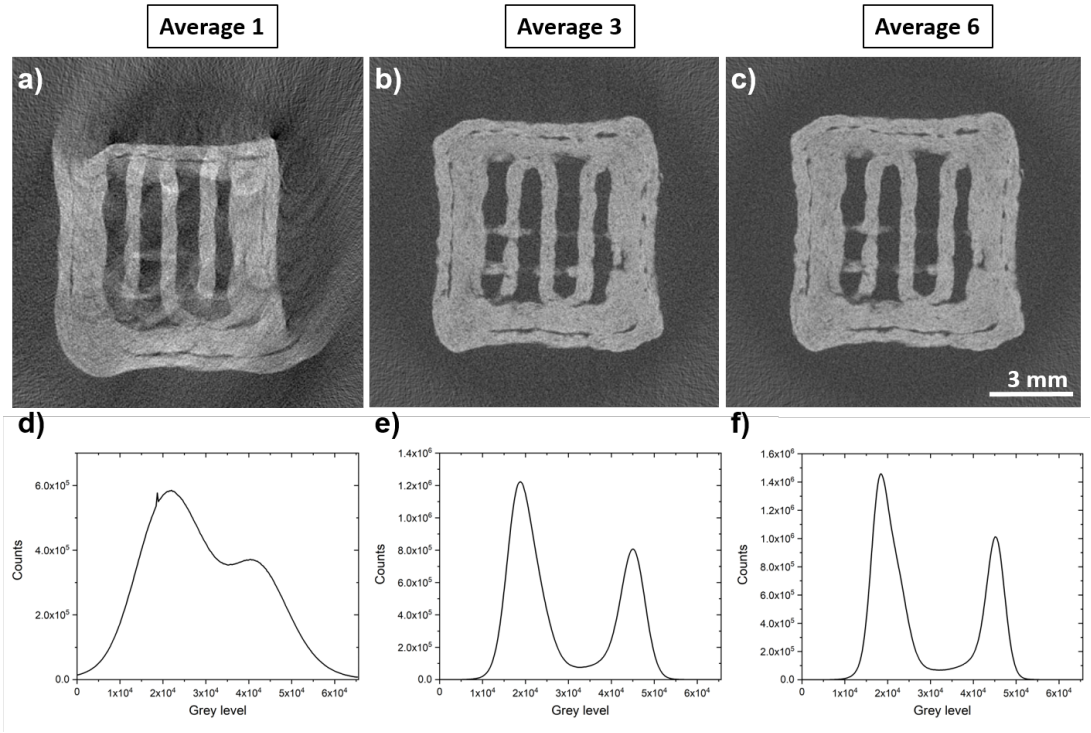

Figure 4.7: 2D reconstructed slices and the corresponding histograms of a 3D printed cube using different number of projection averaging keeping all other CT parameters constant. Number of projection average (a & d) 1, (b & e) 3, (c & f) 6.

In order to quantify the image quality, the effect on the signal-to-noise ratio (SNR) was studied. SNR was computed in a small ROI in the image background in both radiographs and reconstructed slices. The results are illustrated in Figure 4.8 where SNR is plotted as a function of average of the number of projection. It can be seen that the SNR improves with increasing the number of projection averaging from 1 to 3 and after that the increase in SNR is less significant. Moreover, a linear relationship can be observed between the SNR on the radiographs and reconstructed slices, Figure 4.8(b).

Furthermore, the reconstructed CT volumes with average 3 and average 6 were segmented by applying the same threshold to both datasets. The resultant solid volume was computed for both scans from their corresponding segmented datasets and percentage change in volume was analyzed. The resultant change in solid volume was found to be less than 1% which illustrates the similar image quality with average 3 and average 6. Moreover, by using the projection average 6, the scan time increases by the factor of 2, 72 seconds, compared to the projection average 3, 36 seconds. Based on the presented analysis that no significant image quality variation is observed with projection average 3 and 6; projection average 3 was used for the drying in-situ study.

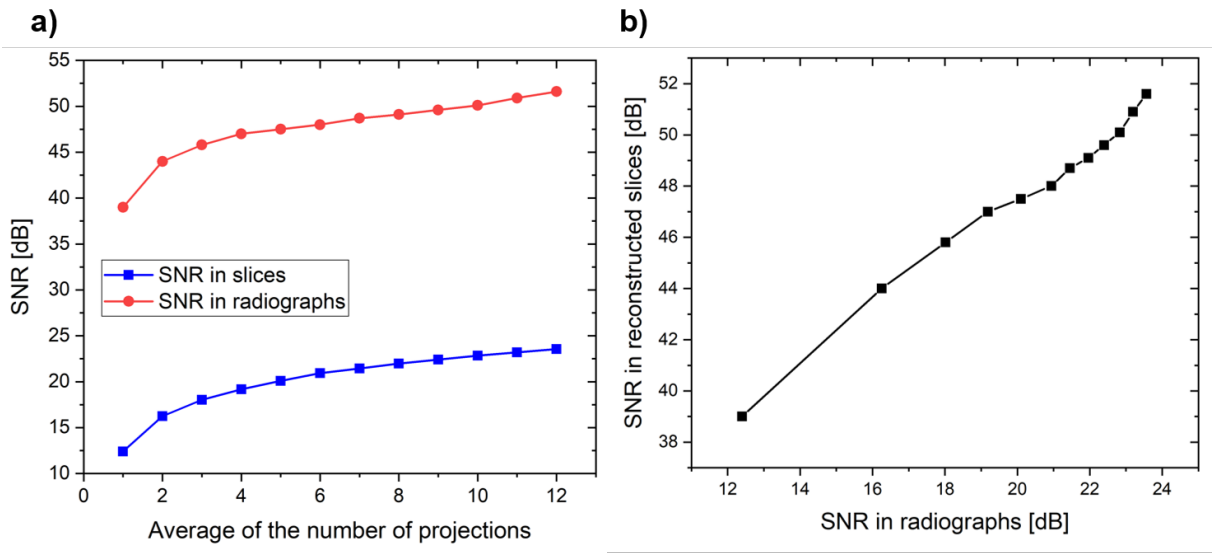

Figure 4.8: (a) Signal-to-noise ratio on the radiograph and on the reconstructed slices as a function of the average of the number of projections with all other CT parameters constant. (b) Relationship between signal-to-noise ratio on the reconstructed slices and on the radiographs with the increasing average from 1 to 12.

4.2.4.6 Proposed optimized configuration

No further analysis was done on the image quality with a projection average 2 or by reducing the number of projections as the scan time with 720 projections and frame average 3 at 60 frames per second is already fast enough and compatible with the drying rate to capture the macroscopic and microscopic deformation. These optimized parameters are summarized in Table 4.1.

Table 4.1: Optimized parameters by experimental screening for drying in-situ test.

Scanning Parameters	**Value**
X-ray voltage [kV]	100
X-ray current [μA]	300
SOD [mm]	42
SDD [mm]	766 (fixed in the tomograph)
Voxel size [μm]	28
Exposure time [s]	0.0167 [60 frames per second]
Average frame	3
Number of projections	720
Scan time [s]	36

4.3 Optimization model parameters and confrontation with the experimental parameters

4.3.1 Input parameters

The optimization model presented in Chapter 3 was used to estimate the suitable acquisition parameters and predicted output configurations are confronted with the experimental configuration.

The geometric, absorption and technical constraints and the aim of analysis were given to the model as input parameters. Cellulose is an organic compound, its chemical formula and density were used as input parameters for the generation of X-ray spectrum to compute the output intensity on the detector pixel and the image contrast. Since the detector position is fixed in the laboratory 3SR tomograph setup, the source-detector distance (SDD) of 766 mm was also fixed in the model.

Detector's binning 4 settings were used as a technical constraint in the model which gives the detector size of 460 x 364 with a pixel pitch of 508 μm. In order to get the output configuration with the full field of view of the specimen, an additional boundary condition was implemented in the model to have the number of pixels in the sample diameter less than 350 in both horizontal and vertical direction (364 is the size of the detector in the vertical direction). Moreover, in order to get the scan time under sub-minute, an exposure time of 0.0167s (60 frames per second) was directly used as a technical constraint. A filament of a mean diameter 720 μm was inserted as the feature of interest. The interface velocity of the filament was measured from the experimental dataset by measuring the change in the thickness of a single filament located on the top side of the cube during the initial two scans and was found to be 20 μm/min. It should be noted that the interface velocity of the filament was not constant during the whole drying phenomena and it changes with the filament location in the cube and with the different drying stages. The different input parameters given to the model are listed in Table 4.2

Table 4.2: Input parameters to the optimization model.

Input parameters	**Value**
Sample diameter [cm]	0.9
Matrix material	Cellulose [$C_6H_{10}O_5$]
Matrix material diameter [cm]	0.45
Matrix material density [g/cm^3]	1.5
Inclusion material	none
Feature of interest [μm]	720
Sample holder diameter [mm]	25
SDD [mm]	766
Range of voltage [kV]	30 to 100, step = 10
Exposure time [s]	0.0167
Range of projection average	1 to 6, step = 1
Detector size	460 x 364
Detector pixel pitch [μm]	508
Kinetic evolution of feature [μm/min]	20
Level of analysis	L3: high-level quantitative

4.3.2 Model output configurations and discussion

Based on the given input parameters and their corresponding iteration step, the optimization model estimated 144 different configurations in the output tabular file along with the estimation of the resolution, contrast, motion, and weighted average error in the segmented volume of the interested feature size. One of the suitable configurations that estimate the minimum weighted average error with sub-minute time scan is presented in Table 4.3(a). The presented model configuration is quite in-line with the experimental configuration that is presented in Table 4.3(c). Table 4.3(b) presents the same model predicted configuration but using SOD 42 mm, which was used during the experiment.

Table 4.3: Comparison of model-based predicted configuration and experimental configuration.

Scanning parameters	**(a) Model parameters**	**(b) Model parameters at SOD 42 mm**	**(c) Experimental parameters**
SOD [mm]	40	42	42
X-ray voltage [kV]	100	100	100
X-ray current [μA]	300	300	300
Contrast	0.56	0.56	0.43
Voxel size [μm]	26	28	28
Magnification	19.4	18.2	18.2
Average frame	3	3	3
Number of projections	540	502	720
Scan time [s]	27	25	36
Number of pixels in the diameter of FOI	28	24	24/25
Motion during a scan [pixels]	0.36	0.32	Less than 1 pixel
Average error in FOI	Less than 1%	Less than 1%	–

A 4x4 binning mode results in higher photon flux on the detector resulting in higher SNR and higher probability of detection of the feature size but at the expense of resolution. According to the output configuration, a slight improvement in the magnification and voxel size can be made by further decreasing the source-object distance (SOD) keeping the SDD fixed at 766 mm to improve the scan resolution. In the present case, the feature size of 720 μm results in 28 pixels in the diameter of the feature in the radiographs and combined with image noise results in the weighted average error of less than 1%. In the noise model, a sphere with a maximum diameter of 20 pixels was modelled so the weighted average error is estimated based on it which might result in small fluctuation in the measurement.

According to the model output parameters, a 100 kV acceleration voltage results in the output image contrast of 0.56. The specimen is made up of homogeneous material (cellulose paste), so the contrast was computed by using the integrated intensity after passing from the specimen and background intensity which results in relatively good contrast at 100 kV voltage. Since the detector response is not modelled in the model, it leads to the over-estimation of the image contrast compared to the experimental value of contrast. Although the lower value of voltage results in higher contrast but no significant change in the weighted average error was

observed due to the reasons explained in Chapter 3, Section 3.3.1 that power is kept constant in the model for changing voltage and criteria on the weighted average error on the basis of voltage needs to be implemented.

In the presented configuration in Table 4.3(a), 25% less number of projections are estimated in the first iteration using the Nyquist sampling theorem, compared to the experimental value. However, as explained previously, this initially estimated number of projections are significantly large and half of them can be used without much affecting the measurement accuracy. Figure 4.9 shows the evolution of the weighted average error and the standard deviation in weighted average error (in secondary y-axis in red color) as a function of the number of projections keeping all other parameters at their optimal value as defined in Table 4.3(a). We can observe that with 270 projections (50% of the initial projection) the weighted average error in the feature size is 2.9% and it increases to 4.4% by further reducing the number of projections to 135.

The projection average 3 is presented in the table as a suitable configuration, but a lower value can be used without affecting the weighted average error. Acquiring 540 projections with average 3 at the exposure time of 0.0167 seconds resulted in a scan time of 27 seconds. During the scan, the estimated motion according to the input interface velocity at a voxel size of 26 μm is 0.36 pixels per scan, which is relatively low.

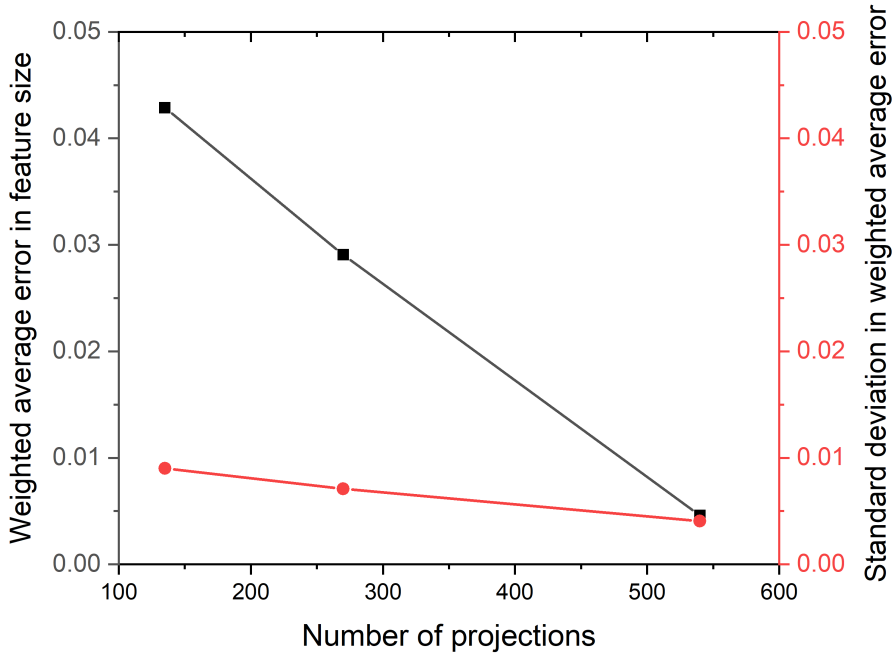

Figure 4.9: The evolution of the weighted average error and the standard deviation in weighted average error (in secondary y-axis in red color) in feature size as a function of the number of projections.

Figure 4.10(a) shows the evolution of the weighted average error and the standard deviation in weighted average error (in secondary y-axis in red color) as a function of the average of the number of projections. It can be noted that measurement accuracy improves with an increase in average. The evolution of the motion in pixels during a scan is presented in Figure

4.10(b) as a function of the average of the number of projections. An increase in the motion with the projection average can be observed in the graph which is due to the increase in scan time keeping 540 projections constant. Furthermore, no change in the weighted average error with increasing the average from 3 to 6 is seen in Figure 4.10(a), this is due to the fact that although the image noise decreases but at the same time an increase in motion results in similar weighted average error value. At average 6, the estimated motion is 0.72 pixels during a scan which is still relatively low and does not significantly affect the measurement accuracy of the feature size.

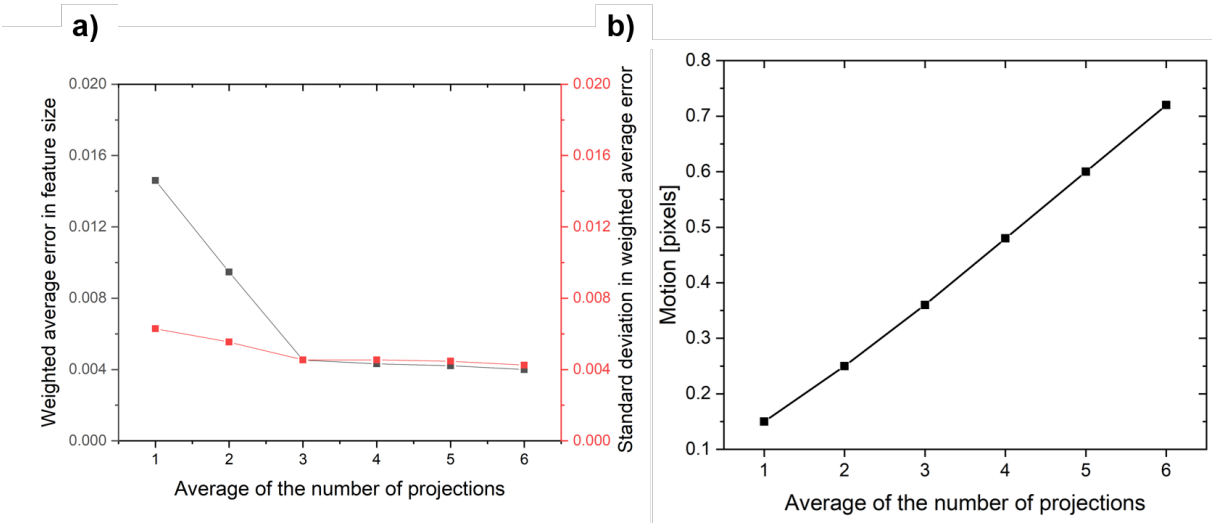

Figure 4.10: (a) The evolution of the weighted average error the standard deviation in weighted average error (in secondary y-axis in red color) in feature size as a function of the average of the number of projections. (b) The evolution of the motion in the feature size as a function of the average of the number of projections.

The optimization model was also run by removing the constraint on the source-detector distance (SDD), but no conclusive trend in weighted average error was found as a function of decreasing SDD due to the reason previously explained in Chapter 3, Section 3.3.1. The decrease in SDD results in a smaller feature size (less number of pixels in the diameter of the feature) due to decreased resolution but also results in a decrease in the image noise due to more flux on the detector. Further criteria on the weighted average error with changing SDD needs to be implemented in the model. By increasing the exposure time from 0.0167 seconds to 0.033 seconds (maximum limit with Binning 4), a slight improvement in weighted was observed. Increasing the exposure time keeping the number of projections and projection average constant increases the scan time which result in an increase in motion of the feature as well.

4.3.3 Conclusion

The model predicted configuration is confronted with the experimental parameters. It is concluded that, for a feature size of 720 μm, both configurations are in-line with each other; and the number of projections could be reduced without affecting the measurement accuracy. In the presented article (next section), only the larger pores with volume greater than 30 voxels were quantified due to the limitation in the spatial resolution that comes from using the binning 4 mode of the detector.

Possibility of higher resolution? For an estimated interface velocity of 20 μm/min the motion of the 720 μm feature is relatively small (less than 1 pixel) with the sub-minute scan time. However, using the binning 2 mode of the detector, the resolution of the scan could have been improved in order to quantify the smaller features in the 3D printed cube to improve the drying quantification. With the same geometry setup, binning 2 mode could result in the voxel size of 14 μm. Although in such case, the limitation of achievable exposure time will increase the scan time resulting in an increase of motion of feature during the scan, but a suitable configuration according to the measurement accuracy can be chosen from the output configurations tabular file of the model in which the effect on the weighted average error with the different number of projections, average, exposure time, and motion is listed. It should be noted that 20 μm/min is an estimated value of the interface velocity, the actual interface velocity in the outermost filament could be higher which will increase the motion of the feature for a given scan time.

Some improvements in the developed optimization model, such as modelling the detector response and improving the noise prediction strategy, as detailed in Chapter 3 Section 3.3, are needed in order to improve the efficiency of the optimization model.

4.4 3D real time monitoring of air-drying of 3D printed part made up of cellulose by fast laboratory X-Ray microtomography

As mentioned in the introduction of this chapter, 3D printing by extrusion has been recently extended to cellulose paste (50% cellulose and 50% water as the binding agent). Once printed, the parts undergo a huge deformation upon air drying. To optimize the printing/drying process of such paste, it is necessary to better understand the drying mechanism and focus on the evolution of deformation at the part's and filament's scale. Based on the optimized configuration obtained experimentally and later validated by the developed model (Section 4.2 and 4.3), real-time monitoring of the air-drying of a cube is performed (Section 4.4.1). The acquired 4D dataset was analyzed qualitatively and quantitatively by applying advanced image analysis protocol (Section 4.4.1) to characterize the drying deformation at the part and filament scale. The obtained results are detailed in Section 4.4.2. The adopted procedure illustrates the possibilities offered by fast quantitative lab-CT imaging to improve the understanding of the drying mechanism of the 3D printed cellulose parts.

4.4.1 Material and methods

4.4.1.1 3D Printed cellulose sample: preparation

One 9^3 mm^3 cube with an inner grid (Figure 4.11a) was printed using an optimized aqueous cellulose-based paste [Thibaut et al., 2019] made up of short cellulose fiber (Figure 4.11c) and Carboxymethyl cellulose (CMC) (Figure 4.11b) using a commercial 3D printer (Prusa i3) upgraded with a liquid deposit modeling (LDM) WASP extruder. The used nozzle had an exit diameter of 0.72 mm. The printing settings specified in the slicing software (Simplify 3D) were as follow: an extrusion width of 0.71 mm, a layer height of 0.45 mm, 2 perimeters shells, a 50% infill with rotation between 0° and 90° angles at every layer, an outline overlap of 60%. The printing speed was 10 mm s^{-1} leading to a printing time of about 3 minutes. The printed cube (Figure 4.11d) was dried at the room temperature at 22±2 °C and 30±3% of relative humidity (Figure 4.11e).

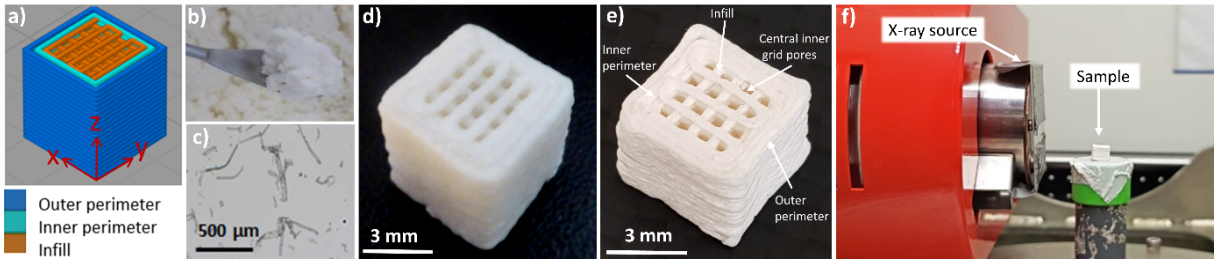

Figure 4.11: (a) 3D STL model of cube. (b) Aqueous carboxymethyl cellulose. (c) Natural cellulose fibers in suspension. (d) Freshly 3D printed cube. (e) 3D printed air dried cube. (f) Sample placed in 3SR laboratory X-ray tomograph.

4.4.1.2 High Speed Laboratory X-ray micro tomography

The monitoring of the drying process of the printed part was performed using the RX Solutions microtomograph located in 3SR laboratory (Figure 4.11f). The acquisition protocol of microtomography was optimized in order to achieve a scanning time of 36 seconds compatible with the typical drying rate [Thibaut et al., 2019] necessary to capture the dynamic material response. The following experimental settings were chosen (i) the X-ray tube (Hamamatsu Corporation L8121-03 X-ray sealed source) was operated in middle focal spot mode at power of 30 W with an acceleration voltage of 100 kV and a filament current of 300 µA. An Aluminum filter, the thickness of whom is 0.5 mm, was placed in front of the X-ray source to eliminate the lower energy photons. (ii) The used detector is an "indirect" flat-panel Varian PaxScan® 2520. It has the capacity to measure the intensity of incident X-ray photons on an array of 1920 × 1536 pixels, with each pixel measuring 127 × 127 µm. The flat-panel Varian was set in binning 4 mode, capturing 60 frames per second with an average of 3 images to produce radiographs. (iii) The distance between the source and the sample was set to 42 mm, and the distance between the sample and the detector was 724 mm. The samples were scanned with the magnification of 18, which gives a voxel size of 28^3 μm^3. (iv) 720 radiographs were recorded over 360 degrees with an acquisition time of 36 s in continuous rotation mode of the rotating stage. This acquisition time was compatible to follow the dynamics of the drying process. Scans were recorded every 4 minutes during 8 hours, leading to a total of 120 scans.

4.4.1.3 Data processing and analysis

4.4.1.3.1 Preprocessing

The acquired 2D radiographs were used to reconstruct the 3D structures using filtered back-projection algorithm implemented by RX solutions. The output is a 3D map of the local coefficient of absorption, which at the first order depends on the local density [Viguie et al., 2011]. Figure 4.12a shows a vertical slice of 3D reconstructed tomography. On the maps, the denser the part, the brighter the grey levels.

4.4.1.3.2 Phase quantification

The output volumes have two phases: a solid and a porous one (Figure 4.12a). These phases can be identified using a thresholding operation. The same threshold was applied to the 120 scans (Figure 4.12b) and was obtained by averaging the threshold value automatically found by iterative intermeans method available in ImageJ [Ridler, 1978a]. The final binarized volumes were cropped (Figure 4.12c) to facilitate the post-processing and to remove the noise that can be observed in Figure 4.12d. Figure 4.12e shows the working volume used to perform the quantitative analysis.

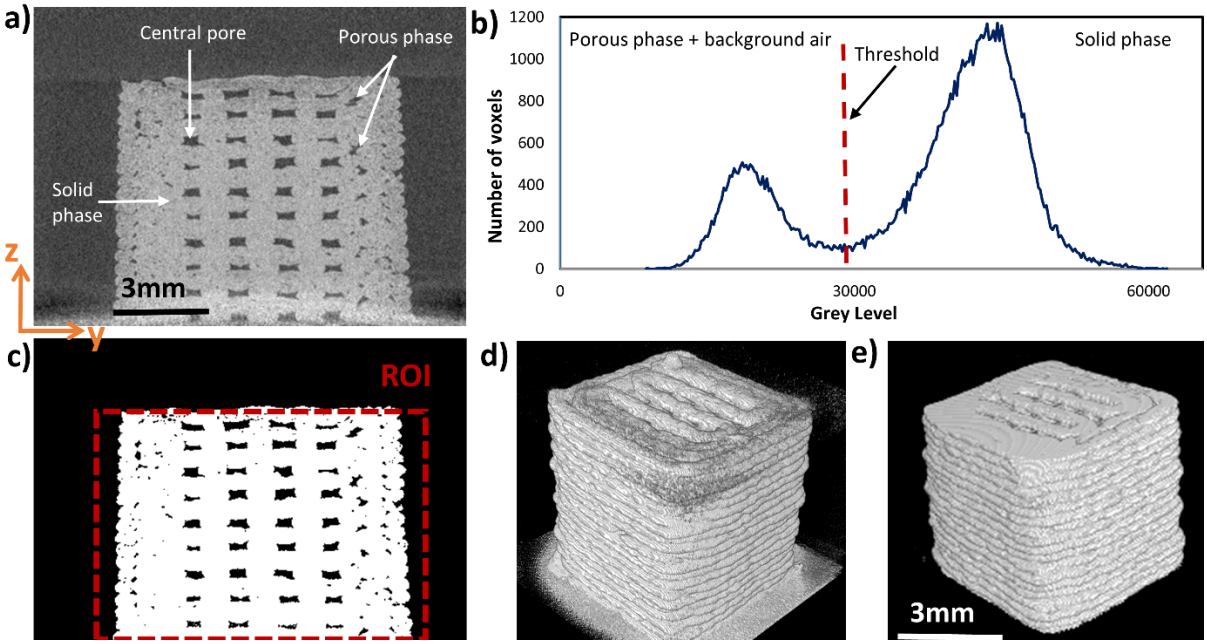

Figure 4.12: (a) Vertical slice of reconstructed radiographs showing cube inner structure and different phases. (b) Histogram of reconstructed volume showing the cut off threshold to distinguish phases. (c) Binarized image of vertical slice of (a), with the region of interest (ROI) marked in dashed red. (d) 3D view of the original binarized volume. (e) 3D view of working volume.

4.4.1.3.3 Microstructural quantification

For such analysis, the binarized volumes were considered.

Volume fraction:

The volume of each phase was computed by multiplying the total number of voxels by the voxel size.

Pore analysis: Identification and characterization:

The pores were identified by labelling the porous phase using the Analysis 3D plugin of ImageJ [Boulos et al., 2012]. It labelled the 3D connected components with a specified connectivity of 26 neighbours. Once identified, the volume and the surface area of each pore were computed using a marching cube algorithm. To quantify the morphology of each pore, its sphericity was computed using Eq. 4.1:

$$Sphericity = 6 * Volume * \sqrt{\frac{\pi}{SurfaceArea^3}} \tag{4.1}$$

The value of sphericity ranges from 0 and 1. A sphericity of 1 corresponds to a perfect sphere whereas a sphericity of 0.1 corresponds to an elongated pore.

4.4.1.3.4 Kinematics analysis

Displacement field and associated strain

In order to study the global and local strain mechanisms during the drying behaviour

of the cube, a 3D Digital Volume Correlation (DVC) technique was used. This technique relies on comparing the pattern matching of two grey intensity images obtained from two consecutive acquisitions [Viguie et al., 2011, Stamati et al., 2020]. This comparison allows the measurement of displacements fields between images of a deforming, drying in our case, sample from which strains can be computed. In this study, the SPAM software [Stamati et al., 2020] was used.

The principle of this software is to divide a reference image into small interrogation windows having a size of N x N x N pixels. Then, the displacement of the summits of small interrogation windows is tracked in the final image using a normalized cross-correlation criterion to find similarities between subsets of the initial image and final image.

- When the interrogation window represents the whole image, the output of the correlation software is an estimate of the global strain in the main direction of the sample. This was used to analyze the macroscopic behaviour during drying.
- When the interrogation window represents a volume of 6 x 6 x 6 pixels centred around the nodes of a 3D regular grid of points (with a node spacing of 4 pixels), the local strains were evaluated at each node. This analysis allows measuring the local strain inside the sample to analyze the microscopic changes that might explain the macroscopic drying behaviour. The local strains were measured in x, y and z direction and were summed to obtain the local volumetric strains.

Pores tracking

To monitor the morphological evolution of pores, they were identified and tracked to follow their evolution during the drying period. For each of the labelled pore obtained using tools presented in Section 4.4.1.3.3 on the binarized data, the centre of mass was identified and the local displacement obtained from the DVC was applied to the centre of the mass. To validate the procedure, we checked for some pores that the pores matching by automatic tracking (via DVC) or manual tracking gave the same results.

4.4.2 Results

4.4.2.1 Preliminary remark

The cropping operation described in Section 4.4.1.3.2 to remove the noise affects only the height of the samples and removed 5% of the total volume. The removed thickness corresponds to less than a filament thickness. Therefore, it does not affect the analysis. In the following, T denotes the time.

4.4.2.2 Analysis at the scale of the part

4.4.2.2.1 Qualitative analysis

Figure 4.13 shows the 3D rendered cross-sectional views corresponding to different acquisition time. We can visually observe a macroscopic shrinkage that stabilized after T = 180 min. This shrinkage occurred mainly in height of the part (z direction). This macroscopic shrinkage was followed by microstructural changes such as crack initiation and propagation which did not affect the outer part of the sample. Moreover, we cannot observe any collapse of the structure. This is due to the rheological behaviour of the paste [Thibaut et al., 2019, Chalencon et al., 2010].

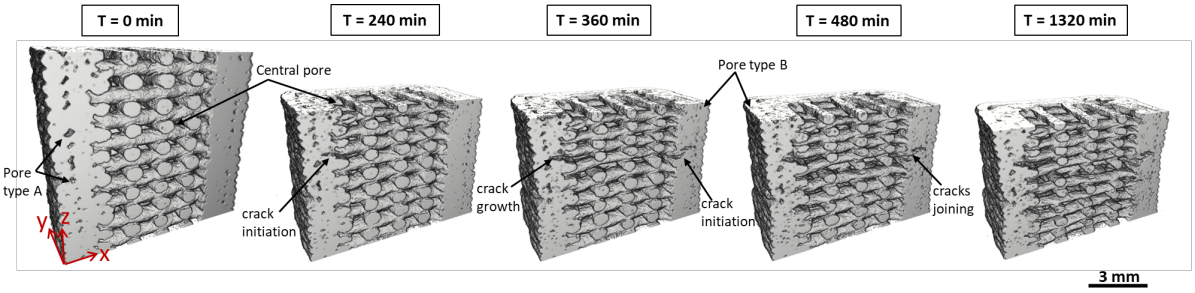

Figure 4.13: 3D rendered cross-sectional view of reconstructed X-ray tomographic scans at different drying time.

4.4.2.2.2 Quantitative analysis

The temporal evolution of strain in the main direction of the cube ϵ_{xx}, ϵ_{yy}, and ϵ_{zz} obtained from the global DVC are plotted in Figure 4.14a. Taking as a reference the first 3D image, the final deformations in x, y and z directions are 5%, 3% and 25%, respectively. This confirms and quantifies the observation made in previous section, where the macroscopic changes occurred mainly in the height of the sample. These orders of magnitudes of variation of the sample's dimensions are consistent with the results reported in [Thibaut et al., 2019], obtained using a calliper or in [Klar et al., 2019] obtained on tomographic data sets.

Moreover, we can observe on Figure 4.14a that the temporal strains ϵ_{xx} and ϵ_{yy} follow the same trend:

- from T=0 to T=120 min, the global strain ϵ_{xx} and ϵ_{yy} exhibit a linear decrease.
- for T > 120 min, the global strain ϵ_{xx} and ϵ_{yy} exhibit a steady-state regime.

We can also observe that the temporal evolution of the deformation ϵ_{zz} exhibits:

- from T=0 to T=480 min an exponential decrease.
- for T > 480 min a steady-state regime.

Comparing the trend of ϵ_{xx}, ϵ_{yy}, and ϵ_{zz}, we can notice a different strain rate of the initial behaviour of the drying process. Part of this anisotropic behaviour can come from the anisotropic drying of a single filament which exhibits larger deformation in the diameter than in the length [Thibaut et al., 2019]. It comes from the high volume fraction of fibres in the paste, these fibres being aligned in the direction of the extrusion and having a lateral shrinkage larger than the axial one upon shrinkage [Wainwright, 1982].

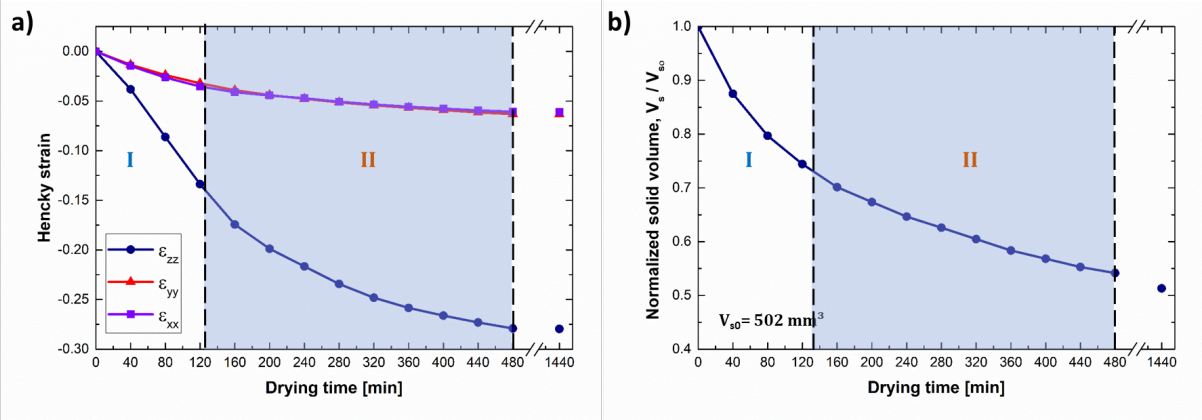

Figure 4.14: (a) Temporal evolution of the Hencky strain in x, y and z direction. (b) Temporal evolution of the normalized solid phase.

Figure 4.14b shows the temporal evolution of the volume of the solid phase normalized by the volume of the solid phase measured on the first 3D data set (evaluated to be 502 mm^3). The final volume at T= 1440 min is 286 mm^3. These orders of magnitudes of mass variations are consistent with the results reported in [Thibaut, 2020].

4.4.2.2.3 Synthesis of the scale part analysis

All the previous remarks/observations are coherent with the measurements obtained with classical procedures on the same types of samples [Thibaut et al., 2019, Thibaut, 2020]. Therefore, further analysis can be carried out at the scale of the constituents that is the pore scale and the filament scale.

4.4.2.3 Filament scale analysis

Figure 4.15a shows 3D views of the local volumetric strain obtained by correlating two data sets for T and T+20 min. Figure 4.15b and Figure 4.15c represent the temporal evolution of the same (y,z) and (x,y) planes, respectively. These figures show that:

- for T = 0-20 min, the local volumetric strains are mainly negative with volumetric strain down to -0.12. These highest negative values are located on the external surfaces of the

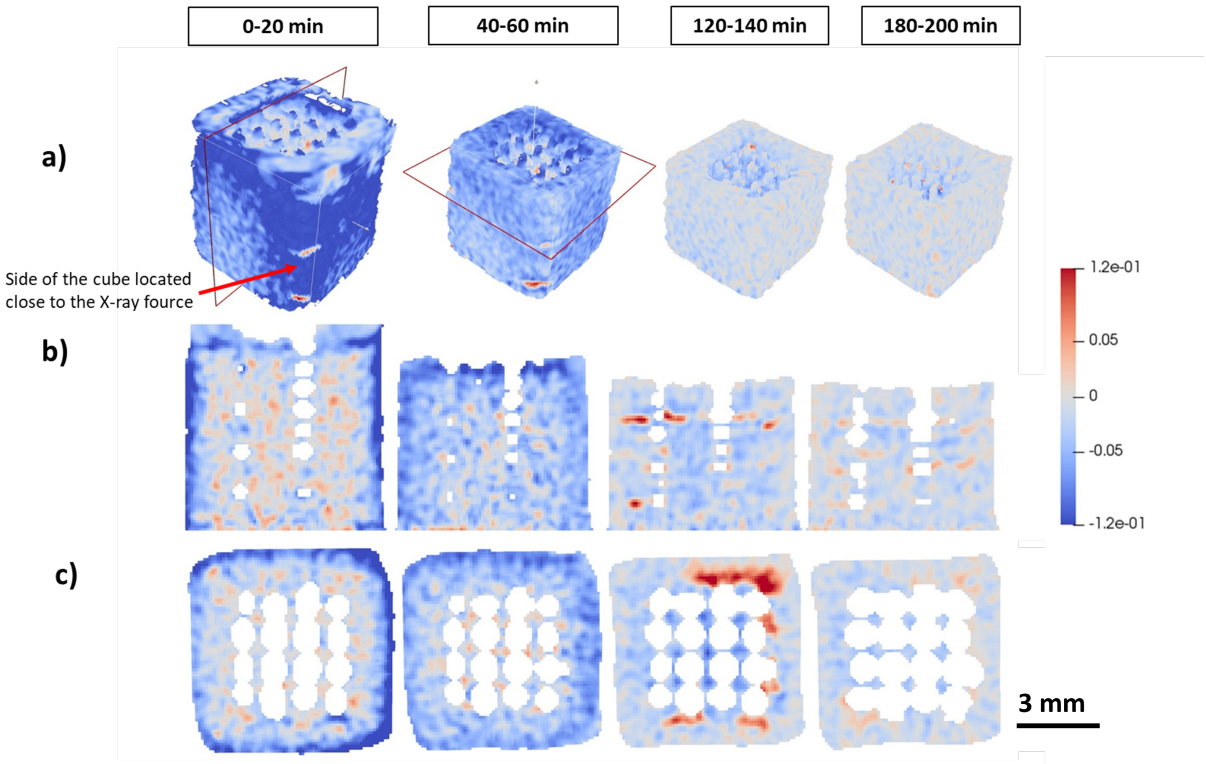

Figure 4.15: Temporal evolution of the volumetric strains (a) 3D views, (b) same vertical slice (c) same horizontal slice.

sample that are the largest areas in contact with air: this facilitated moisture transport [Thiery et al., 2017, Zhou et al., 2019, Tang and Min, 2018]. We can also notice larger local negative volumetric strain on one face compared to the other one. This might be due to faster drying of the side of the cube located closed to the X-ray source. Namely, to stabilize the X-ray source, it was not switched off during the waiting time between two scans. This induced a temperature of 36 °C inside the X-ray source and an estimated temperature gradient around the sample of 3°C/cm. This higher temperature induced upon drying some filaments delamination (illustrated by the local positive volumetric strain close to the red arrow on Figure 4.15a), which did not induce a collapse of the structure. Inside the sample, we do not observe highly negative strains close to the central pore despite the fact that this surface was large enough to facilitate water evaporation. This might be explained by the 50% infill of the printing parameters that created a tortuous central pore, which reduces the drying rate for the parts of the cube in contact with the central part. We can also observe that local negative strains are located inside the filaments and were mainly induced by their vertical shrinkage. This phenomenon appeared to be more pronounced at the bottom of the sample than at its top. On the opposite, we can observe that the local positive strains are located at the edges of the filament in contact with the central pore and correspond to their horizontal expansion. These two observations explain why the final shape of the filament is oval and not circular, as illustrated in Figure 4.13, and already observed in [Klar et al., 2019]: as an homogeneous lateral shrinkage was observed during the drying of a single filament, this anisotropic behaviour of the lateral shrinkage upon drying is a combination of diameter reduction due to drying enhanced by the weight of the upper filaments. The lateral expansion that occurs mainly during the first part of

the drying is referred as "collapse" in [Klar et al., 2019]. This "collapse" is limited and did not induce a collapse of the structure due to the rheological properties of the paste [Thibaut et al., 2019].

- for T = 40-60 min, we can observe homogeneous local volumetric strains, except at the top surface where we can observe the major volumetric strains (down to – 0.12). We can notice that close to the central pore the volumetric strains are close to 0, showing that this region stabilized first, as these areas were in contact with air and that the "collapse" rate of the filament decreased.

- for T = 120-140 min, the correlation did not show any major changes. However, we can observe positive large volumetric strains up to 0.12 which corresponds to the zone where delamination effects took place as illustrated in Figure 4.13. The drying mechanisms modified the structure at a scale that the correlation cannot capture. Namely, capillary effect probably took place during this stage [Thiery et al., 2017, Zhou et al., 2019].

- for T > 180 min, the correlation did not show any major changes in the global shape of the samples or inside the sample.

4.4.2.4 Pore scale analysis

Pores that exhibited a volume smaller than 30 voxels ($6.58\text{x}10^{-4} mm^3$) were discarded as most of these pores can be linked to the threshold sensitivity.

4.4.2.4.1 Pore classification

The 3D images of Figure 4.13 exhibit three types of pores (i) a central pore that exists in the CAD model. It is the single pore to be expected in the 3D printed part, (ii) inter-filament pores that are the pores located in between two filaments and (iii) intra-filament pores that are the pores located inside the filaments. The inter-filament pores are due to the successive deposition of layer during the printing process whereas the intra-filament ones come from the extrusion process of the filament [Thibaut, 2020, Markl et al., 2017]. Figure 4.16a and b represent side and top view of the initial 3D structure: the central, type A and type B pores were labelled in green, red and B blue, respectively. Figure 4.16c shows a 3D rendering of the inter-filament and intra-filament pores where the structural differences between the two types of pores can be observed. These two last types of pores were automatically identified based on their sphericity: inter-filament pores exhibited a sphericity smaller than 0.5 and are referred as pore type A whereas intra-filament pores exhibited a sphericity larger than 0.5 and are referred as pore type B.

4.4.2.4.2 Central pore classification

Figure 4.17a represents the temporal evolution of the volume of the central pores, which was normalized by its initial volume. The initial volume of central pore measured in the ROI was 94 mm^3, this is in accordance with the theoretical initial volume. On Figure 4.17a, we can observe:

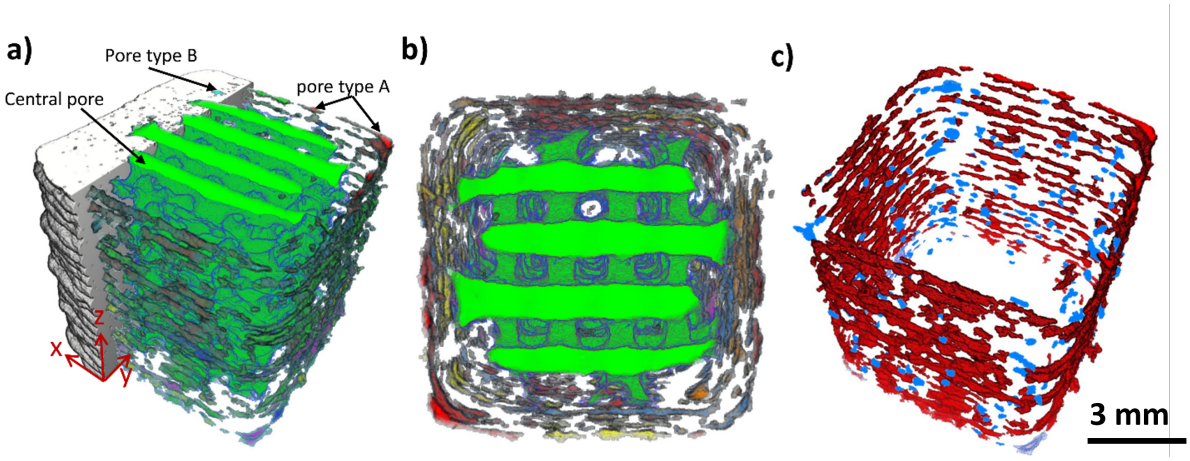

Figure 4.16: (a) 3D rendered view of the sample identifying central pore (green) type A pores and type B pores. (b) 3D rendered top view of the porous phase. (c) Labelled 3D view identifying type A (red) and type B (blue) pores.

- from T=0 to T=80 min, a linear decrease of the volume of central pores with time. The behaviour of the central pore during the first 80 minutes of drying can be directly linked to the macroscopic shrinkage of the sample (Figure 4.14a).
- from T= 80 min to T= 120 min, a less pronounced decrease of the volume of the central part. Compared to the first part of the curve, the rate of the macroscopic shrinkage (Figure 4.14a) remains constant which induces a decrease of the height of the central pore. However, we can observe that inter-filament pores, located close to the borders of the central pore (Figure 4.17a), opened and joined the major pore. This slowed down the volume decrease of the central pore.
- from T= 120 min to T= 160 min, a stabilization of the volume of the central pore. During this time interval, the rate of the macroscopic shrinkage (Figure 4.14a) remains constant which induces a decrease of the height of the central pore which is balanced by the opening of some inter-filament pores joining the central pore.
- for T > 160 min, a linear increase of the volume of the central pore. During this time, we do not observe any macroscopic shrinkage, leading to a stabilisation of the main dimensions of the part. The opening of inter-filament pores joining the central pores, as illustrated in Figure 4.13, explains the increase of the central pore volume.

4.4.2.4.3 Temporal evolution upon drying of inter-filament and intra-filaments pores

Figure 4.17b and Figure 4.17c show the temporal evolution of the total number of pores that is to say the inter-filament pores (type A) and intra-filaments pores (type B) and the temporal evolution of the volume of these pores, respectively. We can observe that the inter filament pores represent, during the whole drying process, the higher number of pores and the higher cumulative volume. Therefore, the temporal evolution of the pores characteristics is mainly driven by the one of the inter-filament pores.

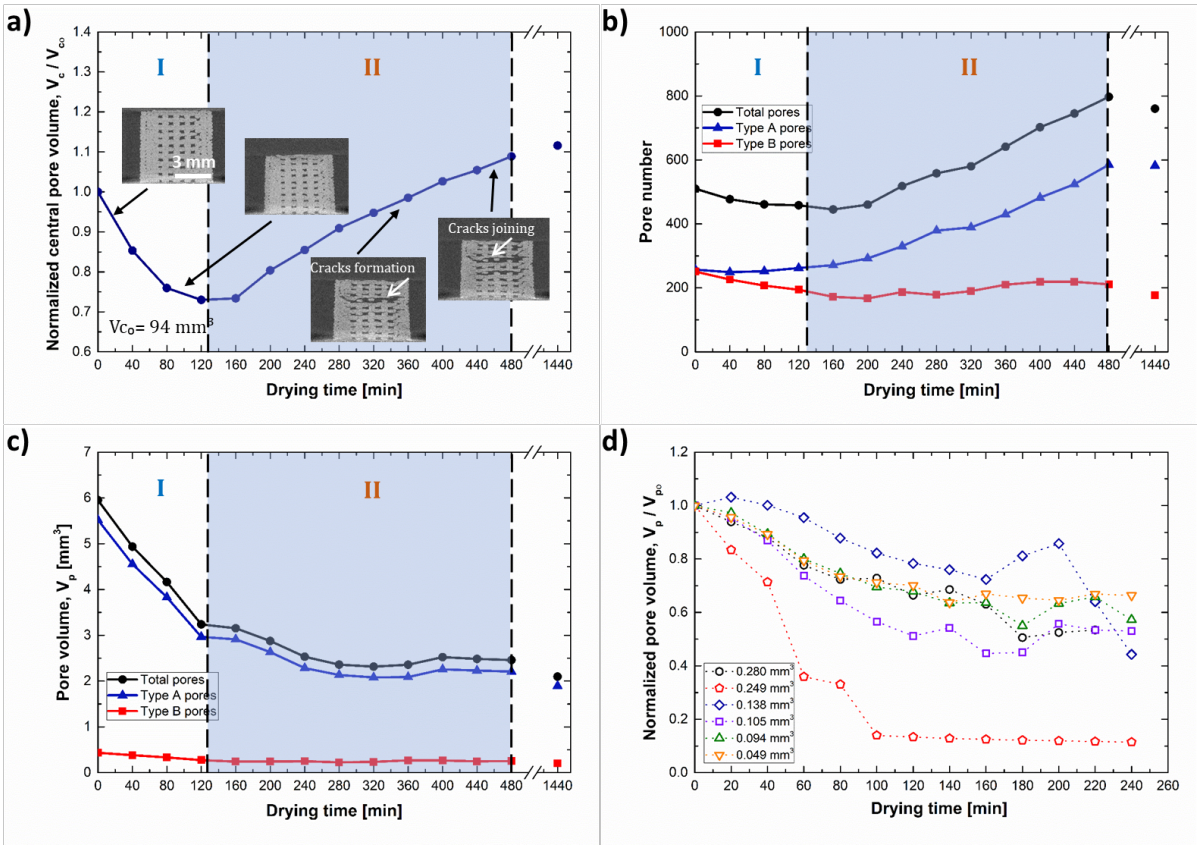

Figure 4.17: (a) Temporal evolution of the normalized volume of the central pore evolution. (b) Temporal evolution of the number of inter-filament and intra-filament pores. (c) Temporal evolution of the cumulative volume of inter-filament and intra-filament of pores. (d) Pore volume evolution of 6 tracked inter-filament pores.

Inter-filament pores (type A)

Figure 4.17b and Figure 4.17c show that:

- from T =0 to T=120 minutes, the number of inter-filament pores is almost constant whereas their cumulative volume decreased linearly with time. The average size of inter-filament pores decreased from 0.021 mm^3 to 0.013 mm^3. This 40% decrease in size is confirmed by the tracking of some inter filament pores (Figure 4.17d). This comes from the fact that the shrinkage of the structure reduced the space between two filaments (Figure 4.15).

- for T=120 min to T=480 min, the number of inter-filament pores increased whereas their total volume remained constant. This might be explained by the threshold value applied during the quantification phase. Namely, the number of pores is sensitive to the threshold used to identify the pore phase. As the structure dried continuously during the experiment (Figure 4.14b), the amount of water decreased, inducing a decrease of about 15% for the grey level, this can be quantified for T larger than 140 min. Therefore, the number of voxels belonging to the porous phase increases inducing, in most cases, larger pores, these larger pores not being excluded due to the threshold on the size of the pores. Moreover, the increase of the number of inter-filament pores can also be due to delamination effects.

Namely, the global DVC (Figure 4.14a) in x and y direction do not show any significant variation, meaning that macroscopic aspect of the part did not change anymore, whereas the local DVC (Figure 4.15) shows that the filaments, especially inside the structure continued drying, leading to smaller diameter, creating new inter-filament pores or increasing their size.

Intra-filament pores (type B)

On Figure 4.17b and Figure 4.17c, we can observe that:

- for T=0 to T=160 min, we can observe a linear decrease of the number of intra-filament pores associated with a decrease of the total volume of pores, leading to a decrease of the mean intra-filament pore size. Combining the two graphs shows that these pores have a small volume with an average size in between 0.001 to 0.003 mm^3. The decrease of their numbers might come from the filament shrinkage due to the load of the above layers as observed in Figure 4.13 and Figure 4.16.
- for T > 160 min, the number of pores increased slowly whereas their cumulative volume remained constant.

4.4.3 What are the microscopic changes during the main phases of the drying?

Figure 4.18 shows the drying rate of the cube as a function of time [Taguchi et al., 2010], obtained in similar conditions of temperature and humidity as the one imaged. The drying rate of the air-dried cube exhibits two main regimes: a constant rate period ($\approx 0.18 kg H_2O.h^{-1}.m^{-2}$) (phase I) that last about 135 minutes followed a falling rate period (phase II). These two periods were reported on the graphs representing the temporal evolution of the microstructural descriptors.

During phase I, the main phenomena that occurred aimed at building the rigid skeleton of the dried cube [Metzger, 2018, Rémond et al., 2010, Sampson and Yamamoto, 2011]: we observe a macroscopic anisotropic shrinkage of the structure, a decrease of the solid fraction of the cube, a decrease of the volume of the central pore, a decrease of the number and of the volume of the inter-filament and intra-filament pores, a change of the shape and dimensions of the cross-section of filaments. At the beginning of phase II, we observe that the previous changes still took place but at a slower rate.

During phase II, most of the changes appear at the filament scale; we observed delamination effects, an increase of number of the inter-filament and intra-filament pores. The quantitative analysis captured the last phenomena after the beginning of phase II defined by Figure 4.18. Therefore, at the observation scale, a transition zone, that took place between 120 minutes and 160 minutes of air drying, might be defined between the two regimes. During this period, it is difficult to define the major mechanisms as they resulted in a competition between the main phenomena taking place during each phase. The length of this transition zone might be explained by 3 factors (i) it was possible to quantify the evolution that took place up to 30 µm, which is enough to explain part of the microscopic changes but as stated by Metzger (2018) [Metzger, 2018] it is complicated to simultaneously image drying phenomena at the three

relevant scales on representative samples (ii) the temperature gradient around the sample modified the drying rate of the sample and might have induced different evolution rates of the 4 faces of the cube (iii) the CMC dissolved in the water to prepare the paste acted as a gelation agent [Edali et al., 2001] and allowed the cellulose fibers to be embedded [Thibaut et al., 2019] and probably modified the drying mechanisms of cellulose fibers and of cellulose fiber mats, compared to paper materials.

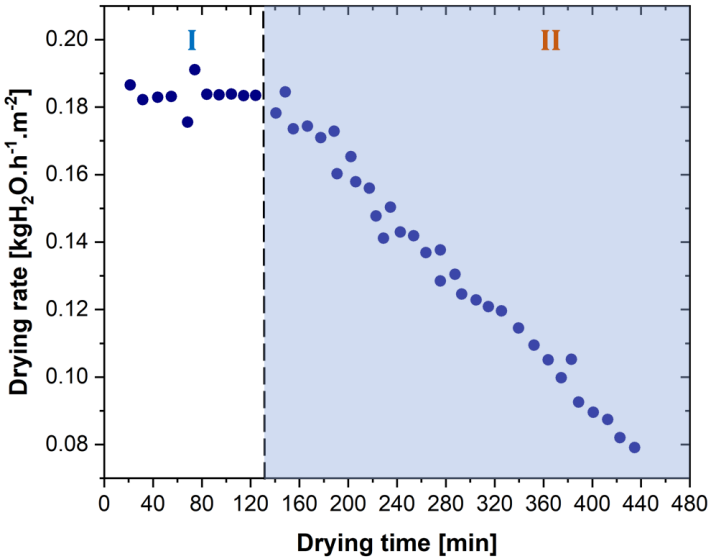

Figure 4.18: Temporal evolution of the drying rate. [Thibaut, 2020]

4.4.4 Conclusion

The objective of this study was to experimentally determine the multi-scale phenomena that occurred during the drying of a 3D printed part obtained by extrusion of cellulose-based paste. Lab X-ray microtomography imaging techniques during air drying tests combined with advanced image analysis were used to reveal the mechanisms that took place at the part scale and at the filament scale. For that purpose, a fast lab X-ray microtomography procedure coupled with quantification of the main structural parameters and kinetics measurements was developed. It allowed the qualitative and quantitative analysis of microstructural changes during the two first phases of the air drying of a cube that are the constant drying rate period (phase I) and the first falling rate period (phase II). During phase I, we quantified the macroscopic anisotropic shrinkage of the structure, a decrease of the solid fraction of the cube, a decrease of the volume of the central pore, a decrease of the number and of the volume of the inter-filament and intra-filament pores, a change of the shape and dimensions of the cross section of filaments. At the beginning of phase II, we observed that the previous changes still took place but at a slower rate. During phase II, most of the changes appeared at the filament scale; we observed delamination effects, an increase of number of the inter-filament and intra-filament pores. A transition zone was therefore defined during which a competition between the main phenomena taking place during each phase occurred.

4.5 Conclusion

In this chapter, a real-time fast in-situ scan performed with the optimized laboratory CT setup is presented. The optimization was done by an experimental screening on an already dried 3D printed cube and a suitable configuration was chosen that allows to quantify the microstructural changes during the air-drying phenomena of a 3D printed cube. The chosen setup limits the voxel size to 28 μm which only allows to quantify the larger microstructural parameters. The experimental configuration was further confronted with the predicted configurations by the optimization model and it was found to be in-line with one of them. The model also predicted the possibility to improve the spatial resolution of the scan by using the binning 2 mode of the detector. It would be interesting to complete these results by performing observations using fast high-resolution X-ray images to better define the microstructural changes at the filament scale and therefore better define and quantify the transition zone and thus the deformation mechanism.

Chapter 5

Conclusions and perspectives

Contents

5.1 Summary of this doctoral work

This doctoral thesis deals with developments to increase the possibilities offered by laboratory X-ray computed tomography for materials characterization by focusing on contrast enhancement and on time resolution aspects.

The limitations of lab-CT in terms of image quality and resolution for steady-state and in-situ acquisitions compared to synchrotrons are detailed in the "literature review", presented in **chapter 1**. A particular attention was paid on the effect of lab-CT scanning acquisition parameters on the resultant image quality and the need of acquisition protocol to select the set of parameters that produce the best quality of images for a CT scan. Moreover the limitations of laboratory-CT for fast in-situ acquisitions were detailed as well.

In order to overcome these limitations we proposed two different but interlinked methodologies. The first methodology is the hardware strategy and involves the use of advanced new generation direct photon-counting detectors (PCDs) that offer enhanced characteristics compared to the standard energy-integration detectors currently in use in lab-CT. These characteristics are direct detection mechanism of X-ray photons and the energy-discriminating capability of the detector. The second methodology is based on developing a global optimization strategy for the suitable selection of acquisition parameters for a CT scan. A model was developed for this purpose that outputs the suitable scanning configurations by taking into account the sample and sample environment specifications and the objectives of the scan. A general summary of work presented in relevant chapters is follows:

- In **chapter 2**: the quantitative characterization of the imaging performance of a photon-counting detector using a lab polychromatic X-ray source is presented. The chapter begins with the description of the working principle of the PCD. Then, the characteristics of four PCDs were examined and a suitable detector, Pixirad-2/pixie-III, was subjected to characterization. The static and time-dependent defects of the detector were characterized and correction procedures based on local median filter and hardware sensor refreshing, were proposed. The classical imaging capabilities of the detector in terms of noise and contrast measurements (SNR, CNR and MTF) were tested and compared to the standard energy-integrating detector flat-panel. The results indicated approximately 15% lower SNR and 12% improved CNR of the Pixirad-2/pixie-III detector. The MTF curve of the Pixirad-2/pixie-III shows a significantly higher spatial resolution, the estimated spatial frequency at 0.5 MTF lines is 0.43 cycle/pixels for Pixirad-2/Pixie-III and 0.17 cycle/pixels for flat-panel. The charge sharing correction performance of the Pixirad-2/pixie-III detector was evaluated by the energy characterization of three available operating modes of the detector. It was concluded that NPISUM mode recovers the shared charges compared to NONPI and NPI mode but the efficiency of the correction is only limited to four neighbouring pixels in the horizontal and vertical direction. The spectral capabilities of the detector was tested by accessing the single-shot radiographic K-edge subtraction (KES) imaging and by estimating the spectral resolution of the detector. An (I-$BaSO_4$-H_2O) phantom was used for this purpose. The radiographic KES image was obtained using the photons of energy in-between 28 and 38 keV by monochromatizing the polychromatic beam using the energy-discrimination feature of the detector. Only the Iodine and Barium Sulphate

solutions were visible in the processed image since the K-edge of Iodine and Barium lie in this range. Such capability of the detector can potentially be used to perform material identification imaging and for their composition analysis. The Spectral resolution of the detector was estimated by measuring the absorption K-edge spectra of Iodine and $BaSO_4$ and was found to be within 2 keV range, which is relatively good for practical applications.

- In **chapter 3**: a model-based approach to select the suitable acquisition configuration for a CT scan was developed. The different modules of the optimization model (i) a noise model, (ii) an X-ray X-ray absorption simulation tool and (iii) a screening algorithm, were detailed. The model takes as input the preliminary knowledge of the sample, the in-situ process, technical constraints of the tomograph and the level of analysis to be performed on the recorded images. The screening algorithm screens over all possible scanning parameters and outputs the different possible scanning configurations. For each configuration, the X-ray absorption simulation tool is used for the computation of contrast and photon flux in the output image. Moreover, for each configuration, the computed contrast, photon flux, resolution and motion of the feature of interest is used to estimated the resultant image quality in the sense of weighted average error in the segmented volume of the feature of interest using the noise model. All possible configurations are output as a tabular file. A proposed cost function makes the trade-off between different output configurations based on the minimum weighted average error criteria taking into account the level of analysis to be performed on the reconstructed images. The efficiency of the model to predict the acquisition parameters is confronted with the experimental datasets and the predicted parameters were found to be consistent with the experimental parameters. However, some variations were observed since the detector response was not implemented in the model. Moreover, the sensitivity of the cost function to the various acquisition parameters was accessed and it was found that a further criteria on the weighted average error with the change in voltage and SDD needs to be implemented to improve the effectiveness of the optimization model.

- In **chapter 4**: a fast in-situ application performed with the optimized laboratory-CT setup was presented. The application belongs to the 3D real-time monitoring and quantitative characterization of the multi-scale phenomena that occurred during the air-drying of a 3D cellulose paste printed sample. The details about the experimental screening for the optimization of the acquisition parameters to enable fast acquisition with quantifiable image quality, on an already dried 3D cellulose paste printed cube were presented. The acquisition configuration was chosen by making the trade-off between the available spatial and temporal resolution and image quality. The selected experimental configuration was confronted with the configurations predicted by the optimization model which were found to be in-line with the chosen setup. The optimized setup led to the acquisition of 120 tomographic scans with a scan time of 36 seconds recorded every 4 minutes during the 8 hour of air-drying monitoring of 3D printed cube. The application of the advanced image analysis tools such as labelling and digital volume correlation on the acquired reconstructed datasets allowed the qualitative and quantitative analysis of microstructural changes during the two phases of the air-drying phenomena that took place at the part scale and at the filament scale. During the constant drying rate period, the macroscopic anisotropic shrinkage of the structure was quantified that resulted in a decrease of the

solid fraction of the cube, a decrease of the volume of the central pore, a decrease of the number and volume of the inter-filament and intra-filament pores, and a change of the shape and dimensions of the cross-section of filaments. At the beginning of the first falling rate period, we observed that the previous changes still took place but at a slower rate. However, most of the changes appeared at the filament scale during the phase, and delamination effects was observed leading to an increase of number of the inter-filament and intra-filament pores.

The application illustrates the quantitative characterization capability of lab-CT for fast in-situ tests.

5.2 Perspectives

This section details some of the perspectives of the work presented in this thesis.

5.2.1 Using Pixirad-2/Pixie-III for tomographic acquisitions

In this thesis the implementation and radiographic characterization of the Pixirad-2/Pixie-III detector was performed using the laboratory source. The detector can be used for the lab-based tomographic acquisitions such as absorption, spectral and in-situ CT. Prior to that, some further analysis on the detector is required as presented below: (it is currently an on-going work in laboratory SIMAP & 3SR and most of the work has been done by Rémi Granger, a post-doctoral researcher working on the photon-counting detectors project.)

- Understand the link between the detector's linearity and saturation behaviour as a function of the acquisition parameters such as input flux, source-detector-distance, and energy-threshold value. Such characterization will be useful to build guidelines for tomographic imaging for the CT users.
- Quantify the effect of pulse-pile up on the recorded output energy spectrum.
- Develop a dedicated post-processing script to improve the radiographs quality. This script would overcome the consequences of the static and dynamic defects present on the detector sensor. Without that it is not possible to obtain the meaningful reconstruction for tomographic acquisitions.
- Explore the potential of the detector to correct the beam-hardening artifacts for high-density materials.
- Developing a KES optimization model to predict suitable lower and upper energy-threshold values according to the scanned specimen's material composition. In the KES radiographic imaging presented in Chapter 2, the E_{th_low} and E_{th_high} value were arbitrarily selected according to the K-edge of the materials. However, in order to improve the efficiency, a KES model based on a contrast-to-noise ratio (CNR) criteria can be build and suitable E_{th_low} and E_{th_high} value can be selected for a scan that estimate the highest CNR.

Once these questions are answered, the detector needs to be used for tomographic acquisitions.
An illustration of the absorption-CT and single-shot KES-CT performed with Pixirad-2/Pixie-III detector is presented in Figure 5.1. The phantom ($BaSO_4$-H_2O-I) consist of Barium Sulphate ($BaSO_4$), distilled water (H_2O) and Iodine (I). The acquisition parameters for both scans are listed in Table 5.1.

For acquisitions, bias voltage was regularly set to 0 V for 5 seconds every approximately 2 minutes to avoid polarization artifacts. For absorption-CT, radiographs were acquired using the photon of energy in-between 15 to 50 keV using the imaging counter 0. For KES-CT both imaging counters were used. For counter 0, the lower and upper thresholds were set to 34 and 39 keV, this defines the energy window for counter 1 in-between 39 to 50 keV.

Table 5.1: Acquisitions parameters for the tomographic scans.

Acquisition	Pixirad-2/Pixie-III Absorption-CT	Pixirad-2/Pixie-III KES-CT
Acquisition parameters		
Number of projections	800	800
Average of the projections	10	10
Exposure time per projection [s]	1	1
Total scan time [hour]	≈ 2	≈ 2
Resolution [μm]	10	10
Source parameters		
Filter	1mm Al	1mm Al
Voltage [kV]	50	50
Current [µA]	200	200
Target	W	W
Pixirad-2/Pixie-III specific parameters		
Energy thresholds [E_{th_low}, E_{th_high}] [keV]	[15,50]	[34,39], [39,50]
Used imaging counter	0	0 and 1

The acquired raw radiographs from both scans were pre-processed by following procedure presented in Chapter 2 (flat-field correction, local defects corrections). For KES scan, 2 datasets were acquired using the imaging counter 0 and 1. After the pre-processing operation, the digital logarithmic subtraction was performed using the counter 1 dataset and counter 0 dataset to obtain the KES dataset. The procedure is previously illustrated in Chapter 2, Section 2.4.5.

Both scans were then reconstructed using filtered back-projection algorithm, using XAct software and the XAct ring filter to remove the artifacts was applied. The reconstructed slices from the absorption scan and KES scan are shown in Figure 5.1(a & b), respectively.

It can be noted that both scans are well reconstructed. The artifacts can be seen in the presented slices which needs to be further corrected. For KES-CT image, Figure 5.1(b), only the ($BaSO_4$) phase is visible since the K-edge of Ba lies within the energy range used for the acquisition. The identification of a specific material based on its K-edge illustrates the potential of Pixirad-2/Pixie-III detector for material identification. Such tomographic acquisitions after fully understanding the detector behaviour can be performed in an efficient way with laboratory setups.

The use of Pixirad-2/Pixie-III for time-resolved CT also needs to be explored. The detector provides the possibility to reduce the exposure time down to 10 milliseconds which could be useful for high-speed in-situ acquisitions.

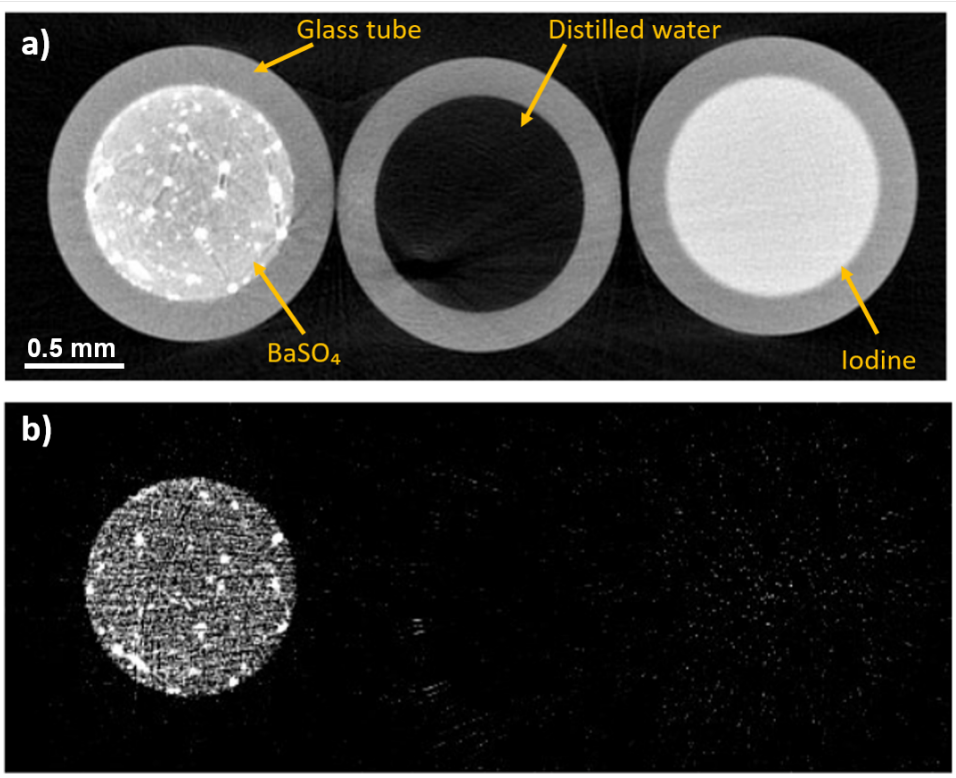

Figure 5.1: The reconstructed 2D slices of ($BaSO_4$-H_2O-I) with Pixirad-2/Pixie-III detector (a) absorption-CT (b) K-edge subtraction (KES) CT.

5.2.2 Optimization model

In the thesis, an optimization model to estimate the suitable scanning configuration for a CT scan is presented. Some recommendation that can be implemented for improving the model efficiency is detailed below:

- In the noise model, the spherical feature of interest of radius 1 to 10 pixels are currently simulated. It needs to be extended to the feature size of larger radius and to different shape as well. 3D grayscale images of different shapes with different sizes can easily be generated by modifying the developed sphere generation script. Instead of simulating different shapes separately, a sphericity function can be implemented in the script which can generate the 3D object with a specified sphericity considering the sphericity of a perfect sphere as 1. The sphericity can be given as an input parameters along with the image and object size. Moreover, the possibility to use other type of feature can be implemented in the noise model.

- The weighted average error is defined based on the criteria of segmented volume of the feature size which comes under the dimensional measurements. The criteria can be extended to form measurements such as sphericity, cylindricity and flatness. The criteria can also be extended to more number of objects as well.

- The threshold limit for the estimation of solid volume was selected at 128, based on an ideal case senior with grayscale value in the background and sample being 0 and 255. The

threshold limit value can be refined by investigating the effect of the lower threshold limit value on the weighted average error and comparing it with the experimental dataset.

- The detector response is not implemented in the optimization model. The experimental dataset of the detection efficiency as a function of photon energy can be implemented in the Beer Lambert's law prior to computing the integration, which will estimate the correct output photons received by the detector. These output photons can further be approximated into the mean grayscale value to be received on the radiograph and can be used for correct estimation of output image contrast. The mean grayscale value can also assists in establishing the boundary conditions for the detector saturation response (overexposure and underexposure) for the given input parameters.

- Currently the weighted average error is estimated as a function of the Gaussian noise. Grayscale values estimated on the radiographs after implementing the detector response can be further used to implement more noise criterion such as signal-to-noise ratio, contrast-to-noise ratio and some other noise metrics to improve the efficiency of the noise model. These metrics might be necessary because different CT configurations can result in similar standard deviation in the radiographs but with different values of other image quality indexes.

- The criteria to compensate motion of the FOI is based on inducing blurring in the simulated 3D grayscale sphere. This was done by generating the series of 3D spheres with varying their x-directional central position and then computing the single averaged sphere. This averaged sphere has more intermediate gray values along the boundary representing blurring but the size of the sphere remains constant. In reality, the motion is caused by the structural change or evolution within the feature of interest and it causes the reduction in the size of the feature. This strategy for the generation of the motion-induced sphere can be improved. However, a detailed experimental validation is needed to validate the motion-induced simulation results for spherical object.

- The sensitivity of the cost function as a function of acquisition parameters showed that a further criteria on the basis of changing source-detector distance (SDD) and voltage is required as presented in the case study.

- The output of the optimization model can be linked with other developed tomographic simulation software such as Novi-Sim (from Novitom) that takes into account the detector response into account and output the reconstructed slice for a given scan setup. The optimized setup predicted by the optimization model can be used as an input in the Novi-Sim to output the simulated reconstructed dataset.

5.2.3 Application: 3D real time monitoring of air-drying of 3D printed cellulose cube

The presented air-drying monitoring application was performed using the optimized setup by experimental screening of acquisition parameters. The optimization model suggest further improvements in the scan setting that can help to improve the image quality.

The current study was performed at 28 μm voxel size. Due to which the smaller inter-filament and intra-filament pores with volume less than 30 voxels were not detectable in the acquired datasets. By utilizing the optimization model, the resolution of the scan can be increased and the similar experiment can be performed using fast high-resolution X-ray setup to better define the microstructural changes at the filament scale and therefore better define and quantify the transition zone.

Model suggests that the binning 2 mode of the detector can be used which will result in the voxel size of 14 μm with the same geometry setup. Although in such case, the achievable exposure time will be limited to 30 frames per second but a suitable configuration according to the measurement accuracy can be chosen from the output configurations tabular file of the model in which the effect on the weighted average error with the different number of projections, average, exposure time, and motion is listed.

Similarly by using the optimization model, other fast in-situ application can be performed with the lab-CT. One such application can be solidification of an metallic alloy.

5.2.4 Application 2: In-situ 4D solidification of an AlSiCu alloy by fast laboratory X-ray micro-CT

This section briefly introduces the second application that was studied. The aim of this application is to demonstrate the potential of laboratory CT for continuous in situ acquisitions and corresponds to the in-situ solidification of aluminium silicon copper Al-Si-Cu alloy.

A trial experiment that was conducted during the first year of the thesis with an optimized laboratory CT setup is briefly presented, along with some qualitative and quantitative results. Some limitations faced in the quantification of liquid and solid phase are discussed, and the potential use of Pixirad-2/Pixie-III detector to improve the spatial and temporal resolution of the scan is analyzed.

5.2.4.1 Introduction

During the solidification process, the alloy consists of a solid-liquid mixture before complete solidification. The presence of two phases (solid and liquid) in the beginning is an origin for microstructural changes such as local variations in volume fractions of solid and liquid and porosity that form at the end of solidification.

The developments of ultra-fast, high-resolution X-ray CT setups at synchrotron made possible the in-situ solidification at high spatial and temporal resolution for microstructural quantification which has been reported by a number of publications [Ludwig et al., 2005, Suéry et al., 2012, Salvo et al., 2012a, Fife et al., 2014, Terzi et al., 2010]. However, no such solidification experiment has been reported with laboratory CT. In this section, we present the first in-situ solidification performed using the optimized laboratory CT setup. Some further improvement in the acquisition setup that can be done is also presented.

5.2.4.2 Material and experimental methods

5.2.4.2.1 Material

The specimen studied is an aluminium alloy Al-Si-Cu (8wt%Si and 4wt%Cu). The thickness of the sample is approximately 1 mm with 2 mm in height. A section of the specimen was scanned with 1 mm diameter and 1.75 mm height.

5.2.4.2.2 Heating furnace

The heating furnace used is a MHI FibHeat200-XRD microheater that has been previously used at ESRF ID16B [Kumar et al., 2019], and temperature as high as $1000°C$ can be reached. The diameter of the furnace is 28 mm.

5.2.4.2.3 The fast lab micro-CT technique

The solidification experiment was performed using the RX Solutions EasyTom XL tomograph located in the laboratory SIMAP. The X-ray micro-focus source (Hamamatsu Corporation L8121-03 X-ray sealed source) and “indirect” flat-panel Varian PaxScan® 2520 was used for the ex-

periment. Figure 5.2(a & b) shows the experimental setup; a heating furnace was mounted in front of X-ray micro-focus source. In order to visualize and quantitatively characterize the microstructural changes during the solidification of 1 mm sample, typically high spatial resolution scan is required. The experiment was performed at the highest possible resolution with the current lab-CT setup.

The flat-panel detector was operated in full acquisition mode without any binning, which gives an array of 1920 × 1536 pixels, with each pixel measuring 127 × 127 μµm. The furnace was mounted at the closest position to the X-ray source output window. The sample was glued on the top of a ceramic rod and inserted in the furnace. The achieved source-object distance (SOD) was 42 mm, considering the distance of 14 mm between the X-ray source focus point and the output window and the diameter of the furnace. The detector was placed at the farthest possible position giving the source-detector distance (SDD) of 668 mm. The combination of SOD and SDD gives a magnification of 15.9 and combined with the detector pixel pitch of 127 μm resulted in a voxel size of 7.9^3 μm^3.

The X-ray tube was operated in small focal spot mode at a power of 10 W with an acceleration voltage of 80 kV and a filament current of 123 μA.

For the experiment, the sample was partially melted at 640 °C and subsequently solidified during which continuously tomography acquisition was performed. The cooling rate was not precisely controlled and was estimated to be 0.1 °C/sec. A single large continuous acquisition containing 6000 radiographs with an average of 3 images at an exposure time of 0.09 seconds was captured during the 30 minutes of cooling. It resulted in a total of 30 turns, and each turn contained 200 radiographs with a scan time of 54 seconds.

This optimized acquisition protocol with a voxel size of 7.9^3 μm^3 and scan time of 54 s leads to scans with enough temporal and spatial resolution to visualize and quantify the larger microstructural features during the solidification process.

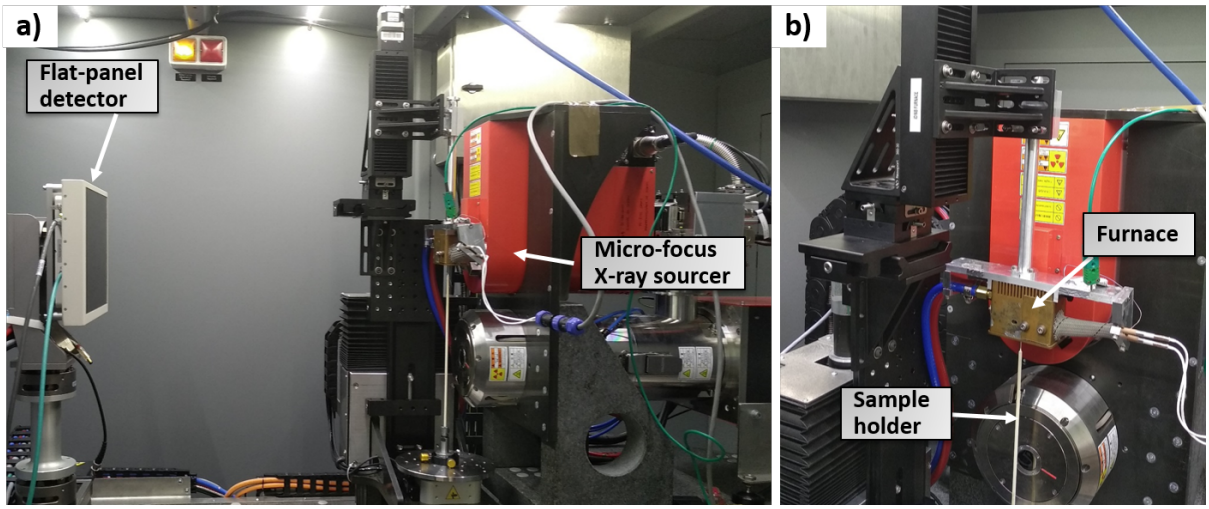

Figure 5.2: Experimental setup with the furnace mounted with laboratory tomography set up for the in-situ solidification experiment. (a) Front view and (b) side view.

5.2.4.2.4 Data processing and analysis

The acquired 2D radiographs were reconstructed using the classical filtered back-projection (FBP) algorithm implemented by RX solutions.

Phase quantification: The output volumes have two phases, a solid-liquid (liquid and solid) and a porous phase, as identified in Figure 5.3(a). Due to the limited resolution and image quality of the scan, it was not possible to quantify the solid and liquid phases. The solid-liquid and porous phase was identified using a thresholding operation. The same threshold was applied to the 30 scans and was obtained by averaging the threshold value automatically found by the iterative intermeans method available in ImageJ [Ridler, 1978b]. Figure 5.3(b) shows the histogram of the 3D reconstructed volume at T = 0 second with solid-liquid and porous phase, and the cutoff threshold is indicated. No median filter or any other post-processing filter was applied on the 3D reconstructed dataset prior to phase quantification for improving the image quality.

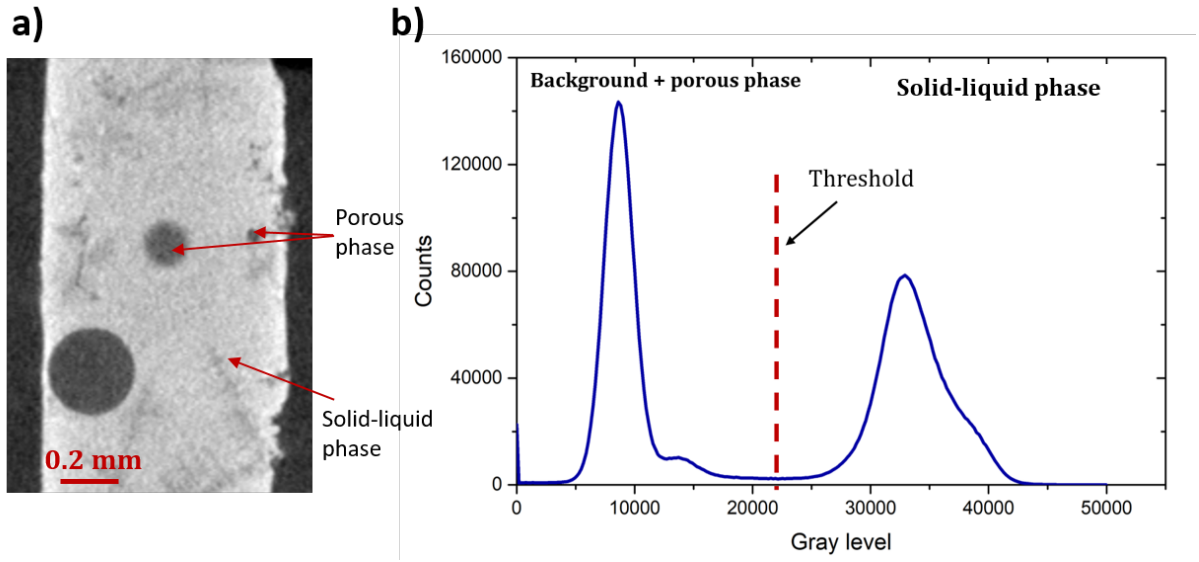

Figure 5.3: a) A 2D reconstructed slice at T = 0 sec with different identified phases in Al-Si-Cu specimen. b) A histogram of reconstructed volume showing the cut off threshold to distinguish the two phases.

Microstructural quantification: The binarized volumes were considered for microstructural quantification. The volume of the solid-liquid and porous phase was computed by counting the total number of voxels of the respective phase and multiplied by the voxel size. The large pores with a volume greater than 20 voxels were identified by labelling the porous phase using the Analysis 3D plugin of ImageJ [Boulos et al., 2012]. It labelled the 3D connected components with specified connectivity of 26 neighbours. After identifying the pores, the volume and the surface area of each pore were computed using a marching cube algorithm [Lorensen and Cline, 1987].

5.2.4.3 Results and Discussion

5.2.4.3.1 Qualitative Results

Figure 5.4 presents a series of 2D reconstructed slices of the Al-Si-Cu specimen at various solidification times. Each slice was extracted from the 3D volume that corresponds to the acquisition time of 54 seconds. Only fourteen 2D images are shown among the 30 reconstructed volumes. It can be seen that images are of sufficient quality to visualize the solidification process. The formation of pores and dendrites can be observed with the acquisition time.

At time T = 0 sec, the sample is in mostly liquid state, and it starts to solidify as the furnace temperature decreases. It can be observed that most of the visible microstructural changes, pores and dendrites formation, occur roughly till the sixth scan, which corresponds to the solidification time of 270 seconds. After some changes at the local microstructural level might occur. The formation of the central pore, located at the center of each slice, and its volume growth can be observed till T = 324 seconds and after no visual change is noticed.

At the beginning of solidification, the solid-liquid phase consists of isolated dendrites, and the connection between dendrites occurs gradually as the temperature decreases with the increase in solidification time. However, the shape of the dendrites is not very clear from the images due to the limited spatial resolution.

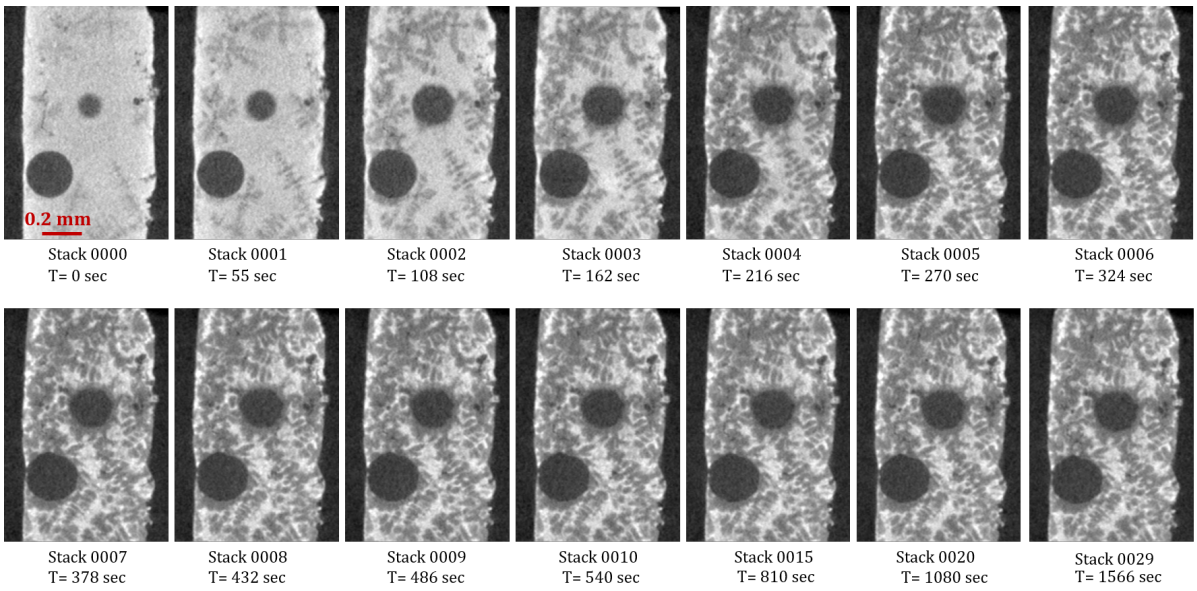

Figure 5.4: 2D reconstructed slices of a Al-Si-Cu specimen alloy during solidification. Each slice was extracted from the 3D volume captured with the acquisition time of 54 seconds.

5.2.4.3.2 Quantitative Results

Figure 5.5 presents the segmented slices extracted from the 3D segmented stacks at different solidification times. The solid-liquid phase is represented by white color and the porous phase with black. The larger pores were well segmented and they can be observed in the grayscale images as well.

Figure 5.6 shows the temporal evolution of the volume of the solid-liquid phase. The

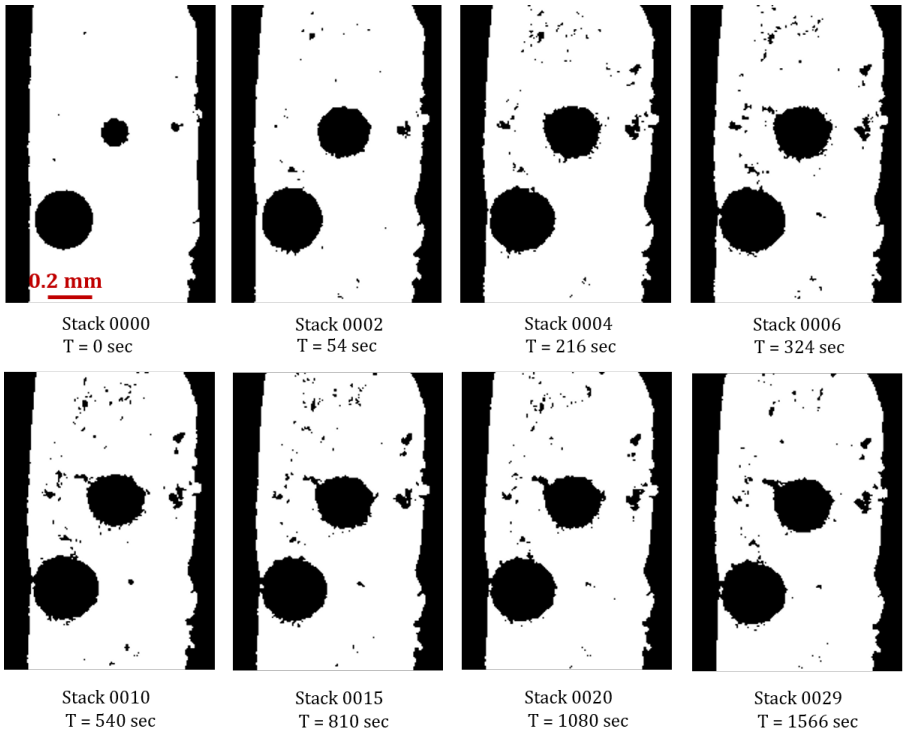

Figure 5.5: 2D segmented slices of the Al-Si-Cu specimen during solidification representing solid-liquid phase in white and porous phase in black color.

volume of the solid-liquid phase was normalised by the volume measured on the first 3D dataset, which was evaluated to be 1.36 mm^3. The final volume at T= 1556 sec is 1.23 mm^3. It can be observed that volume decreases rapidly till the solidification time of 200 seconds, and the decrease in the volume is negligible after 200 seconds. The formation of pores till T = 200 seconds decreases the solid-liquid volume and it also indicates that most of the pores formation happen until this stage.

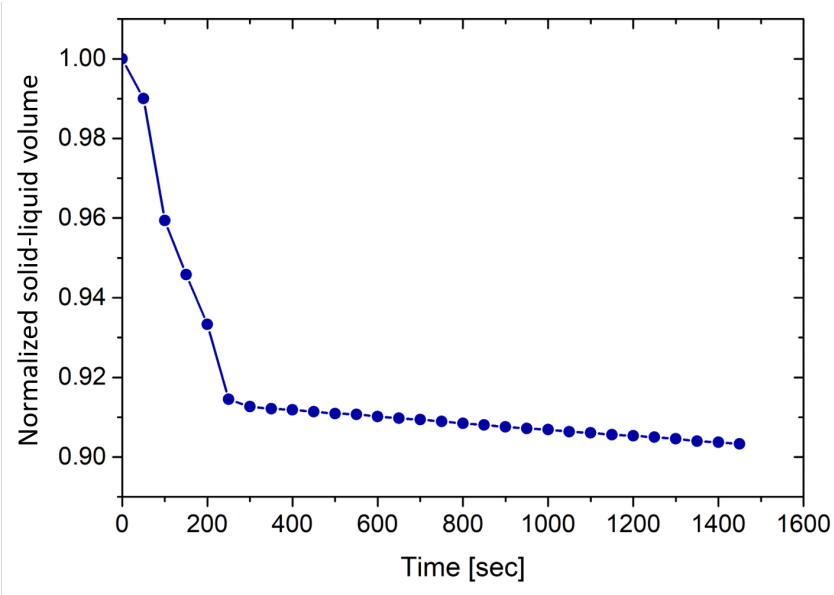

Figure 5.6: Temporal evolution of the normalized solid-liquid phase volume.

Figure 5.7 presents the 3D rendered pore map at different solidification times. Pores that exhibited a volume smaller than 20 voxels ($9.86 * 10^{-5} mm^3$) were discarded as most of these pores might come from the threshold sensitivity due to the limited scan resolution. It can be observed from the figure that at the beginning of solidification, Figure 5.7(a), when the specimen is in a semi-liquid state, only few pores are identified and most of the pore volume is contributed by three large spherical pores. After, as the sample starts to solidify more pores are identified, as seen in the Figure 5.7(b) at T = 162 seconds and Figure 5.7(c) at T = 324 seconds. The three big spherical pores that are visible at T = 0 sec and at T = 162 sec are identified with the image background at T = 324 sec due to the fact that labelling operation labels only 3D connected closed components, and these three pores were present close to the sample boundary which at T = 324 sec got connected with image background. No further changes in the pores are seen at T = 1556 sec compared to T = 324 sec.

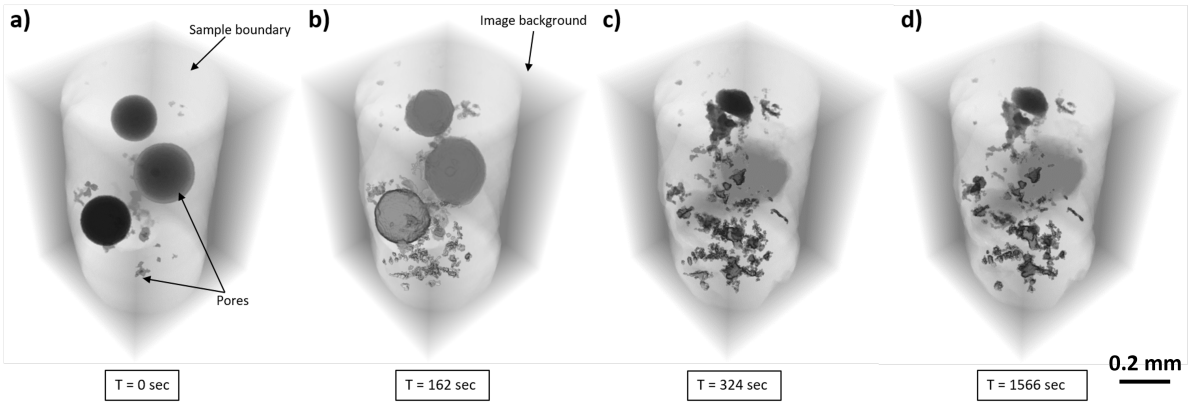

Figure 5.7: 3D rendered pore map at different solidification time. 3D connected pores are labelled and shown with the difference in the gray value.

Figure 5.8 shows the temporal evolution of the total number of pores present in the sample. An increment in the total number of pores can be observed until the solidification time of T = 300 seconds, and no significant trend is observed afterwards. A small fluctuation might be due to the smaller volume pores identified after T = 300 seconds and got connected with the nearby pore or can be due to the pores present near the boundary of the specimen, which got joined with the image background. This initial increase in the pore number and then stabilization is consistent with the qualitative observation from the 3D rendered views, as shown in Figure 5.7.

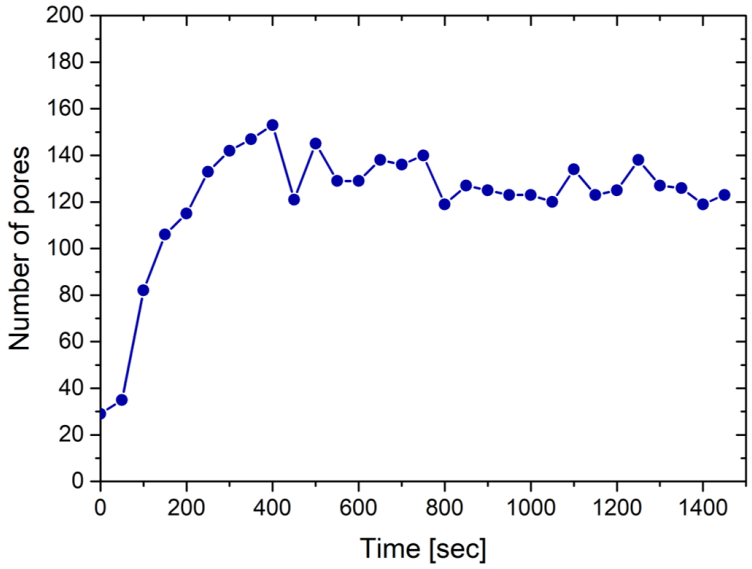

Figure 5.8: Temporal evolution of the total number of pores identified in the sample with the solidification time.

5.2.4.4 Current limitation and further improvements

As discussed earlier, the resolution of the scan was not sufficient to accurately quantify the liquid and solid phases. This primarily comes from the limitation of the CT hardware setup. The diameter of the furnace was approximately 28 mm, which combines with the EasyTom XL geometry constraint and flat-panel detector pixel pitch, limit the voxel size to 7.9 μm. The scan time was restricted to 54 seconds per acquisitions due to the limited efficiency of the flat-panel detector. Due to this relatively longer scan time, it was not possible to study the early stage of solidification because dendrites formation is happening significantly faster during a scan. Moreover, in the current scan, the cooling rate was not controlled.

This indicates the need of a more specialized furnace that can be coupled with laboratory CT setup to improve the spatial resolution and the use of an advance detector that can improve both the spatial and temporal resolution. In the current case, the utilized furnace is the one used at ESRF ID16B but the size of the furnace can be easily reduced that can be placed more closer to the X-ray source. The nano-focus source can also be utilized that can result in the minimum voxel size of 4 μm with the flat-panel detector using the current setup.

The use of Pixirad-2/Pixie-III detector, presented in Chapter 2, can be utilized. The pixel size of the detector is 62 μm (approximately twice smaller than flat-panel) and it will help to reduce the voxel size by two orders of magnitude to 3.89 μm with the micro-focus source and the same geometry setup. The Pixirad-2/Pixie-III detector combined with nano-source can result in a minimum voxel size of 2 μm.

Moreover, the SDD distance can be further reduced to increase the photon flux on the detector that can be advantageous to use the lower exposure time. With the Pixirad-2/Pixie-III detector, the exposure time of 0.01 seconds can be achieved which can significantly reduce the scan time. However, for this, the amount of flux received by the detector at the lowest possible exposure times needs to be studied and a trade-off between spatial and temporal resolution can

be made.

Figure 5.9 illustrates the possible improvements in scan time and voxel size by using the Pixirad-2/Pixie-III detector with the same experimental parameters used in the current study. However, before using the Pixirad-2/Pixie-III, further characterization to understand the detector behaviour needs to be carried out.

The acquisition parameters can be further optimized by using the developed optimization model, presented in Chapter 3. A suitable scanning configuration based on the weighted average error in the interested feature size criteria can be selected according to the objective of scan. Moreover the machine learning and artificial intelligence based reconstruction algorithm can be used to further reducing the scan time for reducing the required number of projections compared to filtered back-projection algorithm [Hendriksen et al., 2019, Pelt et al., 2018, Weigang and Jinxiao, 2021].

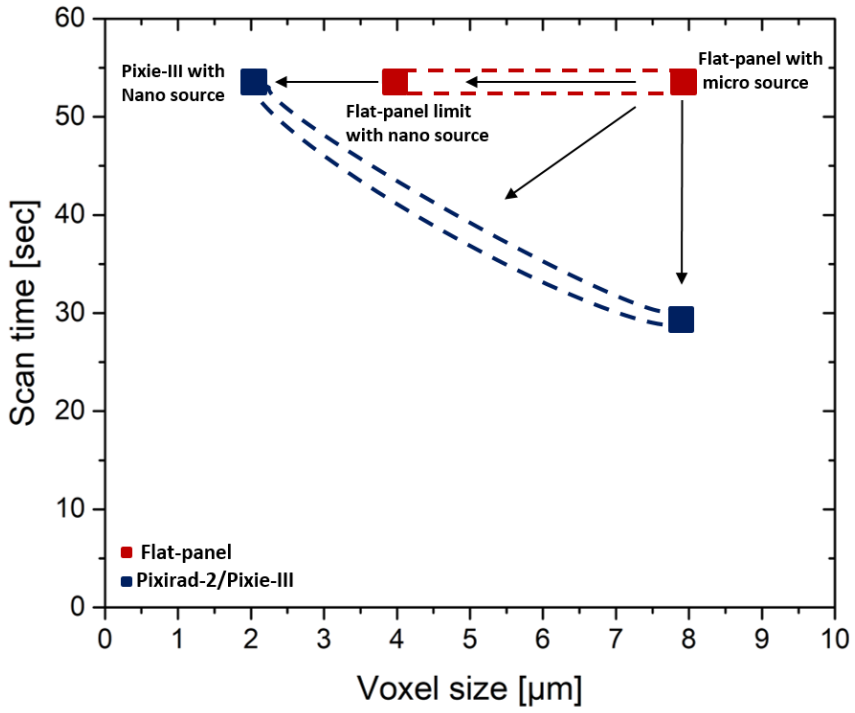

Figure 5.9: Possible reduction in scan time and voxel size by using Pixirad-2/pixie-III detector with the same geometry due to its enhanced characteristics.

5.2.4.5 Conclusion

The first in-situ 3D observations of the solidification of an Al-Si-Cu alloy with laboratory X-ray microtomography is presented. The optimized laboratory CT setup allows investigation of larger microstructural features and enables qualitative and quantitative characterization during the solidification. Based on the preliminary results obtained in this work using fast laboratory microtomography, it is obvious that in the near future by utilising the advanced photon-counting detector, specialized heating furnace and by estimating the acquisition configuration via optimization model, an ultra-fast solidification experiment at high spatial resolution can be carried out.

Appendix A

X-ray CT facility at lab 3SR and lab SIMAP

A.1 X-ray CT scanners

Laboratory 3SR and laboratory SIMAP are equipped with the X-ray CT scanner supplied by RX-Solutions. Both tomographs were extensively used during this thesis. Figure A.1 shows the CT scanners. Both X-ray cabins are large enough to host relatively large and complex equipment.

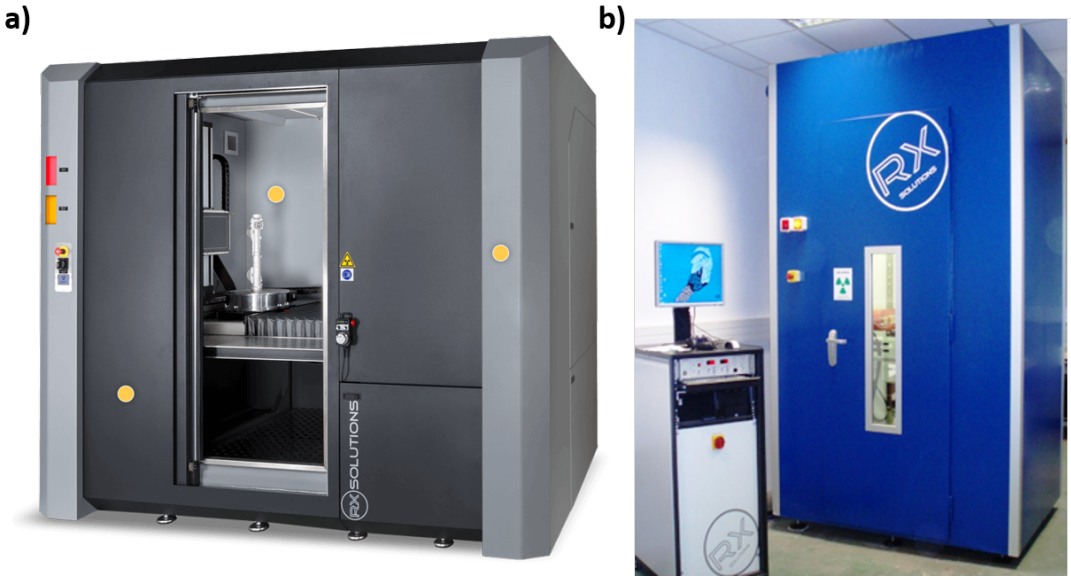

Figure A.1: The X-ray CT scanner located in (a) laboratory SIMAP (b) laboratory 3SR.

Figure A.2 and A.3 show the internal view of the both tomographs.

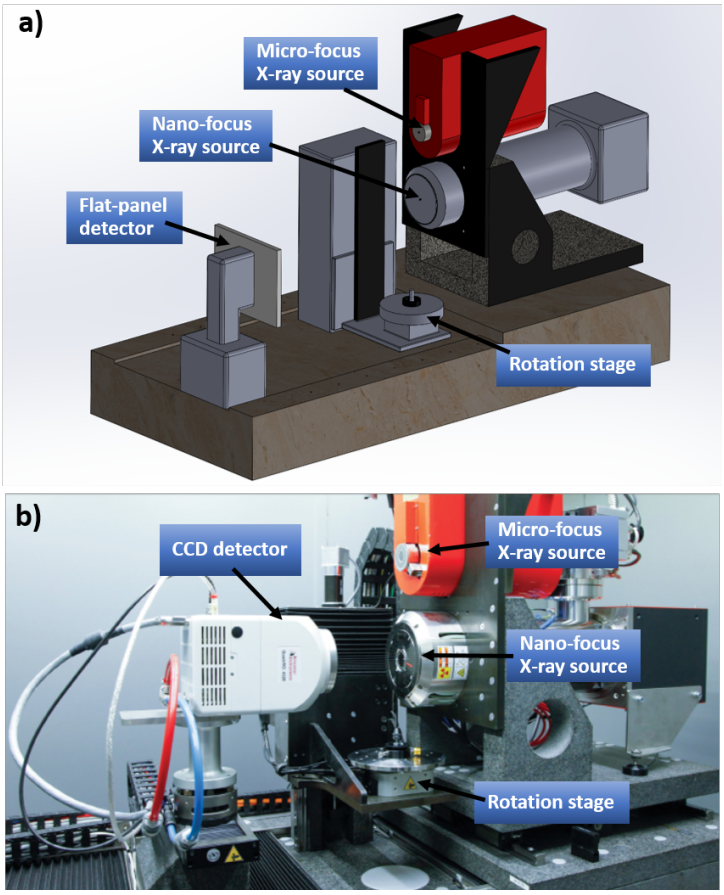

Figure A.2: Tomograph setup at laboratory SIMAP equiipped with micro and nano-focued X-ray sources (a) 3D model view, (b) actual view.

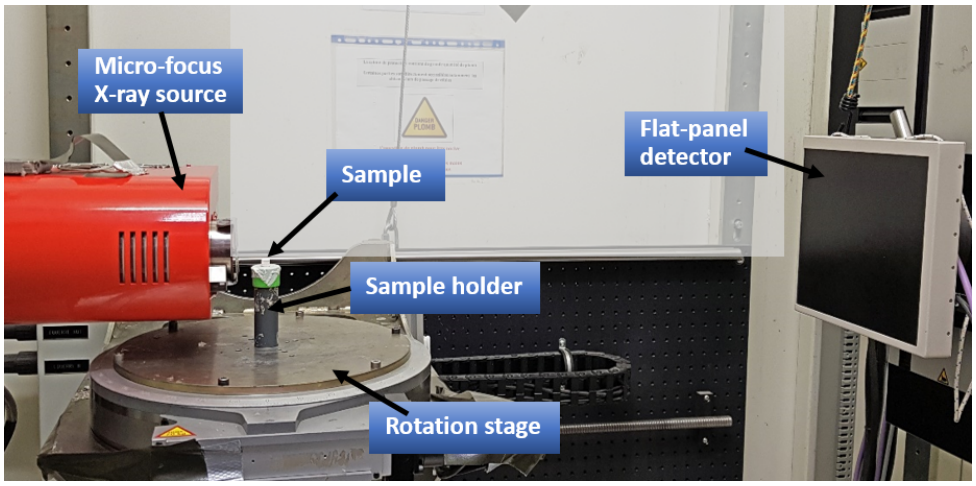

Figure A.3: Tomograph setup at laboratory 3SR equipped with micro-focued X-ray source and flat-panel detector.

A.2 X-ray sources

X-ray scanner at laboratory 3SR is equipped with micro-focus X-ray source and X-ray scanner at laboratory SIMAP is equipped with both micro and nano-focus X-ray sources. The general specifications of the micor and nano-focus X-ray sorces are presented is Table A.1 and A.2.

Table A.1: General specifications for micro-focus X-ray source

Parameter		Description / Valu	Unit
X-ray tube voltage setting range		0 to 150	kV
X-ray tube current setting range		0 to 500	µA
X-ray tube voltage operational range		40 to 150	kV
X-ray tube current operational rang		10 to 500	µA
Maximum output	Small focus mode	10	W
	Middle focus mode	30	
	Large focus mode	75	
X-ray focal spot size (Nominal value)	Small focus mode	7 (5 µm at 4 W)	µm
	Middle focus mode	20	
	Large focus mode	50	
X-ray beam angle		Approx. 43	degree
Focus to object distance (FOD)		Approx. 17	mm
Rated output		Continuous rating	–
Communication method		Interface: RS-232C (9-pin D-sub connector)	–
X-ray output window material / Thickness		Beryllium / 0.2	mm
Target naterial		Tungsten	—
Operating ambient temperature		+10 to +40	°C

Table A.2: General specifications for nano-focus X-ray source

Parameters		Description / Value	
		S mode	W mode
Cathode material		LaB6 (Single crystal)	W (Tungsten)
Maximum tube voltage		110 kV	162 kV
X-ray tube voltage setting range		20 kV to 100 kV	20 kV to 160 k
X-ray tube current setting range		0 µA to 200 µ	
Minimum resolution		0.25 µm	0.8 µm
Maximum target current		30 µA / 80 µ	50 µA / 100 µA
Target type		Transmission type	
X-ray beam angle (Max.)		Approx. 140 degrees	
Target material		Tungsten	
X-ray output window material		Beryllium / Diamond	
Focus to object distance (FOD)		0.5 mm / ¡0.3 mm	
Protection Interlock 1 / Interlock		External short-circuit method (Normally closed) 36 V DC / 12 V D	
Input voltage (AC)	X-ray control unit	100 V to 240 V (50 Hz / 60 Hz)	
	Power supply for turbo pump controller	100 V to 240 V (50 Hz / 60 Hz)	
	Rotary pump	115 V / 230 V (50 Hz / 60 Hz)	
Power consumption (Max.	X-ray control unit	410 VA	
	Turbo pump se	600 W	
Rated output		Continuous operation	
Cooling method		Water cooling	
Weight	X-ray tube unit / X-ray control un	Approx. 82 kg / Approx. 8 kg	
	Rotary pump	Approx. 11 kg	
Operating ambient temperature	X-ray tube unit / X-ray control unit	+15 °C to +40 °C	
Storage temperature	X-ray tube unit / X-ray control unit	+5 °C to +50 °C	
Operating and storage humidit	X-ray tube unit / X-ray control unit	20 % to 85 % (No condensation)	

A.3 X-ray detectors

X-ray CT scanner at laboratory SIMAP is currently equipped with three detectors, flat-panel, CCD (charge-coupled device) camera and a photon-counting detector PixiRad-2/Pixie-III. X-ray CT scanner at laboratory 3SR has only flat-panel detector.

Flat-panel detector is a Varian PaxScan 2520DX with 1536 x 1920 pixels and a pixel size of 127 x 127 μm. CCD camera is a Pixelfly 200 XS with 1392 x 1040 pixels and a pixel size of 6.45 x 6.45 μm. PixiRad-2/Pixie-III is a photon-counting detector with 476 x 1024 pixels and a pixel size of 62 μm.

Bibliography

J. Villanova, R. Daudin, P. Lhuissier, D. Jauffres, S. Lou, C.L. Martin, S. Laboure, R. Tucoulou, G. Martínez-Criado, and L. Salvo. Fast in situ 3d nanoimaging: a new tool for dynamic characterization in materials science. *Materials Today*, 20(7):354–359, 2017. ISSN 1369-7021. doi: https://doi.org/10.1016/j.mattod.2017.06.001.

E.A. Zwanenburg, M.A. Williams, and J.M. Warnett. Review of high-speed imaging with lab-based x-ray computed tomography. *Measurement Science and Technology*, 33(1):012003, nov 2021. doi: 10.1088/1361-6501/ac354a.

V. Cnudde and M.N. Boone. High-resolution x-ray computed tomography in geosciences: A review of the current technology and applications. *Earth-Science Reviews*, 123:1–17, 2013. ISSN 0012-8252. doi: https://doi.org/10.1016/j.earscirev.2013.04.003.

S. Carmignato, W Dewulf, and R. Leach. *Industrial X-Ray Computed Tomography*. Springer International Publishing, jan 2017a. ISBN 9783319595719. doi: 10.1007/978-3-319-59573-3.

Z.S. Li and L.S. Tang. Using synchrotron-based x-ray microcomputed tomography to characterize water distribution in compacted soils. *Advances in Materials Science and Engineering*, 2019:1–11, 05 2019. doi: 10.1155/2019/7147283.

B. Patterson, N. Cordes, K. Henderson, J. Mertens, A. Clarke, B. Hornberger, A. Merkle, S. Etchin, A. Tkachuk, M. Leibowitz, D. Trapp, W. Qiu, Bosheng Zhang, H. Bale, Xuekun Lu, R. Hartwell, P. Withers, and R. Bradley. In situ laboratory-based transmission x-ray microscopy and tomography of material deformation at the nanoscale. *Experimental Mechanics*, 56, 08 2016. doi: 10.1007/s11340-016-0197-3.

A.D. Plessis and W.P. Boshoff. A review of x-ray computed tomography of concrete and asphalt construction materials. *Construction and Building Materials*, 199:637–651, 2019. ISSN 0950-0618. doi: https://doi.org/10.1016/j.conbuildmat.2018.12.049.

P. Latil, L. Orgeas, C. Geindreau, P. Dumont, and S.R.D. Roscoat. Towards the 3d in situ characterisation of deformation micro-mechanisms within a compressed bundle of fibres. *Composites Science and Technology*, 71:480–488, 08 2011. doi: 10.1016/j.compscitech.2010.12.023.

L. Salvo, M. DiMichiel, M. Scheel, P. Lhuissier, B. Mireux, and M. Suery. Ultra fast in situ X-ray microtomography : Application to solidification of aluminium alloys. *Materials Science Forum*, 706-709: 1713–1718, 2012a. ISSN 16629752. doi: 10.4028/www.scientific.net/MSF.706-709.1713.

F. Forsberg, R. Mooser, M. Arnold, E. Hack, and P. Wyss. 3d micro-scale deformations of wood in bending: Synchrotron radiation µct data analyzed with digital volume correlation. *Journal of structural biology*, 164:255–62, 10 2008. doi: 10.1016/j.jsb.2008.08.004.

R.L. Abel, K.G. Johnson, R.C. Roche, R.A. Abel, K.G. Johnson, and C.T. Perry. Quantification of porosity in Acropora pulchra (Brook 1891) using X-ray micro-computed tomography techniques.

Journal of Experimental Marine Biology and Ecology, 396(1):1–9, 2010. ISSN 0022-0981. doi: 10.1016/j.jembe.2010.10.006.

J. Stowe and K. Curran. Suppression of the ct beam hardening streak artifact using predictive correction on detector data. *Universal Journal of Medical Science*, 4:69–80, 03 2016. doi: 10.13189/ujmsj.2016.040203.

W. Vagberg, J.C. Larsson, and H.M. Hertz. Removal of ring artifacts in microtomography by characterization of scintillator variations. *Optics Express*, 25(19):23191–23198, Sep 2017. doi: 10.1364/OE.25.023191.

J. Wiegert. *Scattered radiation in cone-beam computed tomography: analysis, quantification and compensation.* PhD thesis, Rheinisch-Westfälische Technische Hochschule Aachen, Aachen, Germany., 2007.

M.G.R. Sause. *In Situ Monitoring of Fiber-Reinforced Composites: Theory, Basic Concepts, Methods, and Applications.* Springer Series in Materials Science. Springer International Publishing, 2016. ISBN 9783319309545.

M.L. Kataoka, M.G. Hochman, E.K. Rodriguez, P.J.P. Lin, S. Kubo, and V.D. Raptopolous. A review of factors that affect artifact from metallic hardware on multi-row detector computed tomography. *Current Problems in Diagnostic Radiology*, 39(4):125–136, 2010. ISSN 03630188. doi: 10.1067/j.cpradiol.2009.05.002.

S.N. Friedman, G.S.K. Fung, J.H. Siewerdsen, and B. M.W. Tsui. A simple approach to measure computed tomography (CT) modulation transfer function (MTF) and noise-power spectrum (NPS) using the American College of Radiology (ACR) accreditation phantom. *Medical Physics*, 40(5), 2013. ISSN 00942405. doi: 10.1118/1.4800795.

J. Angel and L.D. Chiffre. Comparison on Computed Tomography using industrial items. *CIRP Annals - Manufacturing Technology*, pages 4–7, 2014. ISSN 0007-8506. doi: 10.1016/j.cirp.2014.03.034.

Y. Tan. *Scanning and post-processing parameter optimization for CT dimensional metrology.* PhD thesis, KU Leuven, Leuven, Belgium., 2015.

J. P. Kruth, M. Bartscher, S. Carmignato, R. Schmitt, D.L. Chiffre, and A. Weckenmann. Computed tomography for dimensional metrology. *CIRP Annals - Manufacturing Technology*, 60(2):821–842, 2011. ISSN 00078506. doi: 10.1016/j.cirp.2011.05.006.

S. Luksic, R. Pokorny, J. George, P. Hrma, T. Varga, L. Reno, A. Buchko, and A. Kruger. In situ characterization of foam morphology during melting of simulated waste glass using x-ray computed tomography. *Ceramics International*, 46, 03 2020. doi: 10.1016/j.ceramint.2020.02.215.

D.L. Chiffre, S. Carmignato, J.P. Kruth, R. Schmitt, and A. Weckenmann. Industrial applications of computed tomography. *CIRP Annals - Manufacturing Technology*, 63(2):655–677, 2014. ISSN 17260604. doi: 10.1016/j.cirp.2014.05.011.

S.C. Garcea, Y. Wang, and P.J. Withers. X-ray computed tomography of polymer composites. *Composites Science and Technology*, 156:305–319, 2018. ISSN 02663538. doi: 10.1016/j.compscitech.2017.10.023.

Olga Stamati. *Impact of meso-scale heterogeneities on the mechanical behaviour of concrete : insights from in-situ x-ray tomography and E-FEM modelling.* Theses, Université Grenoble Alpes [2020-....], May 2020.

T. Bultreys, M.A. Boone, , M.N. Boone, , T.D. Schryver, B. Masschaele, L.V. Hoorebeke, and V. Cnudde. Fast laboratory-based micro-computed tomography for pore-scale research: Illustrative experiments and perspectives on the future. *Advances in Water Resources*, 95:341–351, sep 2016. ISSN 03091708. doi: 10.1016/j.advwatres.2015.05.012.

S. Leng, M. Bruesewitz, S. Tao, K. Rajendran, Ahmed F. Halaweish, N.G. Campeau, Joel G. Fletcher, and C.H. McCollough. Photon-counting Detector CT: System Design and Clinical Applications of an Emerging Technology. *Radiographics*, 39(3):729–743, 2019. ISSN 15271323. doi: 10.1148/rg.2019180115.

K. Taguchi and J.S. Iwanczyk. Vision 20/20: Single photon counting x-ray detectors in medical imaging. *Medical physics*, 40(10):100901, 2013. ISSN 00942405. doi: 10.1118/1.4820371.

K. Taguchi. Multi-energy inter-pixel coincidence counters for charge sharing correction and compensation in photon counting detectors. *Medical Physics*, 47(5):2085–2098, 2020. ISSN 00942405. doi: 10.1002/mp.14047.

T. Koenig, J. Schulze, M. Zuber, K. Rink, K. Butzer, E. Hamann, A. Cecilia, A. Zwerger, A. Fauler, M. Fiederle, and U. Oelfke. Imaging properties of small-pixel spectroscopic x-ray detectors based on cadmium telluride sensors. *Physics in Medicine and Biology*, 57(21):6743–6759, 2012. ISSN 00319155. doi: 10.1088/0031-9155/57/21/6743.

R. Bellazzini. PIXIRAD: Introducing a new X-Ray imaging system based on Chromatic Photon Counting technology, 2013.

I. Kumpová, D. Vavřík, T. Fíla, P. Koudelka, I. Jandejsek, J. Jakůbek, D. Kytýř, P. Zlámal, M. Vopálenský, and A. Gantar. High resolution micro-CT of low attenuating organic materials using large area photon-counting detector. *Journal of Instrumentation*, 11(02):C02003–C02003, feb 2016. doi: 10.1088/1748-0221/11/02/c02003.

C. Thibaut. *Development of fibrous cellulosic materials for the production of bio-based 3D printed objects by extrusion.* Theses, Université Grenoble Alpes [2020-....], January 2020.

D. Vavrik, J. Jakůbek, I. Kumpova, and M. Pichotka. Laboratory based study of dynamical processes by 4D X-ray CT with sub-second temporal resolution. *Journal of Instrumentation*, 12(2), 2017. ISSN 17480221. doi: 10.1088/1748-0221/12/02/C02010.

A. Eggert, M. Müller, F. Nachtrab, J. Dombrowski, A. Rack, and S. Zabler. High-speed in-situ tomography of liquid protein foams. *International Journal of Materials Research*, 105(7):632–639, 2014. doi: doi:10.3139/146.111057.

J. Dewanckele, M.A. Boone, F. Coppens, D.V. Loo, and A.P. Merkle. Innovations in laboratory-based dynamic micro-ct to accelerate in situ research. *Journal of Microscopy*, 277, 02 2020. doi: 10.1111/jmi.12879.

L. Salvo, P. Cloetens, E. Maire, S. Zabler, J.J. Blandin, J.Y. Buffiere, W. Ludwig, E. Boller, D. Bellet, and C. Josserond. X-ray micro-tomography an attractive characterisation technique in materials science. *Nuclear Instruments and Methods in Physics Research Section B: Beam Interactions with Materials and Atoms*, 200:273–286, 2003. ISSN 0168-583X. doi: https://doi.org/10.1016/S0168-583X(02)01689-0. Proceedings of the E-MRS 2002 Symposium I on Synchrotron Radiation and Materials Science.

E. Maire and P. J. Withers. Quantitative x-ray tomography. *International Materials Reviews*, 59(1):1–43, 2014. doi: 10.1179/1743280413Y.0000000023.

L. Salvo, M. Suery, A. Marmottant, N. Limodin, and D. Bernard. 3D imaging in material science: Application of X-ray tomography. *Comptes Rendus Physique*, 11(9-10):641–649, 2010. ISSN 16310705. doi: 10.1016/j.crhy.2010.12.003.

J.Y. Buffiere, E. Maire, J. Adrien, J.P. Masse, and E. Boller. In situ experiments with X ray tomography: an attractive tool for experimental mechanics. *Experimental Mechanics*, 50(3):289–305, 2010.

P.J. Withers, C. Bouman, S. Carmignato, V. Cnudde, D. Grimaldi, C.K. Hagen, E. Maire, M. Manley, A.D. Plessis, and S.R. Stock. X-ray computed tomography. *nature Reviews Methods Primers*, 1(1):21, 2021. ISSN 2662-8449.

A. King, P. Reischig, J. Adrien, and W. Ludwig. First laboratory x-ray diffraction contrast tomography for grain mapping of polycrystals. *Journal of Applied Crystallography*, 46, 12 2013. doi: 10.1107/S0021889813022553.

Helene Labriet, David Paganin, Pierre Lhuissier, Luc Salvo, Sam Bayat, Emmanuel Brun, Sébastien Bérujon, Ludovic Broche, Barbara Fayard, Sylvain Bohic, and Olivier Stephanov. 3D histopathology speckle phase contrast imaging: from synchrotron to conventional sources. In *Physics of Medical Imaging*, page 63, San Diego, France, February 2019. SPIE. doi: 10.1117/12.2511944.

S. Carmignato. Accuracy of industrial computed tomography measurements: Experimental results from an international comparison. *CIRP Annals*, 61(1):491–494, 2012. ISSN 0007-8506. doi: https://doi.org/10.1016/j.cirp.2012.03.021.

H.V. Gómez and S.T. Smith. Effect of the number of projections on dimensional measurements with x-ray computed tomography. *Precision Engineering*, 66:445–456, 2020. ISSN 0141-6359. doi: https://doi.org/10.1016/j.precisioneng.2020.08.006.

A. Plessis, C. Broeckhoven, A. Guelpa, and S. Gerhard. Laboratory x-ray micro-computed tomography : a user guideline for biological samples. *GigaScience*, 6(April):1–11, jun 2018. ISSN 2047217X. doi: 10.1093/gigascience/gix027.

G.N. Hounsfield. Computerized transverse axial scanning (tomography): Part I. Description of system. *International Journal of Radiation Oncology, Biology, Physics*, 31(2):393–398, 1973. ISSN 03603016. doi: 10.1016/0360-3016(94)E0127-6.

J.C. Elliott and S.D. Dover. X-ray microtomography. *Journal of Microscopy*, 126(2):211–213, 1982. doi: https://doi.org/10.1111/j.1365-2818.1982.tb00376.x.

L.A. Feldkamp, L.C. Davis, and J.W. Kress. Practical cone-beam algorithm. *J. Opt. Soc. Am. A*, 1(6): 612–619, Jun 1984a. doi: 10.1364/JOSAA.1.000612.

T. Weitkamp, A. Diaz, C. David, F. Pfeiffer, M. Stampanoni, P. Cloetens, and E. Ziegler. X-ray phase imaging with a grating interferometer. *Opt. Express*, 13(16):6296–6304, Aug 2005. doi: 10.1364/OPEX.13.006296.

F. Pfeiffer, C. Kottler, O. Bunk, and C. David. Hard x-ray phase tomography with low-brilliance sources. *Phys. Rev. Lett.*, 98:108105, Mar 2007. doi: 10.1103/PhysRevLett.98.108105.

P.J Withers. X-ray nanotomography. *Materials Today*, 10(12):26–34, 2007. ISSN 1369-7021. doi: https://doi.org/10.1016/S1369-7021(07)70305-X.

E. Maire, C.L. Bourlot, J. Adrien, A. Mortensen, and R. Mokso. 20 hz x-ray tomography during an in situ tensile test. *International Journal of Fracture*, 200, 07 2016. doi: 10.1007/s10704-016-0077-y.

F.G. Garcia-Moreno, P.H. Kamm, T.R. Neu, F. Bulk, M.A. Noack, M. Wegener, V.D.N. Eltz, C.M. Schlepütz, M. Stampanoni, and J. Banhart. Tomoscopy: Time-resolved tomography for dynamic processes in materials. *Advanced Materials*, 33(45):2104659, 2021. doi: https://doi.org/10.1002/adma.202104659.

S.A. McDonald, P. Reischig, C.P. Holzner, E. Lauridsen, P.J. Withers, A.P. Merkle, and M. Feser. Non-destructive mapping of grain orientations in 3d by laboratory x-ray microscopy. *Scientific Reports*, 5, 2015.

W. Huda and R. Abrahams. X-ray-based medical imaging and resolution. *AJR. American journal of roentgenology*, 204:W393–W397, 04 2015. doi: 10.2214/AJR.14.13126.

A. Adibhatla. Latest developments in liquid metal jet technology x-ray sources. In *Advances in X-Ray/EUV Optics and Components XVI*, volume 11837, page 118370K. International Society for Optics and Photonics, 2021.

F. Schafers, M. Mertin, and M. Gorgoi. Kmc-1: A high resolution and high flux soft x-ray beamline at bessy. *The Review of scientific instruments*, 78:123102, 01 2008. doi: 10.1063/1.2808334.

Gema Martínez-Criado, Julie Villanova, Rémi Tucoulou, Damien Salomon, Jussi-Petteri Suuronen, Sylvain Labouré, Cyril Guilloud, Valentin Valls, Ray Barrett, Eric Gagliardini, Yves Dabin, Robert P. Baker, Sylvain Bohic, Cédric Cohen, and John Morse. Id16b: a hard x-ray nanoprobe beamline at the esrf for nano-analysis. *Journal of Synchrotron Radiation*, 23:344 – 352, 2016.

A. Brunetti, M.D.R. Sanchez, B. Golosio, A. Simionovici, and A. Somogyi. A library for x-ray–matter interaction cross sections for x-ray fluorescence applications. *Spectrochimica Acta Part B: Atomic Spectroscopy*, 59(10-11):1725–1731, 2004. doi: 10.1016/j.sab.2004.03.014.

M.J. Darby, D.A. Barron, and R.E. Hyland. *Oxford Handbook of Medical Images*. Oxford University Press, 2011. ISBN 9780199216369.

T.M. Buzug. *Computed tomography From photon statistics to modern cone-beam CT*. Springer, Germany, 2008. ISBN 978-3-540-39407-5.

G.F. Knoll. *Radiation detection and measurement / Glenn F. Knoll*. Wiley New York, 2nd ed. edition, 1989. ISBN 0471815047.

A.R. Cowen, S.M. Kengyelics, and A.G. Davies. Solid-state, flat-panel, digital radiography detectors and their physical imaging characteristics. *Clinical Radiology*, 63(5):487–498, 2008. ISSN 0009-9260. doi: https://doi.org/10.1016/j.crad.2007.10.014.

H.A. Wischmann, H. Luijendijk, H. Meulenbrugge, M. Overdick, R. Schmidt, and K. Kiani. Correction of amplifier nonlinearity, offset, gain, temporal artifacts, and defects for flat-panel digital imaging devices. In *Physics of Medical Imaging*, volume 4682, 05 2002. doi: 10.1117/12.465586.

Y. Yu and J. Wang. Heel effect adaptive flat field correction of digital x-ray detectors. *Medical physics*, 40(8):081913, August 2013. ISSN 0094-2405. doi: 10.1118/1.4813303.

M. Lesser. Charge coupled device (ccd) image sensors. In Daniel Durini, editor, *High Performance Silicon Imaging*, pages 78–97. Woodhead Publishing, 2014. ISBN 978-0-85709-598-5. doi: https://doi.org/10.1533/9780857097521.1.78.

G.E. Smith. The invention and early history of the ccd. *Nuclear Instruments and Methods in Physics Research Section A: Accelerators, Spectrometers, Detectors and Associated Equipment*, 607(1):1–6, 2009. ISSN 0168-9002. doi: https://doi.org/10.1016/j.nima.2009.03.233. Radiation Imaging Detectors 2008.

P. Alle, E. Wenger, S. Dahaoui, D. Schaniel, and C. Lecomte. Comparison of CCD, CMOS and hybrid pixel x-ray detectors: detection principle and data quality. *Physica Scripta*, 91(6):063001, may 2016. doi: 10.1088/0031-8949/91/6/063001.

R. Ballabriga, J. Alozy, M. Campbell, E. Frojdh, E. H.M. Heijne, T. Koenig, X. Llopart, J. Marchal, D. Pennicard, T. Poikela, L. Tlustos, P. Valerio, W. Wong, and M. Zuber. Review of hybrid pixel detector readout ASICs for spectroscopic X-ray imaging. *Journal of Instrumentation*, 11(1), 2016. ISSN 17480221. doi: 10.1088/1748-0221/11/01/P01007.

R. Bellazzini, A. Brez, G. Spandre, M. Minuti, M. Pinchera, P. Delogu, P.L. de Ruvo, and A. Vincenzi. PIXIE III: a very large area photon-counting CMOS pixel ASIC for sharp x-ray spectral imaging. *Journal of Instrumentation*, 10(01):C01032–C01032, jan 2015. doi: 10.1088/1748-0221/10/01/c01032.

L.A. Feldkamp, L.C. Davis, and J.W. Kress. Practical cone-beam algorithm. *Journal of the Optical Society of America A*, 1(January), 1984b.

J. Hsieh. *Computed tomography : principles, design, artifacts, and recent advances*. SPIE Press, 2009a. ISBN 9780819475336.

S. Carmignato, V. Aloisi, F. Medeossi, F. Zanini, and E. Savio. Influence of surface roughness on computed tomography dimensional measurements. *CIRP Annals - Manufacturing Technology*, 66(1): 499–502, 2017b. ISSN 17260604. doi: 10.1016/j.cirp.2017.04.067.

M.J. Willemink. The evolution of image reconstruction for CT — from filtered back projection to artificial intelligence. *European Radiology*, pages 2185–2195, 2019.

S.R.D. Roscoat, J. Bloch, and X. Thibault. Characterisation of the 3D Paper Structure with X-ray Synchrotron Radiation Microtomography. *Advances in Paper Science and Technology*, 2005. Trans. of the XIIIth Fund. Res. Symp. Cambridge.

S.R.D Roscoat, J.M.F. Martins, P. Sechet, E. Vince, P. Latil, and C. Geindreau. Application of synchrotron X-ray microtomography for visualizing bacterial biofilms 3D microstructure in porous media. *Biotechnology and Bioengineering*, 111(6):1265–1271, June 2014. doi: 10.1002/bit.25168.

A. Dadda, C. Geindreau, F. Emeriaut, S.R.D Roscoat, A. Garandet, L. Sapin, and A.E. Filet. Characterization of microstructural and physical properties changes in biocemented sand using 3D X-ray microtomography. *Acta Geotechnica*, 12(5):955–970, October 2017.

G. Viggiani, N. Lenoir, P. Bésuelle, M.D. Michiel, S. Marello, J. Desrues, and M. Kretzschmer. X-ray microtomography for studying localized deformation in fine-grained geomaterials under triaxial compression. *Comptes Rendus Mécanique*, 332(10):819–826, 2004. ISSN 1631-0721. doi: https://doi.org/10.1016/j.crme.2004.05.006.

J. Otani, T. Mukunoki, and Y. Obara. Characterization of failure in sand under triaxial compression using an industrial x-ray ct scanner. *International Journal of Physical Modelling in Geotechnics*, 2(1): 15–22, 2002. doi: 10.1680/ijpmg.2002.020102.

P. Besuelle, G. Viggiani, N. Lenoir, J. Desrues, and M. Bornert. X-ray micro CT for studying strain localization in clay rocks under triaxial compression. In Gioacchino Viggiani Jacques Desrues and Pierre Bésuelle, editors, *GEOX 2006 - 2nd International Workshop on X-Ray CT for geomaterials*, pages 35–52, Aussois, France, 2006. ISTE.

G.F. Zhao, A.R. Russell, X. Zhao, and N. Khalili. Strain rate dependency of uniaxial tensile strength in gosford sandstone by the distinct lattice spring model with x-ray micro ct. *International Journal of Solids and Structures*, 51(7):1587–1600, 2014a. ISSN 0020-7683. doi: https://doi.org/10.1016/j.ijsolstr.2014.01.012.

P. Lhuissier, M. Scheel, L. Salvo, M. Di Michiel, and J.J. Blandin. Continuous characterization by x-ray microtomography of damage during high-temperature deformation of magnesium alloy. *Scripta Materialia*, 69(1):85–88, 2013. ISSN 1359-6462. doi: https://doi.org/10.1016/j.scriptamat.2013.03.001.

P. Lhuissier, M. Scheel, L. Salvo, E. Boller, M. Di Michiel, and J.J. Blandin. 4D damage characterisation during superplastic deformation of magnesium alloys. In *Intern. Conf. on Superplasticity of Advanced Materials (ICSAM)*, ALBI, France, July 2012.

L. Salvo, P. Lhuissier, M. Scheel, S. Terzi, M.D Michiel, E. Boller, J.A. Taylor, A. K. Dahle, and M. Suery. 3d in situ imaging of aluminium alloys during solidification. *Transactions of the Indian Institute of Metals*, 65:623–626, 2012b.

R. Kumar, J. Villanova, P. Lhuissier, and L. Salvo. In situ nanotomography study of creep cavities in al-3.6-cu alloy. *Acta Materialia*, 166:18–27, 2019. ISSN 1359-6454. doi: https://doi.org/10.1016/j.actamat.2018.12.020.

Y. Liu, A.M. Kiss, D.H. Larsson, F. Yang, and P. Pianetta. To get the most out of high resolution X-ray tomography: A review of the post-reconstruction analysis. *Spectrochimica Acta Part B: Atomic Spectroscopy*, 117:29–41, mar 2016. ISSN 0584-8547. doi: 10.1016/j.sab.2016.01.002.

L.W. Goldman. Principles of CT : Radiation Dose and Image Quality. *J. Nucl. Med. Technol.*, 35(4): 213–225, dec 2007. ISSN 00914916. doi: 10.2967/jnmt.106.037846.

H.E. Martz, C.M. Logan, D.J. Schneberk, and P.J. Shull. *X-Ray Imaging: Fundamentals, Industrial Techniques and Applications*. CRC Press, 2016. ISBN 9781420009767.

G.R. Davis and J.C. Elliott. Artefacts in X-ray microtomography of materials. *Materials Science and Technology*, 22(9):1011–1019, sep 2006. ISSN 02670836. doi: 10.1179/174328406X114117.

F. E. Boas and D. Fleischmann. CT artifacts : Causes and reduction techniques. *Imaging Med*, 4(2): 229–240, 2012.

H.S. Park and Y.E. Chung. Computed tomographic beam-hardening artefacts : mathematical characterization and analysis Subject Areas :. *Philosophical Transactions A*, pages 1–11, 2015.

J.J. Lifton, A.A. Malcolm, and J.W. McBride. An experimental study on the influence of scatter and beam hardening in x-ray CT for dimensional metrology. *Measurement Science and Technology*, 015007 (1):15007, dec 2015. ISSN 0957-0233. doi: 10.1088/0957-0233/27/1/015007.

J.A. Meganck, K.M. Kozloff, M.M. Thornton, S.M. Broski, and S.A. Goldstein. Beam hardening artifacts in micro-computed tomography scanning can be reduced by X-ray beam fi ltration and the resulting images can be used to accurately measure BMD. *Bone*, 45(6):1104–1116, dec 2009. ISSN 8756-3282. doi: 10.1016/j.bone.2009.07.078.

J.F. Barrett and N. Keat. Artifacts in CT: Recognition and Avoidance. *Radiographics*, pages 1679–1691, 2004.

J. Jakubek. Data processing and image reconstruction methods for pixel detectors. *Nuclear Instruments and Methods in Physics Research, Section A: Accelerators, Spectrometers, Detectors and Associated Equipment*, 576(1):223–234, 2007. ISSN 01689002. doi: 10.1016/j.nima.2007.01.157.

K. Schorner. *Development of Methods for Scatter Artifact Correction in Industrial X-ray Cone-beam Computed Tomography*. PhD thesis, Technische Universitat Munchen, Munich, Germany, 2012.

W. Fang, L. Li, and Z. Chen. Removing ring artefacts for photon-counting detectors using neural networks in different domains. *IEEE Access*, 8:42447–42457, 2020. doi: 10.1109/ACCESS.2020.2977096.

H.J. Motulsky and R.E. Brown. Detecting outliers when fitting data with nonlinear regression – a new method based on robust nonlinear regression and the false discovery rate. *BMC Bioinformatics*, 20: 1–20, mar 2006. ISSN 14712105. doi: 10.1186/1471-2105-7-123.

X. Yang, Y. Meng, H. Gong, and Y. Deng. Abnormal pixel detection using sum-of- projections symmetry in cone beam computed tomography. *OPTICS EXPRESS*, 20(10):348–354, 2012.

J. Sijbers and A. Postnov. Reduction of ring artefacts in high resolution micro-CT reconstructions. *Physics in Medicine and Biology*, 49(14), jul 2004. ISSN 00319155. doi: 10.1088/0031-9155/49/14/N06.

P.C. Johns and M. yaffle. Scattered radiation on fan beam imaging systems. *Med. Phys*, 9(1982), 1981.

G.H. Glover. Compton scatter effects in CT reconstructions. *Medical Physics*, 860(1982):860–867, 2012. ISSN 00942405. doi: 10.1118/1.595197.

J.H. Siewerdsen and D.A. Jaffray. Cone-beam computed tomography with a flat-panel imager: Magnitude and effects of x-ray scatter. *Medical Physics*, 28(July 2000):220–231, 2001. ISSN 00942405. doi: 10.1118/1.1339879.

H. Park, J. Choi, and J. Seo. Characterization of metal artifacts in x-ray computed tomography. *Communications on Pure and Applied Mathematics*, 70, 06 2014. doi: 10.1002/cpa.21680.

T.D. Schryver, M. Dierick, M.and Heyndrickx, J.V. Stappen, M.A. Boone, L.V. Hoorebeke, and M.N. Boone. Motion compensated micro-ct reconstruction for in-situ analysis of dynamic processes. *Scientific Reports*, 8, 05 2018. doi: 10.1038/s41598-018-25916-5.

C.J. Ritchie, C.R. Crawford, D.J. Godwin, K.F. King, and Y. Kim. Correction of computed tomography motion artifacts using pixel-specific back-projection. *IEEE Transactions on Medical Imaging*, 15(3): 333–342, 1996. ISSN 02780062. doi: 10.1109/42.500142.

E. Samei, M.J. Flynn, and W.R. Eyler. Detection of subtle lung nodules: Relative influence of quantum and anatomic noise on chest radiographs. *Radiology*, 213(3):727–734, 1999. doi: 10.1148/radiology.213.3.r99dc19727. PMID: 10580946.

E. Samei. Performance of digital radiographic detectors : Quantification and assessment methods 1. In *Advances in Digital Radiography: RSNA Categorical Course in Diagnostic Radiology Physics*, 2001.

J.Y. Vaishnav, W.C. Jung, L.M. Popescu, R. Zeng, and K.J. Myers. Objective assessment of image quality and dose reduction in CT iterative reconstruction. *Medical Physics*, 41(July), 2014a. ISSN 00942405. doi: 10.1118/1.4881148.

M.J. Willemink, T. Leiner, P.A.D. Jong, P.AA. Jong, L.M. Heer, R.A.J. Nievelstein, A.M.R. Schilham, and R.P.J. Budde. Iterative reconstruction techniques for computed tomography part 2 : initial results in dose reduction and image quality Iterative Reconstruction in Image Space. *European Radiology*, 23 (6):1632–1642, jun 2013. ISSN 09387994. doi: 10.1007/s00330-012-2764-z.

F. Zarb, L. Rainford, and M.F. McEntee. Radiography Developing optimized CT scan protocols : Phantom measurements of image quality. *Radiography*, 17(2):109–114, may 2011. ISSN 1078-8174. doi: 10.1016/j.radi.2010.10.004.

M.G. Lubner, P.J. Pickhardt, J. Tang, and G.H. Chen. Reduced Image Noise at Low-Dose Multidetector CT of the Abdomen with Prior Image Constrained Compressed Sensing Algorithm 1. *Radiology*, 260 (1), 2011. doi: 10.1148/radiol.11101380/-/DC1.

A. Rose. The Sensitivity Performance of the Human Eye on an Absolute Scale. *Journal of the Optical Society of America*, pages 196–208, 1948.

J. Boone, J. Brink, S. Edyvean, W. Huda, W. Leitz, C. McCollough, and M.G. McNitt. Noise Assessment in CT. *Journal of the International Commission on Radiation Units and Measurements*, 12(1):121–134, 04 2012. ISSN 1473-6691. doi: 10.1093/jicru/ndt002.

J.T. Bushberg, J.A. Seibert, and J.M. Boone. *The Essential Physics of Medical Imaging*. Lippincott Williams & Wilkins, 3 edition, 2012. ISBN 9780781780575.

J.Y. Vaishnav, W.C. Jung, L.M. Popescu, R. Zeng, and K.J. Myers. Objective assessment of image quality and dose reduction in CT iterative reconstruction. *Medical Physics*, 41(7), 2014b. ISSN 00942405. doi: 10.1118/1.4881148.

S.T. Schindera, D. Odedra, A.S. Raza, K.K Tae, H.J. Jang, S.Z Farkas, and P. Rogalla. Iterative reconstruction algorithm for CT: Can Radiation Dose Be Decreased While Low-Contrast Detectability Is Preserved? *Original research n Medical Physics Radiology*, 269, 2013. doi: 10.1148/radiol.13122349/-/DC1.

J.G. Robson and N. Graham. Probability summation and regional variation in contrast sensitivity across the visual field. *Vision Research*, 21(3):409–418, 1981. ISSN 0042-6989. doi: https://doi.org/10.1016/0042-6989(81)90169-3.

R. Ferzli and L.J. Karam. A No-Reference Objective Image Sharpness Metric Based on the Notion of Just Noticeable Blur (JNB). *IEEE Transactions on Image Processing*, 18(4):717–728, 2009. ISSN 10577149. doi: 10.1109/TIP.2008.2011760.

A. Kraemer, E. Kovacheva, and G. Lanza. Projection based evaluation of CT image quality in dimensional metrology. In *Digital Industrial Radiology and Computed Tomography (DIR 2015)*, pages 22–25, June 2015.

M. Reiter, D. Weis, C. Gusenbauer, M. Erler, C. Kuhn, and J. Kastner. Evaluation of a histogram-based image quality measure for X-ray computed tomography. *iCT Conference*, pages 273–282, 2014.

Z. Wang and A.C. Bovik. *Modern Image Quality Assessment Synthesis Lectures on Image, Video, and Multimedia Processing*. Morgan and Claypool Publishers, 2006.

Z. Wang and A.C. Bovik. Mean squared error: Love it or leave it? a new look at signal fidelity measures. *IEEE Signal Processing Magazine*, 26(1):98–117, 2009. doi: 10.1109/MSP.2008.930649.

Z. Kotevski and P.J. Mitrevski. Experimental Comparison of PSNR and SSIM Metrics for Video Quality Estimation, 2010.

O. Ieremeiev, V. Lukin, K. Okarma, and K. Egiazarian. Full-reference quality metric based on neural network to assess the visual quality of remote sensing images. *Remote Sensing*, 12(15), 2020. ISSN 20724292. doi: 10.3390/RS12152349.

A. Mittal, R. Soundararajan, and A.C. Bovik. Making a "completely blind" image quality analyzer. *IEEE Signal Processing Letters*, 20(3):209–212, 2013. doi: 10.1109/LSP.2012.2227726.

Hamid R. Sheikh, Muhammad F. Sabir, and Alan Conrad Bovik. A statistical evaluation of recent full reference image quality assessment algorithms. *IEEE Transactions on Image Processing*, 15:3440–3451, 2006.

L. Zhang, L. Zhang, and A.C. Bovik. A feature-enriched completely blind image quality evaluator. *IEEE Transactions on Image Processing*, 24(8):2579–2591, 2015. doi: 10.1109/TIP.2015.2426416.

A. Cantatore and P. Muller. *Introduction to computed tomography*. DTU Mechanical Engineering, 2011.

A. Buratti, N. Grozmani, C. Voigtmann, L. Sartori, and R. Schmitt. Determination of the optimal imaging parameters in industrial computed tomography for dimensional measurements on monomaterial workpieces. *Measurement Science and Technology*, 29, 09 2018. doi: 10.1088/1361-6501/aae4d6.

M. Reiter, C. Heinzl, D. Salaberger, D. Weiss, and J. Kastner. Study on parameter variation of an industrial computed tomography simulation tool concerning dimensional measurement deviations. In *10th European Conference on Non-Destructive Testing, Moscow, Russia*, 01 2010.

Y. Chahid, A. Townsend, A. Liu, P. Bills, P. Sperling, and R. Racasan. *Optimizing X-Ray Computed Tomography Settings for Dimensional Metrology Using 2D Image Analysis*, pages 88–101. ASTM International, 09 2020. ISBN 9780803177086. doi: 10.1520/stp163120190141.

ISO 15708-1:2017. Bsi bs en iso 15708-2-2019 non-destructive testing—radiation methods for computed tomography part 2: Principles, equipment and samples. Technical report, International Organization for Standardization (ISO), 2019.

VDI. Vdi/vde 2630 part 1.2: Computed tomography in dimensional measurement - influencing variables on measurement results and recommendations for computed tomography dimensional measurements. Technical report, (Verein Deutscher Ingenieure), 09 2010.

S. Zabler, M. Ullherr, C. Fella, R. Schielein, O. Focke, B. Zeller-Plumhoff, P. Lhuissier, W. DeBoever, and R. Hanke. Comparing image quality in phase contrast subμ x-ray tomography—a round-robin study. *Nuclear Instruments and Methods in Physics Research Section A: Accelerators, Spectrometers, Detectors and Associated Equipment*, 951:162992, 2020. ISSN 0168-9002. doi: https://doi.org/10.1016/j.nima.2019.162992.

P. Russo. *Handbook of X-ray Imaging Physics and Technology*. CRC Press Taylor and Francis Group, 2018. ISBN 9781498741521.

A. Ihsan, S.H. Heo, and S.O. Cho. Optimization of X-ray target parameters for a high-brightness micro-focus X-ray tube. *Nuclear Instruments and Methods in Physics Research B*, 264:371–377, 2007. doi: 10.1016/j.nimb.2007.09.023.

F.B.D. Oliveira, M. Bartscher, U.R. Neuschaefer, R. Tutsch, and J. Hiller. *Multi-material Acceptance Testing for CT-Based Coordinate Measurement Systems*, pages 131–154. Springer Verlag, 05 2019. ISBN 978-3-030-18176-5. doi: 10.1007/978-3-030-18177-2_14.

S.O. Kasap and J.A. Rowlands. Review X-ray photoconductors and stabilized a-Se for direct conversion digital ¯ at-panel X-ray image- detectors. *Journal of material science: Materials in electronics*, 1: 179–198, 2000.

T. Kuroda. *Essential Principles of Image Sensors*. CRC Press, 2015. ISBN 9781482220063.

M. Overdick. *Advances in Health care Technology Care Shaping the Future of Medical*. Springer, Dordrecht, 2006.

E. Shefer, A. Altman, R. Behling, R. Goshen, L. Gregorian, Y. Roterman, I. Uman, N. Wainer, Y. Yagil, and O. Zarchin. State of the Art of CT Detectors and Sources: A Literature Review. *Current Radiology Reports*, 1(1):76–91, 2013. ISSN 21674825. doi: 10.1007/s40134-012-0006-4.

S.R. Stock. *Microcomputed tomography methodology and applications*. CRC Press, 2009. ISBN 9781420058765.

K. Kiekens, F. Welkenhuyzen, Y. Tan, Ph Bleys, A. Voet, J. P. Kruth, and W. Dewulf. A test object with parallel grooves for calibration and accuracy assessment of industrial computed tomography (CT) metrology. *Measurement Science and Technology*, 22(11), 2011. ISSN 13616501. doi: 10.1088/0957-0233/22/11/115502.

K. Orhan. *Micro-computed Tomography (micro-CT) in Medicine and Engineering*. Springer, Cham, 2019. ISBN 9783030166403.

K. Tang, L. Wang, R. Li, J. Lin, X. Zheng, and G. Cao. Effect of Low Tube Voltage on Image Quality , Radiation Dose , and Low-Contrast Detectability at Abdominal Multidetector CT : Phantom Study. *Journal of Biomedicine and Biotechnology*, 2012(April 2012), 2015. ISSN 11107243. doi: 10.1155/2012/130169.

A. Kueh, J. Warnett, G. Gibbons, J. Brettschneider, T. Nichols, M. Williams, and W. Kendall. Modelling the penumbra in computed tomography. *Journal of X-ray science and technology*, 24:583–597, 05 2016. doi: 10.3233/XST-160576.

Y. Tan, K. Kiekens, F. Welkenhuyzen, J.P. Kruth, and W. Dewulf. Defining the Optimal Beam Hardening Correction Parameters for CT Dimensional Metrology Applications. In *International Conference on Competitive Manufacturing*, 2013.

S. Mohd, J. Abdullah, M.R. Shari, M.I.I Haikal, and A. Sohaimy. Comparison Types of Filter Used in Viewing Inner Structure of Materials Using X-Ray Computed Tomography. Technical report, Centre for Computed Tomography and Industrial Imaging, 2011.

R. Christoph and H.J. Neumann. X-ray tomography in industrial metrology. *Werth*, page 6, 2012.

M. Tshibalanganda, A.D. Plessis, S.G. Roux, Wendy Taylor, S. Gerhard, L. Roux, and W. Taylor. Systematic experiments to quantitatively assess image quality for CT scans of a Karoo tetrapod fossil. *Palaeontologia Africana*, August 2019.

A. Weckenmann and P. Kramer. Assessment of measurement uncertainty caused in the preparation of measurements using computed tomography. *19th IMEKO World Congress 2009*, 3(May):1787–1791, 2009.

A. Weckenmann and P. Kramer. Predetermination of Measurement Uncertainty in the Application of Computed Tomography. *Product Lifecycle Management: Geometric Variations*, pages 317–330, 2013. doi: 10.1002/9781118557921.ch17.

T. Chighvinadze and S. Pistorius. The impact of the number of projections on image quality in Compton scatter tomography. *Journal of X-Ray Science and Technology*, 23(6):745–758, 2015. ISSN 08953996. doi: 10.3233/XST-150525.

A.E. Castro and D.L. Donoho. Does median filtering truly preserve edges better than linear filtering? *Annals of Statistics*, 37(3):1172–1206, 2009. ISSN 00905364. doi: 10.1214/08-AOS604.

M. Lyra and A. Ploussi. Filtering in SPECT image reconstruction. *International Journal of Biomedical Imaging*, 2011, 2011. ISSN 16874188. doi: 10.1155/2011/693795.

P. Gajjar, J.S. Jorgensen, J.R.A. Godinho, Chris G. Johnson, A. Ramsey, and P.J. Withers. New software protocols for enabling laboratory based temporal CT. *Review of Scientific Instruments*, 89(9), 2018. ISSN 10897623. doi: 10.1063/1.5044393.

M.D. Michiel, J.M. Merino, D. Fernandez-Carreiras, T. Buslaps, V. Honkimaki, P. Falus, Thierry Martins, and O. Svensson. Fast microtomography using high energy synchrotron radiation. *Review of Scientific Instruments*, 76(4), 2005. ISSN 00346748. doi: 10.1063/1.1884194.

A. Rack, F. Garcia-Moreno, C. Schmitt, O. Betz, A. Cecilia, A. Ershov, T. Rack, J. Banhart, and S. Zabler. On the possibilities of hard X-ray imaging with high spatio-temporal resolution using polychromatic synchrotron radiation. *Journal of X-Ray Science and Technology*, 18:429–441, 2010. doi: 10.3233/XST-2010-0273.

D. Wildenschild and A.P. Sheppard. X-ray imaging and analysis techniques for quantifying pore-scale structure and processes in subsurface porous medium systems. *Advances in Water Resources*, 51: 217–246, 2013. ISSN 0309-1708. doi: https://doi.org/10.1016/j.advwatres.2012.07.018.

R. Mokso, F. Marone, D. Haberthür, J. Schittny, G. Mikuljan, A. Isenegger, and M. Stampanoni. Following dynamic processes by x-ray tomographic microscopy with sub-second temporal resolution. *10th International Conference on X-Ray Microscopy*, 1365:38–41, 01 2011.

M. Stampanoni, A. Groso, A. Isenegger, G. Mikuljan, Q. Chen, A. Bertrand, S. Henein, R. Betemps, U. Frommherz, P. Böhler, D. Meister, M. Lange, and R. Abela. Trends in synchrotron-based tomographic imaging: the SLS experience. *Developments in X-Ray Tomography V*, 6318:63180M, 2006. ISSN 16057422. doi: 10.1117/12.679497.

J.S. Jorgensen and E.Y. Sidky. How little data is enough? phase-diagram analysis of sparsity-regularized x-ray computed tomography. *Philosophical transactions. Series A, Mathematical, physical, and engineering sciences*, 373, 2015.

S. Coban, W. Lionheart, and P. Withers. Assessing the efficacy of tomographic reconstruction methods through physical quantification techniques. *Measurement Science and Technology*, 32, 02 2021. doi: 10.1088/1361-6501/abe337.

G.R. Myers, A.M. Kingston, T.K. Varslot, M.L. Turner, and A.P. Sheppard. Dynamic tomography with a priori information. *Applied Optics*, 50(20):3685–3690, Jul 2011. doi: 10.1364/AO.50.003685.

J.N. Gruse, M.J.V. Streeter, C. Thornton, C.D. Armstrong, C.D. Baird, N. Bourgeois, S. Cipiccia, O.J. Finlay, C.D. Gregory, Y. Katzir, N.C. Lopes, S.P.D. Mangles, Z. Najmudin, D. Neely, L.R. Pickard, K.D. Potter, P.P. Rajeev, D.R. Rusby, C.I.D. Underwood, J.M. Warnett, M.A. Williams, J.C. Wood, C.D. Murphy, C.M. Brenner, and D.R. Symes. Application of compact laser-driven accelerator x-ray sources for industrial imaging. *Nuclear Instruments and Methods in Physics Research Section A: Accelerators, Spectrometers, Detectors and Associated Equipment*, 983:164369, 2020. ISSN 0168-9002. doi: https://doi.org/10.1016/j.nima.2020.164369.

B. Hornberger, J. Kasahara, M. Gifford, R.D. Ruth, and R.J. Loewen. A compact light source providing high-flux, quasi-monochromatic, tunable x-rays in the laboratory. In *Optical Engineering + Applications*, 2019.

R. E. Alvarez and A. Macovski. Energy-selective reconstructions in X-ray computerised tomography. *Physics in Medicine and Biology*, 21(5):733–744, 1976. ISSN 0031-9155. doi: 10.1088/0031-9155/21/5/002.

A. So and S. Nicolaou. Spectral computed tomography: Fundamental principles and recent developments. *Korean Journal of Radiology*, 22(1):86–96, 2021. ISSN 12296929. doi: 10.3348/kjr.2020.0144.

X. Wang, D. Meier, K. Taguchi, D.J. Wagenaar, B.E. Patt, and E.C. Frey. Material separation in x-ray ct with energy resolved photon-counting detectors. *Medical Physics*, 38(3):1534–1546, 2011. doi: https://doi.org/10.1118/1.3553401.

T. Sellerer, S. Ehn, K. Mechlem, M. Duda, M. Epple, P. B. Noel, and F. Pfeiffer. Quantitative dual-energy micro-CT with a photon-counting detector for material science and non-destructive testing. *PLOS ONE*, 14(7):1–18, 2019. doi: 10.1371/journal.pone.0219659.

T. G. Flohr, C. H. McCollough, H. Bruder, M. Petersilka, K. Gruber, C. Suss, M. Grasruck, K. Stierstorfer, B. Krauss, R. Raupach, A. N. Primak, A. Kuttner, S. Achenbach, C. Becker, A. Kopp, and B. M. Ohnesorge. First performance evaluation of a dual-source CT (DSCT) system. *European Radiology*, 16(2):256–268, 2006. ISSN 09387994. doi: 10.1007/s00330-005-2919-2.

J. Hsieh. Dual-Energy CT with Fast-KVp Switch. *Medical Physics*, 36(6Part24):2749, jun 2009b. ISSN 0094-2405. doi: https://doi.org/10.1118/1.3182432.

A. Altman and R. Carmi. A Double-Layer Detector, Dual-Energy CT - Principles, Advantages and Applications. *Medical Physics*, 36:2750, 2009.

N. Rassouli, M. Etesami, A. Dhanantwari, and P. Rajiah. Detector-based spectral CT with a novel dual-layer technology: principles and applications. *Insights into Imaging*, 8:589–598, 2017.

C. H. McCollough. Methods for Spectral CT Imaging CT - Computed Tomography : Approaches, Applications, and Operations. In Ehsan Samei and Norbert J Pelc, editors, *Computed Tomography*, pages 223–242. Springer International Publishing, Cham, 2020. ISBN 978-3-030-26957-9. doi: 10.1007/978-3-030-26957-9_12.

T. R. C. Johnson. Dual-energy CT: general principles. *AJR. American journal of roentgenology*, 199(5 Suppl):3–8, 2012. ISSN 15463141. doi: 10.2214/ajr.12.9116.

Y. Garini, I. Young, and G. McNamara. Spectral imaging: Principles and applications. *Cytometry. Part A : the journal of the International Society for Analytical Cytology*, 69:735–47, 08 2006. doi: 10.1002/cyto.a.20311.

P. M. Shikhaliev and G. F. Shannon. Photon counting spectral CT versus conventional CT: Comparative evaluation for breast imaging application. *Physics in Medicine and Biology*, 56(7):1905–1930, mar 2011. doi: 10.1088/0031-9155/56/7/001.

R. Ballabriga, M. Campbell, E. Heijne, X. Llopart, L. Tlustos, and W. Wong. Medipix3: A 64k pixel detector readout chip working in single photon counting mode with improved spectrometric performance. *Nuclear Instruments and Methods in Physics Research Section A: Accelerators, Spectrometers, Detectors and Associated Equipment*, 633:S15–S18, 2011. ISSN 0168-9002. doi: https://doi.org/10.1016/j.nima.2010.06.108. 11th International Workshop on Radiation Imaging Detectors (IWORID).

P. Delpierre, S. Basolo, J.F. Berar, M. Bordesoule, N. Boudet, P. Breugnon, B. Caillot, B. Chantepie, J.C. Clemens, B. Dinkespiler, S. Hustache-Ottini, C. Meessen, M. Menouni, C. Morel, C. Mouget, P. Pangaud, R. Potheau, and E. Vigeolas. Xpad: A photons counting pixel detector for material sciences and small-animal imaging. *Nuclear Instruments and Methods in Physics Research Section A: Accelerators, Spectrometers, Detectors and Associated Equipment*, 572(1):250–253, 2007. ISSN 0168-9002. doi: https://doi.org/10.1016/j.nima.2006.10.315. Frontier Detectors for Frontier Physics.

C. Broennimann, E.F. Eikenberry, B. Henrich, R. Horisberger, G. Huelsen, E. Pohl, B. Schmitt, B.C. Schulze, M. Suzuki, T. Tomizaki, H. Toyokawa, and A. Wagner. The pilatus 1m detector. *Journal of synchrotron radiation*, 13(Pt 2):120—130, March 2006. ISSN 0909-0495. doi: 10.1107/s0909049505038665.

R. Ballabriga, J. Alozy, F. N. Bandi, M. Campbell, N. Egidos, J. M. Fernandez-Tenllado, E. H. M. Heijne, I. Kremastiotis, X. Llopart, B. J. Madsen, D. Pennicard, V. Sriskaran, and L.Tlustos. Photon Counting Detectors for X-ray Imaging with Emphasis on CT. *IEEE Transactions on Radiation and Plasma Medical Sciences*, 7311(c):1–1, 2020. ISSN 2469-7311. doi: 10.1109/trpms.2020.3002949.

G. Prekas, H. Sabet, H.H. Bhandari, G. Derderian, F. Robertson, H. Kudrolli, C.J. Stapels, J. Christian, S. Kleinfelder, S. Cool, L.J. Aries, and V.V. Nagarkar. Direct and indirect detectors for x-ray photon counting systems. In *2011 IEEE Nuclear Science Symposium Conference Record*, pages 1487–1493, 2011. doi: 10.1109/NSSMIC.2011.6154354.

P. M. Shikhaliev. Computed tomography with energy-resolved detection: A feasibility study. *Physics in Medicine and Biology*, 53(5):1475–1495, 2008a. ISSN 00319155. doi: 10.1088/0031-9155/53/5/020.

P. M. Shikhaliev. Energy-resolved computed tomography: First experimental results. *Physics in Medicine and Biology*, 53(20):5595–5613, 2008b. ISSN 00319155. doi: 10.1088/0031-9155/53/20/002.

T.O. Tumer, M. Clajus, G. I. Visser, S. Yin, P.D. Willson, L.D. Aries, K.B. Parnham, B. Glick, J.L. Perry, T. Gamble, G. Creede, E. Worthington, J. Sparling, D. Maeding, and D. Gorzen. Preliminary results obtained from a novel CdZnTe pad detector and readout ASIC developed for an automatic baggage inspection system. In *IEEE Nuclear Science Symposium and Medical Imaging Conference*, volume 1, pages 4/36–4/41 vol.1, 2000. doi: 10.1109/nssmic.2000.949044.

J. P. Schlomka, E. Roessl, R. Dorscheid, S. Dill, G. Martens, T. Istel, C. Bäumer, C. Herrmann, R. Steadman, G. Zeitler, A. Livne, and R. Proksa. Experimental feasibility of multi-energy photon-counting K-edge imaging in pre-clinical computed tomography. *Physics in Medicine and Biology*, 53(15):4031–4047, 2008. ISSN 00319155. doi: 10.1088/0031-9155/53/15/002.

S. Kappler, F. Glasser, S. Janssen, E. Kraft, and M. Reinwand. A research prototype system for quantum-counting clinical CT. In Ehsan Samei and Norbert J Pelc, editors, *Medical Imaging 2010: Physics of Medical Imaging*, volume 7622, pages 664–669. International Society for Optics and Photonics, SPIE, 2010.

F. C. Brunner, D. Benoit, J.F. Bérar, J.C. Clémens, and C. Morel. Study of the charge sharing effect in the photon-counting pixel detector xpad3-s. *Nuclear Instruments and Methods in Physics Research Section A: Accelerators, Spectrometers, Detectors and Associated Equipment*, 633:S111–S113, 2011. ISSN 0168-9002. doi: https://doi.org/10.1016/j.nima.2010.06.139. 11th International Workshop on Radiation Imaging Detectors (IWORID).

S.W. Adam, D. Harrison, V. Lobastov, and J. E. Tkaczyk. Pulse pileup statistics for energy discriminating photon counting x-ray detectors. *Medical physics*, 38 7:4265–75, 2011.

X. Llopart, R. Ballabriga, M. Campbell, L. Tlustos, and W. Wong. Timepix, a 65k programmable pixel readout chip for arrival time, energy and/or photon counting measurements. *Nuclear Instruments and Methods in Physics Research Section A: Accelerators, Spectrometers, Detectors and Associated Equipment*, 581(1):485–494, 2007. ISSN 0168-9002. doi: https://doi.org/10.1016/j.nima.2007.08.079. VCI 2007.

T. Billoud, C. Leroy, C. Papadatos, M. Pichotka, S. Pospisil, and J.S. Roux. Characterization of a pixelated CdTe timepix detector operated in ToT mode. *Journal of Instrumentation*, 12(01):P01018–P01018, jan 2017. doi: 10.1088/1748-0221/12/01/p01018.

A.M. Alessio and L.R. MacDonald. Quantitative material characterization from multi-energy photon counting ct. *Medical Physics*, 40(3):031108, 2013. doi: https://doi.org/10.1118/1.4790692.

T. Maji, M. Matsumoto, F. Kaibuki, and K. Ogawa. Material decomposition using a singular value decomposition method. In *2013 IEEE Nuclear Science Symposium and Medical Imaging Conference (2013 NSS/MIC)*, pages 1–4, 2013. doi: 10.1109/NSSMIC.2013.6829379.

Z. Yu, S. Leng, S.M. Jorgensen, Z. Li, R. Gutjahr, B. Chen, X. Duan, A. F. Halaweish, L. Yu, E.L. Ritman, and C. H. McCollough. Initial results from a prototype whole-body photon-counting computed tomography system. In Christoph Hoeschen and Despina Kontos, editors, *Medical Imaging 2015: Physics of Medical Imaging*, volume 9412, pages 212–218. International Society for Optics and Photonics, SPIE, 2015.

L. Ren, M.U. Ghani, D. Wu, B. Zheng, Y. Chen, and H. Liu. The impact of spectral filtration on image quality in micro-CT system. *Journal of applied clinical medical physics.*, 17(1), 2016.

A. Sarno, G. Mettivier, B. Golosio, P. Oliva, G. Spandre, L.F. Di, C. Fedon, R. Longo, and P. Russo. Imaging performance of phase-contrast breast computed tomography with synchrotron radiation and a cdte photon-counting detector. *Physica medica : PM : an international journal devoted to the applications of physics to medicine and biology : official journal of the Italian Association of Biomedical Physics (AIFB)*, 32(5):681—690, May 2016. ISSN 1120-1797. doi: 10.1016/j.ejmp.2016.04.011.

L. Brombal, S. Donato, D. Dreossi, F. Arfelli, D. Bonazza, A. Contillo, P. Delogu, V.D. Trapani, B. Golosio, G. Mettivier, P. Oliva, L. Rigon, A. Taibi, and R. Longo. Phase-contrast breast CT: the effect of propagation distance. *Physics in Medicine & Biology*, 63(24):24NT03, dec 2018. doi: 10.1088/1361-6560/aaf2e1.

P. Oliva, V.D. Trapani, F. Arfelli, L. Brombal, S. Donato, B. Golosio, R. Longo, G. Mettivier, L. Rigon, A. Taibi, G. Tromba, F. Zanconati, and P. Delogu. Experimental optimization of the energy for breast-CT with synchrotron radiation. *Scientific Reports*, 10(1), oct 2020. doi: 10.1038/s41598-020-74607-7.

K.X. Huang, Z. Deng, X.F. Xu, and Y.X. Xing. Optimized energy thresholds in a spectral computed tomography scan for contrast agent imaging. *Nuclear Science and Techniques*, 30(3):38, 2019. ISSN 2210-3147. doi: 10.1007/s41365-019-0563-9.

P. He, B. Wei, W. Cong, and G. Wang. Optimization of K-edge imaging with spectral CT. *Medical physics*, 39(11):6572–6579, nov 2012. ISSN 0094-2405 (Print). doi: 10.1118/1.4754587.

B. Meng, W. Cong, Y. Xi, D.M. Bruno, and G. Wang. Energy Window Optimization for X-Ray K-Edge Tomographic Imaging. *IEEE transactions on bio-medical engineering*, 63(8):1623–1630, aug 2016. ISSN 1558-2531 (Electronic). doi: 10.1109/TBME.2015.2413816.

F. Brun, D.V. Trapani, D. Batey, S. Cipiccia, and C. Rau. Edge-subtraction X-ray ptychographic imaging with pink beam synchrotron radiation and a single photon-counting detector. *Scientific Reports*, 10 (1):1–7, 2020a. ISSN 20452322. doi: 10.1038/s41598-020-63161-x.

F. Brun, D.V. Trapani, J. Albers, P. Sacco, D. Dreossi, L. Brombal, L. Rigon, R. Longo, A. Mittone, C. Dullin, A. Bravin, and P. Delogu. Single-shot K-edge subtraction x-ray discrete computed tomography with a polychromatic source and the Pixie-III detector. *Physics in Medicine and Biology*, 65(5): 0–20, 2020b. ISSN 13616560. doi: 10.1088/1361-6560/ab7105.

M. Chmeissani, C. Frojdh, O. Gal, X. Llopart, J. Ludwig, M. Maiorino, E. Manach, G. Mettivier, M.C. Montesi, C. Ponchut, P. Russo, L. Tlustos, and A. Zwerger. First experimental tests with a cdte photon counting pixel detector hybridized with a medipix2 readout chip. *Nuclear Science, IEEE Transactions on*, 51:2379 – 2385, 11 2004. doi: 10.1109/TNS.2004.832324.

C. Xu, M. Danielsson, and H. Bornefalk. Evaluation of energy loss and charge sharing in cadmium telluride detectors for photon-counting computed tomography. *IEEE Transactions on Nuclear Science*, 58(3): 614–625, 2011. doi: 10.1109/TNS.2011.2122267.

S. Amendolia, M. Giuseppina, P. Delogu, M. Fantacci, G. Paternoster, V. Rosso, and A. Stefanini. Characterization of a mammographic system based on single photon counting pixel arrays coupled to gaas x-ray detectors. *Medical physics*, 36:1330–9, 05 2009. doi: 10.1118/1.3097284.

L. Ren, B. Zheng, and H. Liu. Tutorial on x-ray photon counting detector characterization. *Journal of X-ray science and technology*, 26 1:1–28, 2018.

K. Taguchi, Eric C. Frey, X. Wang, J. S Iwanczyk, and W. C. Barber. An analytical model of the effects of pulse pileup on the energy spectrum recorded by energy resolved photon counting x-ray detectors. *Medical Imaging 2010: Physics of Medical Imaging*, 7622(August):76221C, 2010. ISSN 16057422. doi: 10.1117/12.843753.

S.S. Hsieh, P.L. Rajbhandary, and N.J. Pelc. Spectral resolution and high-flux capability tradeoffs in cdte detectors for clinical ct. *Medical Physics*, 45(4):1433–1443, 2018. doi: https://doi.org/10.1002/mp.12799.

A. Lindstrom, S. Mirbt, B. Sanyal, and M. Klintenerg. Native defects in cdte. te antisite and cd vacancy. *Journal of Physics: Condensed Matter*, 2015.

M. Niraula, A. Nakamura, T. Aoki, Y. Tomita, and Y. Hatanaka. Stability issues of high-energy resolution diode type CdTe nuclear radiation detectors in a long-term operation. *Nuclear Instruments and Methods in Physics Research, Section A: Accelerators, Spectrometers, Detectors and Associated Equipment*, 491 (1-2):168–175, 2002. ISSN 01689002. doi: 10.1016/S0168-9002(02)01175-0.

H.L. Malm and M. Martini. Polarization phenomena in CdTe nuclear radiation detectors. *IEEE (Inst Elec Electron Eng), Trans Nucl Sci*, NS-21(1):322–330, 1974. doi: 10.1109/TNS.1974.4327478.

R.O. Bell, G. Entine, and H.B. Serreze. Time-dependent polarization of CdTe gamma-ray detectors. *Nuclear Instruments and Methods*, 117(1):267–271, 1974. doi: 10.1016/0029-554X(74)90408-X.

V. Astromskas, E.N. Gimenez, A. Lohstroh, and N. Tartoni. Evaluation of Polarization Effects of e-Collection Schottky CdTe Medipix3RX Hybrid Pixel Detector. *IEEE Transactions on Nuclear Science*, 63(1):252–258, 2016. ISSN 00189499. doi: 10.1109/TNS.2016.2516827.

S.D. Sordo, L. Abbene, E. Caroli, A.M. Mancini, A. Zappettini, and P. Ubertini. Progress in the development of CdTe and CdZnTe semiconductor radiation detectors for astrophysical and medical applications. *Sensors*, 9(5):3491–3526, 2009. ISSN 14248220. doi: 10.3390/s90503491.

P. Delogu, L. Brombal, V. Di Trapani, S. Donato, U. Bottigli, D. Dreossi, B. Golosio, P. Oliva, L. Rigon, and R. Longo. Optimization of the equalization procedure for a single-photon counting CdTe detector used for CT. *Journal of Instrumentation*, 12(11), 2017. ISSN 17480221. doi: 10.1088/1748-0221/12/11/C11014.

M. Chen, C. Li, A.P. Morrison, S. Deng, C. Teng, H. Liu, H. Deng, X. Xiong, and L. Yuan. Design and implementation of a compact single-photon counting module. *Electronics*, 9(7), 2020. ISSN 2079-9292. doi: 10.3390/electronics9071131.

E. Fredenberg. Spectral and dual-energy X-ray imaging for medical applications. *Nuclear Instruments and Methods in Physics Research, Section A: Accelerators, Spectrometers, Detectors and Associated Equipment*, 878:74–87, 2018. ISSN 01689002. doi: 10.1016/j.nima.2017.07.044.

T. Poikela, J. Plosila, T. Westerlund, M. Campbell, M.D Gaspari, X. Llopart, V. Gromov, R. Kluit, M.V Beuzekom, F. Zappon, V. Zivkovic, C. Brezina, K. Desch, Y. Fu, and A. Kruth. Timepix3: A 65K channel hybrid pixel readout chip with simultaneous ToA/ToT and sparse readout. *Journal of Instrumentation*, 9(5), 2014. ISSN 17480221. doi: 10.1088/1748-0221/9/05/C05013.

E. Samei, M.J. Flynn, and D.A. Reimann. A method for measuring the presampled MTF of digital radiographic systems using an edge test device. *Medical Physics*, 25(1):102–113, 1998. ISSN 00942405. doi: 10.1118/1.598165.

V. Di Trapani, A. Bravin, F. Brun, D. Dreossi, R. Longo, A. Mittone, L. Rigon, and P. Delogu. Characterization of the acquisition modes implemented in Pixirad-1/Pixie-III X-ray Detector: Effects of charge sharing correction on spectral resolution and image quality. *Nuclear Instruments and Methods in Physics Research, Section A: Accelerators, Spectrometers, Detectors and Associated Equipment*, 955: 163220, 2020. ISSN 01689002. doi: 10.1016/j.nima.2019.163220.

T. Schoonjans, A. Brunetti, B. Golosio, M. Sanchez del Rio, V.A. Solé, C. Ferrero, and L. Vincze. The xraylib library for x-ray–matter interactions. recent developments. *Spectrochimica Acta Part B: Atomic Spectroscopy*, 66(11):776–784, 2011. ISSN 0584-8547. doi: https://doi.org/10.1016/j.sab.2011.09.011.

M. Khalil, E.S. Dreier, J. Kehres, J. Jakubek, and U.L. Olsen. Subpixel resolution in CdTe Timepix3 pixel detectors. *Journal of Synchrotron Radiation*, 25(6):1650–1657, Nov 2018. doi: 10.1107/S1600577518013838.

E.S. Dreier, C. Silvestre, J. Kehres, D. Turecek, M. Khalil, J.H. Hemmingsen, O. Hansen, J. Jakubek, R. Feidenhans'l, and U.L. Olsen. Virtual subpixel approach for single-mask phase-contrast imaging using timepix3. *Journal of Instrumentation*, 14(01):C01011–C01011, jan 2019. doi: 10.1088/1748-0221/14/01/c01011.

J. Hiller, M. Maisl, and L. Reindl. Physical characterization and performance evaluation of an x-ray micro-computed tomography system for dimensional metrology applications. *Measurement Science and Technology*, 23:085404, 06 2012. doi: 10.1088/0957-0233/23/8/085404.

G. Moroni and S. Petro. A discussion on performance verification of 3d x-ray computed tomography systems. *Procedia CIRP*, 75:125–130, 2018. ISSN 2212-8271. doi: https://doi.org/10.1016/j.procir.2018.04.064. The 15th CIRP Conference on Computer Aided Tolerancing, CIRP CAT 2018, 11-13 June 2018, Milan, Italy.

Á.R. Sanchez, A. Thompson, L. Korner, N. Brierley, and R. Leach. Review of the influence of noise in x-ray computed tomography measurement uncertainty. *Precision Engineering*, 66, 08 2020. doi: 10.1016/j.precisioneng.2020.08.004.

G. Poludniowski, A. Omar, R. Bujila, and P. Andreo. Technical note: Spekpy v2.0—a software toolkit for modeling x-ray tube spectra. *Medical Physics*, 48(7):3630–3637, 2021. doi: https://doi.org/10.1002/mp.14945.

W.T. Elam, B.D. Ravel, and J.R. Sieber. A new atomic database for x-ray spectroscopic calculations. *Radiation Physics and Chemistry*, 63(2):121–128, 2002. ISSN 0969-806X. doi: https://doi.org/10.1016/S0969-806X(01)00227-4.

G.T. Herman. *Fundamentals of computerized tomography: image reconstruction from projections Adv. Pattern Recognit.* Springer Science & Business Media, 01 2010. ISBN 978-1-85233-617-2. doi: 10.1007/978-1-84628-723-7.

F.R. Verdun, D. Racine, J.G. Ott, M.J. Tapiovaara, P. Toroi, F.O. Bochud, W.J.H. Veldkamp, A. Schegerer, R.W. Bouwman, I. Hernandez Giron, N.W. Marshall, and S. Edyvean. Image quality in ct: From physical measurements to model observers. *Physica Medica*, 31(8):823–843, 2015. ISSN 1120-1797. doi: https://doi.org/10.1016/j.ejmp.2015.08.007.

Z. Zhao, Grace J. Gang, and Jeffrey H. Siewerdsen. Noise, sampling, and the number of projections in cone-beam ct with a flat-panel detector. *Medical physics*, 41 6:061909, 2014b.

A.A. Hendriksen, D.M. Pelt, W.J. Palenstijn, S.B. Coban, and K.J. Batenburg. On-the-fly machine learning for improving image resolution in tomography. *Applied Sciences*, 9(12), 2019. ISSN 2076-3417. doi: 10.3390/app9122445.

D.M. Pelt, K.J. Batenburg, and J.A. Sethian. Improving tomographic reconstruction from limited data using mixed-scale dense convolutional neural networks. *Journal of Imaging*, 4(11), 2018. ISSN 2313-433X. doi: 10.3390/jimaging4110128.

A. Weigang and P. Jinxiao. Fast 3d image reconstruction algorithm based on artificial intelligence technology. *The International Journal of Electrical Engineering & Education*, page 002072092098504, 01 2021. doi: 10.1177/0020720920985042.

Q. Wang, J. Sun, Q. Yao, C. Ji, J. Liu, and Q. Zhu. 3d printing with cellulose materials. *Cellulose*, 25, 08 2018. doi: 10.1007/s10570-018-1888-y.

L. Dai, T. Cheng, C. Duan, W. Zhao, W. Zhang, X. Zou, J. Aspler, and Y. Ni. 3d printing using plant-derived cellulose and its derivatives: A review. *Carbohydrate Polymers*, 203:71–86, 2019. ISSN 0144-8617. doi: https://doi.org/10.1016/j.carbpol.2018.09.027.

A. Firmanda, K. Syamsu, Y.W. Sari, J. Cabral, D. Pletzer, B. Mahadik, J. Fisher, and F. Fahma. 3d printed cellulose based product applications. *Mater. Chem. Front.*, pages –, 2022. doi: 10.1039/D1QM00390A.

A. Dufresne. *Nanocellulose: From Nature to High Performance Tailored Materials*. De Gruyter, 2012. ISBN 9783110254600. doi: doi:10.1515/9783110254600.

K. Markstedt, J. Sundberg, and P. Gatenholm. 3d bioprinting of cellulose structures from an ionic liquid. *3D Printing and Additive Manufacturing*, 1(3):115–121, 2014. doi: 10.1089/3dp.2014.0004.

C. Thibaut, A. Denneulin, S. Rolland du Roscoat, D. Beneventi, L. Orgéas, and D. Chaussy. A fibrous cellulose paste formulation to manufacture structural parts using 3d printing by extrusion. *Carbohydrate Polymers*, 212:119–128, 2019. ISSN 0144-8617. doi: https://doi.org/10.1016/j.carbpol.2019.01.076.

V. Klar, P. Karki, H. Orelma, and P. Kuosmanen. Analysis of drying deformation of 3d printed nanocellulose structures. In Ulrich Hirn, editor, *Cellulose Materials Doctoral Students Conference 2017*, pages 85–91. Graz University of Technology, TUG, October 2017. Cellulose Materials Doctoral Students Conference ; Conference date: 23-10-2017 Through 25-10-2017.

R. Rémond, I. Turner, and P. Perre. Modeling the drying and heat treatment of lignocellulosic biomass: 2d effects due to the product anisotropy. *Drying Technology*, 28:1013–1022, 08 2010. doi: 10.1080/07373937.2010.497093.

W.W. Sampson and J. Yamamoto. The drying shrinkage of cellulosic fibres and isotropic paper sheets. *Journal of Materials Science*, 46:541–547, 2011.

G.W. Scherer. Theory of drying. *Journal of the American Ceramic Society*, 73(1):3–14, 1990. doi: https://doi.org/10.1111/j.1151-2916.1990.tb05082.x.

J. Thiery, S. Rodts, D. Weitz, and P. Coussot. Drying regimes in homogeneous porous medium from macro to nano-scale. *Physical Review Fluids*, 2(7), 2017. doi: 10.1103/PhysRevFluids.2.074201.

T. Zhou, K. Ioannidou, F. J. Ulm, M. Z. Bazant, and R. J. M. Pellenq. Multiscale poromechanics of wet cement paste. *Proceedings of the National Academy of Sciences*, 116(22):10652–10657, 2019. ISSN 0027-8424. doi: 10.1073/pnas.1901160116.

Y. Tang and J. Min. Water film coverage model and its application to the convective air-drying simulation of a wet porous medium. *International Journal of Heat and Mass Transfer*, 131:999–1008, 12 2018. doi: 10.1016/j.ijheatmasstransfer.2018.11.094.

T. Metzger. A personal view on pore network models in drying technology. *Drying Technology*, 37:1–16, 10 2018. doi: 10.1080/07373937.2018.1512502.

S. Huan, R. Ajdary, L. Bai, V. Klar, and O.J. Rojas. Low solids emulsion gels based on nanocellulose for 3d-printing. *Biomacromolecules*, 20 2:635–644, 2019.

A. Pfister, R. Landers, A. Laib, U. Hübner, R. Schmelzeisen, and R. Mülhaupt. Biofunctional rapid prototyping for tissue-engineering applications: 3d bioplotting versus 3d printing. *Journal of Polymer Science Part A: Polymer Chemistry*, 42(3):624–638, 2004. doi: https://doi.org/10.1002/pola.10807.

V. Klar, J. Pere, T. Turpeinen, P. Kärki, H. Orelma, and P. Kuosmanen. Shape fidelity and structure of 3d printed high consistency nanocellulose. *Scientific Reports*, 9, 03 2019. doi: 10.1038/s41598-019-40469-x.

T. Joffre, P. Isaksson, P. Dumont, S.R.D. Roscoat, S. Sticko, L. Orgeas, and E. Gamstedt. A Method to Measure Moisture Induced Swelling Properties of a Single Wood Cell. *Experimental Mechanics*, 56(5):723–733, June 2016. doi: 10.1007/s11340-015-0119-9.

J. Viguie, P.J.J. Dumont, E. Mauret, S.R.D. Rolland, P. Vacher, I. Desloges, and J.F. Bloch. Analysis of the hygroexpansion of a lignocellulosic fibrous material by digital correlation of images obtained by X-ray synchrotron microtomography: application to a folding box board. *Journal of Materials Science*, 46(14):pp. 4756–4769, 2011. doi: 10.1007/s10853-011-5386-y.

P. Lhuissier, X. Bataillon, C. Maestre, J. Sijobert, E. Cabrol, P. Bertrand, E. Boller, A. Rack, J.J. Blandin, L. Salvo, and G. Martin. In situ 3d x-ray microtomography of laser-based powder-bed fusion (l-pbf)—a feasibility study. *Additive Manufacturing*, 34:101271, 2020. ISSN 2214-8604. doi: https://doi.org/10.1016/j.addma.2020.101271.

T. Ridler. Picture thresholding using an iterative selection method. *IEEE Transactions on Systems, Man, and Cybernetics*, 8:630–632, 1978a.

V. Boulos, V. Fristot, D. Houzet, L. Salvo, and P. Lhuissier. Investigating performance variations of an optimized GPU-ported granulometry algorithm. In *DASIP 2012 - Conference on Design and Architectures for Signal and Image Processing*, pages 1–6, Karlsruhe, Germany, October 2012.

O. Stamati, E. Ando, E. Roubin, R. Cailletaud, M. Wiebicke, G. Pinzon, C. Couture, R. C. Hurley, R. Caulk, D. Caillerie, T. Matsushima, P. Besuelle, F. Bertoni, T. Arnaud, A. O. Laborin, R. Rorato, Y. Sun, A. Tengattini, O. Okubadejo, J. B. Colliat, M. Saadatfar, F. E. Garcia, C. Papazoglou, I. Vego, S. Brisard, J. Dijkstra, and G. Birmpilis. spam: Software for Practical Analysis of Materials. *Journal of Open Source Software*, 5(51):2286, July 2020. doi: 10.21105/joss.02286.

F. Chalencon, L. Orgeas, P.J.J. Dumont, G. Foray, J.Y. Cavaille., E. Maire, and S.R.D. Roscoat. Lubricated compression and X-ray microtomography to analyse the rheology of a fibre-reinforced mortar. *Rheologica Acta*, 49(3):221–235, 2010.

S. A. Wainwright. *Mechanical Design in Organisms*. Princeton University Press, 1982. ISBN 9780691218090. doi: doi:10.1515/9780691218090.

D. Markl, J. Zeitler, C. Rasch, M.H. Michaelsen, A. Müllertz, J. Rantanen, T. Rades, and J. Bøtker. Analysis of 3d prints by x-ray computed microtomography and terahertz pulsed imaging. *Pharmaceutical Research volume*, 03 2017. doi: 10.17863/CAM.8198.

M. Edali, N. Esmail, and G. Vatistas. Rheological properties of high concentrations of carboxymethyl cellulose solutions. *Journal of Applied Polymer Science*, 79:1787–1801, 03 2001. doi: 10.1002/1097-4628(20010307)79:103.0.CO;2-2.

O. Ludwig, M. Di Michiel, L. Salvo, M. Suery, and P. Falus. In situ Three-Dimensional microstructural investigation of solidification of an Al-Cu alloy by ultra-fast X-Ray microtomography. *Metallurgical and Materials Transactions A*, 36A:1515–1523, 2005. doi: 10.1007/s11661-005-0243-8.

Michel Suéry, Sofiane Terzi, Bastien Mireux, Luc Salvo, Jérôme Adrien, and Eric Maire. Fast in situ X-Ray microtomography observations of solidification and semisolid deformation of Al-Cu alloys. *JOM Journal of the Minerals, Metals and Materials Society*, 64(1):83–88, 2012. doi: 10.1007/s11837-011-0219-7.

J.L. Fife, J.W. Gibbs, E.B. Gulsoy, C.L. Park, K. Thornton, and P.W. Voorhees. The dynamics of interfaces during coarsening in solid-liquid systems. *Acta Materialia*, 70:66–78, May 2014. ISSN 1359-6454. doi: 10.1016/j.actamat.2014.01.024.

S. Terzi, L. Salvo, M. Suery, A.K. Dahle, and E. Boller. Coarsening mechanisms in a dendritic al–10 *Acta Materialia*, 58(1):20–30, 2010. ISSN 1359-6454. doi: https://doi.org/10.1016/j.actamat.2009.08.052.

T. Ridler. Picture thresholding using an iterative selection method. *IEEE Transactions on Systems, Man, and Cybernetics*, 8:630–632, 1978b.

W. Lorensen and H. Cline. Marching cubes: A high resolution 3d surface construction algorithm. *ACM SIGGRAPH Computer Graphics*, 21:163–, 08 1987. doi: 10.1145/37401.37422.

Abstract

This study deals with developments to increase the possibilities offered by laboratory X-ray computed tomography (CT) in material science by focusing on contrast enhancement and on time resolution aspects. First, the feasibility of using a new generation photon-counting detector (PCD) in lab-CT was evaluated. The characterization of the standard imaging performances and the spectral capabilities of four PCDs were carried out and compared to a standard flat-panel detector. The potential of PCD towards spectral and single-shot K-edge imaging was investigated. Second, a model-based optimization strategy is developed to define the suitable CT scanning parameters for dynamic in situ acquisitions with an image quality allowing qualitative or quantitative analysis. The model is based on three modules: modelling noise in the feature of interest, X-ray absorption simulation tool, and the screening algorithm that outputs the different possible scanning configurations associated with the probability of detection of the interested feature size for each configuration. A real-time in-situ test with the sub-minute temporal resolution was performed with the experimentally optimized CT setup. The experimental configuration is confronted with the proposed optimization model configurations, which were found to be in-line with the chosen setup. The application corresponds to the real-time monitoring of microstructural evolution of 3D printed cellulose parts during air-drying phenomena with qualitative and quantitative analysis. It illustrates the quantitative characterization capabilities of lab-CT for high-speed in-situ imaging.

Keywords: X-ray tomography, In-situ tomography, Time-resolved imaging, Photon-counting detector, Parameter optimization, Image analysis